İZMİR KÂTİP ÇELEBİ ÜNİVERSİTESİ
2010
GRADUATE SCHOOL OF NATURAL AND APPLIED SCIENCES

Evaluation of the Displacement Behavior of Wide Beam Frames Using Nonlinear Static and Dynamic Analyses

Submitted to the Graduate School of Natural and Applied Sciences in partial fulfillment of the requirements for the degree of

Doctor of Philosophy

in Civil Engineering

by

Ornela Şen

ORCID 0000-0001-8902-1120

May, 2022

This is to certify that we have read the thesis **Evaluation of the Displacement Behavior of Wide Beam Frames Using Nonlinear Static and Dynamic Analyses** submitted by **Ornela Şen**, and it has been judged to be successful, in scope and in quality, at the defense exam and accepted by our jury as a DOCTORAL THESIS.

APPROVED BY:

Advisor: **Prof. Dr. Mehmet Çevik**
İzmir Kâtip Çelebi University

Committee Members:

Prof. Dr. Ali Haydar Kayhan
Pamukkale University

Assoc. Prof. Dr. Mutlu Seçer
İzmir Kâtip Çelebi University

Assist. Prof. Dr. Selçuk Saatcı
İzmir Institute of Technology

Assist. Prof. Dr. Mehmet Alper Çankaya
İzmir Kâtip Çelebi University

Date of Defense: May 12, 2022

Declaration of Authorship

I, **Ornela Şen**, declare that this thesis titled **Evaluation of the Displacement Behavior of Wide Beam Frames Using Nonlinear Static and Dynamic Analyses** and the work presented in it are my own. I confirm that:

- This work was done wholly or mainly while in candidature for the Doctoral degree at this university.
- Where any part of this thesis has previously been submitted for a degree or any other qualification at this university or any other institution, this has been clearly stated.
- Where I have consulted the published work of others, this is always clearly attributed.
- Where I have quoted from the work of others, the source is always given. This thesis is entirely my own work, with the exception of such quotations.
- I have acknowledged all major sources of assistance.
- Where the thesis is based on work done by myself jointly with others, I have made clear exactly what was done by others and what I have contributed myself.

Date: 12.05.2022

Evaluation of the Displacement Behavior of Wide Beam Frames Using Nonlinear Static and Dynamic Analyses

Abstract

Wide beam frames are a substructural type of reinforced concrete frames, in which the beam sections are shallow and wide. Typically, the depth of the beams is the same as the depth of the slabs, and therefore these beams are hidden from view and provide aesthetically appealing ceilings in residential structures. However, since the beam sections are slender and flexible, RC structures constructed with wide beams are deemed not suitable to withstand moderate to high seismic action. These types of frames are often deemed to not be capable of ductile behavior.

An analytical investigation of 30 frame models is presented in this thesis. The frame models have different geometric configurations were designed according to the Turkish Building Earthquake Code. Of these models, 10 were conventional beam frames used as reference, and 20 were wide beam frames. Their seismic capacities were obtained from pushover analyses. A considerable number of time-history analyses were performed on each model to obtain their displacement demands. The data obtained from the time-history analyses were statistically processed to obtain expected (mean) displacement demands, demand ranges for a desired confidence level and fragility functions. The displacement demand was mainly assessed in terms of global drift ratio and was compared to the displacement capacities obtained from pushover analyses. The interstory drift ratios were also estimated and were used to obain insight into the damage spread among the floors. Besides displacement

parameters, initial stiffness and energy dissipation values were also computed for the frame models.

The results of these analyses showed that code-compliant wide beam frames perform satisfactory under seismic loading. They are more flexible than the conventional beam frames and are subjected to higher displacement demands, but they also have greater displacement and energy dissipation capacities. An important outcome of this study was the generation of the fragility functions of the global drift ratios for all the frames.

Keywords: wide beam frames, RC frames, pushover analyses, time history analyses, FEMA P-58, fragility functions, displacement demand, global drift ratio

Doğrusal Olmayan Statik ve Dinamik Analizler Kullanarak Yassı Kirişli Çerçevelerinin Yer Değiştirme Davranışının Değerlendirilmesi

Öz

Yassı kirişli çerçeveler, kiriş kesitlerinin sığ ve geniş olduğu bir betonarme çerçeve tipidir. Genel olarak, bu kirişlerin derinliği döşemelerin derinliği ile aynıdır ve tavanda görünmemektedir, böylece daha estetik bir görünüm sağlamaktadır. Ancak, kiriş kesitleri narin ve esnek olduğundan, yassı kirişlerle inşa edilen betonarme yapıların, orta ila yüksek sismik sarsıntılara karşı dayanıma sahip olmadığını düşünülmektedir. Bu tip çerçevelerin genellikle sünek davranışa sahip olmadığını kabul edilir.

Bu tezde 30 çerçeve modelinin analitik bir incelemesi sunulmaktadır. Farklı geometrik konfigürasyonlara sahip çerçeve modelleri, Türkiye Bina Deprem Yönetmeliği'ne göre tasarlanmıştır. Bu modellerden 10 tanesi referans olarak kullanılan normal kirişli çerçeveler olup 20 tanesi ise yassı kirişli çerçevelerdir. Çerçevelerin sismik kapasiteleri itme analizlerinden elde edilmiştir. Yer değiştirme taleplerini elde etmek için her model üzerinde çok sayıda zaman tanım alanı analizi yapılmıştır. Zaman tanım alanı analizlerinden elde edilen veriler, beklenen (ortalama) yer değiştirme taleplerini, istenen güven düzeyi için talep aralıklarını ve kırılganlık fonksiyonlarını elde etmek için istatistiksel olarak işlenmiştir. Yer değiştirme talepleri esas olarak ötelenme oranı cinsinden değerlendirilmiştir ve itme analizlerinden elde edilen yer değiştirme

kapasiteleriyle karşılaştırılmıştır. Göreli kat ötelenme oranları da değerlendirilmiştir ve katlarda oluşan hasar hakkında fikir edinmek için kullanılmıştır. Çerçeve modelleri için yer değiştirme parametrelerinin yanı sıra başlangıç rijitliği ve enerji tüketim değerleri de hesaplanmıştır.

Bu analizlerin sonuçları, kurallara uygun tasarlanan ve inşa edilen yassı kirişli çerçevelerin sismik yüklerin altında tatmin edici bir performans sergilediğini göstermiştir. Yassı kirişli çerçevelerin, normal kirişli çerçevelerden daha esnek oldukları ve daha yüksek yer değiştirme taleplerine sahip oldukları gözlenmiştir, ancak aynı zamanda daha büyük yer değiştirme ve enerji tüketim kapasitelerine sahiplerdir. Bu çalışmanın önemli bir çıktısı, bütün çerçeveler için üretilmiş olan kırılganlık fonksyonlarıdır.

Anahtar Kelimeler: yassı kiriş, betonarme çerçeveler, itme analizi, zaman tanım analizi, FEMA P-58, kırılganlık fonksyonları, deplasman talebi, ötelenme oranı

This thesis is dedicated to my closest and dearest family who supported me and motivated me to go through even when I had no hope and aspiration left. I dedicate this work particularly to my husband, who has been a constant and immense source of support, motivation, and inspiration during the time it took to complete this work. Thank you for being my most trusted companion and teacher during this journey, whose end I would have probably never seen without your presence

Acknowledgment

The author would like to thank the support and guidance provided by the thesis supervisor Prof. Dr. Mehmet Çevik throughout the course of the studies. Special thanks go to Prof. Dr. Ali Haydar Kayhan for his support and guidance with the time-history analyses and the statistical evaluation of the results; and to Dr. Ahmet Demir for providing the ground motion record sets that were used in this thesis. The author is also thankful to the jury members Assoc. Prof. Dr. Mutlu Seçer and Dr. Selçuk Saatcı for their feedback, positive criticism and suggestions, which helped improve the scope of this thesis. The author would also like to thank the TÜBİTAK 2215 Graduate Scholarshıp Program for Internatıonal Students for their support from May 2014 to May 2018. Finally, many thanks to my husband and our families. Their understanding and support on what seemed an endless endevour has been very important.

Table of Contents

List of Figures

List of Tables

List of Abbreviations

ANOVA	Analysis of Variance
BHC	Building Height Class
CBF	Conventional Beam Frames
CD	Controlled Damage
CoV	Coefficient of Variance
CP	Collapse Prevention
FEMA	Federal Emergency Management Agency
GDR	Global Drift Ratio
HDC	High Ductility Class
IDR	Interstory Drift Ratio
LD	Limited Damage
LDC	Limited Ductility Class
MDC	Mixed Ductility Class
MIDR	Mean Interstory Drift Ratio
PGA	Peak Ground Acceleration
PNE	Probability of Non-exceedance
RC	reinforced concrete
SDC	Seismic Design Class
TBEC	Turkish Building Earthquake Code
TEC	Turkish Earthquake Code
WBF	Wide Beam Frames

List of Symbols

A_c	Total concrete area of a section
a_d	Equivalent width of an infill wall
a_i	Centerline-to-centerline distance between the longitudinal reinforcement
A_s	Total area of the longitudinal reinforcement of a section
A_{sw}	Total area of the transverse reinforcement of a section
b_0	The width of the concrete core of a section between the transverse reinforcement legs, measured centerline-to-centerline
b_c	Column width
b_e	Effective width of the flange of T-beams
b_w	Beam width
d	Section depth
d_b	The average diameter of the reinforcement rebars in an RC section
D_c	Cracking displacement of infill wall
D_m	Displacement at the maximum force of infill wall
D_u	Ultimate displacement of infill wall
E	Energy dissipation
E_c	Elastic modulus of concrete
E_d	Elastic modulus of the infill wall
E_{sec}	Secant elastic modulus of confined concrete at the peak stress
F_1	Local soil coefficient for 1 s period
f_c	Compressive stress of confined concrete
F_c	Cracking force of infill wall

f_{cc}	Compressive strength of confined concrete
f_{co}	Compressive strength of unconfined concrete
f_{ctd}	Tensile strength of concrete
f_e	Effective confinement strength for confined concrete
F_m	Maximum force of infill wall
F_S	Local soil coefficient for short period
f_s	Reinforcement steel stress
f_{su}	Tensile strength of reinforcement steel
f_{sy}	Yield strength of reinforcement steel
f_{tp}	The strength of the infill wall determined from diagonal compression tests
f_{ywd}	Yield strength of transverse reinforcement steel
g	Dead load
g_w	Infill wall load
G_w	Shear modulus of the infill wall
H	Total building height
h_0	The height of the concrete core of a section between the transverse reinforcement legs, measured centerline-to-centerline
h_c	Column height
H_w	Height of the infill wall
i	Number of the set of ground motion records
I_k	Moment of inertia of column
j	Number of the record within a set
k	Floor number
K_e	Lateral confinement coefficient for concrete
k_e	Initial stiffness of the frames
K_i	Initial stiffness of the infill wall
l	Beam length

L_p	Length of plastic hinge
L_s	Shear span of the element
L_w	Length of the infill wall
M_w	Earthquake magnitude
m_{GDR}	The mean GDR of a set of time-history analyses
m_{IDRk}	The mean IDR of a set of time-history analyses for the k-th floor
N_d	The axial load acting on a section
q	Live load
r_d	Length of the diagonal of the infill wall
s	Stirrup spacing
S_1	Spectral acceleration for 1 s period
S_{ae}	Horizontal elastic design spectral acceleration
S_{D1}	Design spectral acceleration coefficient for 1 s period
S_S	Short period spectral acceleration
T_A	Corner period of the response spectrum
T_B	Corner period of the response spectrum
t_d	Thickness of the infill wall
T_L	Constant displacement zone period
T_p	Fundamental period of the structure
V	Base shear
V_{max}	Maximum base shear of a structure
V_r	Shear capacity of an RC section
V_y	Yield base shear of a structure
W	Total weight of a structure
x	The normalized concrete strain with respect to strain at peak strength for confined concrete
α_1	Mass participation factor for the first vibration mode

α_2	Mass participation factor for the second vibration mode
β_c	Dispersion for the construction quality assurance
β_{gm}	Dispersion due to ground motion variability
β_m	Total modeling dispersion
β_q	Dispersion for the quality of the analytical model
Δ	Rooftop displacement
Δ_{max}	Maximum rooftop displacement obtained from time-history analyses
δ_{max}	Maximum interstory displacement obtained from time-history analyses
Δ_y	Rooftop displacement when the structure has yielded
ε_c	Concrete strain
ε_{c0}	Strain at peak stress for unconfined concrete
ε_{cc}	Strain at peak stress for confined concrete
ε_{sh}	Strain hardening strain of reinforcement steel
ε_{su}	Ultimate strain for reinforcement steel
ε_{sy}	Yield strain of reinforcement steel
γ	Coefficient that reflects the effect of the axial load on the cracking capacity of a section
λ_d	Coefficient of the equivalent compression strut
μ	Ductility
μ_{GDR}	The mean GDR of 30 sets of time-history analyses
μ_{IDRk}	The mean IDR of 30 sets of time-history analyses for the *k-th* floor
ϕ_u	Curvature of an RC section at collapse prevention
ϕ_y	Curvature of an RC section at yield
σ	Standard deviation
θ	The angle of the diagonal of the infill wall with respect to the horizontal axis
θ_p^{CD}	Plastic rotation for CD

θ_p^{CP}	Plastic rotation for CP
θ_p^{LD}	Plastic rotation for LD

Chapter 1

Introduction

The improvements in construction technology and the increase in the knowledge of the behavior of structures have led to a rapid increase in construction of residential and commercial or governmental structures around the world. This has been followed by more regulations regarding urban planning and cityscapes. Additionally, to appeal to customers, architects have come up with more creative solutions to make the structures they design more functional and aesthetically pleasing. One of the outcomes of these changes is the emergence of the use of hidden beams in reinforced concrete construction. They are more common in residential structures, where suspended ceilings are not widely used.

Hidden beams are, as the name itself suggests, beams that are not visible to the eye. They perform two main duties. Being hidden in the ceiling, they are more aesthetically pleasing than normal beams who may run through in the middle of the ceiling of the rooms and show. They also create more headspace and may facilitate the installation of HVAC systems. Hidden beams are generally encountered in ribbed slab systems.

A ribbed slab, as shown in Figure 1.1 consists of a thin concrete layer, 5-7 cm thick, reinforced by a grid of steel bars running in both directions. A series of ribs placed at regular intervals runs in one direction, thus making this slab system a one-way slab. The ribs, shown in close-up in Figure 1.2 are generally small and have nominal reinforcement. The space between the ribs can be filled to make the plastering and finishing work on the ceiling easier. One option is polystyrene, which can be used as a filler, due to its negligible weight. However, polystyrene is a controversial material, because it is highly flammable, non-biodegradable and it is thought to be cancerogenic. Another alternative are hollow bricks, which add little weight to the slab itself. On the other hand, they add some rigidity to the ribbed slabs.

Figure 1.1: A ribbed slab during construction

Figure 1.2: Close-up of the rib beams in a ribbed slab

Flat slab systems are similar to ribbed slab systems, but the beam type used in the flat slabs is different. In flat slabs, strips of slabs are more heavily reinforced and detailed as beams, while in ribbed slabs, actual beams, sometimes normal, sometimes hidden

beams are used. Hidden beams are more commonly referred to as wide beams, which will be the term used in this thesis from this point on.

Wide beams are quite common in buildings in Turkey. They are generally found in the ribbed slab systems called *asmolen*, after the name of the brick type used for filling the space between the ribs. They can be used throughout the whole structure, or in some of the floors only. Besides Turkey, many other Mediterranean countries, such as Italy, Spain, Greece and Albania also use this type of construction. Both ACI 318 [1] and Eurocode [2] regulate the design and construction of ribbed slabs.

1.1 Summary of Important Seismic Events in the Last Decades

The Mediterranean basin is a highly seismic region, with many moderate and heavy earthquakes that have occurred even in the recent years. Often times, even moderate earthquakes turn out to be devastating due to the poor quality of the buildings, which may be traced to both design and construction practices. For instance the earthquake that hit Molise in Italy in 2002 had a magnitude of M_w=5.7, resulted in the collapse of many schools and the death of 27 children [3]. The inspection that followed afterwards, resulted in unsafe placarding of 40% of structures, due to their high vulnerability [4]. In 2009 a moderate earthquake of magnitude M_w=6.3 hit L'Aquila, Italy, which resulted in 308 casualties and considerable damage to the structures [5]. Most of the damage was imparted to nonstructural elements such as infill walls [6, 7]. One year later, the region of Emilia-Romagna was hit by another devastating series of earthquakes, with the main shocks having a magnitude of M_w=5.8-5.9. Considerable damages were observed in structures [8], and life loss and heavy economic damages were also reported to have incurred [9].

The city of Lorca in Spain was hit by an earthquake of magnitude M_w=5.1 in 2011. It caused only two collapses, but the damages on older structures were considerable [10, 11]. Damage to infill walls and other nonstructural elements was reported and the need to account their seismic response in design was put forth [12]. Two more notable earthquakes have hit Spain in the recent years, the deep earthquake of Granada in 2010

[13], which caused no damages, and the Alboran Sea earthquake of 2016, which caused damages to mostly nonstructural members [14].

Greece also has a very high seismic activity. In the recent times several large earthquakes have occurred, of which some have caused damages and some not. To mention a few are the earthquake of Aigio in 1995 [15], which despite its magnitude of M_w=6.4 caused little damage even to buildings not designed for seismic forces. The high variability in ground motion intensity across the affected area was thought to be the reason for lesser damages than expected from an earthquake of such magnitude. In 1999, an earthquake of magnitude M_w=5.9 hit Athens and resulted in 150 deaths and 80 collapses [16]. Many reinforced concrete structures suffered damages in spite of good workmanship observed [17]. The Greek islands of Lesvos and Kos were hit by moderate earthquakes in 2017. In Lesvos, the earthquake of magnitude M_w=6.3 caused considerable damages to reinforced concrete structures [18, 19]. The earthquake that hit the island of Kos caused a tsunami which was responsible for damages both in the island of Kos and in mainland Turkey, in Bodrum province [20, 21].

Turkey is another large country in the Mediterranean basin, which has experienced several big earthquakes and heavy damages from time to time. The earthquakes of İzmit and Düzce in 1999 were two earthquakes with very high magnitude and catastrophic consequences. The İzmit earthquake had a magnitude of M_w=7.4 and the Düzce earthquake had a magnitude of M_w=7.2 [22]. A large number of buildings, including reinforced concrete collapsed or were heavily damaged during these two earthquakes. The structural damages were often the result of poor material properties, poor workmanship and insufficient design practices of the previous codes [23]. These seismic events set the stage for the revision of seismic design practices and the publication of the Turkish Building Code [24]. It also set the stage for the assessment and strengthening of many structures, mostly public buildings such as schools, hospitals and municipalities. Finally, it started the process of Urban Regeneration, which continues to this day. In this process, residential structures are assessed per the will of the owners, and if found at high risk, deals are made with construction companies, which otherwise would not be able to build in highly populated and central areas, due to the lack of developable land. Nonetheless, several more serious earthquakes have hit Turkey from these two pivotal events. In 2003, the province of

Bingöl was hit by an earthquake of magnitude M_w=6.3. A total of 1351 buildings were reported to be heavily damaged or collapsed [25]. In 2010 and earthquakes of magnitude M_w=5.5-6.1 hit the province of Elazığ and caused the collapse and damage of many structures. The main cause of damage was noted to be poor workmanship and material quality [26, 27]. The Van earthquakes of 2011 had magnitudes M_w=5.6 and M_w=7.1. 600 casualties were reported [28] and the number of damaged or collapsed buildings reached 35000 [29]. It was noted that the response spectra calculated from the earthquake that hit Van was lesser than the code-based spectra of the design code in power at the time, leaving place for questioning whether the designs were not code-compliant or the application was not done properly [30]. Bikçe and Çelik [31] partially answered this question, when investigating a new structure designed according to the Turkish Earthquake Code (TEC) and found that while the design of the case study structure was code-conforming, the construction was not performed in accordance with the project and TEC. One of the recent damaging seismic events in Turkey is the Elazığ-Sivrice earthquake of 2020 which had a magnitude of M_w=6.7 [32]. A quick assessment performed after the event reported that 547 buildings collapsed, 6270 buildings were heavily damaged and 962 buildings were moderately damaged [33]. The death toll of this earthquake was 41. The last major earthquake to date to hit Turkey was in 30 October 2020 in vicinity of the province of İzmir and Samos Island. Considerably more damage was observed in İzmir than in Samos due to several reasons. For once, the soft soils that make up the downtown İzmir amplified the spectral accelerations in the mid-to-long period range. Additionally, the building stock of İzmir is characterized by mid-to-high rise RC structures, while in Samos low rise masonry structures are more prominent. Finally, İzmir is a highly populous and dense city thus heavier damages were observed [34].

Albania is a small country in the western Balkans, which is also included in the Mediterranean region, and is considered to have a relatively high seismic activity. The earthquake that hit Tirana in 1988 and had an intensity of M_w=5.7 was the last earthquake with serious consequences until recently. No collapses nor casualties were reported for this event; however damages were observed in some of the buildings located in the area affected. The buildings were mostly masonry structures [35]. In 2019 the city of Durres was hit by two major earthquakes, one in September and then in November [36]. The earthquakes were felt in the nearby city of Tirane and in Italy,

Greece, Montenegro and North Macedonia [37]. This earthquake killed 51 people, injured 3000-5000 others, and left 14000 people homeless. A considerable amount of structures collapse or became unusable due to the high risk. The observed damages were either located in nonstructural elements such as infill walls, or caused by their collapse [38].

So far, major seismic events that have occurred in the last 20-30 years in the neighboring region were summarized. In the next paragraphs, some of the most devastating seismic events that have occurred around the world, mostly in the region known as the Ring of Fire, the region around much of the rim of the Pacific Ocean, are presented.

In 1985 a devastating earthquake of magnitude M_s=8.1 hit Mexico City, followed by an aftershock of magnitude M_s=7.5. The intensity of the ground motion exceeded the expected intensities relayed in the seismic codes. This factor, together with the long duration of the ground motion contributed to the extensive damages that were observed. These damages included a death toll of approximately 20000, and 800-1000 buildings either collapsed or were heavily damaged [39]. High rise structures, which were designed according to the best practices available at the time suffered damages, top floor collapse was observed in a considerable portion of these buildings [40, 41].

The West Coast of the United States of America was hit by two major earthquakes in 1989 in Loma Prieta and 1994 in Northridge. The Loma Prieta earthquake had a magnitude of 7.1 and caused 64 deaths [42] as wells as structural damage predominantly due to pounding, mostly in older structures [43]. The Northridge earthquake had a magnitude of M_w=6.7 and was considered the most costly earthquake in USA since the seismic event of 1906 [44]. It caused the loss of 33 lives and injured and left thousands of people homeless. Buildings and lifelines, such as major highways were heavily damaged, resulting in a monetary loss between 13-20 billion USD. Old non-ductile RC structures were heavily damaged, among which several waffle slab structures were reported to have collapsed [45].

2010 was a devastating year in terms of massive earthquakes. In January 2010, an earthquake of magnitude M_w=7 hit the island state of Haiti and killed 217000 people, injured 300000 people and affected the lives of five million more. Residential and

governmental buildings, mostly reinforced concrete, roads and other facilities suffered great damages, mostly due to inappropriate seismic design [46]. In February 2010, an earthquake of magnitude M_w=8.8 hit Chile and left 432 people dead and many more injured. 810000 houses were damaged, among which 160000 either collapsed or were heavily damaged [47]. Damages greater than expected on new and well-designed buildings, alongside with the prevalence of nonstructural damages, pushed forth the need for the revision of the Chilean Seismic Code [48].

New Zealand was also hit by a series of seismic events in 2010-2011, which is known as the Canterbury earthquake swarm, and counted 3690 main events and aftershocks. The main shock of the Darfield earthquake had a magnitude of M_w=7.1 while the Christchurch main shock had a magnitude of M_w=6.2. Considerable damages were inflicted to buildings, particularly to unreinforced masonry structures [49]. Damages to nonstructural components, such as chimneys, parapets, gable walls and racks and shelves, were a major cause of the economic loss from the Darfield event [50]. The Christchurch event caused the death of 181 people [51] and damages of varying intensity to more than 2200 buildings, mostly masonry structures of some type [52]. This event saw the infliction of severe damages or collapse of 135 RC structures; the collapse of two midrise buildings was the cause of death of 135 of the victims of the Christchurch earthquake [53].

The discussion on some of the major seismic events that have hit two of the most seismically active regions in the world, the Mediterranean region, and the Ring of Fire, shows that time and again devastating earthquakes will occur. While some of the events mentioned in the paragraphs above have had outstanding magnitudes, in many cases the inadequacy of the design and construction practices are the cause of the extensive damages that were observed. A good example of this is the Durres earthquake of 2019, which was a moderate earthquake, but caused severe damages to the poor country of Albania. The construction practices are highly debatable, and the seismic code in use has not been updated in almost 40 years.

1.2 Problem Statement

Main earthquake events are generally followed by site visit from teams of specialists, who then report the findings of the visit in their scientific publications. There is a limited number of reports which explicitly mention damages to wide beam structures, or even further correlate the damages to this type of structure.

Waffle slab structures with hidden beams seem to have been common in Mexico until the earthquake of 1985. Esteva [54] and Meli and Avila [55] describe the damages suffered by several waffle slab structures during this earthquake, however in most of the cases a mix of several reasons such as poor detailing of columns, ribs etc., contributed to the ultimate damage state of these structures. This was likely in part due to the design of waffle slabs using the same procedure used in the design of conventional solid slabs, which are more rigid than waffle slabs [56]. Sordo et al. [57] investigated a 12 story waffle slab RC building with wide beams, and reported damages on columns and shear walls as well as bending cracks in the slabs. They noted that the formation of flexural cracks in the slabs enabled the structure to reach some ductility, thus they concluded that waffle slabs can develop ductile behavior if designed to avoid early shear failure. Though waffle slab structures that were severely damaged or collapsed constituted about 41% of the total number of damaged structures, only 4% of the failures occurred due to punching of waffle slabs [54, 58].

Wide beams seem to be more problematic in the Mediterranean region. The observations of damages from the site visit after the Durres earthquake of 2019 reported the lack of conventional beams and the predominance of wide beams as one of the major factors that contributed to the unsatisfactory performance of the damaged buildings [38]. Doğangün [25] reported that buildings with ribbed slabs and shallow beams suffered heavy damages and one such building collapsed causing the loss of 30 lives. The considerable damages after the Lorca earthquake were also partially attributed to the widespread use of wide beam frame systems [59]. Some more examples from Turkey include the damaged Provincial Hall during the Adapazarı earthquake of 1967 [60]; most of the residential structures that were damaged during the Adana-Ceyhan earthquake of 1998 [61]; and the reinforced concrete building stock of Erzincan that were hit by the 1992 earthquake [62]. During both the Haiti earthquake

and the Chile earthquake of 2010, the damage reports showed wide beam structures among the damaged buildings, or stated their presence, but did not relate damages to the structural type [46, 47].

In Turkey, residential structures are often constructed using ribbed and sometimes waffle slabs, in which the main load carrying beams are shallow beams. The ribbed slabs are locally known as *asmolen*, after the type of brick that is commonly used to fill the void between the ribs, and this type of construction is known as wide beam structures. The wide beams are preferred mostly due to architectural reasons since the beams remain hidden in the slabs and make for very aesthetically appealing interiors. However, there seem to be concerns regarding the ability of WBF to sustain seismic loads, which is why the newly updated Turkish Building Earthquake Code (TBEC) [63] contains restrictions regarding this type of construction.

The main perceived issues with wide beam frames are excessive deformation and lack of ductility capacity. This perceived lack of ductility capacity is reflected in the seismic standards of some countries which denote wide beam frames as Limited or Mixed Ductility class [63-65]. Even though wide beams have widths considerably large to compensate for the limited depth and provide the required capacity, they are less stiff than an equivalent conventional beam. This translates in lower lateral stiffness for the frames, and therefore higher expected demands.

Some of the questions that could be asked are:

- What is the seismic demand of wide beam frames?
- Is it that much higher than the seismic demand of conventional beam frames designed similarly?
- If yes, does this type of structures possess sufficient capacity to withstand the higher demand?
- Are the code provisions regarding wide beam frames too demanding?
- Can any of these provisions be loosened without negatively affecting the performance of this type of structures in case of an actual seismic event?

This thesis sets out to answer the above questions by performing a thorough analytical investigation on wide beam frames that are designed according to the clauses of TBEC 2018. TBEC2018 was chosen for design, in order to focus on new, code-conforming

construction. 30 frames were designed, and then analyzed to obtain their capacities and their expected seismic demand. The capacities of the frames were obtained from nonlinear static analyses. The seismic demands were obtained from nonlinear dynamic analyses, performed using ground motion records pertaining to past earthquakes. Seismic demand was measured in terms of interstory and global drift ratio.

While earthquakes cannot be predicted and the good or bad performance of a structure to a particular earthquake is not a definite indicator of said structure to any given earthquake, performing many analyses using many ground motion records, which are selected randomly, but are compatible with the seismicity of the presumed location of construction can give a good idea of demand. Such an approach is suggested in US Federal Emergency Management Agency, Seismic Performance Assessment of Buildings Guide (FEMA P-58), which is the document used as the main guideline for the assessment of seismic demand. 330 demand data were obtained; 30 sets of time-history analyses for each of the frame models, and they were processed to obtain the expected seismic demand.

For this purpose, 30 simple and symmetric frames were designed. While the study aims to assess the role of wide beams on the performance of structures, other parameters were tested as well. Half of the frames were designed for soil class C and the rest for soil class D. Most of the frames were regular and symmetric in elevation with four and six stories, and two, four and six bays, while some of the frames were designed to have different story heights and bay lengths. They were denoted as irregular frames. Two dimensional (2D) frames were used in order to be able to perform more analyses, since less time is required for modeling and analyzing 2D frames rather than three dimensional (3D) frames. The response of 3D frames is also obtained in each direction separately generally, thus 2D frames were found suitable. Each type of frame, defined by a soil class, number of stories and bays was designed three times, once with conventional beams, to be used as reference models, and the other two with wide beams. Two approaches were used for the selection of the size of wide beams. In one case, small width wide beams were used, their width set equal to the column width on which they are supported. In the second case, great width wide beams were used, in which the width is set to the maximum permissible value by TS500.

1.3 Thesis Outline

This thesis is composed of eight main chapters and three appendices. Below are given detailed information about the content of each chapter.

Chapter 1 – Introduction provides some general information regarding wide beam frames, their use, spread and related problems. In this chapter some of the most notable seismic events and their consequences in the last decades have been summarized. The literature was investigated to gather information about damages to wide beam frames during earthquakes, whether mentioned explicitly or implicitly. Afterwards, the problem statement was laid out and the method with which this problem was addressed in this thesis is briefly discussed.

Chapter 2 – Literature review presents a summary of work previously done, solely on the topic of wide beams and related structures and substructures. The stances of the major codes on the topic of wide beams were initially discussed. Afterwards, experimental studies on wide beam-column connections were summarized. Finally, a review of the analytical work on wide beam structures was presented.

Chapter 3 – Design of models presents information about the code procedure (TBEC) for the design of wide beam structures. It was followed by a detailed explanation and description of the frame models that were used in this thesis. Additionally, the parameters that were varied in the model database were also discussed.

Chapter 4 – Creating the Nonlinear Models presents the approach used to model the nonlinear behavior of the reinforced concrete frames and their constituting elements. Nonlinear material properties were discussed in this chapter, and then the nonlinear formulations of structural elements were presented. The assumptions and simplifications for some of the structural elements or analyses choices were explained as well.

Chapter 5 – Pushover Analyses initially presents the method used to perform pushover analyses and analyze the outcome that was used in this thesis. Afterwards, the results of the pushover analyses for all the models are presented. An assessment and discussion on the behavior of the frames is presented based on the capacities and mechanisms obtained from the pushover analyses.

Chapter 6 – Time-History Analyses initially presents the method used to select ground motion records and obtain seismic demand from time-history analyses. Afterwards the demand results were reported for all the frames. A discussion of the demand obtained from time-history analyses was presented at the end of this chapter.

Chapter 7 – Reliability Assessment. This chapter presents the method laid out in FEMA P-58 for the assessment of seismic demand. It includes a discussion on uncertainties, and the code-based and probabilistic assessment of the seismic demand of the frame models were presented. The chapter was concluded with an interpretation and discussion of the obtained results.

Conclusion summarizes the work that was done in this thesis and the findings that were obtained. It assesses the completeness of the work and provides suggestions on how it can be furthered.

Appendix A contains all the detailed drawings of the frame sections and the gravity load configurations.

Appendix B lists the ground motion records of all the sets. 30 sets were selected each for Soil Class C and S_{DS}=0.5, Soil Class D and S_{DS}=0.5, and Soil Class D and S_{DS}=0.75. The compatibility of the ground motion records of each set with the corresponding response spectrum is also shown in this Appendix. Graphs containing the acceleration spectra of the ground motion records, their mean spectrum and the target spectrum for each set of ground motion records are provided for all 90 sets.

Appendix C contains the results of the time-history analyses that were not presented in Chapter 5. These include the graphs of variance of global drift ratios, the graphs of interstory drift ratios and the graphs of their variance for each story and each frame.

Chapter 2

A Summary of the Research Pertaining to Wide Beam Structures

Reinforced concrete construction is at the same time an ancient and a new technology. It is ancient in that concrete was a known construction material in the Roman Empire. It is new in that it has seen a surge in use, development and regulation in the 20th century. Consequently, wide beam structures are a relatively new form of construction. Nonetheless they have gained popularity especially in regions in which reinforced concrete framed structures are commonly used. Wide beams are often found in one-way joist slab systems.

Sometimes wide beam structures are recognized as a separate form of construction, while in other cases they are not distinguished from other type of reinforced concrete frame construction. This chapter focuses on the works published on the topic of wide beam construction. A revision of pertinent code provisions is presented initially, followed by a summary of experimental studies on wide beam column connections, and concluded by a review of analytical studies on wide beam frames.

2.1 Review of Code Provisions and Regulations Regarding Wide Beam Structures

The Turkish Building Earthquake Code of 2018 (TBEC2018) [63] defined wide beam moment-resisting frames, which in Turkey are commonly known as *asmolen*, as Limited Ductility Class (LDC). Moment frames and shear wall dual systems containing *asmolen* slabs and wide beams can be designed as Mixed Ductility Class (MDC). This definition has implication with respect to wide beam structures. It limits

the number of stories a WBF can have and where it can be constructed. WBF without shear walls can be constructed only in areas with Seismic Design Coefficient (SDC) 3 or 4. TBEC2018 keeps the provisions of TS500 [66] regarding beam section depth, width and flange width. TEC2007 [24] on the other hand did not automatically define wide beam structures as Nominal Ductility Class. Italian [67] and Spanish [64] seismic codes have defined structures containing wide beams or ribbed slabs as Low Ductility Class as well, similar to the approach of TBEC2018. The definition of wide beam structures as LDC again has implications with respect to the seismic hazard for which they can be designed.

ACI standards recognize wide beams as a type of structural member which can display different structural behavior than other types of flexural members. ACI 318 [1] relates the maximum width permissible for wide beams to the size of the column on which it is supported rather than the depth of the beam itself. ACI 352 [68] emphasizes this relationship is important to ensure the formation of plastic hinges on the wide beam rather than the column. ACI 352 also states that provisions for shear reinforcement of wide beams are too restrictive, since wide beams generally are subjected to low shear stresses.

Other codes do not pay particular attention to wide beams, but they provide minimum and maximum section sizes for beams in general. The defined maximum beam widths accommodate wide beam sections as well. This approach is taken by Eurocode 8 [69], New Zealand Standard [70] and Greek Seismic Code [71]. Eurocode 2 [2] regulates the section aspect ratio for beams to avoid excessive slenderness and second order effects, while the National Building Code of Canada [72] defines the minimum ratio of width to depth for members of ductile moment-resisting frames.

2.2 Wide Beam – Column Connections

A considerable amount of research is available on wide beam column connections. Mostly, these are experimental studies that have focused on different aspects of design and performance of wide beam connections. Most of the studies have focused on beam-column connections designed according to the seismic codes used at the time of

publication. However, a few studies have focused on connections that represent existing structures, and connections that have been designed for gravity loads only.

Hatamoto et al. [73] investigated the effect of the ratio of beam width to column width and the amount of beam longitudinal reinforcement that can be placed outside the column core. They found that the ideal beam width to column width ratio limit is 2, larger ratios result in smaller beam effective widths. The longitudinal reinforcement of the beam placed outside the column core resulted in torsional stress in the outside portions of the beams and reduced the energy dissipation capacity, therefore it was suggested that the maximum amount of reinforcement that will not pass through the column should be limited. The effect of beam longitudinal reinforcement not passing through the column was investigated by Popov et al. [74] as well. They found that the rebars located outside the column core were strained sufficiently to contribute to the lateral resistance and energy dissipation capacity of wide beam connections, and that well designed transverse beams were important for the good behavior of these bars.

Gentry and Wight [75] tested exterior connections designed according to ACI352 and reported that wide beam column connections are suitable for construction in zones of high seismic risk when these connections are designed and detailed appropriately. They stated that the torsional demand in the transverse beams should be controlled in order to allow the wide beam to develop a flexural hinge. LaFave and Wight [76] also reported torsional cracking in the transverse beams of exterior wide beam connections. However, the performance of the connections was satisfactory even when most of the wide beam longitudinal reinforcement was anchored outside the column core. Furthermore, the portions of the wide beam outside the column were found to contribute to the joint shear strength, thus very little joint shear cracking was observed. The wide beams did not experience any shear cracking at all. Another study from LaFave and Wight compared exterior wide beam connections to conventional beam connections [77]. They reported that well designed wide beam connections were capable of dissipating similar amount of energy to conventional beam connections and exhibit similar displacement behavior as well. Wide beam connections experienced less joint and beam shear cracking than conventional beam connections. Greater slab participation was observed in wide beam connections. Regarding the torsion stresses in the transverse beams, they reported that proper design was sufficient to keep these

stresses low, and not affect the overall behavior of the connections. Quintero-Febres and Wight [78] investigated the effect of the beam width to column width ratio in interior connections. Larger column sections, thus lower ratios would be beneficial to reduce or eliminate pinching in the hysteretic curve of the interior wide beam connections. Another important factor affecting the hysteretic behavior of the connections was the amount of longitudinal reinforcement of the wide beams passing outside the column core. On the other hand, proper design of the connections was reported to guarantee adequate behavior, strength, and deformation capacity. This study confirmed slab contribution to the capacity of the beams as well. LaFave [79] summarized the studies on wide beam connections and suggested that transverse reinforcement requirements for wide beams can be relaxed. He also concluded that the wide beam contributes to the shear capacity of the joints, and that torsional cracking of transverse beams is observed on both wide and conventional beam connections, but as long as transverse beam reinforcement yield is prevented this cracking is not problematic.

The anchoring of wide beam longitudinal bars was seen as a problem in wide beam connections because the load transferred from these bars caused torsional stresses and cracking in the transverse beams. Several studies [80-84] focused on intentional rebar debonding as a strategy to avoid torsion failure of transverse beams. They reported that while wide beam connections built according to the local seismic code performed satisfactorily for low seismic risk, debonding of wide beam longitudinal bars outside the column core improved the behavior of the connections and made them suitable for construction in zones of high seismicity. Bar debonding reduced torsional stresses in the transverse beams. Another suggestion for improving the seismic behavior of wide beam connections was to focus most of the bottom beam reinforcement within the column core.

Kulkarni and Li [85] and Li and Kulkarni [86] investigated the behavior of interior and exterior wide beam connections respectively. They used experimental tests to calibrate finite element (FE) models and perform parametric studies on the effect of column axial load, transverse beam, and wide beam longitudinal bar anchorage ratio. They reported that column axial load levels up to 40% for interior and 25% for exterior connections can be beneficial for their behavior. They found that torsional behavior of

the transverse beams can control the overall behavior and capacity of the connections and suggested proper design of these members. The bars anchored outside the column core yielded after the bars anchored within the column core, and this resulted in the delay in the formation of plastic hinges in the wide beams. The study concluded that wide beam connections that were properly designed and detailed to resist seismic forces displayed adequate behavior and reached their lateral load and displacement capacities.

Masi et al. [87] and Masi and Santarsiero [88] tested exterior wide beam connections designed according to the local code for three seismic zones. They reported that the insufficient anchorage length of beam longitudinal reinforcement can result in poor bonding and bar slip. Larger amounts of longitudinal reinforcement were also found to be not beneficial, and result in earlier formation of shear cracks in the joints.

Benavent-Climent [89] tested wide beam-column connections designed primarily for gravity loads on a shaking table and found that wide beam connections had very low initial lateral stiffness and the behavior of the connections was generally controlled by the torsion in the transverse beam. Surprisingly, the beam-column joints did not fail, and while the tested exterior connections exhibited strong column-weak beam behavior, the interior connections displayed weak column-strong beam behavior. The torsional cracking and failure of the transverse beams was observed from Benavent-Climent et al. [90], which tested interior connections under cyclic loading. They found that this behavior prevented the wide beams from reaching their full moment capacities and resulted in low ductility. The exterior connections representative of connections found in the moderate seismicity areas of the Mediterranean region during the 1970-1990 and tested by Benavent-Climent et al. [91] also displayed low ductility. Furthermore, drift ratios several times higher than the drift ratio suggested by Eurocode 8 for Damage Limitation were observed. Low energy dissipations were exhibited by the interior and exterior wide beam connections tested on both above mentioned studies.

However, Elsouri and Harajli tested both interior [92] and exterior [93] wide beam connections that were primarily designed for gravity loads, but seismic detailing were added to some of the connections. They reported that detailing the connections according to ACI318 guidelines for seismic resistant structures improved considerably

their energy dissipation, lateral load and displacement capacities. The failure mode shifted from joint shear to beam flexural failure.

Fadwa et al. [94] compared both interior and exterior wide beam connections to conventional beam connections designed for modern codes and found their behavior satisfactory. They reported that the wide beam connections had higher energy dissipating capacity and better hysteresis response than conventional connections. They noted that the presence of longitudinal reinforcement in the transverse beams helped avoid torsion failure of the connection and led to a pure flexural failure. Mirzabagheri and Tasnimi [95] tested roof connections with wide and conventional beams and found that while wide beam connections were more ductile, there were no significant differences between the load and energy dissipation capacity between the specimens. None of the specimens reached their design strength, but the joint shear design was adequate in wide beam connections. Mirzabagheri et al. [96] further investigated the transverse beams of wide beam column connections. They tested two interior connections, in which one had a transverse beam on one side only, and the other connection had transverse beams on both sides. They reported that the presence of transverse beams on both sides provided better confinement for the joint and resulted in better overall behavior. Pakzad and Khanmohammadi [97] also tested four wide beam-column connections that were properly designed and detailed to withstand seismic action and reported that the expected capacities were exceeded and ductile behavior was observed. They noted that beam flexure determined the response of the connections, while brittle mechanisms such as shear and torsion were not observed. They also noted the importance of proper detailing and adequate transverse beams. Using conventional beams as transverse beams for wide beams considerably reduced the torsional strains in the reinforcement of the transverse beams itself.

Huang et al. [98] investigated the effect of design shear force to nominal shear strength ratio on exterior wide beam connections designed for modern codes. They reported that premature joint shear failure was not observed in any of the specimens tested, however the ratio affected the behavior. The first specimen with a joint shear force to strength ratio of one exhibited a ductile behavior, only wide beam flexural failure was observed. The other specimen which had a joint shear force to strength ratio of 1.7 displayed joint shear failure after the wide beam had hinged and the maximum capacity

was reached. Behnam et al. [99] tested four exterior wide beam connections with different beam width to column ratios and different joint shear ratios. They concluded that for connections with low beam width ratio and joint shear ratio the behavior was governed by the flexural hinge of the beam, and very few if any cracks were formed in the joint region. Connections with higher ratios displayed shear cracking in the joint region. The behavior of the specimen with beam width ratio of 2.5 was governed by the torsional failure of the transverse beam. However, they noted that the portions of the wide beams outside the column core contribute to the joint shear capacity. Beam width ratios lesser than two were reported to produce more favorable behavior in wide beam connections. Behnam and Kuang [100] investigated the effect of transverse beams on wide beam connections by using specimens that had the same column and wide beam, but transverse beams with varying geometry and reinforcement. They reported that transverse beams with no reinforcement at all produced pure torsional failure of the connections. Conventional beams used as transverse beams did not contribute considerably to the shear capacity of the joints, while well detailed wide beams used as transverse beams provided the solution for avoiding both transverse beam torsion failure and joint shear failure. Another study from Huang at al. [101] investigated the effect of longitudinal reinforcement ratio of the wide beams on the behavior and failure mode of exterior connections. They found that connections with low beam reinforcement ratios (0.84%) displayed purely ductile behavior, while in the other specimens with reinforcement ratios greater than 1%, joint shear cracking was observed after the yielding of the wide beams, thus beam flexure-joint shear failure mode occurred. The transverse beams were designed according to ACI318 and did not experience any damage.

The shear design of wide beams was investigated by Serna-Ros et al. [102] through a series of tests on wide beams of different reinforcement configurations. They recommended that the spacing between the stirrup legs should be around the value of the effective depth of the beams, and thus two-legged stirrups should not be used in wide beams. They found that the ACI318 shear capacity formulations underestimated the shear strength of wide beams, and that the spacing requirements are conservative. This study suggests a spacing of 0.8 times the depth for the stirrups of wide beams. These observations were confirmed by Shuraim [103] as well.

2.3 Wide Beam Frames

The performance of WBF have been studied analytically, and different parameters have been evaluated. In some instances, the behavior of existing WBF was of interest, in some other cases, design and regulation requirements were put to test.

As it is obvious from the literature, WBF have been quite common in Spain for about half a century. The earthquake that hit the city of Lorca in 2011 caused considerable damage even though it had a moderate intensity [59].

Donaire-Avila et al. [104] reported that a considerable number of WBF were subjected to different levels of damage during this earthquake. It was noted that the irregular distribution of infill walls in the elevation of the WBF, particularly the lack of infills in the ground floors resulted in soft story mechanisms, and ground floor collapses. Soft and weak story mechanisms are a commonly reported failure mode in conventional RC structures as well, both due to the lack of infills and higher story height in the ground floors, that are generally used for commercial purposes [23, 25, 29, 30].

The effect of infill walls on the performance of existing WBF in Spain, representative of typical buildings for different time periods, was investigated in several studies. Benavent-Climent at al. [105] reported that infill walls can reduce the seismic capacity of structures and adversely affect their behavior by increasing the risk of local damages. Lopez-Almansa et al. [106] reported that while infill walls can increase the seismic capacity of WBF, the effect is short-lived, since infill walls are known to crack and fail at early stages. Dominguez et al. [107] noted that even infill walls could not improve the behavior of existing WBF sufficiently to resist the Lorca earthquake. Finally, Dominguez et al. [59] investigated the contribution of infill walls in association with the level of seismic design of the WBF. They reported that structures that were not designed for any seismic action would collapse from Lorca earthquake with or without the contribution of infill walls. However, they found that infill walls seem to improve the behavior of seismically designed WBF and upgrade their performance to moderate-to-severe damage.

Vielma et al. [108] investigated the performance of waffle slabs buildings, flat beam frame buildings and moment resisting frame buildings in Spain through pushover and

time-history analyses. While all the assessed models displayed higher behavior factors than the code required values, waffle slabs buildings and flat beam frame buildings were reported to be more likely to reach severe damage than moment resisting frame structures. On the other hand, Benavent-Climent at al. [105] suggested that applying capacity design to WBF could reduce the damage level of the structures to moderate or severe damages and thus avoid collapse. Research on WBF designed with modern codes, such as Eurocode 8, displayed a more positive situation. Gomez-Martinez et al. [109, 110] assessed the need for the reduced behavior factor which is required by both NTC and NZSE for WBF, but not by Eurocode 8. They reported that Eurocode 8 designed WBF had capacities similar to normal beam RC frames, and that designing the WBF for Damage Limit States makes the use of a reduced behavior factor unnecessary. Similarly, the ductility of WBF was investigated by Gomez-Martinez et al. [111]. Again NTC and NZSE classify WBF as Limited Ductility Class, while Eurocode 8 does not make a differentiation. They found that modern code seismic design procedures, such as those described in Eurocode 8 guarantee sufficient ductility for WBF as well. They reported that the ductility of WBF relies more on the lateral stiffness of the frames than the local rotational ductility of wide beams. The low local rotation ductility of wide beams that results from limited heights and high reinforcement ratios has been often thought to be one of the reasons of unsatisfactory performance of WBF [59, 106].

The situation of WBF in Turkey and the corresponding design practices and provisions of TEC were investigated by Dönmez [112]. It was reported that the force-based methods may not be sufficient to provide adequate design for WBF, and rather displacement-based design was suggested. It was also noted that WBF designed according to TEC did not meet the performance criteria of that code and displayed behavior that was not sufficiently ductile.

2.4 Summary and Discussion of Literature Regarding Wide Beam Structures

Reinforced concrete construction containing wide beams of some form has been around for the last 50-60 years. There is still no consensus whether this type of

construction should be treated as a separate substructure or not. Wide beams are acknowledged in ACI 318, AC1 352 and NZS but no limitation besides the maximum beam width is provided. On the other hand, countries in the Mediterranean region such as Turkey, Italy and Spain, where this type of beam is quite common, and the seismic hazard is high, do not treat wide beams as equivalent alternatives to conventional beams. Limitations regarding ductility class and permissible seismic hazard are present in the national codes of these countries. The rest of the summarized seismic codes do not provide any clauses pertaining wide beams.

There is almost a universal agreement that wide beam connections are more flexible than conventional beam connections, however LaFave and Wight [77] found this discrepancy to be smaller in the experimental estimation of initial stiffness than from the analytically determined initial stiffness of wide beam and conventional beam connections. Wide beams are generally subjected to low shear stresses and the shear reinforcement requirements can be relaxed. Wide beams were also found to contribute to the shear capacity of the joints. Joint shear cracking was generally not the main failure mode of wide beam connections. There is no definite consensus on the torsion behavior of transverse beams. In some cases, torsion failure of transverse beams seems to govern the behavior of the connections, while in some other studies it is reported that proper design and detailing of the transverse beams is sufficient to prevent such brittle failure. Wide beams up to 1000 mm, and connections with beam width to column width ratio up to three were tested. While it was reported that even such connections can perform well under quasi-static loading, connections with beam width to column width ratio of two or less performed better. In such connections more of the beam longitudinal bars are anchored within the column core, and it was reported by several studies that anchoring a higher percentage of longitudinal bars within the joint yields better seismic performance. Mostly well-designed wide beam-column connections seem to attain satisfactory load, displacement, and energy dissipation capacities, comparable to the capacities of conventional connections. Connections representing existing structures did not perform particularly well, essentially due to poor design.

Analytical studies on existing WBF concluded that their capacities are often insufficient, and even infill wall contribution does not provide adequate strength

against seismic action. Methods such as Capacity Design, designing for Damage Limit State or Displacement-Based Design were reported to result in WBF that were ductile and performed comparably to CBF. It was also noted that the larger displacements observed in WBF are due to larger chord-rotations that results in columns due to greater length, and in beams due to smaller depths [109, 110].

In overall, the key takeaway from the experimental studies conducted on wide beam connections is that specimens that are properly designed and detailed to resist seismic forces, have a limited beam width to column width ratio and a limited percentage of beam longitudinal reinforcement anchored outside the joint perform satisfactorily and comparatively to conventional beam connections. Analytical studies on WBF also pinpoint modern seismic design practices as fundamental for good seismic performance. Therefore, a satisfactory or non-satisfactory performance of WBF is more connected to good design practices, rather than inherent to the structural type.

Chapter 3

Frame Models and Design According to TBEC

An extensive analytical procedure was designed to assess the behavior and performance of WBF. This procedure aimed to provide answers to the questions that were pondered in the Introduction and sufficient data to validate the results. For this purpose, 30 frames with different properties were designed according to TBEC. Besides the type of beam, conventional or wide, some other design features were varied as well. These features were soil class, number of stories, number of bays and regularity. Most analytical studies, and the majority of the work presented in this thesis as well make use of regular and symmetric models. Such simple models have two-fold advantages: (1) they enable observing the effect of a parameter in the outcome more easily due to their simplicity; (2) they enable performing more analyses due to the reduced time and computational effort required in the design, modeling, analysis, and assessment stages. On the other hand, irregularity is more difficult to include due to its own nature. Besides the regular frames, several irregular frames are further analyzed.

Some design parameters such as material grades and column section type were decided based on the available literature. The rest of the design features were determined according to TBEC, which has provisions for the design of wide beam frames which limit parameters such as total building height and design seismic hazard. Therefore, firstly a brief summary of the TBEC clauses relevant to the design of wide beam frames were summarized in this chapter. Afterwards the geometrical features of the frames and other design parameters were explained in detail, followed by a summary of the models and discussion on the outcomes of the design.

The design procedure of TBEC is based on capacity design, which implies that a certain hierarchy of failure is expected for code-compliant structures. Capacity design stipulates a failure hierarchy both among the members and among the failure modes within a member. The basis of it is that no brittle failure modes should occur before the ductile failure modes, and the member failure chain should be beams-columns-shear walls-joints. Therefore, when designing a structure, after the calculation of internal actions from the external forces, the following should be ensured:

- The shear capacity of beams and columns is greater than the shear forces resulting as both the action of external forces and moments at the end of the members. This will make sure that beams and columns reach their moment capacities before their shear capacities.
- The moment capacities of the beams in a joint should be less than the moment capacities of the columns intersecting them. This condition, also known as strong column-weak beam behavior, ensures that beams reach their moment capacities before columns that intersect them do.
- Beam-column joints should remain elastic meanwhile.

3.1 Turkish Building Earthquake Code of 2018 and Wide Beam Frames

The Turkish Building Earthquake Code [63] defines three ductility classes for reinforced concrete construction, Limited, Mixed and High. Each of the Ductility Classes comes with the permissible Seismic Design Categories (SDC), and each substructure type comes with a permissible Building Height Class (BHC). Ribbed slab (*asmolen*) structures without shear walls are defined as Limited Ductility Class (LDC). The maximum permissible BHC is 7, so the total height of WBF without shear walls cannot exceed 17.5 m. WBF without shear walls can only be constructed in seismic zones defined as SDC3 and SDC4. The corresponding maximum short period spectral acceleration coefficient S_{DS} is 0.5. The behavior factor and overstrength of WBF are 4 and 2.5 respectively.

Since WBF are designated as LDC, all the structural elements, such as columns, beams and joints, are designed as Limited Ductility elements. TBEC requires that the smallest

dimension of RC columns be not less than 300 mm, and that the beam width be not less than 250 mm. The Turkish Standard [66] regulates the rest of the section size requirements, such as minimum beam depth and maximum beam width. These are defined as:

- Minimum beam depth should not be less than 300 mm or three times the depth of the slab, whichever is the smallest.
- Maximum beam width should not be more than the summation of the beam depth and column width (the size of the column perpendicular to the axis of the beam)

Designing beam and column sections and joint panels as LDC yields to greater reinforcement ratios and smaller transverse reinforcement spacing. Additionally, LDC structures are not checked for compliance with the strong column-weak beam mechanism.

3.2 Seismic Action

The frame models were designed for the maximum permissible seismic hazard, that is SDC3 and short period spectral acceleration coefficient S_{DS}=0.5. Normally TBEC is accompanied by an interactive digital seismic hazard map for Turkey [113], shown in Figure 3.1. Most commercial design programs available in Turkey have this map embedded. For design purposes, the location of the building to be designed is entered, the seismic design coefficients are retrieved, and the response spectrum is generated.

In this thesis the process of calculating the response spectrum went in the opposite direction. The models are hypothetical and there is no location to start with, but there is a preferred seismic hazard level known in terms of short period spectral acceleration coefficient S_{DS}. The acceleration spectrum of TBEC is defined by Equations (3.1) to (3.4), where:

S_{ae} – horizontal elastic design spectral acceleration

S_{DS} – short period design spectral acceleration coefficient

S_{D1} – design spectral acceleration coefficient for 1 s period

T_A, T_B – corner periods

T_L – constant displacement zone period

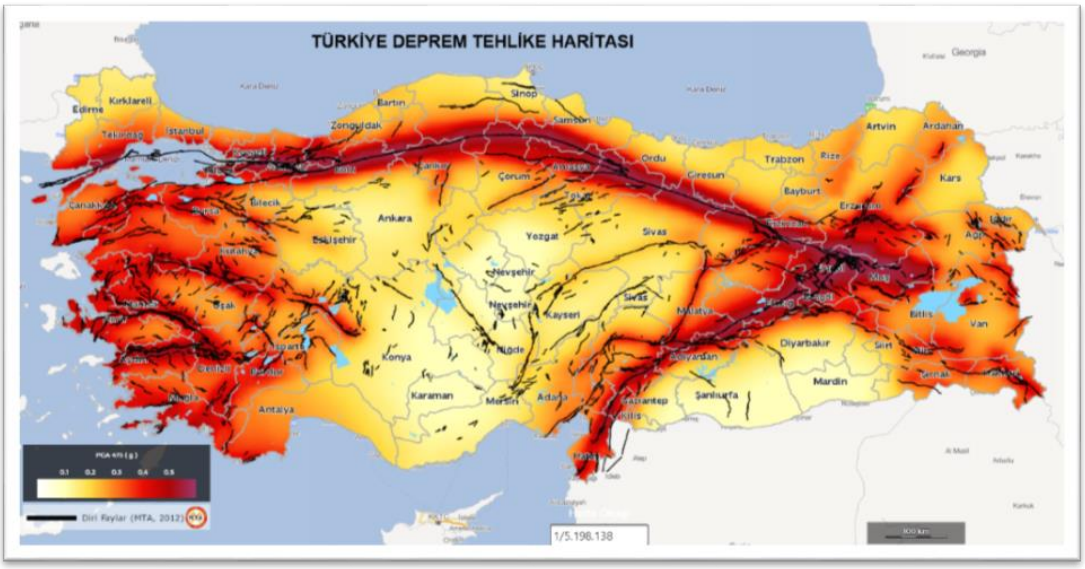

Figure 3.1: Seismic Hazard Map of Turkey in terms of PGA

$$S_{ae} = \left(0.4 + 0.6\frac{T}{T_A}\right)S_{DS} \qquad (0 \le T \le T_A) \tag{3.1}$$

$$S_{ae} = S_{DS} \qquad (T_A \le T \le T_B) \tag{3.2}$$

$$S_{ae} = \frac{S_{D1}}{T} \qquad (T_B \le T \le T_L) \tag{3.3}$$

$$S_{ae} = \frac{S_{D1}T_L}{T^2} \qquad (T_L \le T) \tag{3.4}$$

The corner periods of the response spectrum are calculated by Equations (3.5) and (3.6). S_{D1} parameter is unknown and should be retrieved from the interactive Turkish Seismic Hazard Map. This again requires building location coordinates, which is not possible for the models presented in this thesis.

$$T_A = 0.2\frac{S_{D1}}{S_{DS}} \tag{3.5}$$

$$T_B = \frac{S_{D1}}{S_{DS}} \tag{3.6}$$

On the other hand, both S_{DS} and S_{D1} can be calculated using Equations (3.7) and (3.8) respectively. S_S and S_1 are short period spectral acceleration and spectral acceleration for 1 s period respectively. F_S and F_1 are local soil coefficients for short period and 1 s period respectively. The values of F_S and F_1 are tabulated in TBEC and are dependent of soil class and the corresponding spectral acceleration coefficients. Parameters S_S, S_1, F_S and F_1 are necessary to generate the design elastic spectrum.

$$S_{DS} = S_S F_S \tag{3.7}$$

$$S_{D1} = S_1 F_1 \tag{3.8}$$

Table 3.1: F_S values suggested in Table 2.1 in TBEC[63]

Local Soil Class	Local Soil Effect Coefficient for Short Period Zone					
	$S_S \leq 0.25$	$S_S = 0.50$	$S_S = 0.75$	$S_S = 1.00$	$S_S = 1.25$	$S_S \geq 1.25$
ZA	0.8	0.8	0.8	0.8	0.8	0.8
ZB	0.9	0.9	0.9	0.9	0.9	0.9
ZC	**1.3**	**1.3**	**1.2**	**1.2**	**1.2**	**1.2**
ZD	**1.6**	**1.4**	**1.2**	**1.1**	**1.0**	**1.0**
ZE	2.4	1.7	1.3	1.1	0.9	0.8
ZF	*Field assessment to be performed*					

S_S and F_S were obtained from Table 3.1. The soil classes of interest are C and D. In order to obtain an S_{DS} =0.5, the S_S and F_S parameters are taken as below: Interpolation was used when necessary to calculated F_S.

- For soil class C, S_S=0.385 and F_S=1.30
- For soil class D, S_S=0.324 and F_S=1.54. Interpolation was used to obtain F_S.

TBEC provides a similar table that relates parameters S_1 and F_1 as well, shown here in Table 3.2. However, it is not possible to determine these parameters from the information available.

Table 3.2: F_1 values suggested in Table 2.2 in TBEC[63]

Local Soil Class	Local Soil Effect Coefficient for 1 s Period Zone					
	$S_S \leq 0.10$	$S_S = 0.20$	$S_S = 0.30$	$S_S = 0.40$	$S_S = 0.50$	$S_S \geq 0.60$
ZA	0.8	0.8	0.8	0.8	0.8	0.8
ZB	0.8	0.8	0.8	0.8	0.8	0.8
ZC	**1.5**	**1.5**	**1.5**	**1.5**	**1.5**	**1.4**
ZD	**2.4**	**2.2**	**2.0**	**1.9**	**1.8**	**1.7**
ZE	4.2	3.3	2.8	2.4	2.2	2.0
ZF	*Field assessment to be performed*					

3.2.1 Determining S_1 and Calculating S_{D1}

The use of spectral acceleration coefficients and local soil parameters to estimate the seismic hazard of a zone is an approach taken by modern codes, such as IBC [114]. Several studies [115-117] have provided some statistical relationship between the new spectral acceleration coefficients and PGA, but they seem to vary. Therefore, the author of this thesis set out to determine the relation of coefficient S_1 to S_{DS} for the seismic hazard in Turkey. For this reason, random points were selected in the interactive seismic map of Turkey, and the S_S and S_1 parameters for each of these locations were obtained. In order to avoid choosing the same location multiple times, or clustered points, one dataset was obtained for each province in Turkey, resulting in a dataset containing 82 data points. PGA was also noted for each of the locations and was used as the common factor, to which a relationship of S_S and S_1 was sought for.

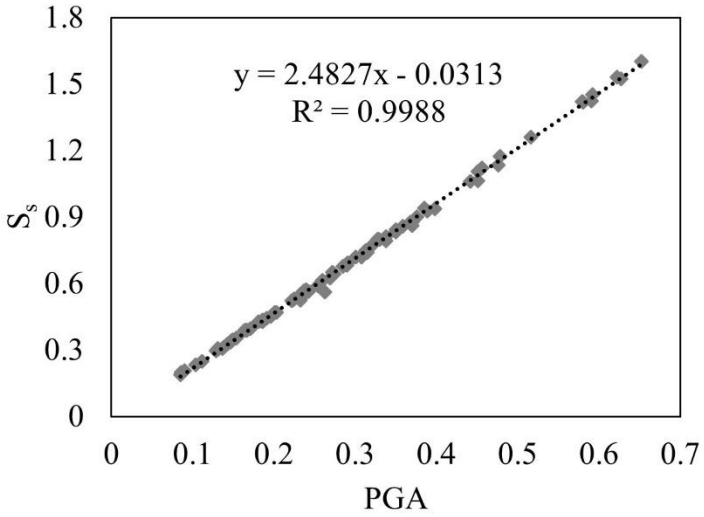

Figure 3.2: Relationship of S_S to PGA

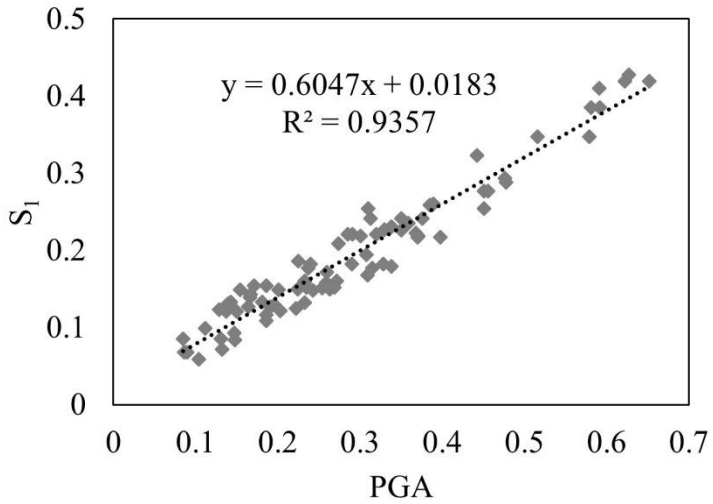

Figure 3.3: Relationship of S_1 to PGA

The relationship of both S_S and S_1 to PGA was almost linear. Figure 3.2 and Figure 3.3 depict these relationships. The correlation between the spectral acceleration parameters and PGA was very good, since R^2 was very close to 1 on both cases. The equations of the linear fits (Equations (3.9) and (3.10)) were used for the calculation of the desired S_1 parameters. Since the S_S was already estimated, the corresponding PGA was calculated from Equation (3.9). The corresponding PGA coefficients for soil class C and D were 0.167 and 0.143, respectively. The values of S_1 were calculated from Equation (3.10) as 0.120 and 0.105 for soil class C and D respectively. The F_1

values were obtained from Table 3.2, and are 1.5 for soil class C and 2.39 for soil class D. The S_{D1} coefficient was calculated using Equation (3.8), as 0.179 for soil class C and 0.251 for soil class D.

$$S_s = 2.4827PGA - 0.0313 \tag{3.9}$$

$$S_1 = 0.6047PGA + 0.0183 \tag{3.10}$$

3.2.2 Response Spectra for Soil Class C and D and S_{DS}=0.5

The spectral acceleration coefficients and soil related parameters for soil classes C and D and for S_{DS}=0.5 were calculated in the previous section and are summarized in Table 3.3. Consequently, the design elastic response spectra for the two soil classes were calculated using Equations (3.1) to (3.4), and were plotted into a graph, that is shown in Figure 3.4.

Table 3.3: Seismic hazard parameters for soil classes C and D and S_{DS}=0.5

	Soil Class C	Soil Class D
S_{DS}	0.500	0.500
S_S	0.385	0.324
F_S	1.30	1.54
S_1	0.120	0.105
F_1	1.50	2.39
S_{D1}	0.179	0.251
T_A	0.072	0.100
T_B	0.359	0.502

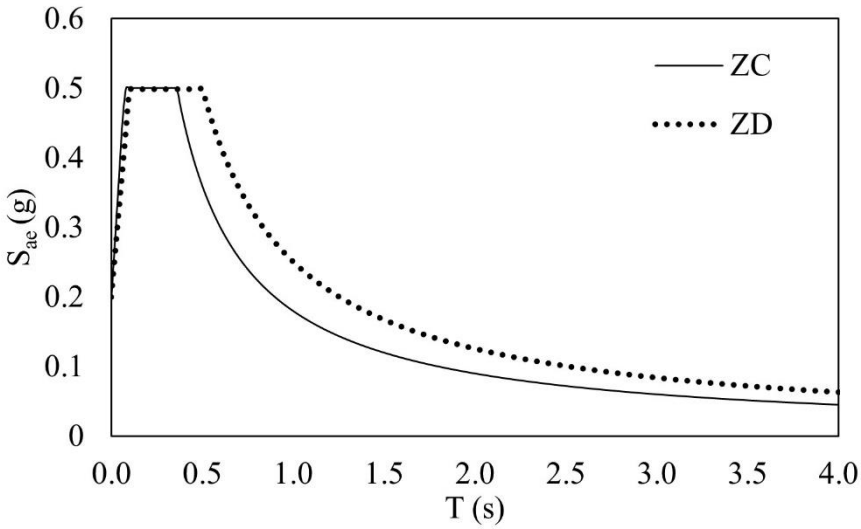

Figure 3.4: Elastic Design Acceleration Response Spectrum for soil classes C and D and S_{DS}=0.5

3.3 Gravity Loads and Infill Walls

The models were designed as residential buildings, therefore typical loadings for residential structures were used. The slabs were assumed to have typical layers found in residential structures, such as plumbing, filling, plastering, and tiling. The dead load of the slabs was calculated using these layers and the average unit weights reported in TS498 [118]. The live loads of residential structures per TS98 are 2 kN/m^2 for living areas, 3.5 kN/m^2 for stairs, 5 kN/m^2 for balconies and 1.5 kN/m^2 for the rooftops. But since the floor plans were hypothetical and simple, and no architectural plans were prepared, stairs were ignored, and all the slabs were assumed to have 2 kN/m^2 live loads uniformly distributed in the normal floors and 1.5 kN/m^2 in the rooftops. In the irregular frames, balconies were assigned the required 5 kN/m^2.

To make up for neglecting some areas typical of residential structures with higher live loads, a uniform infill wall distribution was assumed. On the perimeter beams, 20 cm thick infill walls were assumed to be continuous and without openings or discontinuities. On all the internal beams, 13 cm thick infill walls were assumed to be continuous and without openings or discontinuities. These assumptions both simplified modeling the magnitude and distribution of infill wall load and compensated for neglecting higher live loads for some areas by considering full walls

without openings, which is seldom the case. The load of infill walls was calculated based on the assumed layers, a core made of hollow bricks, plastered on both sides. The gravity load configurations for the frame models are provided in Appendix A, section A.1.

TBEC allows for two approaches for modeling infill walls when RC infilled frames are designed. The walls can be modeled as isolated and non-isolated from the frame itself. When the walls are isolated from the frame, an isolating seismic joint is expected to be applied around the wall to avoid the interaction of the frame and the infill. Non-isolated infill walls do not need such a detail. Consequently, the displacement criteria for which the frames are required to comply with change depending on whether the walls are to be designed and constructed as isolated and non-isolated.

When infill walls are isolated from the frames, their contribution to the stiffness and strength of the frame is neglected. Therefore, more flexible frames are obtained, which require smaller sections and lower reinforcement ratios. This is an attractive alternative to design engineers, who need to consider construction costs carefully when making decisions about structural layouts, elements and design approaches. Therefore, in this thesis the infill walls were designed as isolated.

3.4 Material Grades and Structural Elements

The effect of material properties was reported by Dominguez et al. [59]. As expected, concrete and steel grade affected the response of WBF, concrete strength affected response more than steel strength. Therefore, material properties were not a parameter of interest in the present study. TBEC requires that concrete of grade C25 or higher be used in reinforced concrete superstructures, with C30 being the most commonly used concrete quality. It also mandates the use of ribbed steel rebars of yield 420 MPa and higher. The frame models were designed with concrete grade C30 and steel grade B420C. The material properties suggested in TBEC were used during design and analysis.

The structural elements comprising the frame models were columns, beams and slabs. Infill walls are regarded as nonstructural elements in TBEC, and therefore they are included only as loads in the models (Section 3.3). The size of the structural elements

was determined by minimum section requirements posited in TBEC, load and displacement demand imposed on the frames during design, and typical section sizes observed in the Turkish Building Stock.

The section size requirements of TBEC include:

- The smallest side of rectangular columns should not be less than 300 mm
- The beam width should not be less than 250 mm
- The beam depth should not be less than 300 mm or three times the depth of the slab
- The maximum beam depth should not be more than 3.5 times the width of the beam
- If the beam depth exceeds one fourth of the clear span of the beam, it should be designed as a deep beam
- The maximum beam width should not be more than the summation of the beam depth and column width
- The depth of two-way monolithic slab should not be less than 80 mm
- The topping of ribbed slabs should not be less than 70 mm

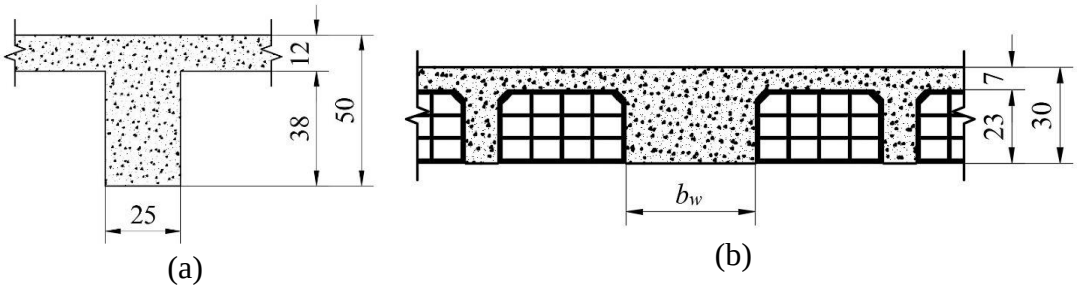

Figure 3.5: Slab and beam sections (a) conventional beam and monolithic slab; (b) wide beam and ribbed slab

These requirements provided the basis for column and beam sizing. The depth of the slabs was decided based on typical values found in the Marmara Region in Turkey, as reported by Bal et al. [119]. This study reported that the mean slab thickness of 12 cm was typical for conventional RC construction, while the thickness of the code-compliant ribbed slabs is 7-12 cm for the concrete topping and 33 cm total slab depth.

The mean depth of code-compliant conventional beams was found to be 48 cm, and 33 cm for code-compliant wide beams. Based on these observations the following decisions were made:

- Monolithic slab depth → 12 cm
- Monolithic beam sections → 25×50 cm
- Ribbed slab depth → 30 cm
- Wide beam depth → 30 cm

The CBF were designed with monolithic slabs while the WBF were designed with ribbed slabs. The ribs were filled with hollow bricks, and this contributed to the dead load of the slabs. Sections of the two beam types together with the respective slabs are shown in Figure 3.5.

The sections of columns and the width of wide beams were decided by section design. Square columns were used in order to avoid the effect of the weak or strong axis. Besides it was found that the type of column section [106] does not significantly affect the response of RC frames.

Bal et al. [119] also reported that the mean story height of RC structures was 2.8 m, however in this study the story height was taken as 2.9 m since it fulfills the architectural story height requirements. Code-compliant RC structures were reported to have a soft story-to-normal story height ratio of 1 most of the cases, therefore the regular frames were designed with a uniform story height distribution. However, some frames were designed with elevation irregularities, and a higher ground story was one of the irregularities included.

A study investigated the effect of beams spans among other parameters [106] and reported that longer beam spans contributed to greater damage levels to WBF. Therefore, beam spans were not a parameter of interest in the regular frames and a value of 5 m was used throughout the regular models. The frames designated as irregular do not comply with the story height and span length values used in the regular frames.

3.5 Frame Models Database

Some aspects of the design of the frames, such as column type, slab depths and material properties were decided based on either code requirements or evidence from the literature. The rest of the design aspects were included as parameters, and varied among the models, in order to obtain a larger and more varied set of models and assess their effect as well. These parameters are:

- Soil class. Two soil classes were considered, soil class C and D. Half of the frames were designed for soil class C and half of the frames were designed for soil class D.
- Number of stories. Since the total height of the buildings was limited to 17.5 m, at most six story frames could be designed. In this study four and six story frames were considered.
- Number of bays. two, four and six bays were considered.
- Regular vs. irregular. Most of the frames used in this study are regular frames, but six frames were designed with elevation irregularities.
- Type of beam. Three types of beam sections were used in the models separately. Each frame had only one type of beam section assigned to it. The beam types were conventional, small wide beams and large wide beams.

The frames were grouped in groups of three, which had identical elevation configuration and were designed to serve the same purposes, thus similar loads were imposed. So, the frames in each group were designed for the same soil class and had the same number of stories and number of bays. There were 10 frame groups, which differed from one another in terms of elevation layout, or design soil class.

The frame groups are summarized in Table 3.4. In this table the names of the frame groups are given in the first column. The names of the regular frames contain one letter between two numbers. The first number indicates the number of stories, the letter indicates the soil class for which the frames were designed, and the second number indicate the number of bays. For example, the frames that contain 4C6 in the name are regular frames designed for soil class C, have four stories and six bays. The irregular frames are denoted simply as IC or ID. A letter or a letter and a number were added in front of the names to indicate the type of beam that was used in each frame. For frames

with conventional beams the letter C was added. For frames with small wide beams W1 was added, and for frames with large wide beams W2 was added in front of the frame names.

Table 3.4: Summary of frame groups, and design parameters

Frame groups	Regular/Irregular	Soil Class	Nr. Stories	Nr. Bays
4C4	Regular	C	4	4
4D4	Regular	D	4	4
4C2	Regular	C	4	2
4D2	Regular	D	4	2
4C6	Regular	C	4	6
4D6	Regular	D	4	6
6C4	Regular	C	6	4
6D4	Regular	D	6	4
IC	Irregular	C	4	4
ID	Irregular	D	4	4

Six models were designed as regular frames with four stories and four bays, three for soil class C and three for soil class D. The elevation view of these frames is shown in Figure 3.6. Frames C-4C4, C-4D4, W1-4C4, W1-4D4, W2-4C4 and W2-4D4. Six models were designed as regular frames with six stories and four bays, three for soil class C and three for soil class D. The elevation view of these frames is shown in Figure 3.7. Frames C-6C4, C-6D4, W1-6C4, W1-6D4, W2-6C4 and W2-6D4. Six models were designed as regular frames with four stories and two bays, three for soil class C and three for soil class D. The elevation view of these frames is shown in Figure 3.8. Frames C-4C2, C-4D2, W1-4C2, W1-4D2, W2-4C2 and W2-4D2. Six models were designed as regular frames with four stories and six bays, three for soil class C and three for soil class D. The elevation view of these frames is shown in Figure 3.9. Frames C-4C6, C-4D6, W1-4C6, W1-4D6, W2-4C6 and W2-4D6.

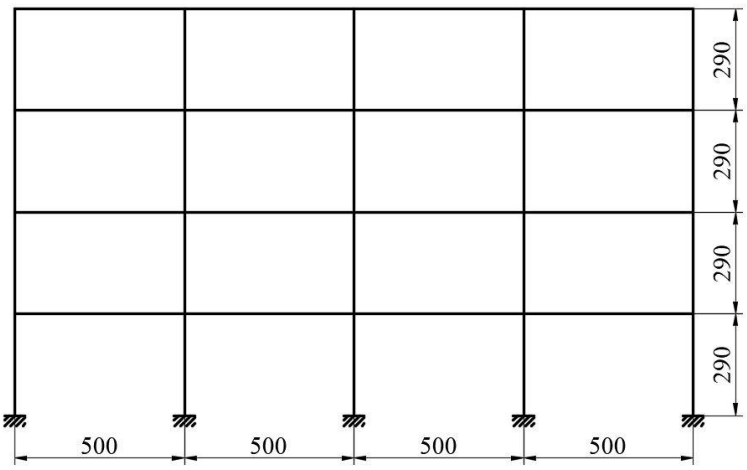

Figure 3.6: Elevation view of frames 4C4 and 4D4. The dimensions are given in cm.

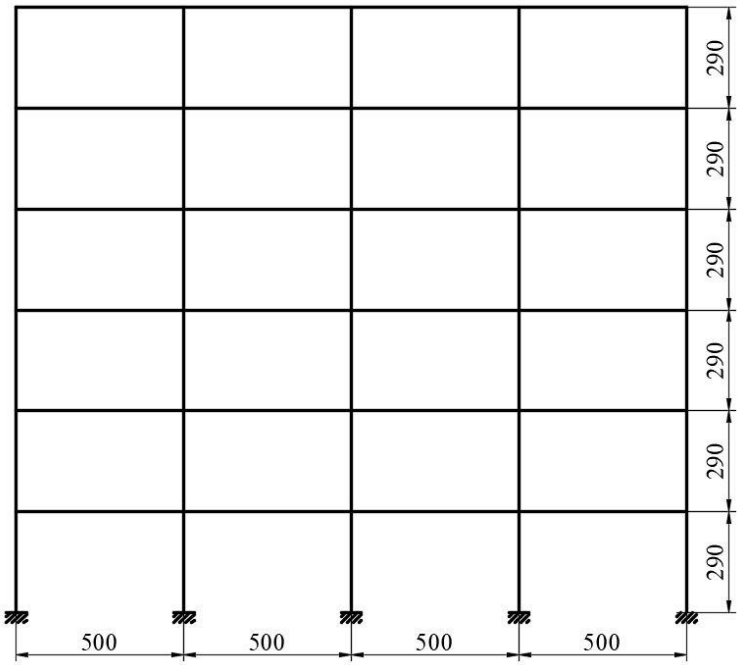

Figure 3.7: Elevation view of frames 6C4 and 6D4. The dimensions are given in cm.

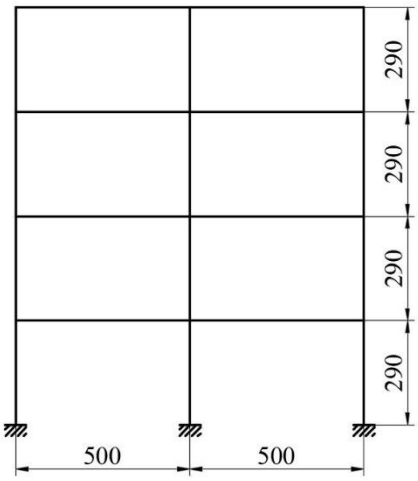

Figure 3.8: Elevation view of frames 4C2 and 4D2. The dimensions are given in cm.

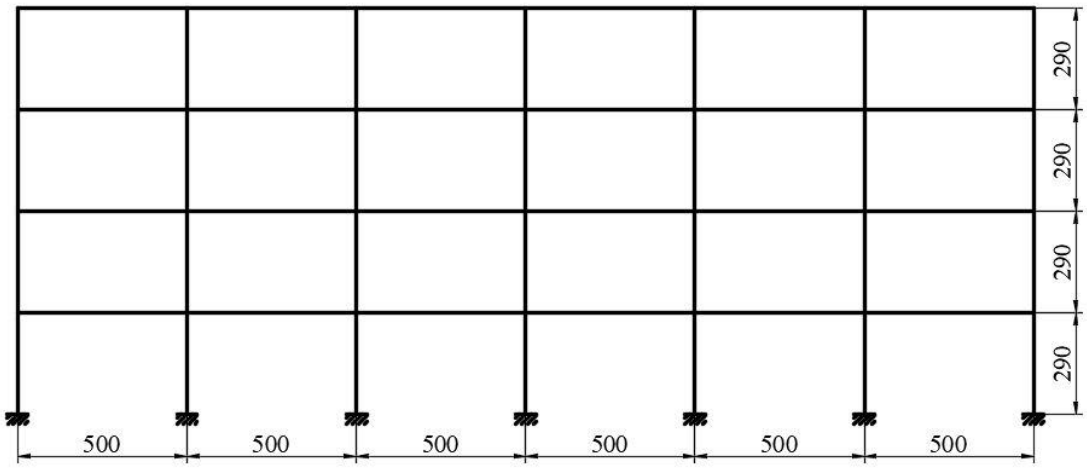

Figure 3.9: Elevation view of frames 4C6 and 4D6. The dimensions are given in cm.

The last six models were designed as irregular frames, three for soil class C and three for soil class D. The elevation view of these frames is shown in Figure 3.9. Frames C-IC, C-ID, W1-IC, W1-ID, W2-IC and W2-ID. These elevation irregularities were deviations from the simplicity and symmetry of the other frames. The irregularities that were considered in this study can be summarized as:

- Ground story height is 3.5 m, while the height of the rest of the stories is 2.9 m
- Different bays have different lengths, varying from 3 to 7 m
- There are overhangs on both sides
- The number of bays reduces towards the roof

The irregular frames were characterized by smaller column sections than their regular counterparts. This is related to the reduction of the bays towards the roof floor, which resulted in a reduction of total building weight and therefore lower design equivalent earthquake loads and lower lateral displacements. However, the reinforcement ratios in the member sections of the irregular frames were higher than those in the corresponding regular frames. This was true particularly for the beams of the WBF models, since smaller column sections resulted in smaller wide beam sections as well. The higher reinforcement ratios were required to provide sufficient capacity for the internal actions on the members. These internal actions were particularly high in the longer beams, such as the 7 m span beams.

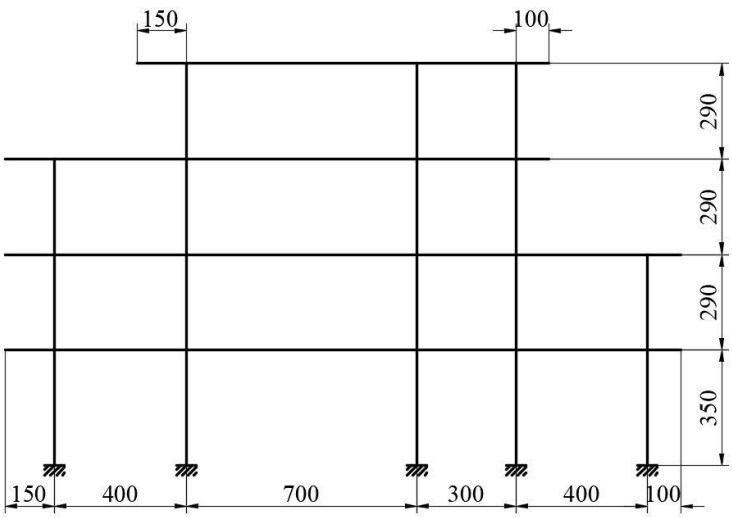

Figure 3.10: Elevation view of frames IC and ID. The dimensions are given in cm.

3.5.1 Conventional Beam Frames

Three dimensional frames were used during design, but two-dimensional frames were used for the nonlinear analyses. The middle frames of the floor plan were chosen to perform the nonlinear static and dynamic analyses. The conventional beam frames were designed as High Ductility Class (HDC). The behavior factor for HDC is 8 and the overstrength factor is 3. Two-way, rigid, monolithic slabs were used, and they contributed to the overall stiffness of the frames. Figure 3.11 shows the floor plan for

the frames with four stories and four bays and six stories and four bays. The frame that was used for nonlinear analyses is encased in the dashed line rectangle.

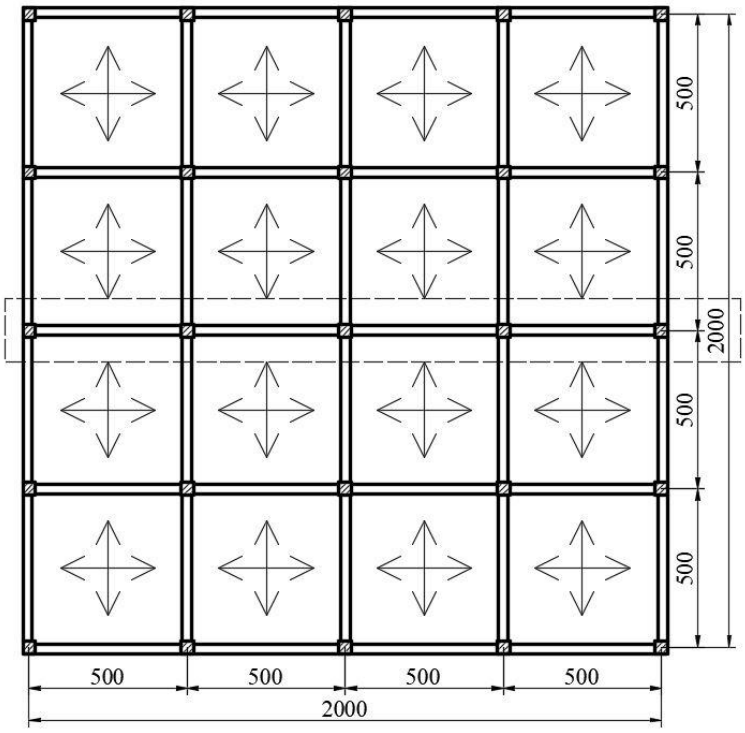

Figure 3.11: Typical floor plan for frames C-4C4, C-4D4, C-6C4 and C-6D4. The dimensions are in cm.

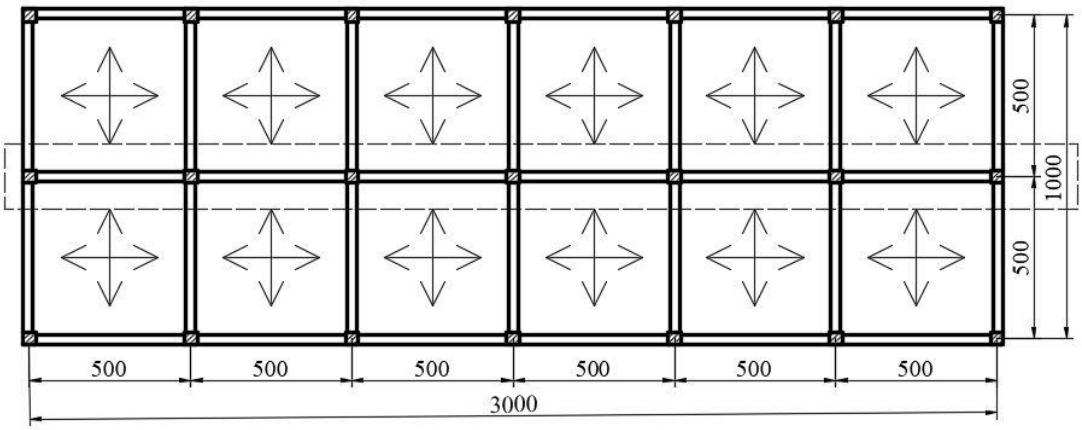

Figure 3.12: Typical floor plan for frames C-4C6 and C-4D6. The dimensions are in cm.

Figure 3.12 shows the floor plan for the frames with four stories and six bays while Figure 3.13 shows the floor plan for the frames with four stories and two bays. The frames that were used for nonlinear analyses are encased in the dashed line rectangles.

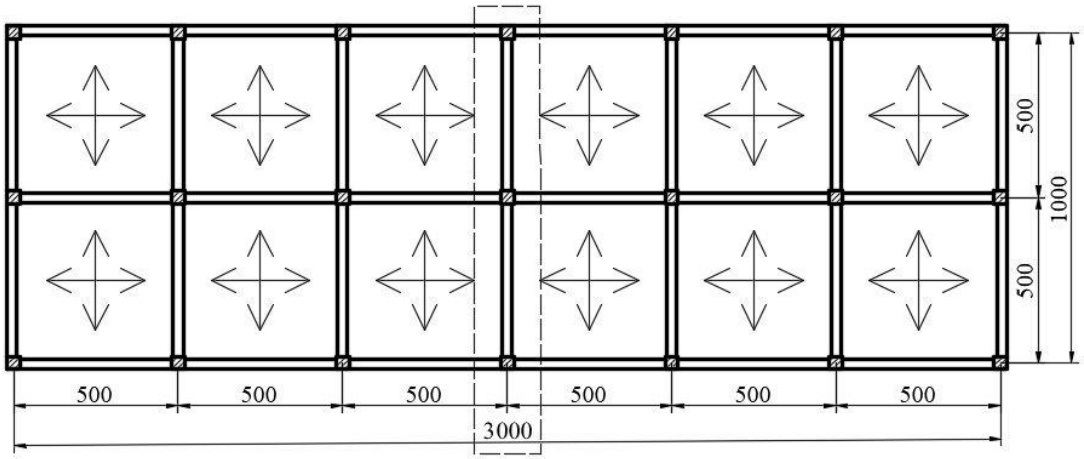

Figure 3.13: Typical floor plan for frames C-4C2 and C-4D2. The dimensions are in cm.

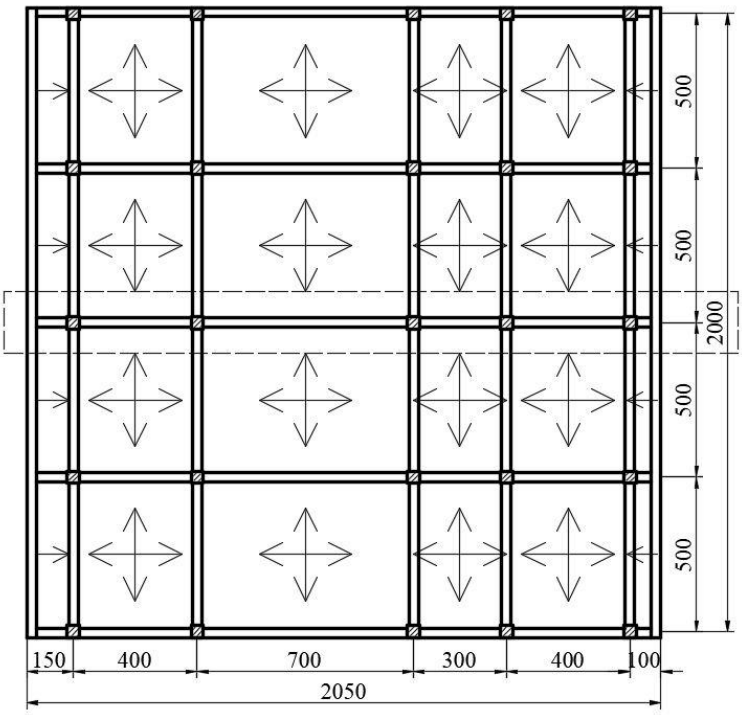

Figure 3.14: Typical floor plan for frames C-IC and C-ID. The dimensions are in cm.

The floor plan of the conventional irregular frames is shown in Figure 3.14. The frame that was used for nonlinear analyses is encased in the dashed line rectangle.

Normal beams of section 25x50 cm were used in these frames. Figure 3.15 shows an example of CBF and member sections besides, not to scale. The example shown was the four story two bay frame. CBF were checked for conformity to strong column-weak beam mechanism. The resulting design of CBF were characterized by small column sections, since the deep beams and the monolithic slabs contributed considerably to the rigidity of the structures. The detailed drawings of the CBF are given in Appendix A, section A.2.

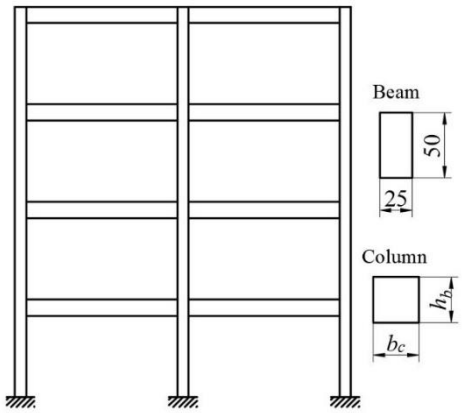

Figure 3.15: Elevation view and typical section of beam and columns for a CBF. All dimensions are in cm.

3.5.2 Wide Beam Frames

The WBF were designed as Limited Ductility Class, and therefore the strong column-weak beam check was not performed. The beams and columns were designed as Limited Ductility elements. The ribbed slab depth and the height of the wide beams was 30 cm. The width of the beams in the W1 frames is defined by Equation (3.11), and Equation (3.12) defines the width of the beams in the W2 frames. Figure 3.16 shows the elevation view of example WBF with the member sections to the right, not to scale.

$$b_w = b_c \tag{3.11}$$

$$b_w \leq h_b + b_c \tag{3.12}$$

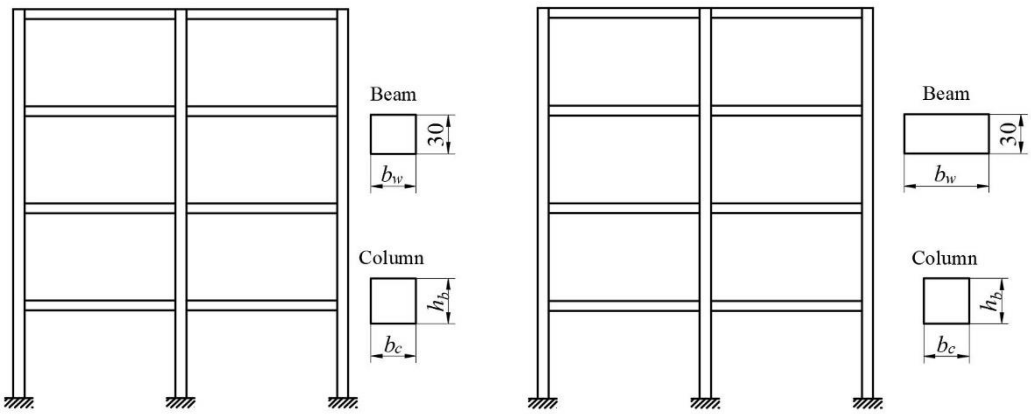

(a) (b)

Figure 3.16: Elevation view and typical section of beam and columns for the WBF (a) W1; (b) W2. All dimensions are in cm.

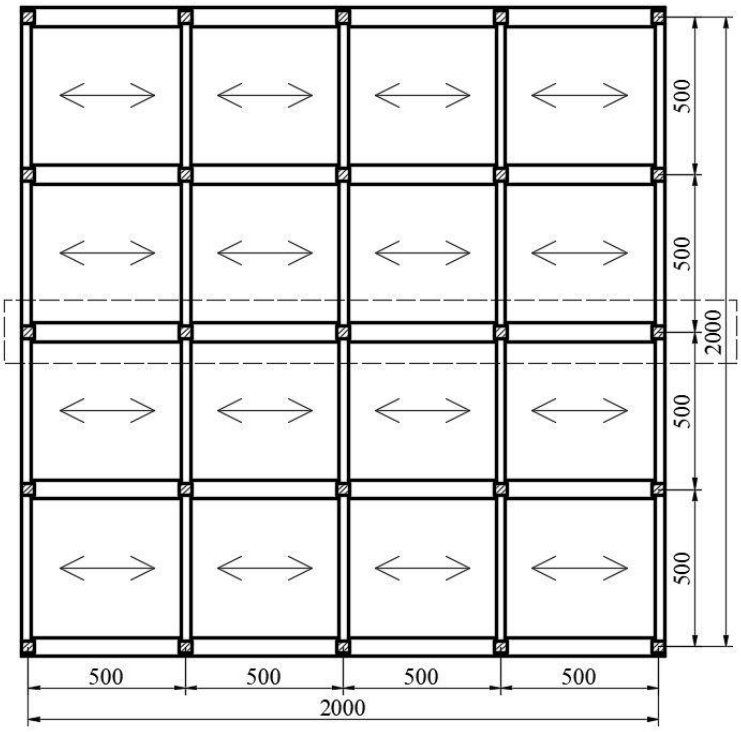

Figure 3.17: Typical floor plan for frames W1-4C4, W1-4D4, W1-6C4, W1-6D4, W2-4C4, W2-4D4, W2-6C4 and W2-6D4. The dimensions are in cm.

WBF had one-way ribbed slabs, distributing the gravity loads on the transverse beams, which were designed as conventional beams. It was shown that the use of conventional beams in the transverse direction considerably reduced the torsional strains in the reinforcement of the transverse beams [97]. Figure 3.17 shows the floor plan for the frames with four stories and four bays and six stories and four bays. Figure 3.18 shows the floor plan for the frames with four stories and six bays, while Figure 3.19 shows the floor plan for the frames with four stories and two bays. The frames that were used for nonlinear analyses are encased in the dashed line rectangle in each of these figures.

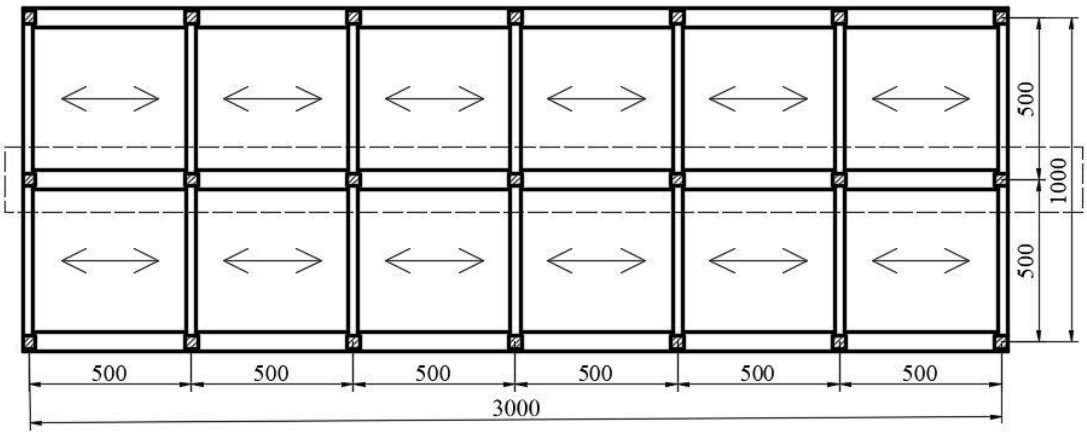

Figure 3.18: Typical floor plan for frames W1-4C6, W1-4D6, W2-4C6 and W2-4D6. The dimensions are in cm.

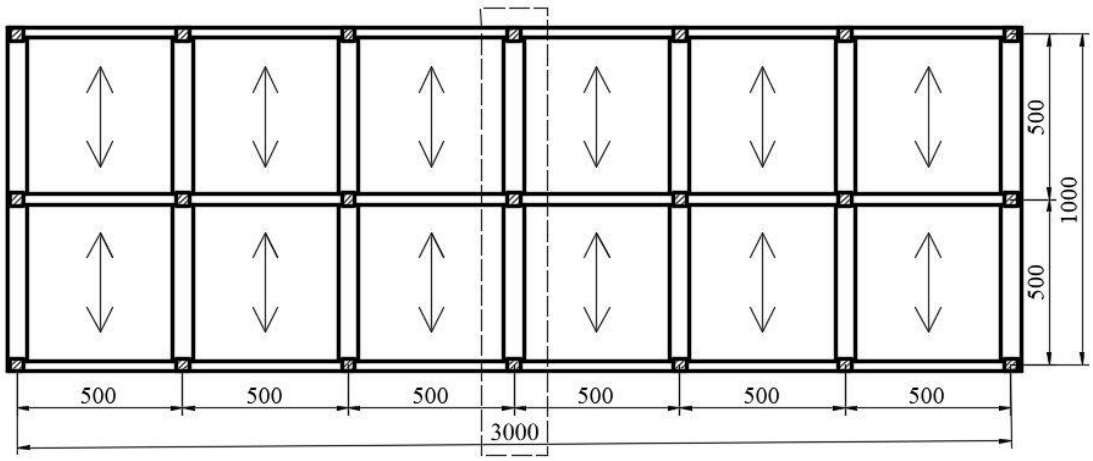

Figure 3.19: Typical floor plan for frames W1-4C2, W1-4D2, W2-4C2 and W2-4D2. The dimensions are in cm.

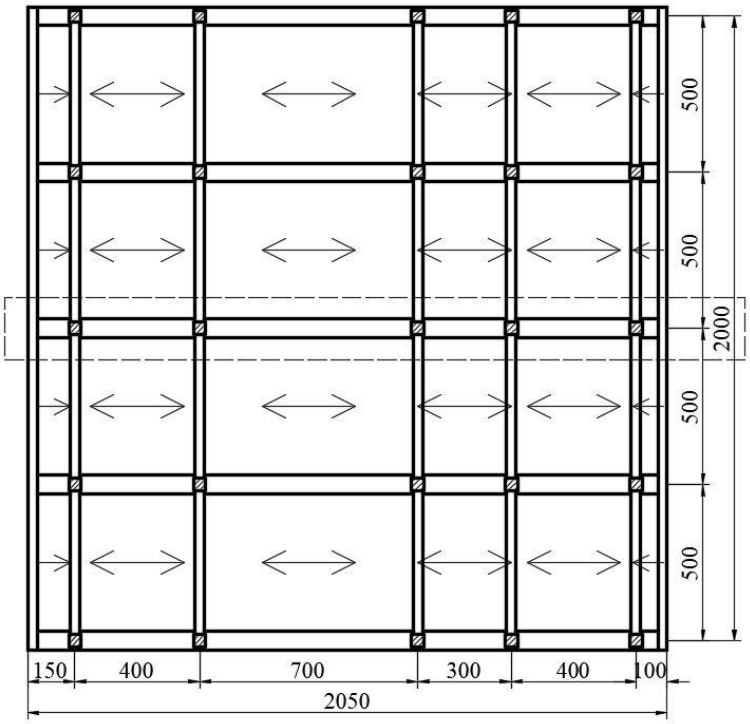

Figure 3.20: Typical floor plan for frames W1-IC, W1-ID, W2-IC and W2-ID. The dimensions are in cm.

The floor plan of the wide beam irregular frames is shown in Figure 3.20. The frame that was used for nonlinear analyses is encased in the dashed line rectangle. Frames W1 have the smallest and the most slender beam sections. Therefore, relatively large column sections were required to compensate the flexibility of the beams and slabs. Column sections as large as 500x500 were required in some of the frame models. The detailed drawings of the frames W1 are given in Appendix A, section A.3. On the other hand, frames W2 had larger and stiffer beams than frames W1. Smaller column sections were needed, therefore. The column layout of these frames was more similar to the column layout of CBF. The largest columns that were used were 400x400, therefore beams up to 700x300 were also used. The large beam sections even though oriented along the weak axis made up for the flexibility of the slabs. The detailed drawings of the frames W1 are given in Appendix A, section A.4.

Chapter 4

Methodology – Creating the Nonlinear Models of the Frames

The nonlinear models of the frames were created using SAP2000 [120]. SAP2000 is a finite element structural analysis program that contains various element types, such as truss/beam, area, shell, and solid elements. SAP2000 can perform a variety of analyses such as linear and nonlinear static analyses, linear and nonlinear dynamic analyses, and modal analyses to name a few. It can model the nonlinear behavior of frame elements as lumped plasticity, by using either automatic hinges or user-defined ones. Therefore, it is well suited for nonlinear modeling and analysis of frame structures.

In this thesis, the nonlinear models were created using line elements for beams and columns. The foundation conditions were not modeled explicitly, but fixed supports were applied at the bottom of the columns on the ground floor. The nonlinear behavior of beams and columns was modeled using load-deformation plastic hinges. Infill walls were generally modeled as gravity loads only. Beam-column joints were modeled as semi-rigid and elastic since they are assumed to remain elastic in the capacity design hierarchy. The configuration of the gravity loads for each of the frames has been depicted in Appendix A.

4.1 Nonlinear Properties of Materials

The effect of different material properties was not considered in this thesis, as it has already been explored elsewhere [59]. For all the frames, C30 was considered throughout all the structural members, and B420C steel was used for both longitudinal

and transverse reinforcement. Concrete and steel properties such as cracking/yield and ultimate strength, and stiffness were taken from TBEC.

4.1.1 Confined and Unconfined Concrete

The core of the member sections was modeled using confined concrete material, while the concrete cover was modeled using unconfined concrete material. The TBEC uses the Mander model [121] for confined and unconfined concrete. Figure 4.1 schematically shows the stress-strain curves for both confined and unconfined concrete.

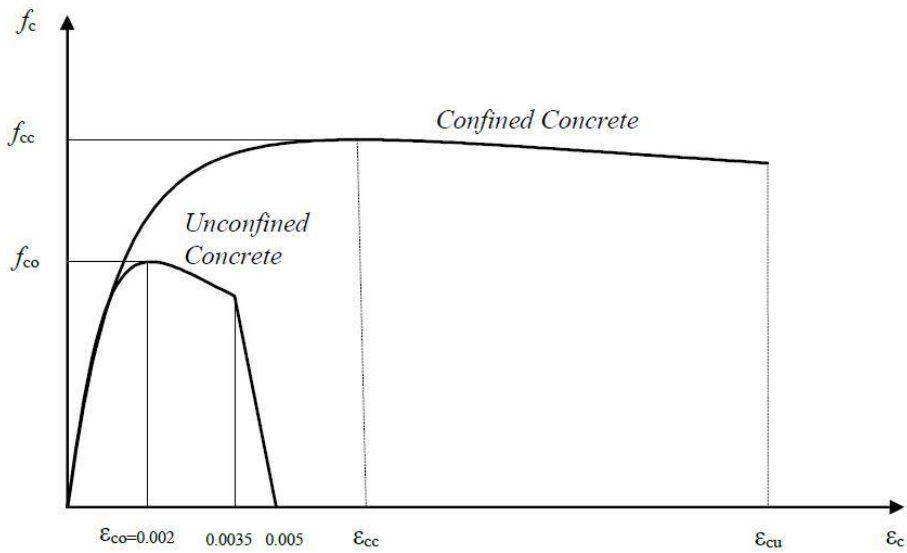

Figure 4.1: Stress-strain relationship for confined and unconfined concrete, per TBEC, using the Mander Concrete Model [63]

The unconfined concrete is characterized by the compressive strength f_{co} and strains for peak stress, crushing and complete failure, which are 0.002, 0.0035 and 0.005 respectively. The confined concrete stress-strain relationship is defined by Equation (4.1), where f_c is the compressive stress and f_{cc} is the compressive strength of confined concrete. x and r are parameters that introduce strain and material elastic modulus to this equation. The calculation of these variables is explained later.

$$f_c = \frac{f_{cc} x r}{r - 1 + x^r} \tag{4.1}$$

The compressive strength of confined concrete is related to its characteristic strength using Equation (4.2). The λ_c coefficient is calculated using Equation (4.3).

$$f_{cc} = \lambda_c f_{co} \tag{4.2}$$

$$\lambda_c = 2.254\sqrt{1 + 7.94\frac{f_e}{f_{co}}} - 2\frac{f_e}{f_{co}} - 1.254 \tag{4.3}$$

The f_e variable in the equation of λ_c stands for the effective confinement strength and for rectangular sections can be calculated as the average of the effective confinement strength calculated for each individual direction (Equation (4.4) and (4.5)).

$$f_{ex} = K_e \rho_x f_{yw} \tag{4.4}$$

$$f_{ey} = K_e \rho_y f_{yw} \tag{4.5}$$

where:

K_e is the lateral confinement coefficient for concrete and is calculated using Equation (4.6). In this equation, the parameters included are as listed:

a_i – the centerline-to-centerline distance between the longitudinal reinforcement

b_o – the width of the concrete core of a section between the transverse reinforcement legs, measured centerline-to-centerline

h_o – the height of the concrete core of a section between the transverse reinforcement legs, measured centerline-to-centerline

s – the spacing of transverse reinforcement

A_s – longitudinal reinforcement total area

$$K_e = \left(1 - \frac{\sum a_i^2}{6b_o h_o}\right)\left(1 - \frac{s}{2b_o}\right)\left(1 - \frac{s}{2h_o}\right)\left(1 - \frac{A_s}{b_o h_o}\right)^{-1} \tag{4.6}$$

x is the normalized strain ε_c with respect to strain at peak strength ε_{cc} for confined concrete (Equation (4.7)). ε_{cc} is also dependent on the λ_c coefficient, as shown in Equation (4.8), and ε_{co} is strain at peak stress for unconfined concrete, and should be taken as 0.002.

$$x = \frac{\varepsilon_c}{\varepsilon_{cc}} \tag{4.7}$$

$$\varepsilon_{cc} = \varepsilon_{co}\left[1 + 5\left(\lambda_c - 1\right)\right] \tag{4.8}$$

r is defined by Equation (4.9), where E_c and E_{sec} are the elastic modulus of concrete and the secant elastic modulus of confined concrete at the peak respectively. They can be calculated using Equations (4.10) and (4.11).

$$r = \frac{E_c}{E_c - E_{sec}} \tag{4.9}$$

$$E_c = 5000\sqrt{f_{co}} \tag{4.10}$$

$$E_{\sec} = \frac{f_{cc}}{\varepsilon_{cc}} \tag{4.11}$$

4.1.2 Reinforcement Steel

B420C steel was used for both longitudinal and transverse reinforcement in all the frames. The properties of the reinforcement steel are given in Table 4.1, where f_{sy} is the yield strength and f_{su} is the tensile strength of the steel. The ratio of the yield-to-ultimate strength was taken as 1.25, which is the average of the suggested range. ε_{sy}, ε_{sh}, and ε_{su} are the yield, strain hardening and ultimate strains respectively. A trilinear curve with strain hardening is used to describe the stress-strain relationship of steel, as shown in Figure 4.2.

Table 4.1: Defining properties of reinforcement steel for grade B420C

B420C	
f_{sy} (MPa)	420
ε_{sy}	0.0021
ε_{sh}	0.008
ε_{su}	0.08
f_{su}/f_{sy}	1.15-1.35

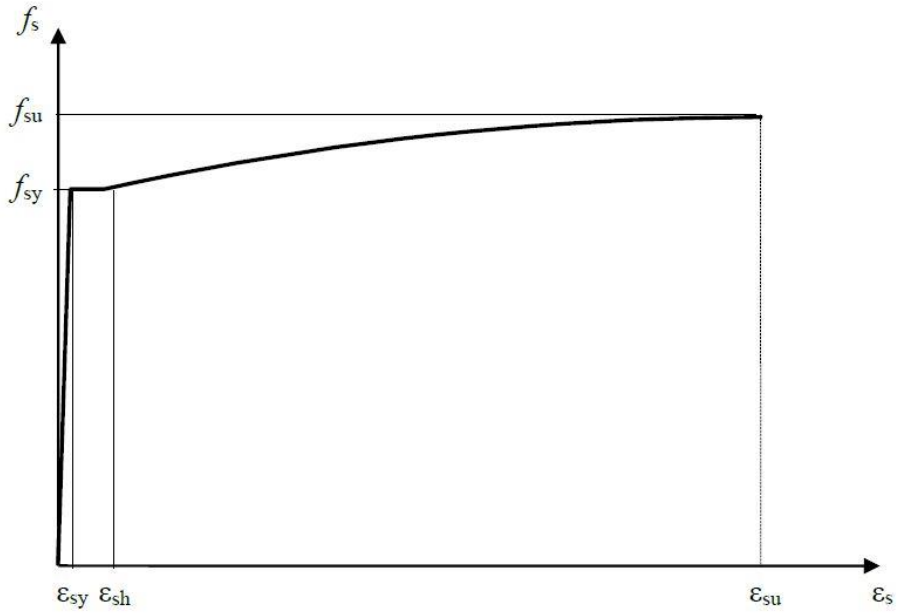

Figure 4.2: Stress-strain relationship for reinforcement steel

The piecewise function used to calculate the stress-strain curve of the reinforcement steel is given in Equation (4.12). The first segment of the curve describes the linear-elastic behavior of steel, followed by the yield plateau, and the second-degree curve describing the strain hardening that takes place after the steel yields.

$$f_s = \begin{cases} E_s \varepsilon_s & \left(\varepsilon_s \le \varepsilon_{sy}\right) \\ f_{sy} & \left(\varepsilon_{sy} < \varepsilon_s \le \varepsilon_{sh}\right) \\ f_{su} - \left(f_{su} - f_{sy}\right)\left(\dfrac{\varepsilon_{su} - \varepsilon_s}{\varepsilon_{su} - \varepsilon_{sh}}\right)^2 & \left(\varepsilon_{sh} < \varepsilon_s \le \varepsilon_{su}\right) \end{cases} \tag{4.12}$$

4.2 Modeling Structural Elements

The structural elements were modeled using line elements with lumped plasticity in the form of user-defined plastic hinges. Beams and columns were expected to display flexural behavior, therefore flexural hinges were calculated and assigned at the plastic hinge regions of these members. The flexural hinges were calculated using XTRACT [122], an FE section analysis software. XTRACT uses the concrete and steel models that were described in Section 4.1. The member sections are meshed, and the loads are applied incrementally to obtain the force-deformation curves desired. At each load application step, convergence is checked. These nonlinear models were used for both pushover and time-history analyses; therefore, non-symmetric plastic hinges were used to capture the effect of load reversals in time-history analyses. Shear capacities were also calculated; however, it was not expected that any member reaches the shear capacity prior to the flexural capacity. As concrete cracks early when subjected to lateral loads, coefficients for reduction of the stiffness of RC sections are applied generally. Various coefficients are suggested from different studies [69, 123] but TBEC suggests reduction coefficients of 0.35 and 0.7 for the sectional moment of inertia of beams and columns respectively.

4.2.1 Beams

Beams were modeled as T-beams in order to include the contribution of slabs in the capacity and stiffness of the beams and subsequently, include the contribution of slabs in the lateral stiffness of the frames. This was done both when assigning sections to the beam members in the SAP2000 models, and when calculating the flexural hinges of the beams. TS500 defines the width of the flanges for beams (b_e) as given by Equation (4.13), where l_p is defined by Equation (4.14) and b_w is the width of the beam web. ACI318 defines the effective width of the wide beams as given by Equation

(4.15). In this equation, b_c and h_c are the width and height of the column on which the beam is supported. LaFave and Wight [76] and Quintero-Febres and Wight [78] reported that this equation satisfactorily accounts for slab contribution to the capacity of wide beams.

$$b_e = b_w + 0.2l_p \tag{4.13}$$

$$l_p = \begin{cases} 0.8l & \text{for continuous beam and exterior span} \\ 0.6l & \text{for continuous beam and interior span} \end{cases} \tag{4.14}$$

$$b_e = \frac{1}{2}(b_w + b_c) + 2h_c \tag{4.15}$$

The moment-curvature curves of the beams were converted into bilinear curves with defined yield and maximum capacity, by applying the equal energy principle. Figure 4.3 shows an example of beam flexural hinges that were used in this thesis. The post peak behavior was assumed to be a simple capacity drop to $0.2M_{max}$. Takeda hysteresis model [124] was used in the plastic hinges of the beams.

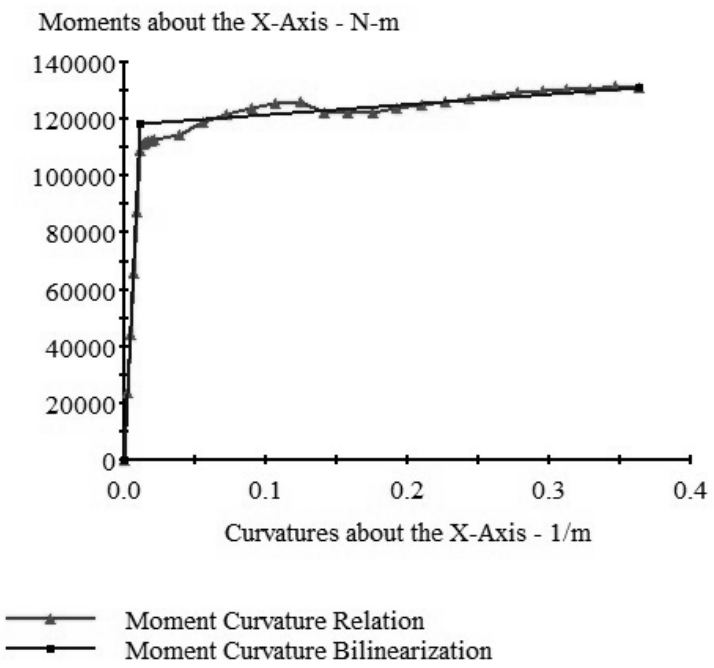

Figure 4.3: Continuous and Bilinear Moment-Curvature Curve for Beams

4.2.2 Columns

The flexural behavior of the columns is affected by the level of axial load applied. Therefore, hinges that account for this interaction were used to define the nonlinear behavior of columns. Since 2D frames were used, PM3 hinges were sufficient. The interaction curves were symmetric since the column sections used in this thesis were square and their reinforcement details were generally symmetric on each axis. An example of the axial load-moment interaction curves is shown in Figure 4.4. Moment-curvature relationships were calculated for each column sections at seven levels of axial load: 0%, 10%, 20%, 30%, 40%, 50%, and 60% of concrete section axial capacity. Values of moment and curvature for axial loads in between these levels were interpolated. Figure 4.5 shows an example of moment-curvature curves of a column section at a certain axial load level.

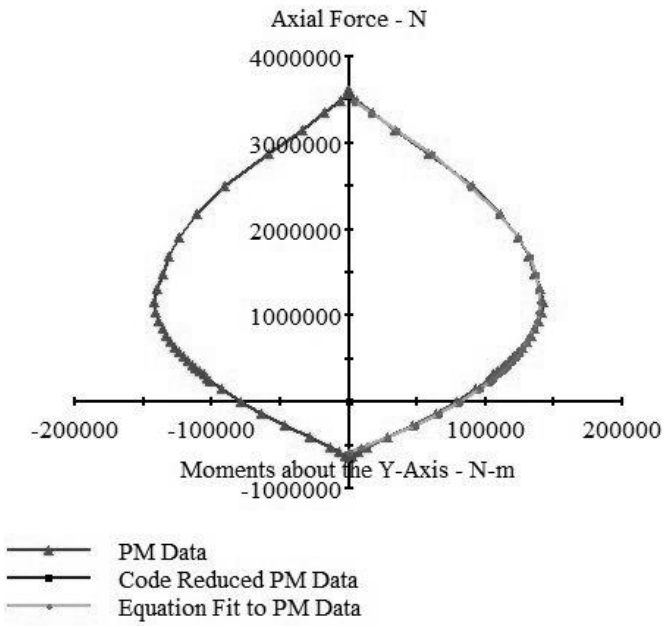

Figure 4.4: Axial load-moment interaction for columns

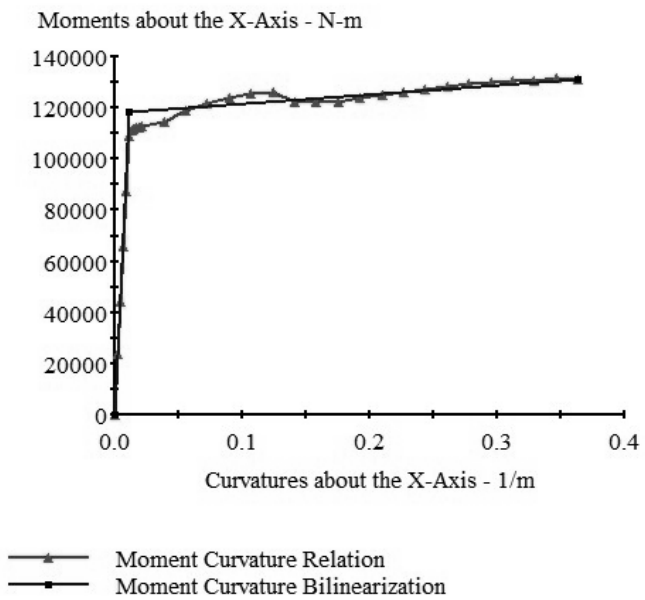

Figure 4.5: Moment-curvature curves for columns for a certain level of axial load

4.2.3 Performance Levels for Flexural Elements

TBEC defines three performance levels for RC sections, Limited Damage (LD), Controlled Damage (CD) and Collapse Prevention (CP). These performance levels are defined based on strains for distributed plasticity models and based on rotations for lumped plasticity models.

For plastic hinges for RC column and beam sections, the plastic rotation of the CP performance level is defined by Equation (4.16). The parameters present in this equation are as follows:

ϕ_u – curvature at collapse prevention

ϕ_y – curvature at yield

L_p – length of plastic hinge

L_s – shear span of the element

d_b – the average diameter of the reinforcement rebars

$$\theta_p^{CP} = \frac{2}{3}\left[\left(\phi_u - \phi_y\right)L_p\left(1 - 0.5\frac{L_p}{L_s}\right) + 4.5\phi_u d_b\right] \tag{4.16}$$

The plastic rotations of the LD and CD performance levels are given by Equations (4.17) and (4.18) respectively.

$$\theta_p^{LD} = 0 \tag{4.17}$$

$$\theta_p^{CD} = 0.75\theta_p^{CP} \tag{4.18}$$

The total rotations of each of these performance levels would be the summation of the yield rotation, which is obtained from the idealized moment-curvature curves of the sections, and the plastic rotation corresponding to that performance level.

4.2.4 Shear Capacity of Beams and Columns

Shear failure is generally not expected to be observed in code-compliant structures. However, the shear capacities of beam and column sections were calculated and modeled as brittle hinges. The shear capacity of a RC section is the summation of the shear capacity of the concrete section and the shear strength provided by the transverse reinforcement. Equation (4.19) gives the formula for the shear capacity of RC sections, according to TS500 and TBEC.

$$V_r = 0.52 f_{ctd} b_w d\left(1 + \gamma\frac{N_d}{A_c}\right) + \frac{A_{sw}}{s} f_{ywd} d \tag{4.19}$$

where:

f_{ctd} – the tensile strength of concrete

d – the effective depth of the section

γ – the coefficient that reflects the effect of the axial load on the cracking capacity of a section

N_d – axial load acting on the section

A_c – the total concrete area of the section

A_{sw} – the area of the transverse reinforcement

s – the spacing of the transverse reinforcement

f_{ywd} – the yield strength of the transverse reinforcement

4.2.5 Strut Model for Infill Walls

Studies on frames with normal beams have shown that infill walls can have both a positive and negative effect on RC framed structures. Infill walls can increase the strength and initial stiffness of RC frames [125, 126]. On the other hand, infill walls may induce other failure modes such as soft story [127] and short column effect [128]. A study on old conventional RC frame structures [129] reported that strong infill walls not only increased the strength and the stiffness of the frames but changed the response and failure mechanisms as well. A study on special moment resisting frames with infill walls [130] also reported improved strength and stiffness, but the ductility and energy dissipation capacity decreased with the inclusion of infill walls. Infill walls make the structures more rigid [131], but the contribution is often short-termed, and when the capacity of the infill walls is reached, a considerable degradation of the capacity and stiffness is observed [132]. Dominguez et al. [59] reported that the effect of infill walls was particularly positive in code compliant WBF structures that are designed for seismic action. Lopez-Almansa et al. [106] reported that infill walls increased the lateral capacity of existing WBF but resulted in premature failure. Benavent-Climent et al. [105] concluded that infill walls may result in damage concentrations and therefore negatively affect the seismic behavior of existing WBF.

Infill walls are considered nonstructural elements and may or may not be included in structural models. When infill walls are to be included in nonlinear models with line elements and lumped plasticity, TBEC, FEMA356 and FEMA 306 suggest using equivalent compression strut models. The simplest approaches use a single compression strut to model any given infill wall panel. The equivalent strut width can be computed with Equation (4.20). In this equation, h_c is the length of the columns

while r_d is the diagonal length of the infill wall. The parameter λ_d is given in Equation (4.21).

$$a_d = 0.175\left(\lambda_d h_c\right)^{-0.4} r_d \tag{4.20}$$

$$\lambda_d = \left[\frac{E_d t_d \sin 2\theta}{4 E_c I_k H_w}\right]^{\frac{1}{4}} \tag{4.21}$$

where:

E_d – the elastic modulus of the infill wall

t_d – the thickness of the infill wall

θ – the angle of the diagonal of the infill wall with respect to the horizontal axis

E_c – the elastic modulus of concrete

I_k – the moment of inertia of the column

H_w – the height of the wall

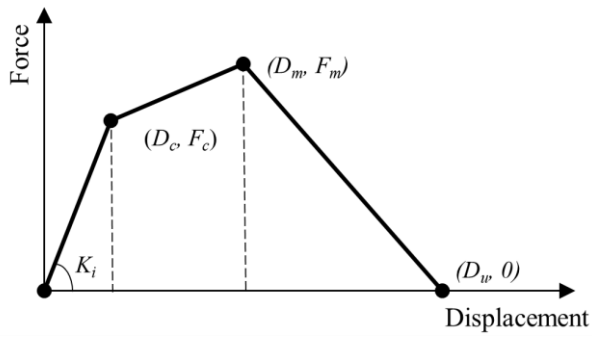

Figure 4.6: Force-displacement relationship used to describe the nonlinear behavior of the equivalent struts

FEMA356 suggests that a force-displacement relationship should be suggested to be used to define the capacity of the equivalent struts. There are a few models available that describe the force-displacement relationship of single struts, such as Panagiotakos

and Fardis [133] and [134]. The model of Panagiotakos and Fardis, shown in Figure 4.6 has been used with success by other researchers [129, 132, 135], and it was used in this thesis as well.

The force-displacement curve is composed of three segments. The first segment, up to point (D_c, F_c), indicate the initial shear response of the uncracked wall. The point (D_c, F_c) is the cracking point of the infill wall. The second segment indicates the formation of the compression strut, while the last part of the curve shows the softening of the infill wall. While some residual capacity can be assumed at the ultimate displacement D_u, some sources [132] assume no residual capacity at all, as indicated in Figure 4.6. Considering the brittle nature of unreinforced infill walls, this approach was used in this thesis as well. The maximum force F_m attained by the equivalent strut is calculated by Equations (4.22) and (4.23), proposed by Zarnic and Gostic [136]. The initial stiffness K_i of the force-displacement curve is defined by Equation (4.24). The rest of the parameters were defined by Dolsek and Fajfar [132, 137], as shown in Equations (4.25), (4.26) and (4.27).

$$F_m = 0.818 \frac{f_{tp} L_w t_w}{C_1} \left(1 + \sqrt{\left(C_1^2 + 1\right)}\right) \tag{4.22}$$

$$C_1 = 1.925 \frac{L_w}{H_w} \tag{4.23}$$

$$K_i = \frac{G_w L_w t_w}{H_w} \tag{4.24}$$

$$D_m = 0.2\% \tag{4.25}$$

$$\frac{D_u}{D_m} = 5 \tag{4.26}$$

$$\frac{F_y}{F_m} = 0.6 \tag{4.27}$$

where:

f_{tp} – the strength of the infill wall determined from diagonal compression tests

L_w – length of the infill wall

H_w – the height of the infill wall

G_w – the shear modulus of the infill wall. Due to the analytical nature of the study, G_w was taken as 40% of the E_w, as suggested by TBEC.

The material properties for infill walls made of factory grade hollow bricks are:

E_d=2000 MPa; f_d=3.0 MPa; τ_d=0.20 MPa

4.2.6 Length and Location of Plastic Hinges

The length of plastic hinges has been defined in various forms, such as shown in Equations (4.28) and (4.29). The first approach by Park and Paulay [138] is simple and is currently suggested by TBEC as well. The hinge length expressed by equation (4.29) was suggested by Priestley et al. [139].

$$L_p = 0.5h \tag{4.28}$$

$$L_p = 0.08L + 0.022\, f_{ye} d_{bl} \geq 0.044\, f_{ye} d_{bl} \tag{4.29}$$

In these equations, h stands for the height of the section for which the hinge has been calculated, L denotes the distance between the location of the hinge to the point of inflection for the structural member, while f_{ye} and d_{bl} are the yield strength of the longitudinal reinforcement and its diameter respectively. The hinge length suggested by TBEC (Equation (4.28)) was used in this thesis. The locations of the hinges have been calculated using the approach proposed by Inel and Ozmen [140]. Figure 4.7 visually depicts the location of hinges and Equations (4.30), (4.31) and (4.32) give the formulations that can be used to calculate the location of the hinges.

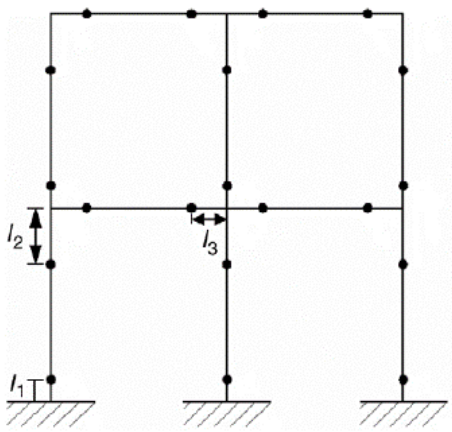

Figure 4.7: Location of flexural plastic hinges assigned to beams and columns

$$l_1 = \frac{L_p}{2} \tag{4.30}$$

$$l_2 = h_b + \frac{L_p}{2} \tag{4.31}$$

$$l_3 = \frac{h_c}{2} + \frac{L_p}{2} \tag{4.32}$$

Chapter 5

Seismic Capacity and Behavior of Wide Beam Frames

In this chapter the seismic capacity and behavior of WBF are assessed and compared to the capacity and behavior of CBF. The lateral load carrying capacities and displacement capacities are estimated for each of the frames. The energy dissipation capacities are calculated as well. Qualitative and quantitative assessments of ductility are obtained from plastic mechanisms and capacity curves, respectively. The effects of beam type, story number, number of bays, soil class and elevation irregularity on these performance parameters are also discussed separately.

One of the simplest tools that can be used to obtain all this information is pushover analysis. Pushover analysis is a simple nonlinear static analysis procedure that helps capture the nonlinear and plastic behavior of structures when subjected to lateral loads. These loads are applied incrementally and after every step, the state of structural elements is checked, and the overall stiffness of the structure is recalculated.

The nonlinear analyses on the frames were performed using structural analysis software SAP2000 [120]. The nonlinear models were created using line elements for beams and columns. The nonlinear behavior of beams and columns was modeled using the force-deformation plastic hinges that were described in Chapter 4. The nonlinear behavior of beam-column joint panels was not modeled because they are expected to remain elastic, since TBEC uses capacity design for the design of RC structures. This approach ensures that only ductile mechanisms are activated under seismic actions. It also defines a hierarchy of member failure to ensure an overall ductile behavior. Therefore, beam-column joints were designed in such a way that they will remain elastic. The frames were designed as separated from the infill walls; therefore, the

walls were modeled as gravity loads only in most of the cases. Some of the frames were analyzed for a second time by explicitly modeling the infill walls as well. These frames were designed for soil class D. Gravity loads as depicted in Appendix A were applied on the frames.

5.1 Pushover and Modal Analysis

There are different types of lateral load configurations that can be used for pushover analyses, such as uniformly distributed lateral load, inverted triangle and mass proportional distribution (Figure 5.1). Alternatively, the distribution of the lateral force can be modeled according to the first vibration mode shape if that is dominant, or according to multiple mode shapes that dominate the vibration of the structure. TBEC suggests performing pushover analysis based on the first mode shape in cases that the modal mass for the first mode shape is higher than 0.7, otherwise pushover analysis based on multiple dominant mode shapes is to be carried out.

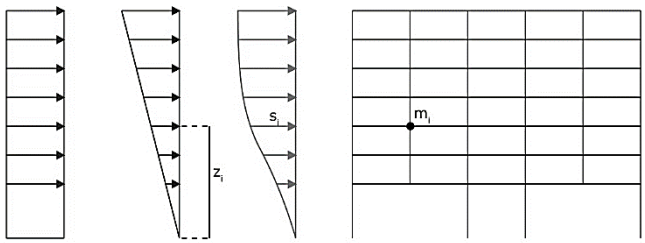

Figure 5.1: Types of lateral load patterns that can be used for pushover analyses, from left to right: uniformly distributed, inverted triangle and modal lateral load pattern

Pushover analysis based on the first vibration mode shape was adequate for all the frame models. Table 5.1 lists the dynamic properties of the models, including fundamental period of mass participation factor for the first mode shape. Frames with wide beams have higher fundamental periods than frames with conventional beams, therefore they are more flexible.

Table 5.1: Dynamic properties of frame models

Frame	T_1(s)	α_1	T_2(s)	α_2	$\alpha_1+\alpha_2$
C-4C4	0.975	0.881	0.324	0.090	0.971
W1-4C4	1.291	0.801	0.418	0.127	0.928
W2-4C4	1.307	0.855	0.419	0.102	0.957
C-4C2	0.849	0.871	0.285	0.093	0.964
W1-4C2	1.195	0.802	0.375	0.117	0.919
W2-4C2	1.280	0.849	0.406	0.104	0.954
C-4C6	0.848	0.867	0.292	0.091	0.958
W1-4C6	1.221	0.777	0.402	0.134	0.911
W2-4C6	1.115	0.786	0.374	0.130	0.915
C-6C4	1.284	0.842	0.444	0.097	0.939
W1-6C4	1.750	0.777	0.601	0.117	0.894
W2-6C4	1.745	0.779	0.585	0.119	0.898
C-IC	0.773	0.883	0.296	0.079	0.962
W1-IC	1.313	0.855	0.476	0.104	0.959
W2-IC	1.202	0.871	0.443	0.095	0.966
C-4D4	0.975	0.881	0.324	0.090	0.971
W1-4D4	1.153	0.793	0.353	0.125	0.918
W2-4D4	1.190	0.828	0.396	0.117	0.945
C-4D2	0.849	0.871	0.285	0.093	0.964
W1-4D2	0.961	0.785	0.289	0.127	0.912
W2-4D2	1.085	0.806	0.358	0.118	0.923
C-4D6	0.807	0.844	0.282	0.099	0.943
W1-4D6	1.145	0.798	0.377	0.121	0.919
W2-4D6	1.035	0.786	0.349	0.130	0.915
C-6D4	1.284	0.842	0.444	0.097	0.939
W1-6D4	1.474	0.774	0.464	0.117	0.892
W2-6D4	1.568	0.785	0.551	0.117	0.902
C-ID	0.773	0.883	0.296	0.079	0.962
W1-ID	1.238	0.852	0.456	0.108	0.961
W2-ID	1.202	0.871	0.443	0.095	0.966

It can also be noted that frame models that were designed for soil class D have lower fundamental periods than the same frames that were designed for soil class C. In general, the first vibration mode was dominant for all the models, since the mass participation factor was greater than 0.7. When running pushover analyses, convergence and tolerances were adjusted in order to obtain a significant number of steps and reach structural instability. Convergence error was mostly kept at 0.005-0.001. The analyses were run until an apparent strength degradation of 20-30% from the point in which the pushover curves ceased to be linear was reached.

5.2 Structural Acceptance Criteria

One of the most important tasks to be completed when structural assessment is being carried out is to determine the performance level of the structure as a whole. TBEC defines three structural performance levels followed by the state of collapse. These are Limited Damage (LD), Controlled Damage (CD) and Collapse Prevention (CP). The criteria for these damage levels are expressed in percentage of members of any given floor that pertain to a certain section Damage Level. The section Damage Levels are shown in Figure 5.2. If the deformation of a member is less than the deformation corresponding to LD than the said member belongs to the Limited Damage Region. If the deformation of a member exceeds the LD limits but not the CD limit, then this member belongs to the Significant Damage Region. The rest of the Damage Regions can be interpreted similarly.

The criteria for the performance levels of the structures applicable to the frame models that have been analyzed in this study are summarized below.

A building belongs to the *Limited Damage Performance Level* when at most 20% of the beams in any given floor have passed to the Significant Damage Region, while the rest of the structural members remain in the Limited Damage Level.

A building belongs to the *Controlled Damage Performance Level* if:

- At most 35% of beams of any given floor have passed to the Advanced Damage Region;

- In any given floor, columns that belong to the Advanced Damage Region do not provide more than 20% of the total floor shear capacity. This limit is raised to 40% for the topmost floor;
- The rest of the structural elements belong to either Limited Damage Region or Significant Damage Region. However, if in any given floor there are columns that have reached the Significant Damage Region in both top and bottom sections, the shear capacity of these columns should not exceed 30% of the total shear capacity of the floor.

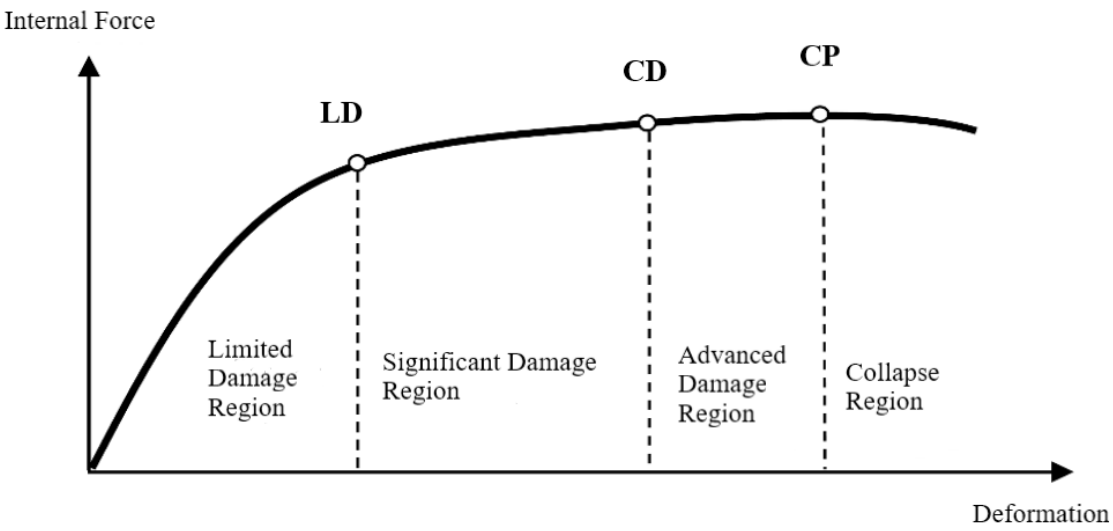

Figure 5.2: Section Damage Levels

A building belongs to the *Collapse Prevention Performance Level* if:

- At most 20% of beams of any given floor have passed to the Collapse Region;
- The rest of the structural elements belong to either Limited Damage Region, Significant Damage Region or Advanced Damage Region. However, if in any given floor there are columns that have reached the Significant Damage Region in both top and bottom sections, the shear capacity of these columns should not exceed 30% of the total shear capacity of the floor.

Collapse state is reached when a structure no longer complies with the limits of the *Collapse Prevention Performance Level*.

Table 5.2: Number of beams in each floor that should be in a damage level to define the performance of the structures.

Nr. of bays	LD	CD	CP
	Maximum number of beams in Significant Damage Region	*Maximum number of beams in Advanced Damage Region*	*Maximum number of beams in Collapse Region*
2	0[1]	1	0[2]
4	1	1	1
6	1	2	1

[1] *This was interpreted as the last step before one beam enters the Significant Damage Region.*
[2] *This was interpreted as the last step before one beam enters the Collapse Region.*

Since in this thesis two dimensional frames are used, the number of structural members in each floor is limited. Frames with two bays have only two beams in each floor, frames with four bays have four beams, and frames with six bays have six beams in each floor. Table 5.2 summarizes the assumptions regarding the maximum number of beams in each floor that should belong to a certain damage level in order to put the frame in the corresponding performance level.

5.3 Capacity Curves

The pushover curves were obtained in terms of base shear (V) and rooftop displacement (Δ). The base shear was normalized with respect to the weight of frames defined as $G+0.3Q$, and the unitless ratio V/W is the lateral load coefficient. The rooftop displacement was normalized with respect to the total height of the frames (Equation (5.1)) to obtain the Global Drift Ratio (GDR). GDR is expressed in percent in order to increase the accuracy of reported values while avoiding working with very small numbers.

$$GDR = 100 \times \frac{\Delta}{H} \qquad (\%) \tag{5.1}$$

5.3.1 Regular Frames Designed for Soil Class C

Figure 5.3 presents the pushover curves for the regular frames that were designed for soil class C. The first thing that can be observed from this figure is that CBF always reach higher lateral load coefficients than WBF. The maximum lateral load coefficient varies from 0.1 for the six story frame, to 0.14 for the four bay and four story frame, and 0.16 for the other two frames. CBF are characterized by lower drift ratios overall and visibly higher initial stiffness. The pushover curves of the WBF on the other hand do not have a clear peak, the overstrength factor is very small. WBF are more flexible than CBF, they have lower initial stiffness and in overall display higher displacements. Among the two types of WBF, W1 frames generally reach higher lateral load capacities than W2 frames, while their displacements are comparable. The only exceptions to this are frames W1-4C6 and W2-4C6. In this case the W2 frame has greater lateral load capacity than the W1 frame.

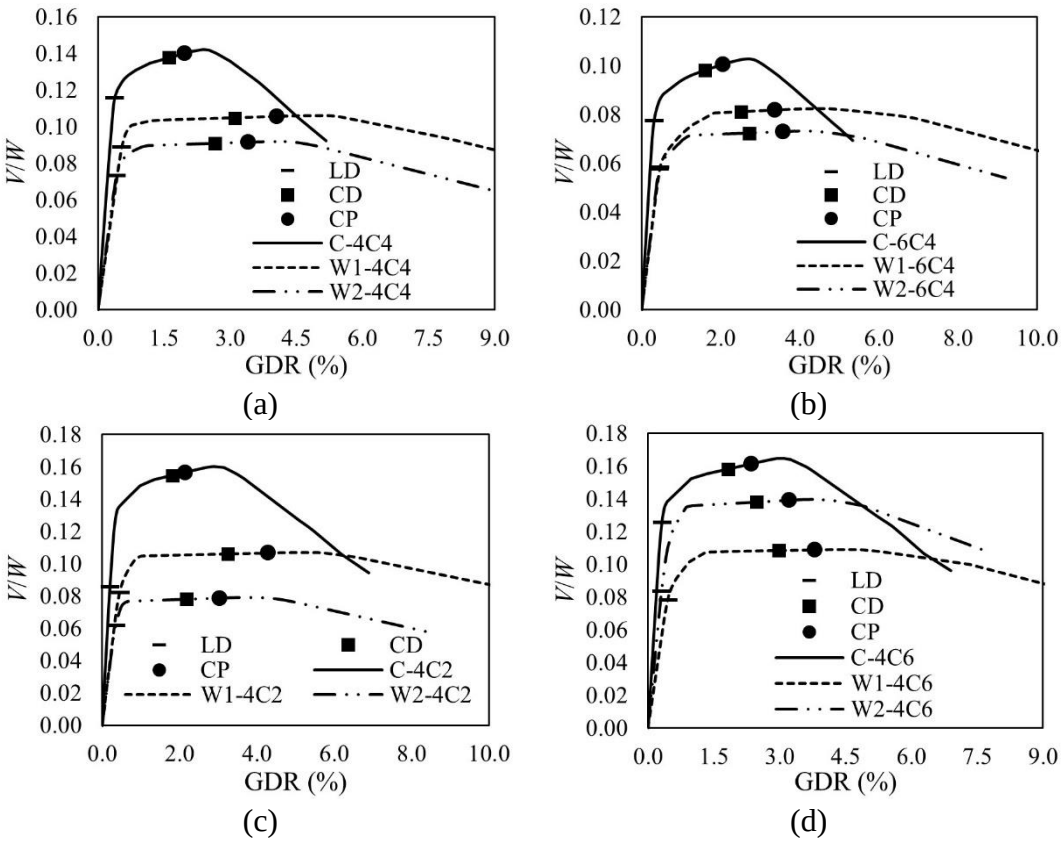

Figure 5.3: Pushover curves for regular frames designed for soil class C: (a) 4C4; (b) 6C4; (c) 4C2; (d)4C6.

The structural performance levels are marked in the pushover curves in Figure 5.3. It is observed that the drift ratio limit for LD of the CBF is in the range of 0.20-0.38%, of W1 frames this range is0.45-0.54%, and of W2 frames the LD drift ratio limit varies in the 0.31-0.45% interval. Similarly, the ranges of the drift ratio limit for CD are 1.59-1.82% for CBF, 2.52-3.24% for W1 frames and 2.18-2.72% for W2 frames. The ranges of the drift ratio limit for CP are noted to be 1.98-2.36% for CBF, 3.36-4.27% for W1 frames and 3.04-3.58% for W2 frames.

The drift ratios corresponding to the maximum lateral load are in the range of 2.38-3.00% for CBF, 4.54-5.11% for W1 frames and 3.63-4.26% for W2 frames. This point is located in the Collapse Region for all the regular frames designed for soil class C.

The type of wide beam used in WBF affected the capacity of the frames designed for soil class C. In general, the W1 frames displayed higher lateral load capacities and higher displacement capacities. This was mostly due to the larger column sizes that were required in the design stage to comply with code requirements for lateral displacements, since the wide beams of W1 frames had narrower sections than the beams of W2 frames. The beams of W2 frames had widths between 600 mm and 700 mm, therefore they provided more stiffness to the frames, and thus required smaller column sections. However, since the effective depth of all wide beams was the same, the W2 beams had only slightly higher moment capacities than W1 beams, the contribution of the beams to the strength of the frames was similar on both cases. Thus, frames W1 which had larger columns per design requirements, generally displayed higher capacities than frames W2.

5.3.2 Regular Frames Designed for Soil Class D

The seismic capacities of the regular frames designed for soil class D are graphically depicted in Figure 5.4. Similar to the observations made for the regular frames designed for soil class C, CBF are characterized by higher lateral load capacities, higher initial stiffnesses and overall lower displacements than WBF. However, the differences in lateral load capacity are less pronounced in these frames, and CBF have only slightly higher capacities than WBF. For instance, the maximum lateral load coefficient of the six story frames (Figure 5.4b) is almost the same, around 0.10. The four story and six bay frames (Figure 5.4d) have more pronounced differences, and in

this case again, the W2 frames reach greater capacities than W1 frames. The initial stiffness of the WBF is very similar among them, and their displacement behavior as well.

The performance levels are marked in the pushover curves shown in Figure 5.4. The limiting drift ratios for LD were in the ranges of 0.23-0.38% for CBF, 0.45-0.59% for W1 frames and 0.42-0.51% for W2 frames. The limiting drift ratios for CD were in the ranges of 1.57-2.05% for CBF, 2.71-3.33% for W1 frames and 2.78-3.57% for W2 frames. The limiting drift ratios for CP were in the ranges of 1.98-2.45% for CBF, 3.43-4.33% for W1 frames and 3.53-4.49% for W2 frames. The drift ratio at the maximum base shear ranged between 2.38-2.82% for CBF, 4.21-5.10% for W1 frames and 3.98-5.03% for W2 frames. The point of maximum base shear was located in the Collapse Region for the regular frames designed for soil class D.

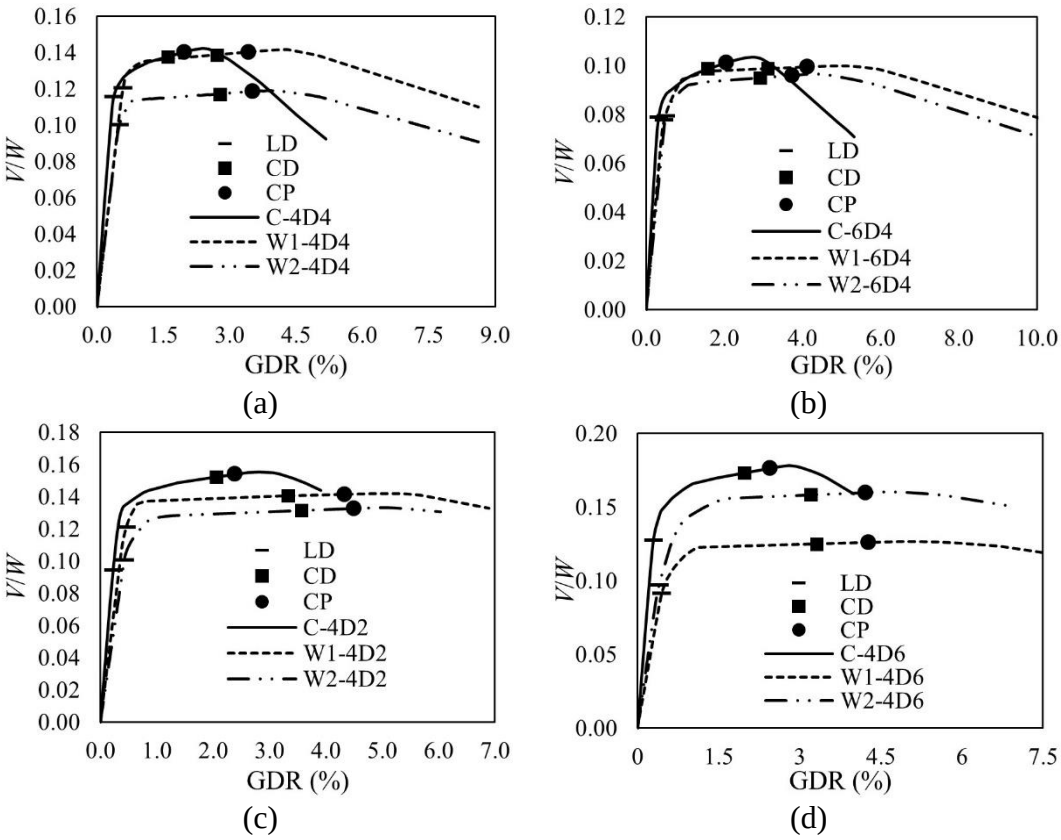

Figure 5.4: Pushover curves for regular frames designed for soil class D: (a) 4D4; (b) 6D4; (c) 4D2; (d)4D6.

The effect of the wide beam width was less pronounced in the WBF designed for soil class D. For instance, in the 6D4 and 4D2 frames the differences are small. The effect of the beam width is more pronounced in the 4D4 and 4D6 frames. Similarly to the frames that were designed for soil class C, W1 frames that have narrower beams have larger column sections, while W2 frames have smaller column sections. However, the frames that were designed for soil class D were subjected to greater equivalent lateral forces because they generally have smaller periods (Table 5.1) than their soil class C counterpart frames and the response spectrum of the soil class D has greater ordinates than the response spectrum of soil class C.

5.3.3 Irregular Frames

The difference between CBF and WBF was even more pronounced in the irregular frames. The irregular CBF frames reached maximum lateral load coefficients as high as 0.21, while the maximum lateral load coefficient was 0.11 for W1-IC and W2-IC and 0.16 for W1-ID and 0.15 for W2-ID. Irregular WBF were more flexible and reached greater displacements than irregular CBF. For instance, frames C-IC and C-ID reached their maximum base shear at a GDR of 2.31%. Frames W1-IC and W1-ID reached the maximum base shear at a drift ratio of 4.00 and 5.18% respectively, while frames W2-IC and W2-ID reached that at 3.57% and 4.10% drift ratio, respectively. As it is seen from Figure 5.5 all the frames are in the Collapse Region when they reach their maximum base shear capacity.

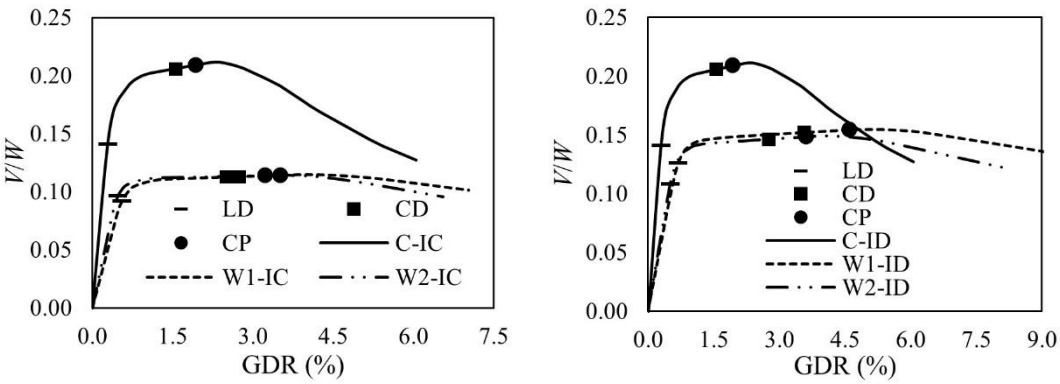

(a) (b)

Figure 5.5: Pushover curves of irregular frames (a) IC; (b) ID

The performance levels are marked in the pushover curves shown in Figure 5.5. The drift ratio limits for the LD performance level are 0.29% for C-IC and C-ID, and 0.55%, 0.68%, 0.48% and 0.50% for W1-IC, W1-ID, W2-IC and W2-ID respectively. The drift ratio limits for the CD performance level are 1.55% for C-IC and C-ID, and 2.75%, 3.56%, 2.50% and 2.75% for W1-IC, W1-ID, W2-IC and W2-ID respectively. The drift ratio limits for the CP performance level are 1.93% for C-IC and C-ID, and 3.51%, 4.61%, 3.23% and 3.62% for W1-IC, W1-ID, W2-IC and W2-ID respectively. Again, CBF reach damages states much early than WBF, and WBF display greater deformation capacities.

In the case of irregular frames, the width of the wide beam makes very little difference. The pushover curve of frame W1-IC is almost identical to that of frame W2-IC, and the curves of W1-ID and W2-ID are also very similar.

5.4 Assessment of Initial Stiffness, Ductility and Energy Dissipation Capacity

Capacity curves can offer considerable insight besides the base shear capacity and displacement of the frame models. Energy dissipation is an important indicator of seismic behavior of structures; ductile and seismically resistant frames dissipate more energy than deficient frames. The energy capacity of the frame models can be calculated as the area beneath the capacity curve using numerical integration.

Initial stiffness and ductility are also indicators of seismic performance. Ductile structures generally perform better than brittle structures or structures with limited ductility. Observations about the initial stiffness and the ductility of the frame models can be made from the pushover curves, but exact values cannot be readily obtained. To calculate both initial stiffness and ductility the yield point of a structure should be determined. However, RC frames do not have a clearly defined yield point. Structural yield can be approximated by converting the continuous and smooth capacity curves into idealized bilinear curves.

ASCE/SEI 41-06 [141] and FEMA356 [142] offer an iterative method for the calculation of structural yield idealization of pushover curves, shown schematically in

Figure 5.6. The basic principle behind the idealization of capacity curves is that the total energy expressed by the original pushover curve is the same as the total energy of the idealized curve. The total energy dissipated is calculated as the area under the pushover curve until a point of interest. ASCE/SEI 41-06 determines the point of interest as lesser of the point of maximum base shear or the point of target displacement, but the point of maximum base shear is commonly used [143, 144]. In this thesis point (Δ_d, V_d) is the point of maximum base shear V_{max}.

Referring to Figure 5.6 the yield point (Δ_y, V_y) is defined as such that the first part of the idealized curve is secant to the actual pushover curve at $0.6V_y$. The post-peak branch of the idealized curve depicts some amount of strength degradation, which per state-of-the-art practice can range from 20% to 40%. ASCE/SEI 41-06 suggests 40% strength degradation, while Paulay and Priestley [123] suggest a 20% strength degradation. The approach of Paulay and Priestley has been used in this thesis, because it produces more meaningful data. As was noted from the pushover curves displayed in Figure 5.3 to Figure 5.5, WBF reach high drift ratios with small strength degradations. Strength degradations of 20-40% could refer to high and unrealistic drift ratios. From these figures it was also observed that the point of maximum base shear is past the CP point and within the Collapse Region. Therefore, the point of maximum base shear was considered a meaningful representative of collapse and ultimate displacement. This definition which is based on global deformations is less sensitive to the rotation ductility of the beams, either normal or wide and was henceforward used for the idealization of the pushover curves and calculation of energy dissipation and ductility capacities.

$$k_e = \frac{V_y}{\Delta_y} \tag{5.2}$$

$$\mu = \frac{\Delta_{V_{\max}}}{\Delta_y} \tag{5.3}$$

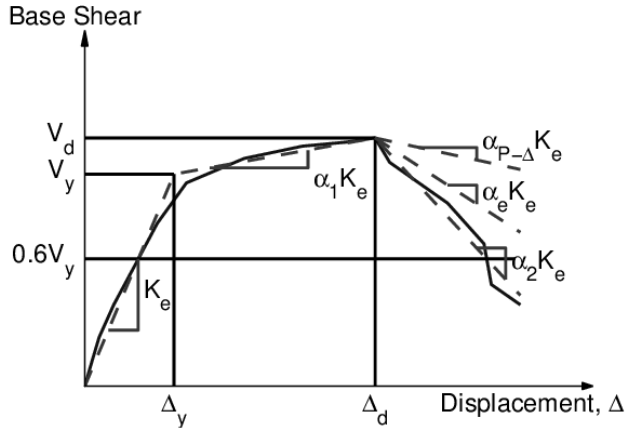

Figure 5.6: Idealization of pushover curve per ASCE/SEI 41-06

Table 5.3: Deformation and energy parameters of the frame models

Frame	***E*** **(kNm)**	k_e **(kN/m)**	μ	**Frame**	***E*** **(kNm)**	k_e **(kN/m)**	μ
C-4C4	116.3	9817.7	6.25	**C-4D4**	116.3	9817.7	6.25
W1-4C4	220.3	5502.5	8.38	**W1-4D4**	240.1	6986.9	6.59
W2-4C4	164.2	6123.2	8.75	**W2-4D4**	196.4	7028.3	7.30
C-4C2	85.1	6519.1	8.55	**C-4D2**	80.9	6570.2	8.47
W1-4C2	115.5	3358.9	9.36	**W1-4D2**	159.8	5190.1	10.30
W2-4C2	63.2	3300.3	8.91	**W2-4D2**	148.8	4265.2	9.48
C-4C6	256.7	18614.4	8.79	**C-4D6**	260.4	19866.7	8.13
W1-4C6	294.0	8780.3	7.83	**W1-4D6**	383.0	10235.4	8.68
W2-4C6	264.7	11207.2	7.76	**W2-4D6**	396.8	11168.8	7.91
C-6C4	221.8	8131.4	8.18	**C-6D4**	224.3	8134.0	8.14
W1-6C4	344.8	4432.1	7.84	**W1-6D4**	507.7	6513.2	9.83
W2-6C4	281.8	4729.1	7.93	**W2-6D4**	410.2	5829.0	7.89
C-IC	156.0	12420.2	6.11	**C-ID**	156.0	12420.2	6.11
W1-IC	166.7	4844.8	6.56	**W1-ID**	295.3	5420.7	7.04
W2-IC	156.7	6219.7	7.13	**W2-ID**	229.9	6199.6	6.41

The energy dissipated until the point of collapse (Δ_{Vmax}, V_{max}) was calculated by dividing the area beneath the pushover curves into thin trapezoidal slices. Through a

series of iterations a suitable value of V_y was estimated, such that both the area beneath the two curves until (Δ_{Vmax}, V_{max}) is the same, and the two curves intersect at the point of 0.6 V_y.

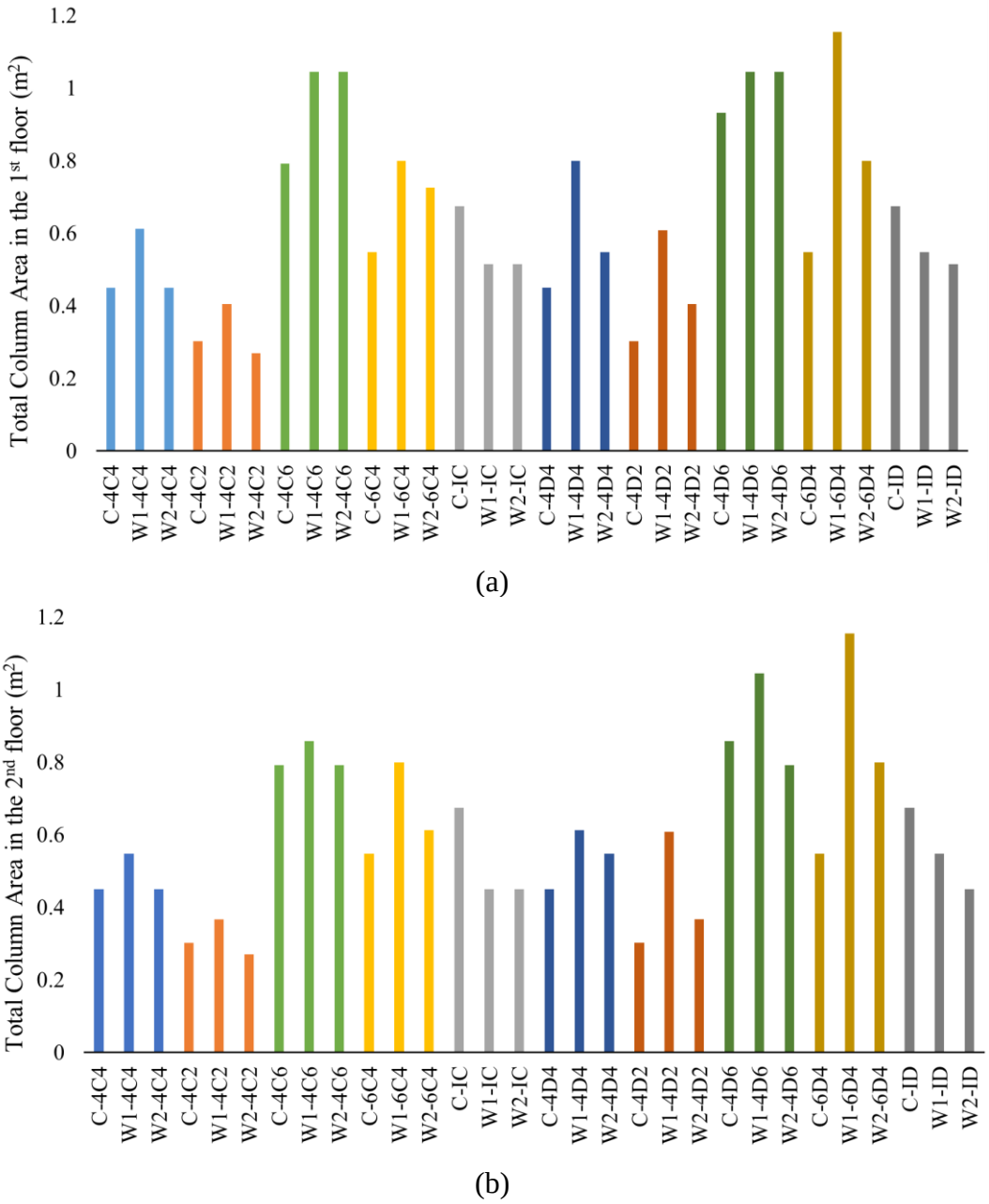

Figure 5.7: Total column area for all the frames, presented separately for (a) the first floor; (b) the second floor.

Table 5.3 summarizes the energy dissipation, initial stiffness and ductility values calculated after the yield base shear coefficient was estimated through this iterative process. The initial stiffness k_e is the slope of the first segment of the bilinearized capacity curve (Eq. (5.2)), and global ductility μ is the ratio of the displacement at V_{max} to the displacement at yield (Eq. (5.3)).

The general consensus from both the capacity curves shown in Figure 5.3, Figure 5.4 and Figure 5.5, and from the values of the initial stiffness k_e in Table 5.3 is that WBF are considerably more flexible than CBF. In general, W1 frames are more flexible than W2 frames. It should be noted that W1 frames generally have the largest column sections. To illustrate this, the total column areas for the first two floors for all the frames have been separately plotted in Figure 5.7. From this figure it is evident that W1 frames have the largest columns in the first and second floors. Generally, W2 frames have larger column section than CBF, but this is not always the case. Particularly the irregular CBF have larger column sections than the irregular WBF. Even though frames W1 have the largest column sections among the rest of the frames in each group, their initial stiffness is the smallest. This observation highlights the importance of the beam type on the lateral stiffness of frames. Chopra [145] presents a simple example, in which the stiffness of the beam in a simple one story-one bay frame can affect the linear stiffness of the frame up to four times.

5.5 Sequence of Hinge Formation and Plastic Mechanisms

The sequence of hinge formation was observed during the assessment of the performance levels of the frame models. It was noted that only flexure mechanisms were activated in all the frames. Generally, the yielding of beam end sections in either WBF or CBF took precedence to the yielding of any column section. Yielding of some columns, mostly the sections at the base of the columns on the first floor, was noticed at higher lateral displacement levels. At later stages, it was observed that some beam sections reached their ultimate capacities, but such a milestone was not observed for any of the column sections. Considering yielding of a section and a member reaching their ultimate capacities as two important events, the mechanisms at collapse were

investigated in this Section. Figure 5.8 to Figure 5.14 summarize these mechanisms. In these figures, a section that has yielded is denoted by an empty circle (○), and a section that has reached its capacity is denoted by a full circle (●).

5.5.1 Regular Frames with Four Stories and Four Bays

The mechanisms at collapse for the regular frames with four stories and four bays, shown in Figure 5.8, consisted of multiple story mechanisms, generally containing three stories. All the beams in the first three stories for frames C-4C4, W1-4C4, W2-4C4, and W1-4D4 had either yielded or reached their ultimate capacities, while in frames C-4D4 and W2-4D4 only beams in the first two stories either yielded or reached collapse. In the case of frames C-4C4, W1-4C4, W2-4C4, and W1-4D4, most of the beams in the first two stories had reached their ultimate capacities, while in frames C-4D4 and W2-4D4 only some of the beams on the first floor reached their capacities.

The type of beam had a small effect on the story mechanisms, since both WBF and CBF displayed ductile multistory mechanisms at collapse. However, the WBF of type W1 (Figure 5.8c and d) displayed a more spread damage compared to the either CBF (Figure 5.8a and b) or W2 type frames (Figure 5.8e and f). This was likely due to greater flexibility of the wide beams in frames of type W1 when compared to the normal beams of CBF or the wide beams of type W2.

The damage was more spread and typically included three floors in frames designed for soil class C (Figure 5.8a and e), and less spread and included only two floors in their counterparts designed for soil class D (Figure 5.8b and f). While all the frames were designed to comply with the same lateral deformation limits, the design base shear coefficients were smaller for the C-frames, resulting in greater overstrength factors, when compared to the D-frames. Therefore, the frames designed for soil class C had greater reserve capacities, and thus behaved in a slightly more ductile manner than frames designed for soil class D.

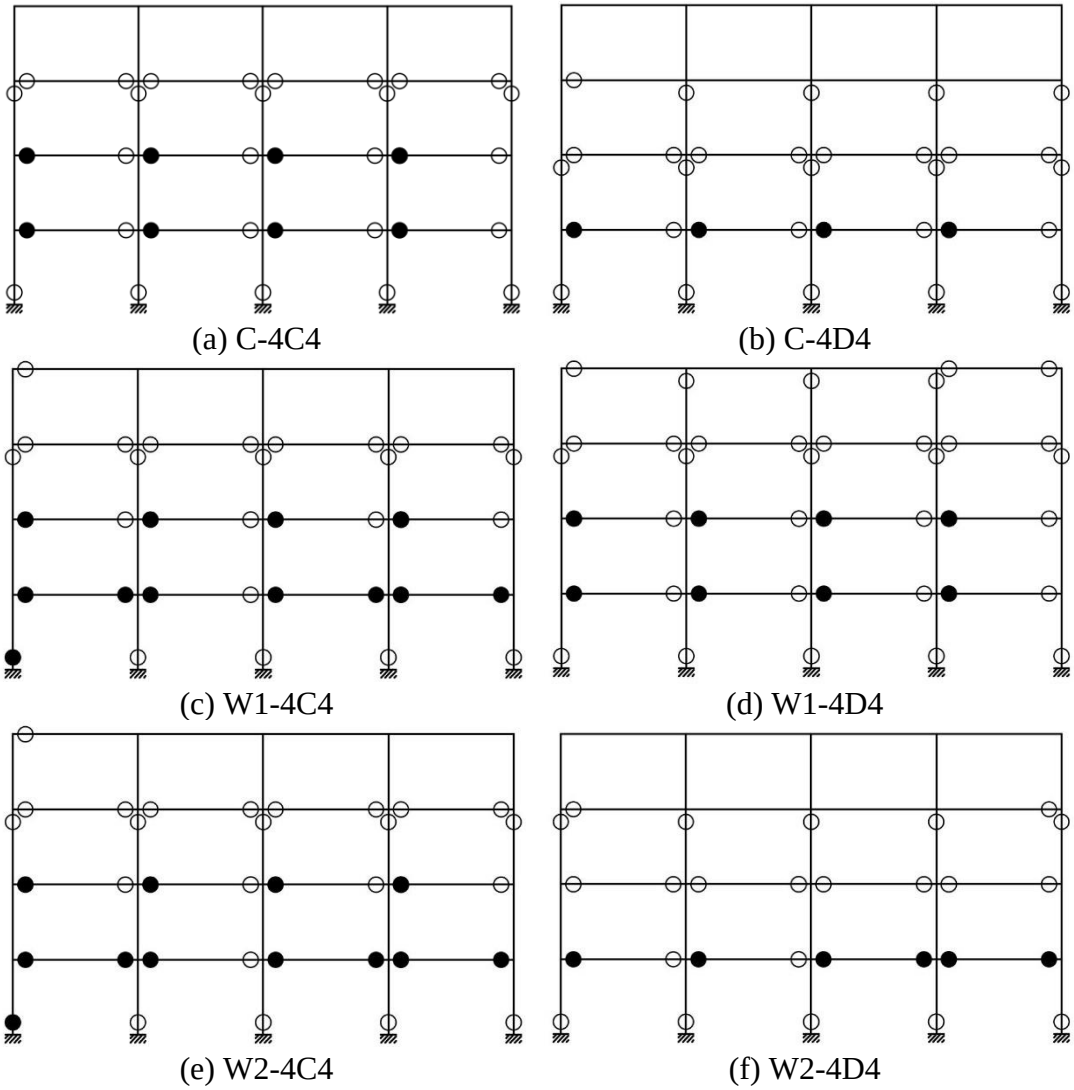

Figure 5.8: Plastic mechanisms at collapse of regular frames with four stories and four bays (○: Section has yielded; ●: Section has reached its capacity)

5.5.2 Regular Frames with Six Stories and Four Bays

The mechanisms at collapse for the regular frames with six stories and four bays, shown in Figure 5.9, consisted of multiple story mechanisms, generally containing four to five stories. The mechanisms at collapse of the CBF (Figure 5.9a and b) included the first four stories. The base sections of the columns on the first floor and the top sections of the columns on the fourth floor yielded, as had all the beam sections in the second, third and fourth floors of frames C-6C4 and C-6D4. Most of the beams on the first floor of these two frames reached their ultimate capacities.

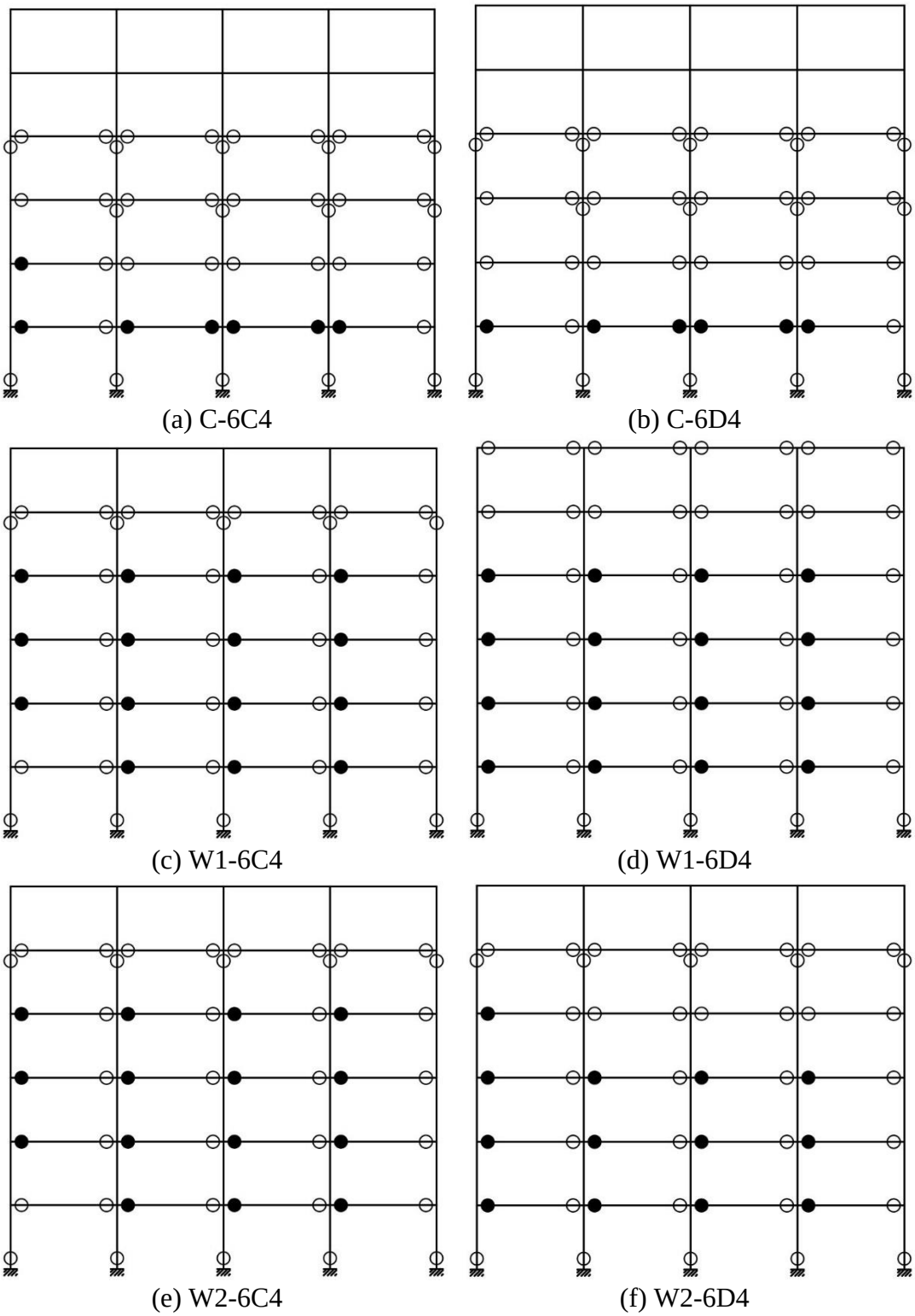

Figure 5.9: Plastic mechanisms at collapse of regular frames with six stories and four bays (○: Section has yielded; ●: Section has reached its capacity)

The mechanisms of the six story WBF generally included five stories (Figure 5.9b, e and f), with frame W1-6D4 (Figure 5.9d) being the only exception where the beams

of the last floor have also yielded. Most of the beams in the first four floors of the WBF had reached their capacities as well. The base sections of the columns on the first floor and the top sections of the columns on the fifth floor of frames W1-6C4, W2-6C4 and W2-6D4 yielded, while only the base sections of the columns on the first floor of frame W1-6D4 yielded at collapse stage.

The “type of beam” had a considerable effect on the story mechanisms of the six story frames. The WBF (Figure 5.9c, d, e, and f) clearly displayed wider spread damages than the CBF (Figure 5.9a and b). However, there were no considerable differences between the WBF of type W1 and W2 in the mechanisms of the six story regular frames. Soil class also had a negligible effect on the mechanisms of 6C4 and 6D4 frames, because the overstrength factors of the six story frames were smaller and less affected by the soil class.

5.5.3 Regular Frames with Four Stories and Six Bays

The mechanisms at collapse for the regular frames with four stories and six bays, shown in Figure 5.12, consisted of multiple story mechanisms, containing three or four stories. Frames C-4C6 and C-4D6 (Figure 5.12a and b) displayed similar mechanisms. All the beams in the first three stories either yielded or reached their capacities when structural collapse occurred. On the other hand, the plastic damage was spread on all the floors of the WBF, except for frame W2-4C6 (Figure 5.12a), in which none of the members of the last floor either yielded or reached their capacities. Frames W1-4C6, W1-4D6 and W2-4D6 (Figure 5.11a and b, and Figure 5.12b, respectively) behaved very similarly. All the beams of the first three floors either yielded or reached their capacities, and the bottom sections of the columns on the first floor and the top sections of the columns in the last floor had yielded. Typically, more beams reached their ultimate capacities in the WBF than in the CBF. The effect of the beam type was more pronounced when comparing WBF to CBF. The presence of wide beams in the regular four story-six bay frames resulted in plastic damage spread throughout all the floors and more beams reaching their capacity at structural collapse, while the presence of conventional beams resulted in slightly more limited damage. Soil class had a negligible effect on the mechanisms of 4C6 and 4D6 frames, because the overstrength factors of the six story frames were smaller and less affected by the soil class.

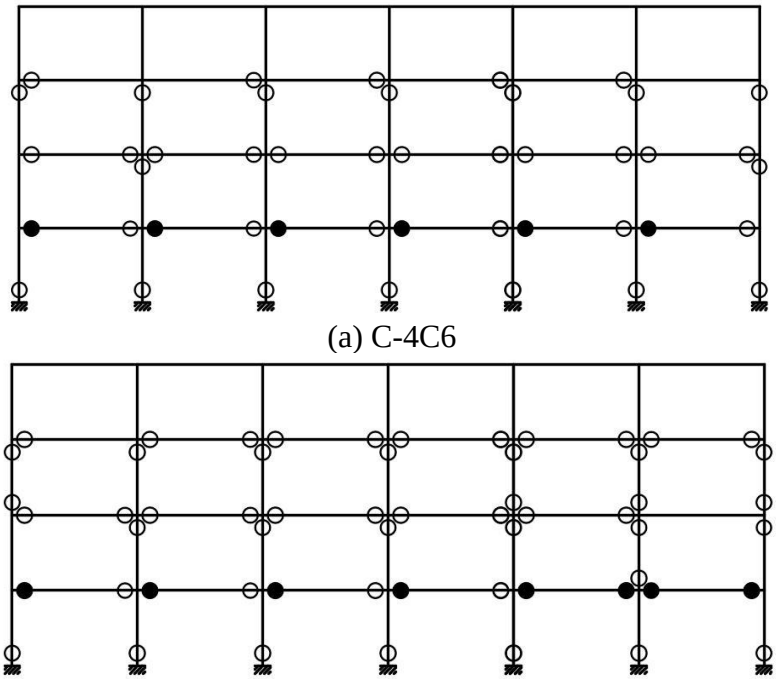

(a) C-4C6

(b) C-4D6

Figure 5.10: Plastic mechanisms at collapse of regular CBF with four stories and six bays (○: Section has yielded; ●: Section has reached its capacity)

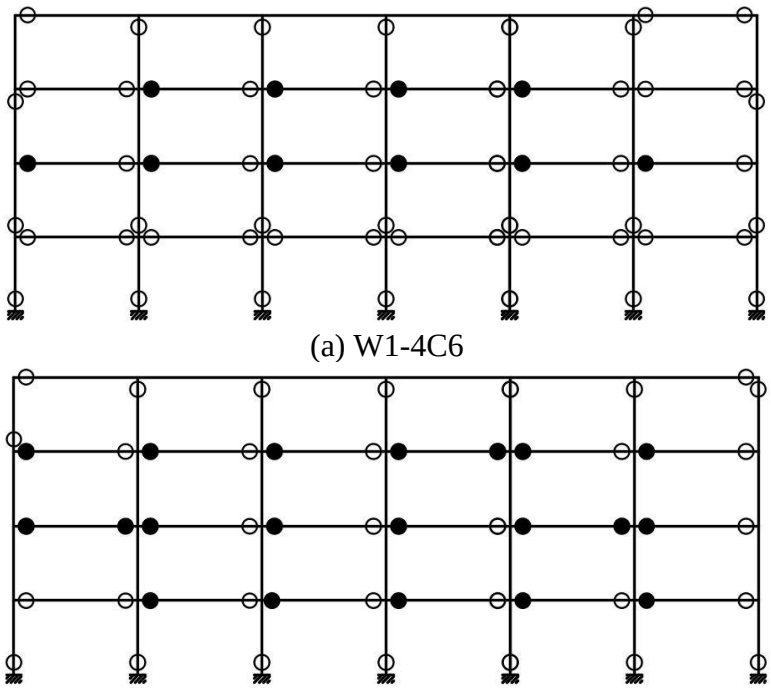

(a) W1-4C6

(b) W1-4D6

Figure 5.11: Plastic mechanisms at collapse of regular W1BF with four stories and six bays (○: Section has yielded; ●: Section has reached its capacity)

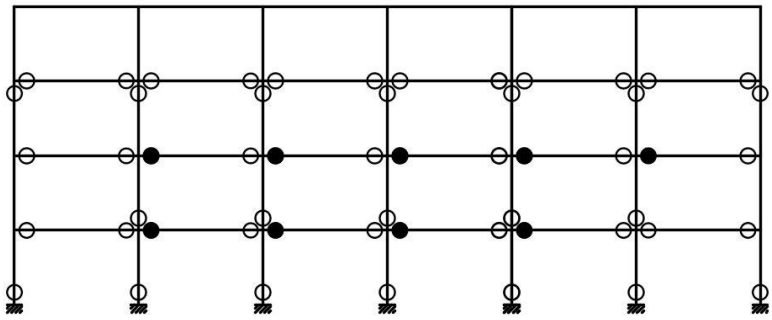

(a) W2-4C6

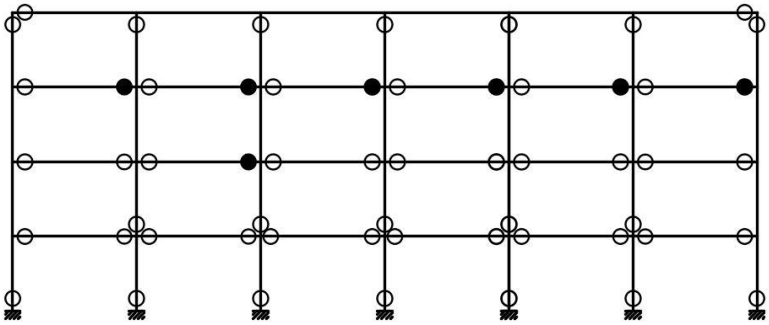

(b) W2-4D6

Figure 5.12: Plastic mechanisms at collapse of regular W2BF with four stories and six bays (○: Section has yielded; ●: Section has reached its capacity)

5.5.4 Regular Frames with Four Stories and Two Bays

The mechanisms at collapse for the regular frames with four stories and two bays, shown in Figure 5.13, consisted of multiple story mechanisms, containing three or four stories. Frames C-4C2 and C-4D2 (Figure 5.13a and b) displayed similar mechanisms. All the beams in the first three stories had either yielded or reached their capacities when structural collapse occurred. On the other hand, the plastic damage was spread on all the floors of the WBF, except for frame W2-4C2 (Figure 5.13e), in which none of the members of the last floor either yielded or reached their capacities.

Frames W1-4C2, W1-4D2 and W2-4D2 (Figure 5.13c, d and f respectively) behaved very similarly. All the beams of the first three floors either yielded or reached their capacities, and the bottom sections of the columns on the first floor and the top sections of the columns in the last floor also yielded. Typically, more beams reached their ultimate capacities in the WBF than the CBF. The effect of the beam type was more pronounced when comparing WBF to CBF. The presence of wide beams in the regular four story-six two bay frames resulted in plastic damage spread throughout all the

floors and more beams reaching their capacity at structural collapse, while the presence of conventional beams resulted in slightly more limited damage. Soil class had a negligible effect on the mechanisms of 4C2 and 4D2 frames, because the overstrength factors of the six story frames were smaller and less affected by the soil class.

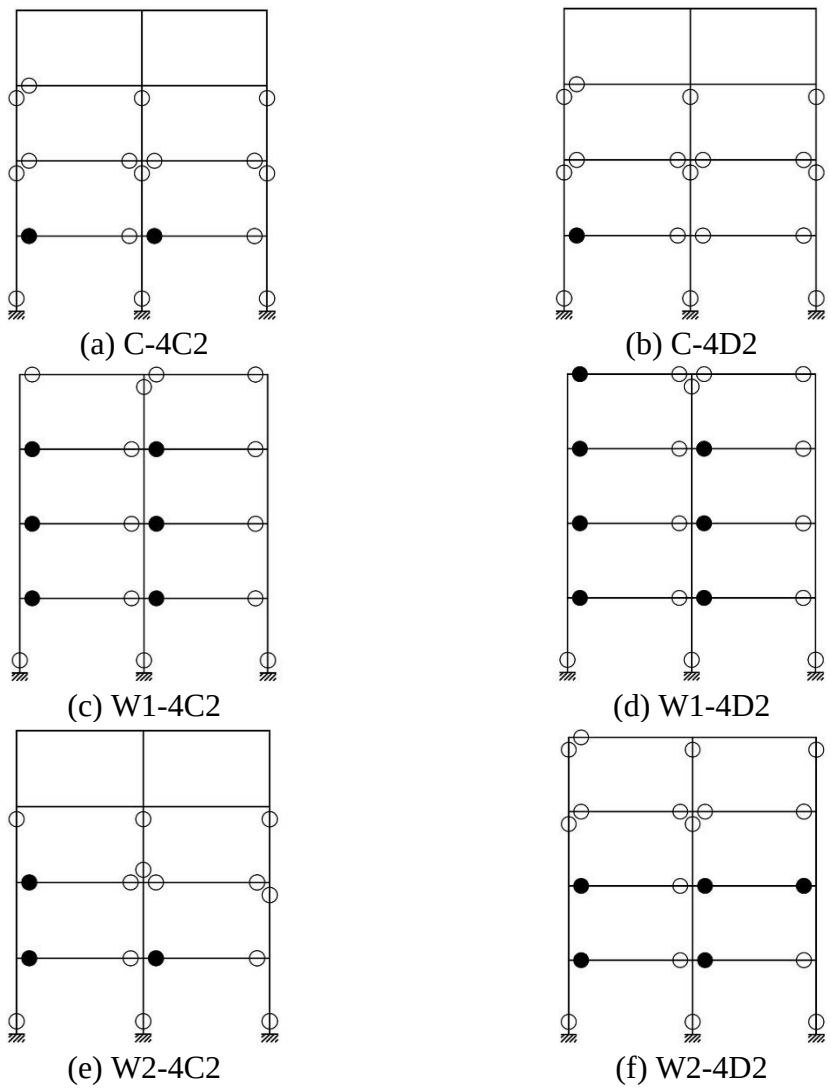

Figure 5.13: Plastic mechanisms at collapse of regular frames with four stories and two bays (○: Section has yielded; ●: Section has reached its capacity)

5.5.5 Irregular Frames

The mechanisms at collapse of the irregular frames shown in Figure 5.14, consisted of multiple story mechanisms, containing three or four stories. The irregular CBF (Figure

5.14a and b) behaved very similarly, all the beams of the first two floors and two beam sections on the third floor yielded. Three-story mechanisms were observed in frames C-IC and C-ID, and two beam sections on the first floor reached their capacities. The soil class did not affect the behavior of the irregular CBF.

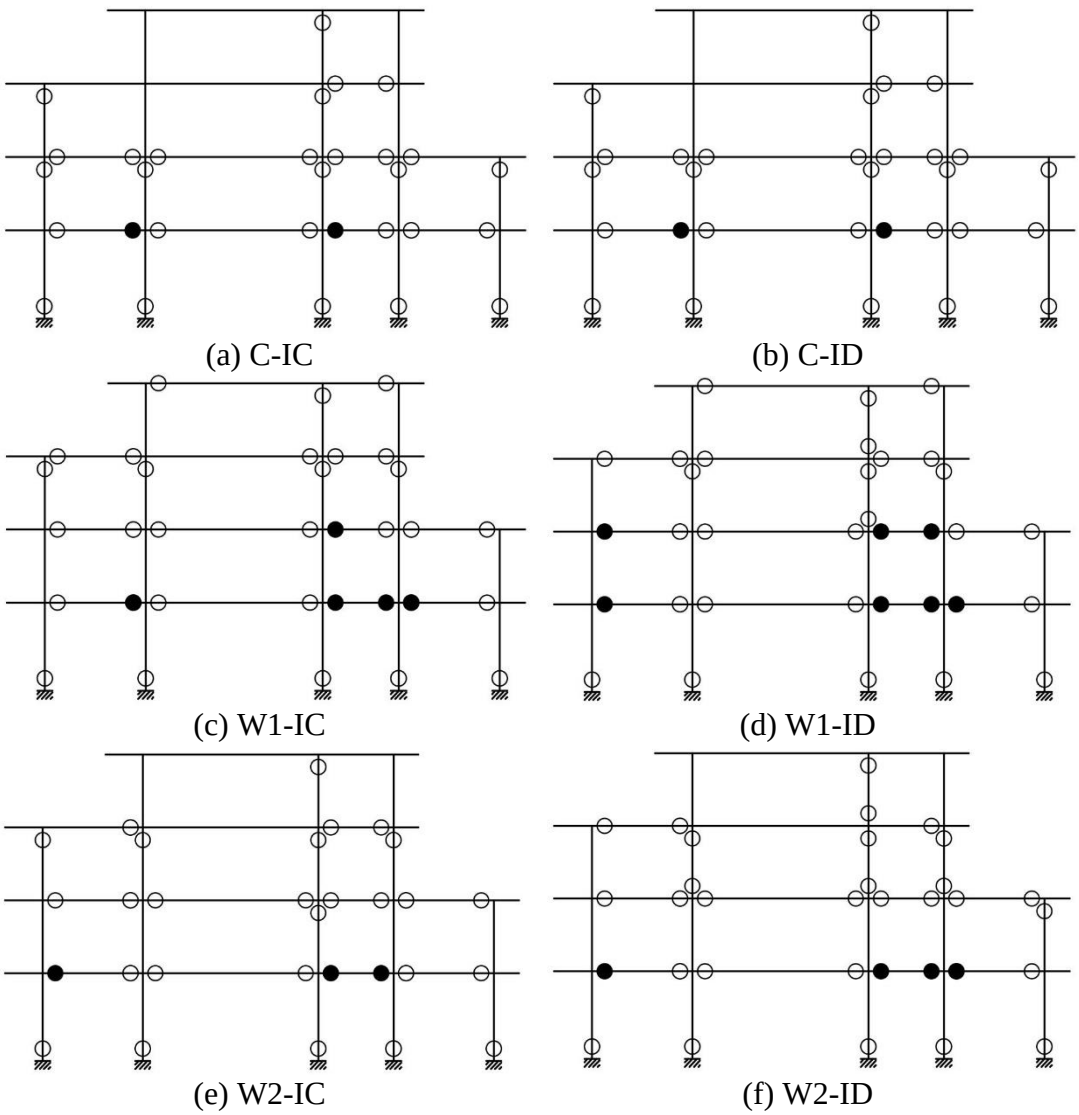

Figure 5.14: Plastic mechanisms at collapse of irregular frames (○: Section has yielded; ●: Section has reached its capacity)

The WBF of type W1, shown in Figure 5.14c and d, also behaved very similarly regardless of the soil type used for the design of the frames. All the beams of the frames W1-IC and W1-ID either yielded or reached their capacities when structural collapse

occurred. The base sections of the columns on the first floor and the top sections of the columns on the third floor yielded, while some beams in the first two floors had reached their ultimate capacities. The damage was slightly more extensive in frame W1-ID than in frame W1-IC, since two more beam sections of frame W1-ID had reached their capacities when structural collapse was observed.

Frames W2-IC and W2-ID (Figure 5.14e and f) also behaved similarly. The W2 type frames displayed three story mechanisms, similarly to the W1 frames. The main difference was that only some beams on the first floor of the W2 frames reached their capacities, as opposed to beam sections in the first two floors of the W1 frames having reached their capacities.

The soil class had negligible effects on the behavior and collapse mechanisms of the irregular frames. On the other hand, the type of the beam used had a more pronounced effect. Frames with wide beams displayed more extended mechanisms than CBF. Additionally, the collapse mechanisms of W1 frames were more spread among the floors than the collapse mechanisms of W2 frames. This was mostly due to the smaller sections of the wide beams that were used in W1 frames, and therefore they either yielded or reached their capacities more readily than the larger wide beams used in the W2 frames.

5.6 Frames with Infill Walls

The frame models discussed in Sections 5.3.1 to 5.3.3 include infill walls as loads only. This is supported by the design approach suggested in TBEC, in which the RC frames and the infill walls are separated via special joints, and there is no interaction between frame and wall. In this section the effect that the explicit modeling of infill walls can produce is investigated. Furthermore, the following are considered:

- Designing frames as separated from infill walls results in more flexible structures and therefore lower seismic forces.
- Lower design lateral forces produce smaller sections and lower reinforcement ratios; thus, the overall design of the structures is more economic. Both designers and contractors aim to keep the costs as low as permissible by the constraints of the projects.

- However, using the necessary joints to separate frames from walls require more materials, and specialized workmanship, which in turn increases the cost of the construction.
- In Turkey, often times deficiencies of the building stock have been associated with either faulty and non-code-compliant design, or with faulty applications which differ from the design projects and are not code-compliant as well.

Therefore, when explicitly modeling the infill walls, the following assumption was made:

> "The frames with explicitly modeled infill walls present faulty construction practices, in which frames that have been designed as separated from the infill walls, have been constructed without the proper details and are in fact not separated from the infill walls."

Frames C-4D4, W1-4D4, W2-4D4, C-ID, W1-ID and W2-ID were used for this purpose. Three scenarios were considered:

- In the first scenario, the infill walls were modeled as loads on the beams only. These frames are the same as the frames that were discussed in Sections 5.3.2 and 5.3.3. The name notations for these frames are kept unchanged.
- In the second scenario, compressive struts were used to model infill walls in all the floors and all the bays. These frames were considered fully infilled, and the letter *F* was added in the beginning of the name to denote it, for example FC-4D4.
- In the third scenario, infill walls were omitted from the first floor, to simulate the often observed soft and weak story which occurs in residential buildings that have commercial spaces on the first floor. These frames were considered partially infilled, and the letter *P* was added in the beginning of the name to denote it, for example PW1-ID.

5.6.1 Pushover and Modal Analyses

Nonlinear static analyses were performed as it was described in Section 5.1. The distribution of the lateral push load was based on the first vibration mode. The dynamic

properties of the frames for the first vibration mode are listed in Table 5.4. Judging by the fundamental periods, WBF are generally characterized by greater periods than the CBF. However, the presence of infill walls in all floors reduces the period to almost half the period of bare frames, independent of the type of beam, wide or conventional. Partially infilled frames appear more robust than bare frames, but less rigid than fully infilled frames. In general, it was noticed that the vibration of the frames is governed by the first mode, as indicated by the modal mass participation factor, which is greater than 0.7 for all the frames.

Table 5.4: Dynamic properties of frame models with infill walls

Frame	**T(s)**	α_1	***W* (kN)**	**Frame**	**T(s)**	α_1	***W* (kN)**
C-4D4	0.975	0.881	3418	**C-ID**	0.773	0.883	3025
FC-4D4	0.502	0.891	3418	**FC-ID**	0.674	0.886	3025
PC-4D4	0.723	0.975	3418	**PC-ID**	0.720	0.909	3025
W1-4D4	1.153	0.793	3877	**W1-ID**	1.238	0.852	3360
FW1-4D4	0.523	0.857	3877	**FW1-ID**	0.559	0.881	3360
PW1-4D4	0.644	0.932	3877	**PW1-ID**	0.853	0.976	3360
W2-4D4	1.190	0.828	3945	**W2-ID**	1.202	0.871	3472
FW2-4D4	0.549	0.874	3945	**FW2-ID**	0.567	0.884	3472
PW2-4D4	0.749	0.961	3945	**PW2-ID**	0.880	0.98	3472

5.6.2 Capacity Curves

The capacity curves were obtained from pushover analyses and plotted as base shear coefficient (V/W) versus global drift ratio (Δ/H). From capacity curves in Figure 5.15, it is observed that the infill walls improve the initial stiffness and lateral load capacity in all the cases, as was reported by Al-Chaar et al. [125] and Lee and Woo [126]. However, after the complete failure of some of the struts, a considerable reduction in strength was observed, which was observed by Dolsek and Fajfar [132]. It was followed by a second peak of strength, due to the strain-hardening that takes place in

beams and columns. The capacity curves of the infilled or partially infilled frames fit the description of the idealized capacity curves for infilled RC frames described by Dolsek and Fajfar [137]. All the infilled frames with the exception of PC-4D4 display two peaks. The first peak is greater than the second peak, and accounts for the contribution of the infill walls. The sudden reduction in strength occurs at low drift ratios, around 1% for the CBF and W1BF, and around 1.5% for the W2BF.

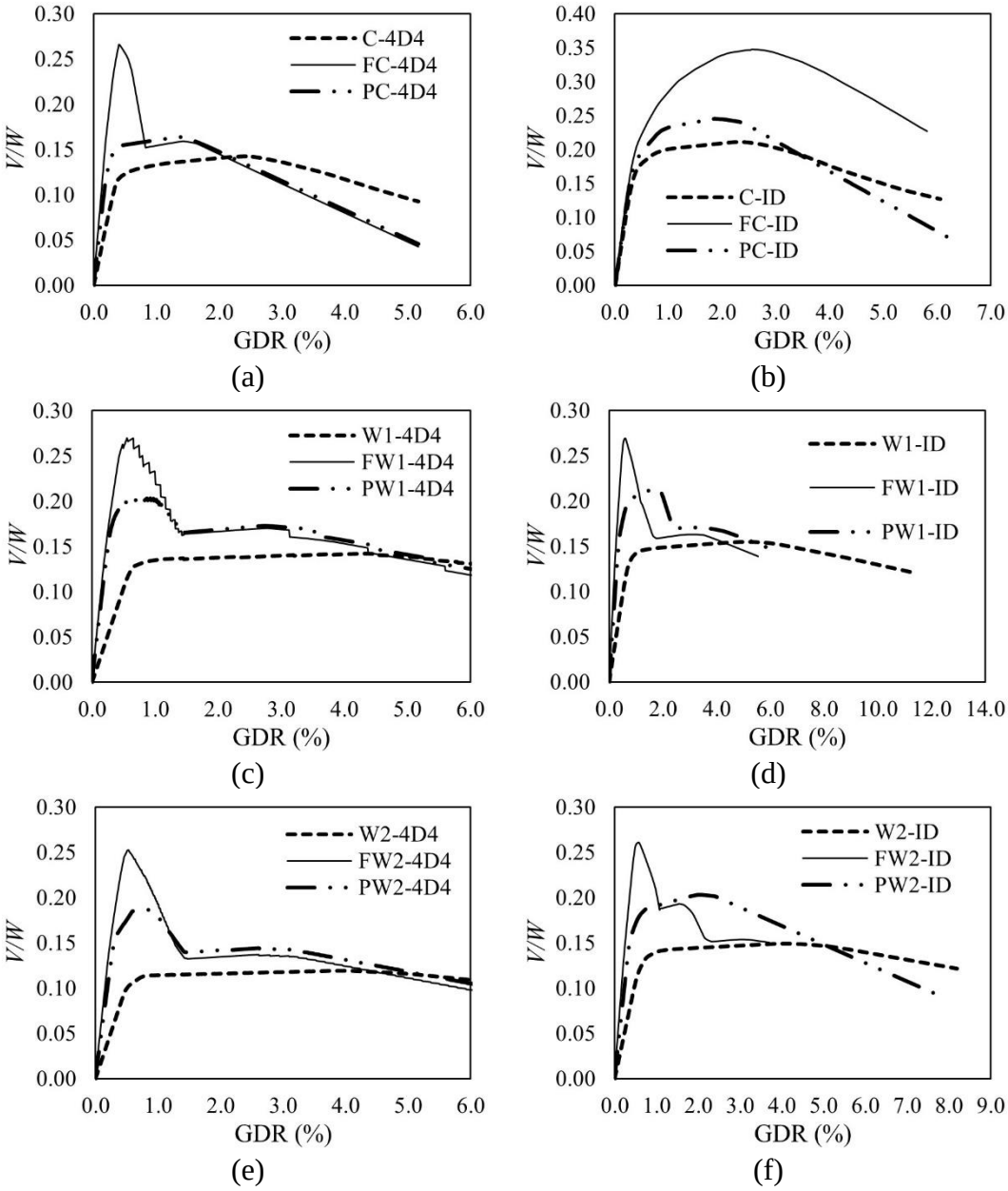

Figure 5.15: Pushover curves of frames with infill walls; (a) C-4D4; (b) C-ID; (c) W1-4D4; (d) W1-ID; (e) W2-4D4; (f) W2-ID

The second peaks of the fully infilled frames and partially infilled frames coincide well, both in terms of strength and deformation. The infilled frames exhibit greater strengths at their second peak, compared to the lateral load capacity of the bare frames. The bare frames are more flexible and reach their capacities at higher drift ratios.

When the frames reach the second peak in base shear coefficient, such mechanisms have formed that the structures have lost their stabilities. The conventional frames reach the maximum base shear at 2.39% drift ratio for frame C-4D4, 1.43% drift ratio for frame FC-4D4 and 1.36% drift ratio for frame PC-4D4. The W1 frames reach the maximum base shear at 4.30% drift ratio for frame W1-4D4, 2.78% drift ratio for frame FW1-4D4 and 2.75% drift ratio for frame PW1-4D4. The W2 frames reach the maximum base shear at 3.98% drift ratio for frame W2-4D4, 2.61% drift ratio for frame FW2-4D4 and PW2-4D4.

5.6.3 Plastic Mechanisms

The plastic mechanisms of the bare frames were already presented in Figure 5.8 and Figure 5.14 and discussed in Sections 5.5.1 and 5.5.5 respectively, and therefore are not repeated in this section.

The mechanisms of the fully infilled frames are shown in Figure 5.16. Not only is the damage more distributed in the WBF, but it is also often offset from the first floor. In the CBF on the other hand, the damage is concentrated in the infill walls and bottom sections of the first floor. The fully infilled frames display somewhat ductile behavior, where infill collapses are generally followed by mechanisms similar to the mechanisms of the bare frames.

The partially infilled frames do not display desirable mechanisms. The partially infilled CBF, shown in Figure 5.17a and b, display a soft story behavior, the only members that reach their capacity are the columns of the first floor. PW1-4D4and PW2-4D4 frames (Figure 5.17c and e) experience more extensive damages at peak base shear values. During the first peak, the infill walls of the second story reach their capacities, followed by the capacity loss of some beam sections and some columns on the first floor during the second peak. The presence of infill walls in the irregular WBF

makes very little difference, as is the case of frames PW1-ID and PW2-ID (Figure 5.17d and f), which display mechanisms very similar to frame PC-ID (Figure 5.17a).

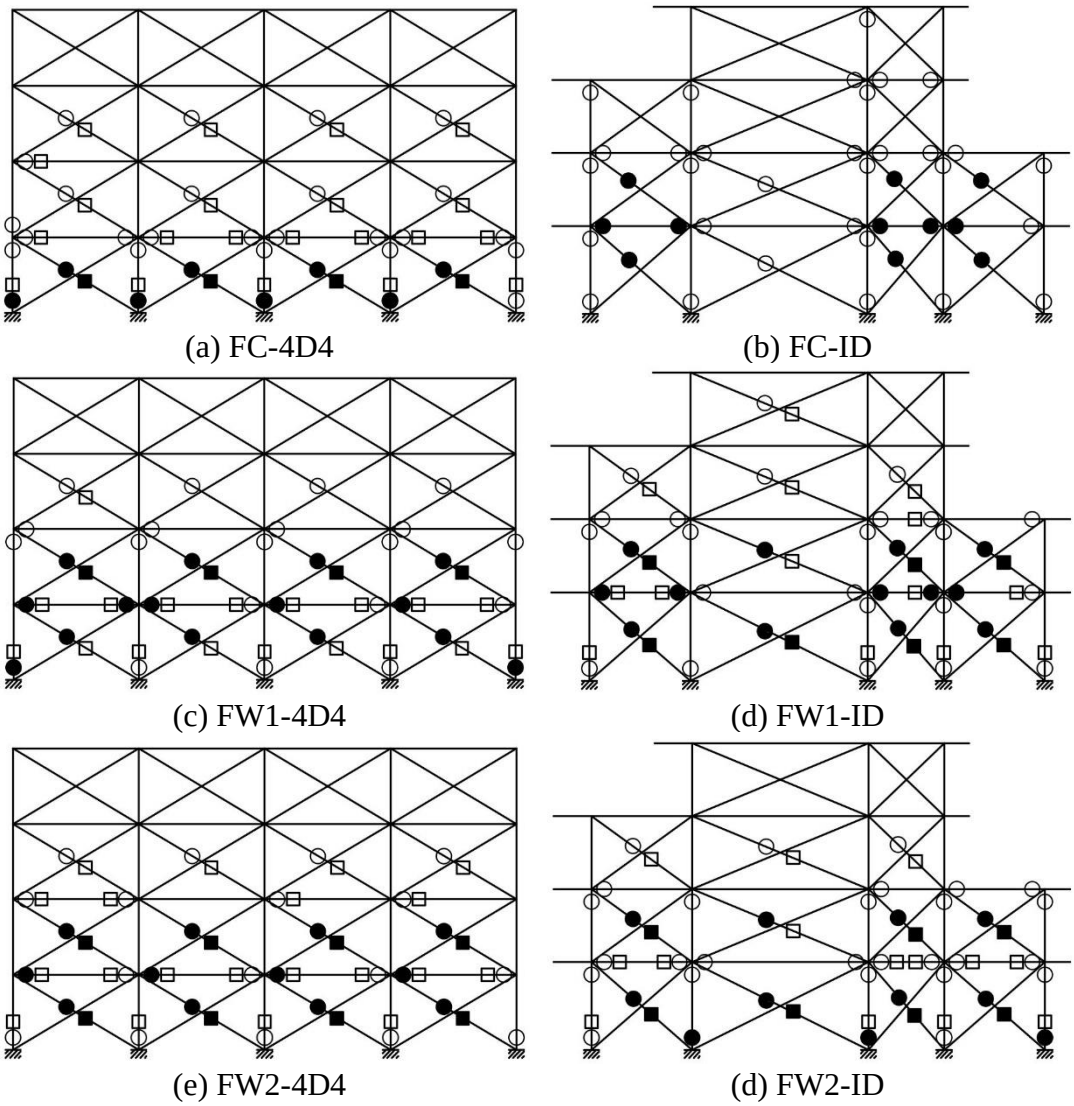

(a) FC-4D4 (b) FC-ID

(c) FW1-4D4 (d) FW1-ID

(e) FW2-4D4 (d) FW2-ID

Figure 5.16: Failure mechanisms of the fully infilled frames

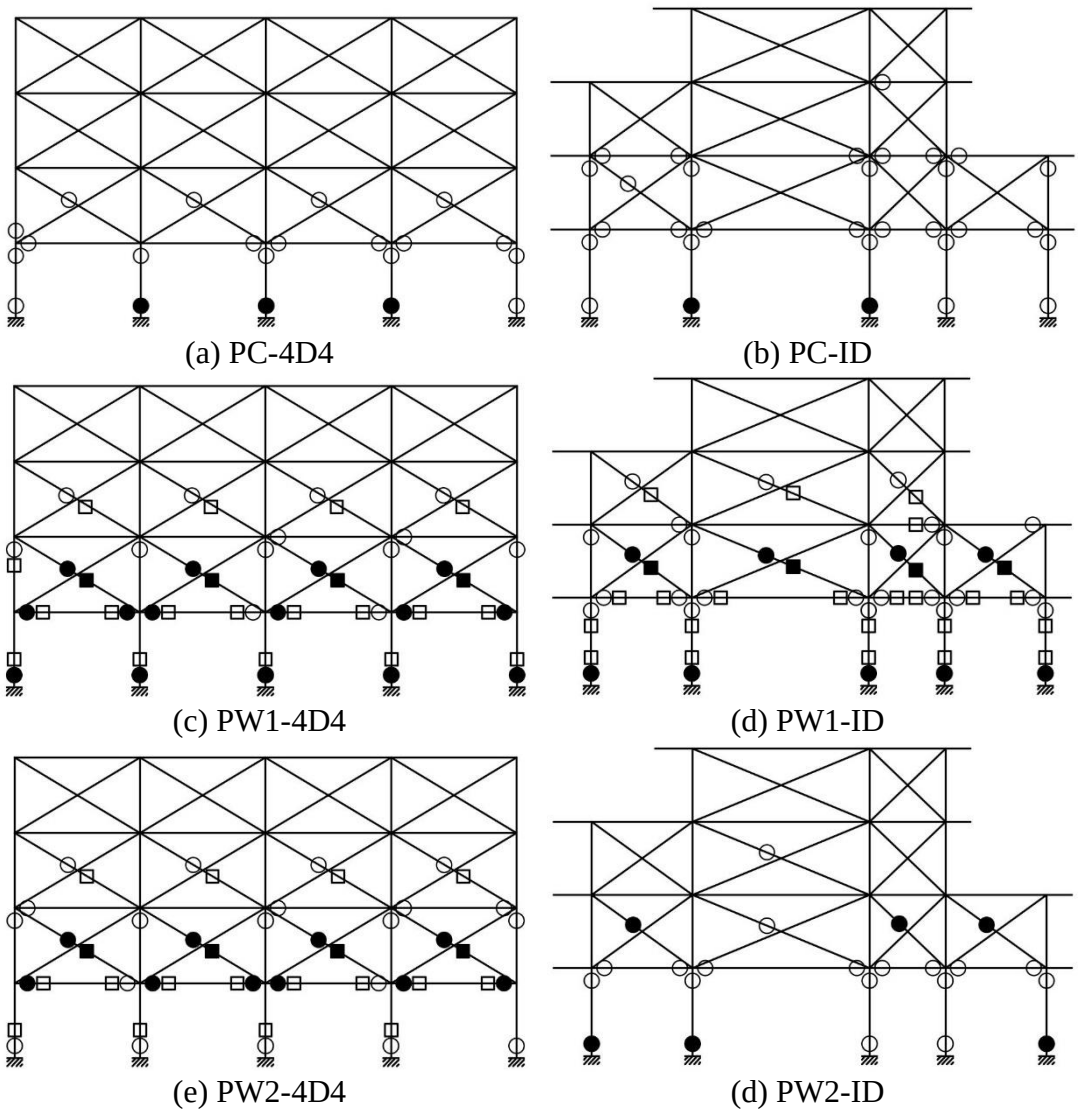

Figure 5.17: Failure mechanisms of the partially infilled frames

So, to summarize, the behavior of the frames where the infills were not explicitly modeled was very ductile and was governed by the flexural failure of the beams. The mechanisms at the maximum base shear were ductile and comprised several floors. This is a code-compliant behavior. The failure mechanisms of the WBF with infills contained more extended damage, with complete plastic hinges forming in the struts, beams, and columns. The fully infilled CBF displayed a clear soft story mechanism, in which only the infills of the first floor collapse, prior to the failure of the columns of the first floor. The collapse mechanism of partially infilled CBF was a pure soft story mechanism, in which the only sections to reach the capacity were three of the first floor columns. The fully infilled and partially infilled WBF displayed more

favorable mechanisms than their CBF counterparts. The inclusion of the infill walls in the nonlinear models was mostly beneficial in the case of the fully infilled regular and irregular WBF.

5.6.4 Energy Dissipation

The energy dissipation of the frames up until the maximum base shear coefficient was calculated. For the infilled frames, which displayed two peaks, the energy dissipation was calculated up until the second peak, which accounts for the formation of the plastic mechanisms in beams and columns more extensively.

The presence of infill walls reduces the energy dissipation capacity of the frames, as reported by Jalaeefar and Zargar [130] as well. Furthermore, the absence of infills on the first floor presented an even less favorable situation. However, it was observed (Figure 5.18) that WBF have higher energy dissipation capacities than CBF. This statement is valid for bare, infilled and partially infilled WBF.

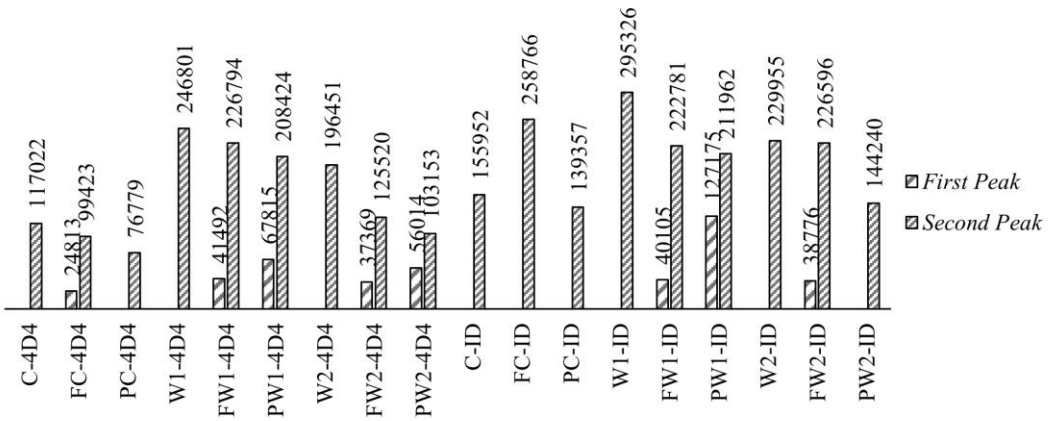

Figure 5.18: Energy dissipation (Nm) for the first and second peaks of capacity for all the frames, when applicable.

5.7 Summary: Assessing the Effect of Various Parameters on Capacity and Behavior of WBF and CBF

In this chapter, the capacity of the conventional and wide beam frames was assessed using pushover analyses. A considerable amount of information was obtained from these analyses such as capacity curves, performance levels, initial stiffness, ductility, energy dissipation and plastic mechanisms, and they were discussed separately throughout this chapter. In this summary, the effect that parameters such as number of stories, number of bays, soil class, elevation irregularity and inclusion of infill walls in the model is assessed. It was observed that most of these parameters either did not affect the results of the pushover analyses, or the effect was as expected. This allowed to create a larger and varied pool of frame models, in which the effect of the desired parameter, that is the type of the beam, could be observed with respect to pushover analyses.

5.7.1 Number of Stories

To assess the effect of the number of stories, 4C4, 6C4, 4D4 and 6D4 frames were used. They are similar, since they have the same number of bays, but the number of stories changes from four to six. The four story frames attain higher base shear coefficients than the six story frames (Figure 5.3a and b, and Figure 5.4a and b). The frames with four stories are stiffer than the frames with six stories, but the latter dissipate larger amounts of energy. The differences are minor and can be attributed to design. The size of the columns of the four story frames is mostly governed by lateral deformation criteria, since the structural members of the four story frames comply more easily with the internal force demands. The size of the columns of the six story frames is governed by both the global stiffness demand and internal force demand imposed on the structural members. The plastic mechanisms are also similar. The main difference was that the multistory mechanisms of the six story frames contained two-to-five stories, while the multistory mechanisms of the four story frames contained one-to-three stories. It is important to note that independent of the number of floors, similar trends were observed when comparing the CBF and the WBF.

5.7.2 Number of Bays

To assess the effect of the number of bays, frames with two, four and six bays that have the same number of stories (four) were analyzed and presented in this chapter, namely 4C2, 4D2, 4C4, 4D4, 4C6 and 4D6. The number of bays slightly affected the base shear coefficient but affected the initial stiffness and energy dissipation considerably. The base shear coefficient was less affected by the number of bays, since it is a unitless measure normalized by the weight of the structures. On the other hand, the six bay frames had the higher initial stiffness and energy dissipation, followed by the four story frames and then by the two story frames. This is an expected behavior, since the six story frames had more structural elements to provide higher capacity, stiffness and redundancy which increases the energy dissipation capacity. The two bay frames on the other hand were the frames with the least amount of redundancy and thus displayed lower energy dissipation capacity and initial stiffness. The plastic mechanisms are also similar in terms of damage dispersal and number of stories involved in the multistory mechanisms. It is important to note that independent of the number of floors, similar trends were observed when comparing the CBF and the WBF.

5.7.3 Soil Class

To assess the effect of soil class all the frames were designed once for soil class C and then for soil class D. In overall, the frames designed for soil class D displayed higher base shear coefficients, higher initial stiffness and greater energy dissipation capacities. This occurred due to the higher design base shear imposed on the frames designed for soil class D, due to the shape of the response spectrum of ZD as compared to ZC. Therefore, the obtained results with respect to soil class were expected. It is important to note that independent of the number of floors, similar trends were observed when comparing the CBF and the WBF.

5.7.4 Effect of Irregularity

To assess the effect of irregularity, the IC and ID frames were designed as counterparts of 4C4 and 4D4 frames. They all had four stories and four bays, but while the story

height and bay length of the 4C4 and 4D4 frames was constant, frames IC and ID had a higher ground floor, and bays of different lengths. In terms of base shear coefficient, initial stiffness and energy dissipation, the C-IC and C-ID outperformed C-4C4 and C-4D4 respectively. However, the effect was negligible in the irregular WBF.

5.7.5 Infill wall

The modeling approach used to model infill walls had a great impact on the behavior of the frames that were modeled. As was stated in Section 5.6, infill walls were explicitly included in the nonlinear models on purpose, even though the frames were designed based on the assumption that the walls are separated and do not interact with the frame members.

Explicitly modeling infill walls considerably increased the base shear capacity and initial stiffness of the frame models but decreased the energy dissipation capacity. It also negatively affected the plastic mechanism of the fully or partially infilled frames, in some cases creating soft stories, which were not observed in the bare frames. This observation highlighted the importance of construction practices that are compatible with the design assumptions.

5.7.6 Beam type

The above-mentioned parameters had little-to-no effect on the capacity behavior of the frames that were discussed in this chapter. However, the type of beam affected capacity and behavior of the frames in a consistent manner. Regardless of the number of stories, bays, soil class and regularity, the frames with conventional beams consistently displayed higher base shear coefficients, higher initial stiffness, and lower ductility and lower energy dissipation capacity than the frames with wide beams. So, while CBF were stiffer and stronger than WBF, WBF displayed slightly more ductile behavior. This was evident from the plastic mechanisms, in which WBF experienced more spread damages than CBF. However, CBF still displayed highly ductile behavior and mechanisms.

Among the frames with wide beams, WBF of type W1 displayed more a slightly ductile behavior, and higher energy dissipation capacities than WBF of type W2. W1

type frames had narrower wide beams and thus required greater column sections than W2 frames, which made W1 frames more flexible and ductile. W2 frames displayed slightly higher base shear coefficients. In overall, both types of WBF displayed ductile behavior, which is desired for construction in seismic areas.

Chapter 6

Time-History Analyses

Time-history analyses were used as a first step for the estimation of seismic demand of the frame models. The parameter that was used to represent seismic demand is drift ratio, in the form of global drift ratio (GDR) and interstory drift ratio (IDR). The time-history analyses were performed using real and unscaled ground motion records. The ground motion record used for the time-history analyses were selected based on the procedure laid out in TBEC [63], which requires sets of 11 ground motion records compatible with the elastic spectrum used in the design of structures. 30 such sets were selected for each soil class.

6.1 Selecting Ground Motion Records for Time-History Analyses

Ground motion records vary significantly from one another therefore performing time-history analyses using a single event can only provide insight on the performance of a structure when subjected to a certain earthquake that has already occurred and is unlikely to be exactly replicated in the future. Therefore, it is rather suggested to use sets of ground motion records when performing time-history analyses, rather than a single record. Regarding the suitable number of ground motions that consists of a set, and the criteria how these records are selected, there have been several developments [146]. FEMA P-58 suggests the use of at least seven ground motion records, though 11 or more are expected to provide better estimates of demand [147]. Reyes and Kalkan [148] tested the use of less than seven ground motion records and more than seven ground motion records, and concluded that sets that have at least seven records provide satisfactory results. Palanci et al. [149] reached a similar conclusion by testing

sets of 7, 11 and 15 ground motion records. Huang et al. [150] also employed sets of 11 ground motion records for time-history analyses.

TBEC [63] mandates that time-history analyses should be performed by using sets of ground motion records that are scaled to match the elastic response spectrum used to design the structure that is being analyzed. The number of ground motion records required to form a set are dependent on the dimensionality of the structure being analyzed. One and two-dimensional structures can be analyzed using sets containing 11 ground motion records. TBEC defines a set of 11 ground motion records to be compatible with a response spectrum, if for a period range of $0.2T_p$ and $1.5T_p$, the ordinates of the mean response spectrum of the set are not less than the 0.9 times the ordinates of the elastic spectrum. The ground motion records in the set can be scaled or unscaled to obtain this compatibility. Similarly, FEMA P-58 suggests the use of sets containing 7-11 ground motion records. The selection and scaling of ground motions for scenario-based assessment is similar to the procedure described in TBEC. Two-dimensional frames were used in the time-history analyses in this thesis, therefore the ground motion record set contained 11 records.

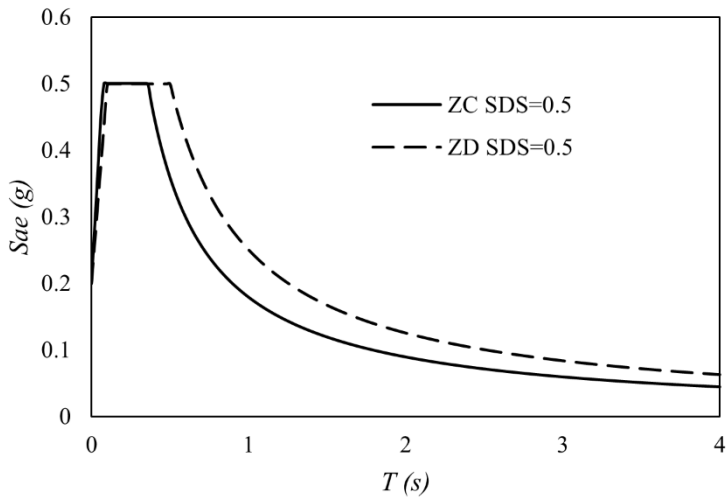

Figure 6.1: Elastic target spectra for soil classes C and D used for the selection of the ground motion records sets

A catalog of ground motion records was created using records obtained from the European Strong Motion Database (ESMD) [151], Resorce [152] and PEER strong motion database [153]. The records included in this catalog had a magnitude M_w>5.0, that were recorded using stations whose distance from the fault is between 10-60 km. Since the frame models were designed for soil classes C and D, records pertaining to these two soil classes were chosen for the selection of ground motion record sets. The problem of selecting ground motion records that are compatible with code design spectra can be defined as an engineering optimization problem and solved as such [154]. In this study, the approach suggested by Kayhan [155] was used to obtained the ground motion sets. 30 sets that are compatible with the code design spectrum were obtained in this manner for each soil class. It is possible to use different scale factors for each record when selecting a set of ground motion records. In this study the scale factor for all the ground motion records is one, so real and unscaled earthquake records were used. The target response spectra used for the design of the frame models and the selection of the ground motion record sets are shown in Figure 6.1.

Using one set of ground motion records compatible with the target spectrum will yield a set of displacement demand data for GDR and IDR, from which the mean GDR and IDR displacement demands for the set can be calculated. However, repeating the analysis using a different set, that is compatible with the same target spectrum will yield slightly different mean GDR and IDR displacement demand data. While both could be correct estimations of displacement demand there is obviously a bias involved when using the results of a single set of ground motion records for this calculation. To solve this problem, in this thesis 30 sets of ground motion records were used to obtain the displacement demand for each of the frames. 30 sets of ground motion records recorded on soils of type C and compatible with the target spectrum of soil class C were selected and used to analyze all the frames designed for soil class C. Similarly, 30 sets of ground motion records recorded on soils of type D and compatible with the target spectrum of soil class D were selected and used to analyze all the frames designed for soil class D.

Appendix B lists the ground motion record for each set that were used in this thesis. The compatibility of the ground motion records of any given set with the

corresponding target spectrum was checked by plotting the acceleration spectra of the individual records, the mean spectra of the set and the target spectrum in a single graph.

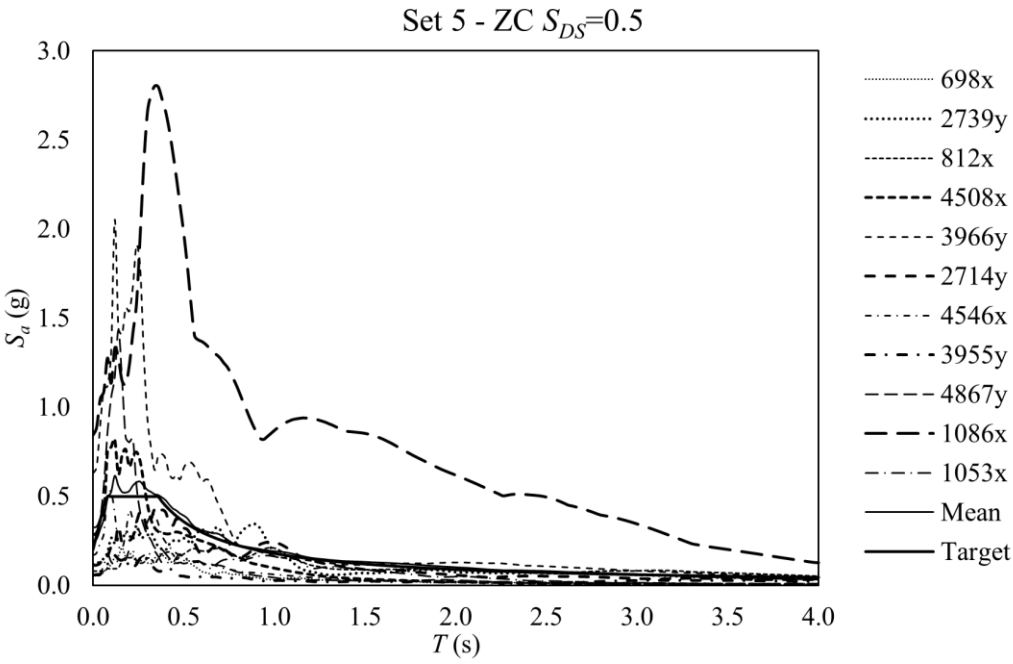

Figure 6.2: Compatibility check for the ground motion records of Set 5, soil class C

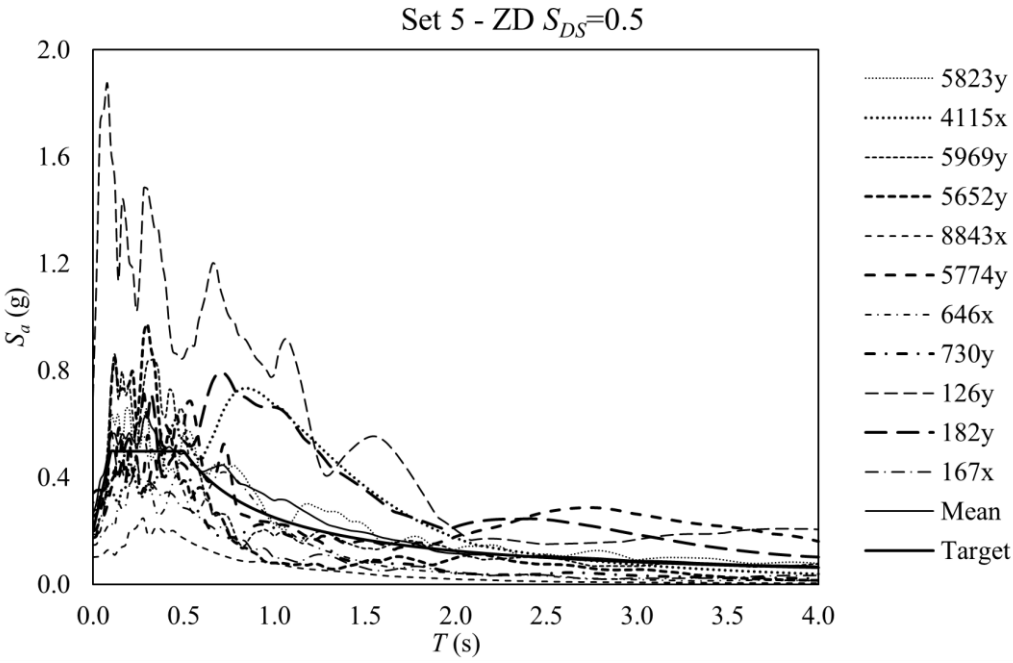

Figure 6.3: Compatibility check for the ground motion records of Set 5, soil class D

Examples of this compatibility check are shown in Figure 6.2 and Figure 6.3 for soil class C and D, respectively. From these figures it can be noticed that the record sets are compatible with the target spectrum for periods of at least 3 s, which sets the fundamental period of the structures T_p=2 s. Referring to Table 5.1, the fundamental period of all the analyzed frame models is less than 2 s, and therefore the selected sets of ground motion records are suitable to be used to perform time-history analyses on all the frames.

6.2 Time-History Analyses

Time-history analyses were performed on the 2D frame models used previously for the pushover analyses. The analyses were performed using direct integration as a solution method, and large displacements were taken into consideration. Hilber-Hughes-Taylor numerical integration was employed. Rayleigh damping, where the first two vibration modes had damping ratio equal to 0.05, was used to model viscous damping. This decision was justified because the behavior of the frames was largely governed by the first two modes of vibration. Table 5.1 lists the periods and the modal mass participation factors for the first two vibration modes for each of the frames. The total of the modal mass participation factors for the first two vibration modes ($\alpha_1+\alpha_2$) is about 0.9 or higher in all cases. Therefore, the sum of the contribution of all the other vibration modes is less than 10%, in some cases as low as 3-4%. In this situation calculating the damping from the first two modes only and neglecting the contribution of the higher modes will not result in significant error and considerable overdamping of the higher modes.

6.2.1 Record-Base Results

The results of the time-history were estimated in terms of interstory and global drift ratios. For each ground motion record, the maximum global displacement Δ_{max} and the maximum interstory displacement for the i-th story $\delta_{max,i}$ were obtained and were converted into maximum drift ratios by dividing with the total frame height and individual story height respectively. These maximum drift ratios varied considerably from record to record within the same set of analysis for any given frame.

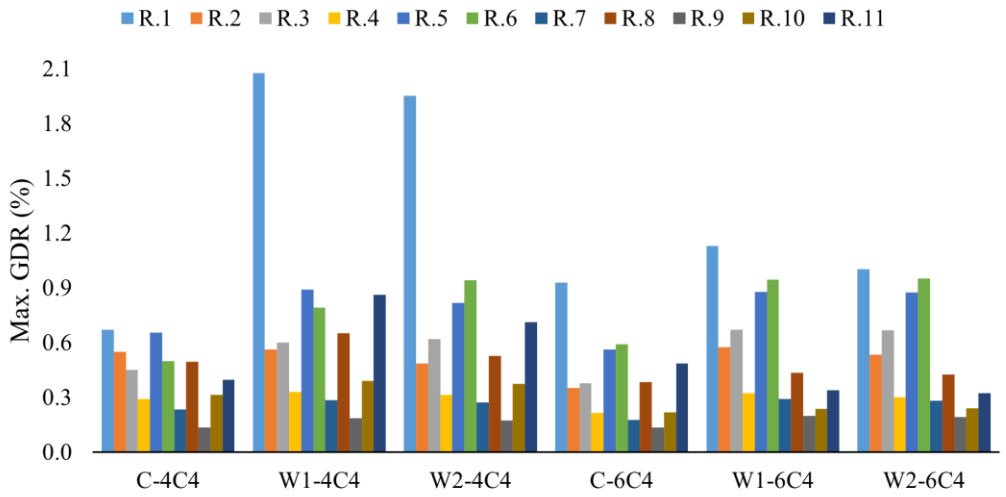

Figure 6.4: Maximum GDR for each ground motion record of set 10 and soil class C for the 4C4 and 6C4 frames

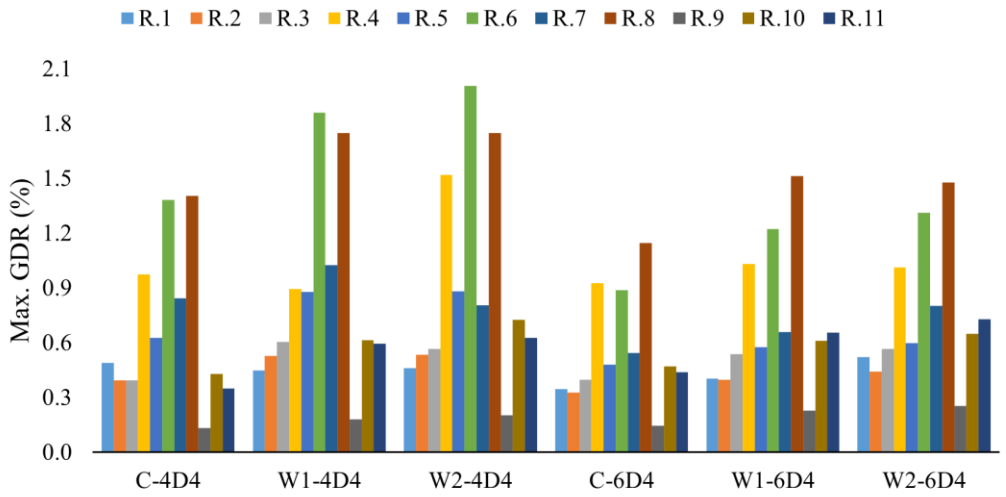

Figure 6.5: Maximum GDR for each ground motion record of set 15 and soil class D for the 4D4 and 6D4 frames

As an example, Figure 6.4 and Figure 6.5 show the maximum GDR that was computed for the regular four bay, four and six story frames from the records of Set 10 of soil class C and Set 15 of soil class D. The maximum GDR varies considerably from record to record within the same set for the same frame model. For instance, the maximum GDR obtained for frame W1-4C4 ranged from 0.188% for record R.9 to 2.075% for record R.1. Similarly, the maximum GDR obtained for frame W2-4D4 ranged from 0.203% for record R.9 to 2.006% for record R.6.

6.2.2 Set-Based Results

TBEC suggests using the mean deformation of a set as a measure of demand. Therefore, for each frame and *i-th* set of analysis, the mean of the maximum GDR, denoted as $m_{GDR,i}$, and the mean of the maximum IDR for the *k-th* story, denoted as $m_{IDRk,i}$, were calculated using Equations (6.1) and (6.2) respectively. For sake of simplicity, from here forward, m_{IDRk} were denoted as MIDR# standing for mean interstory drift ratio, and the symbol # is a placeholder for the number of the floor. So, MIDR1 is the mean interstory drift ratio for the first floor, MIDR2 is the mean interstory drift ratio for the second floor, and so on. In these equations, *i* denotes the number of the set for which the mean drift ratio is being calculated, *j* denotes the number of the record within the *i-th* set, *n* is the number of records within a set which is 11 for all the sets considered in this study, and *k* denotes the number of the story for which the mean IDR is being calculated. The variance was measured by the Coefficient of Variance (CoV), which is calculated as the ratio of the standard deviation σ to the mean drift ratio *m* (Equation (6.3)). The standard deviation was computed as shown in Equations (6.4) and (6.5) for GDR and IDR, respectively.

$$m_{GDR,i} = \frac{\sum_{j=1}^{n} \left(\Delta_{\max} / H \right)_j}{n} \tag{6.1}$$

$$m_{IDRk,i} = \frac{\sum_{j=1}^{n} \left(\delta_{\max,k} / h_k \right)_j}{n} \tag{6.2}$$

$$CoV = \frac{\sigma}{m} \tag{6.3}$$

$$\sigma_{GDR,i} = \sqrt{\frac{\sum_{j=1}^{n} \left(\left(\Delta_{\max} / H \right)_j - m_{GDR,i} \right)^2}{n-1}} \tag{6.4}$$

$$\sigma_{IDRk,i} = \sqrt{\frac{\sum_{j=1}^{n} \left(\left(\delta_{\max,k} / h_k \right)_j - m_{IDRk,i} \right)^2}{n-1}} \tag{6.5}$$

Figure 6.6 shows the mean GDR (m_{GDR}) for frames 4C4 plotted for all 30 sets of time-history analyses. The variation of the m_{GDR} from set to set is obvious in this figure. However, peaks of m_{GDR} generally coincide, since the analyses were performed using

the same record set for all three frames. This agreement is more evident among W1-4C4 and W2-4C4. The conventional frame C-4C4 generally experience lower values of m_{GDR}, while the values of m_{GDR} of the two WBF were considerably close.

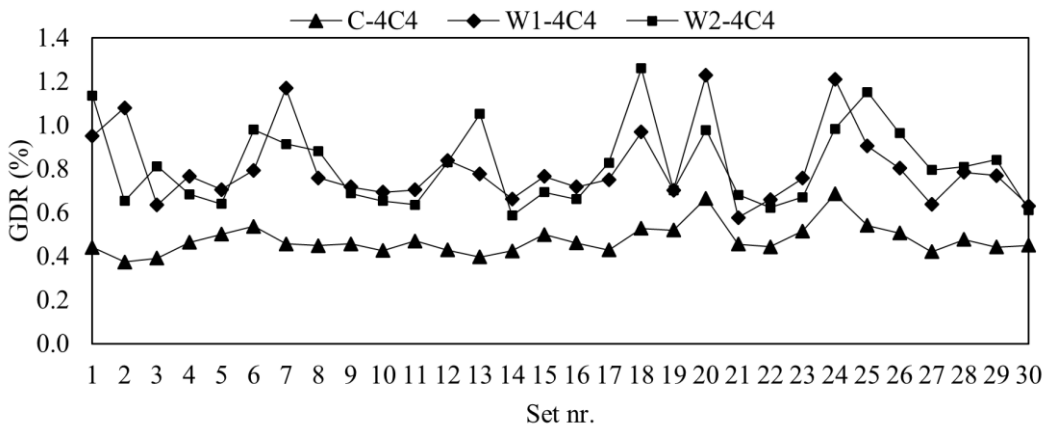

Figure 6.6: Set-to-set variation of m_{GDR} for frames 4C4

The in-set variance of the drift ratios was exemplified in Figure 6.4 and Figure 6.5. Figure 6.7 shows the in-set CoV of the GDR for frames 4C4. The values of CoV for any given set are similar among frames C-4C4, W1-4C4 and W2-4C4. Therefore, the source of variance within the sets is the randomness of the ground motion records that compose the set, rather than the properties of the frames that were being analyzed.

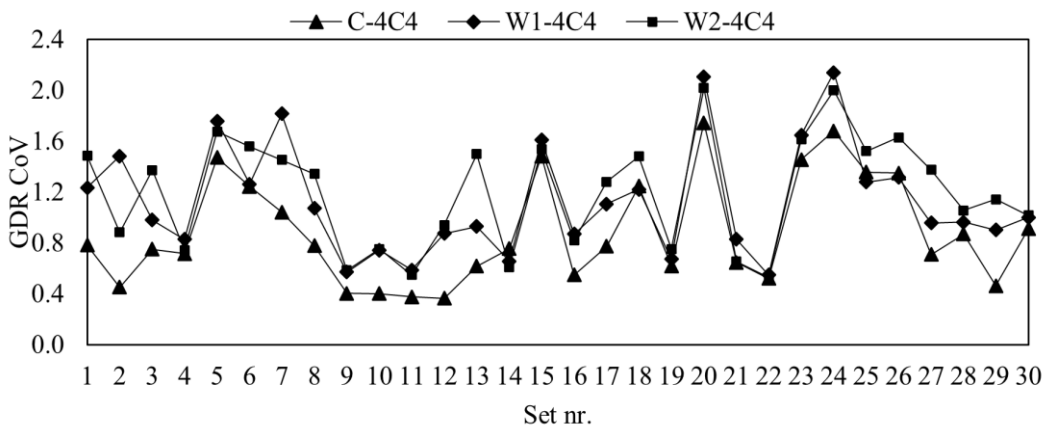

Figure 6.7: Set-to-set CoV of m_{GDR} for frames 4C4

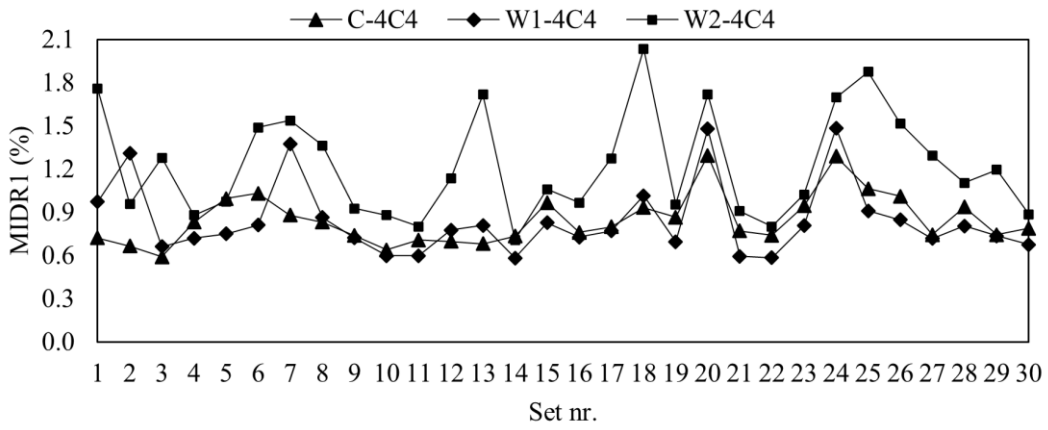

(a) m_{IDR1}

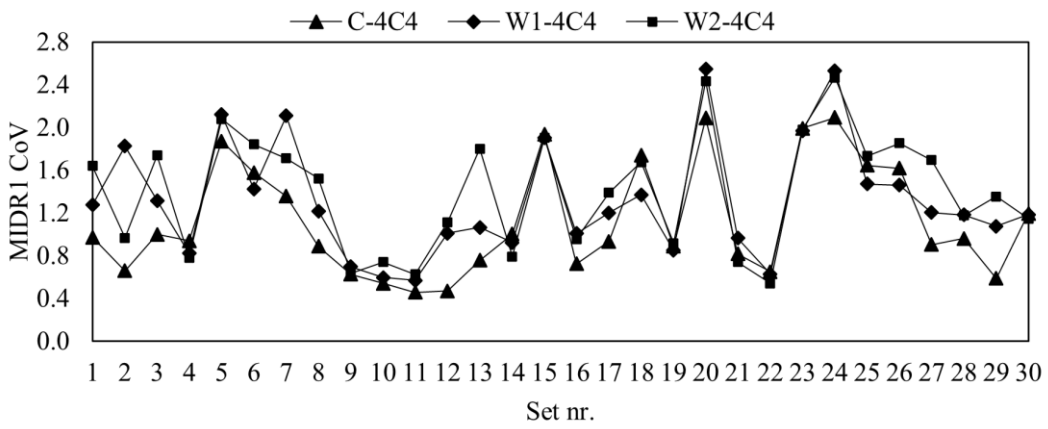

(b) CoV of m_{IDR1}

Figure 6.8: Set-to-set results for MIDR1 for 4C4 frames

The IDR were also investigated in a similar manner. Figure 6.8 shows the plots of MIDR1 and CoV of MIDR1 for the 4C4 frames. The values of MIDR1 varied considerably from set to set (Figure 6.8a), however there was less difference between the MIDR1 of the three frames. Generally, frame W2-4C4 displayed higher peak values than the other two frames, while the values of MIDR1 for frames C-4C4 and W1-4C4 were more similar. The values of CoV of MIDR1 (Figure 6.8b) were very similar for all three 4C4 frames. Thus again, it can be stated that the source of variance within the sets is the randomness of the ground motion records that compose the set, rather than the properties of the frames that were being analyzed.

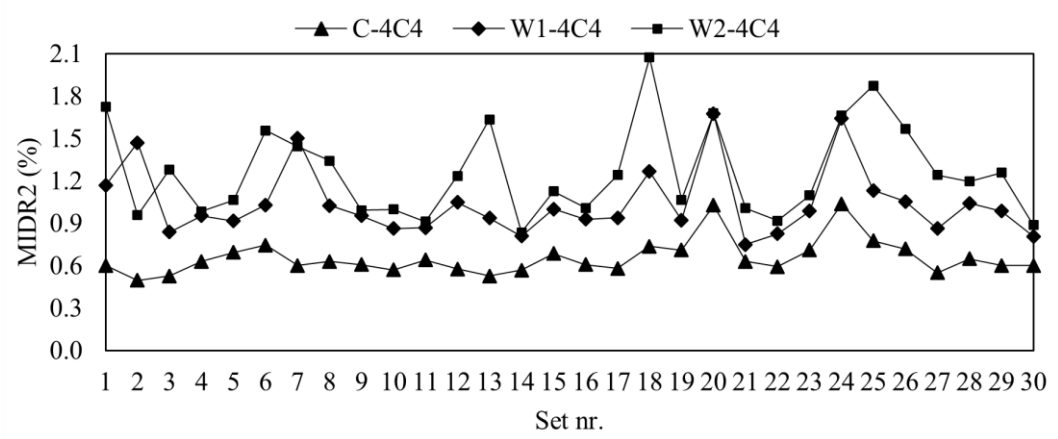

(a) m_{IDR2}

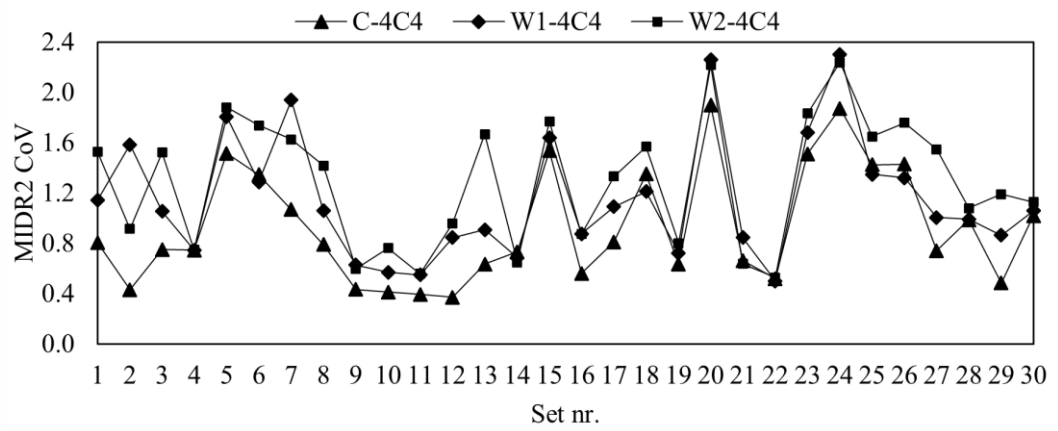

(b) CoV of m_{IDR2}

Figure 6.9: Set-to-set results for MIDR2 for 4C4 frames

Similar observations regarding the MIDR and CoV were made for the other three floors as well. The variances, shown in Figure 6.9b, Figure 6.10b, and Figure 6.11b display the same trends the variance of the GDR and MIDR1, shown in Figure 6.7 and Figure 6.8b respectively. MIDR2 values (Figure 6.9a) follow the following trend: C-4C4 experiences the smallest values of MIDR2, followed by W1-4C4, while frame W2-4C4 generally experiences the highest values of MIDR2.

The conventional frame experiences the lowest values of MIDR3 as well, as shown in Figure 6.10a. However, frame W1-4C4 displays higher values of MIDR3 than frame W2-4C4. A similar situation is observed in Figure 6.11a for MIDR4 as well.

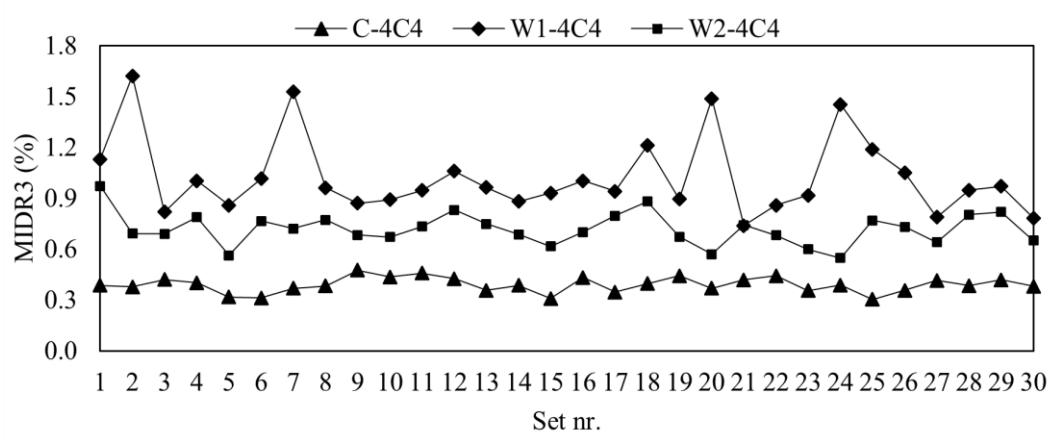

(a) m_{IDR3}

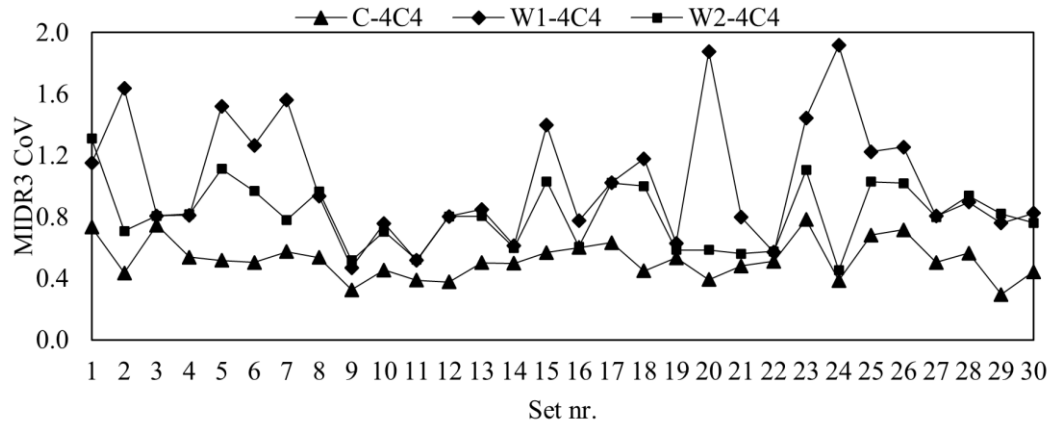

(b) CoV of m_{IDR3}

Figure 6.10: Set-to-set results for MIDR3 for 4C4 frames

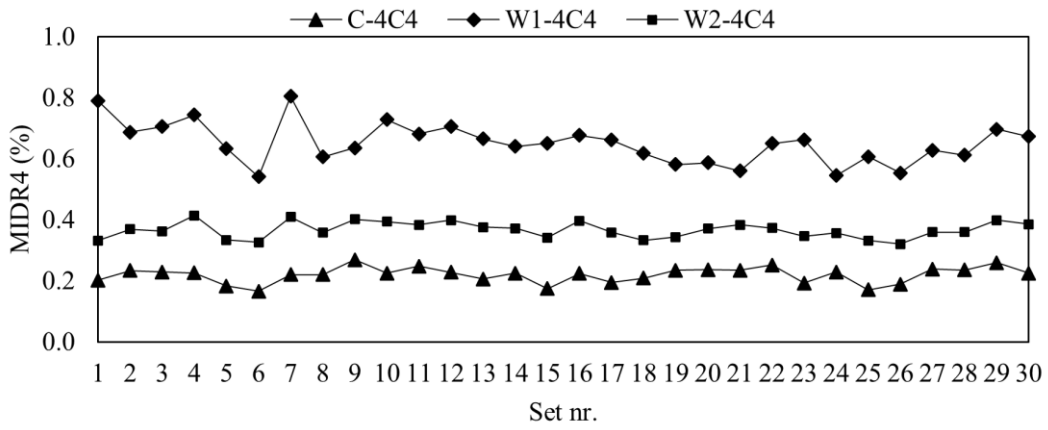

(a) m_{IDR4}

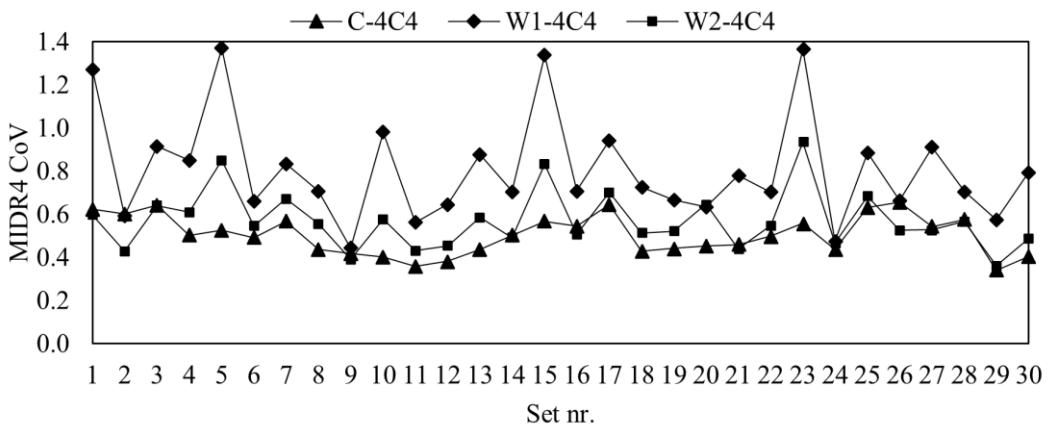

(b) CoV of m_{IDR4}

Figure 6.11: Set-to-set results for MIDR4 for 4C4 frames

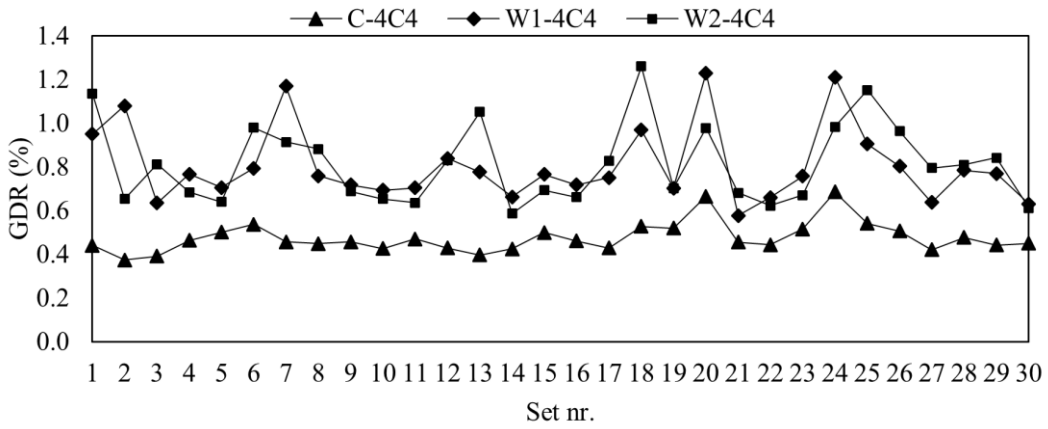

Figure 6.12: Set-to-set variation of m_{GDR} for frames 4D4

The mean GDR and IDR for all the floors were computed and plotted for all the frames and all the sets of analyses, and similar trends were observed. Therefore, in this section only the mean GDR plots are presented, while the rest of the graphs are given in Appendix C. The plots of m_{GDR} for frames 4D4, 6C4, 6D4, 4C2, 4D2, 4C6, 4D6, IC and ID are shown in Figure 6.12, Figure 6.13a, Figure 6.13b, Figure 6.14a, Figure 6.14b, Figure 6.15a, Figure 6.15b, Figure 6.16a, and Figure 6.16b respectively. Among all the frames, the CBF displayed the smallest set-to-set variation of m_{GDR}, and the overall smallest values of m_{GDR}. The WBF displayed very similar values of m_{GDR}, however W1 frames generally reached higher peaks of GDR.

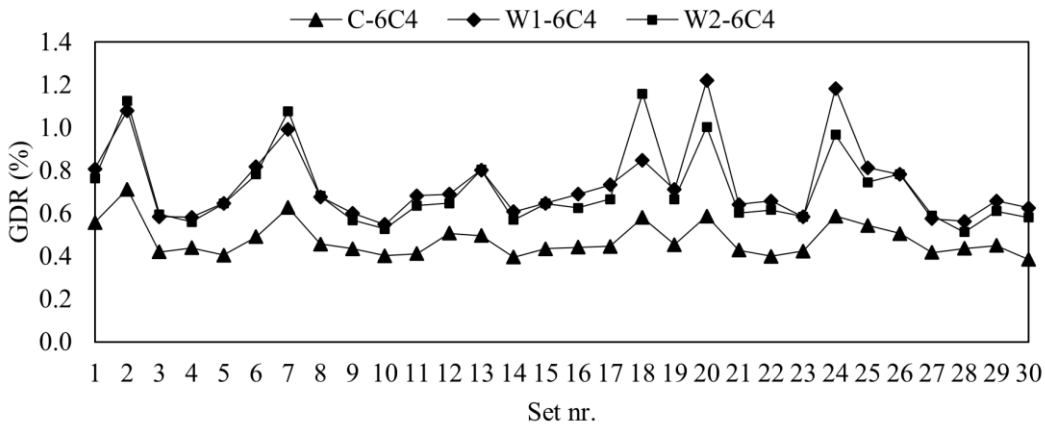

(a) 6C4

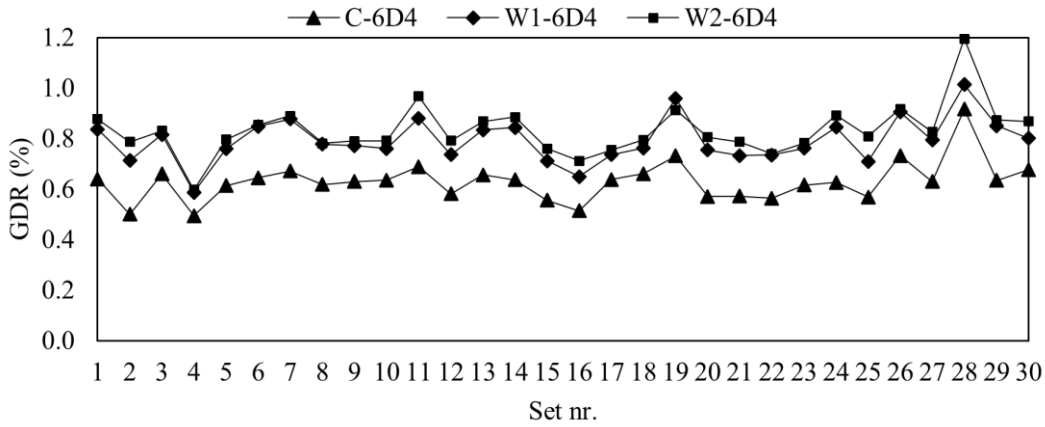

(b) 6D4

Figure 6.13: Set-to-set variation of m_{GDR} for frames 6C4 and 6D4

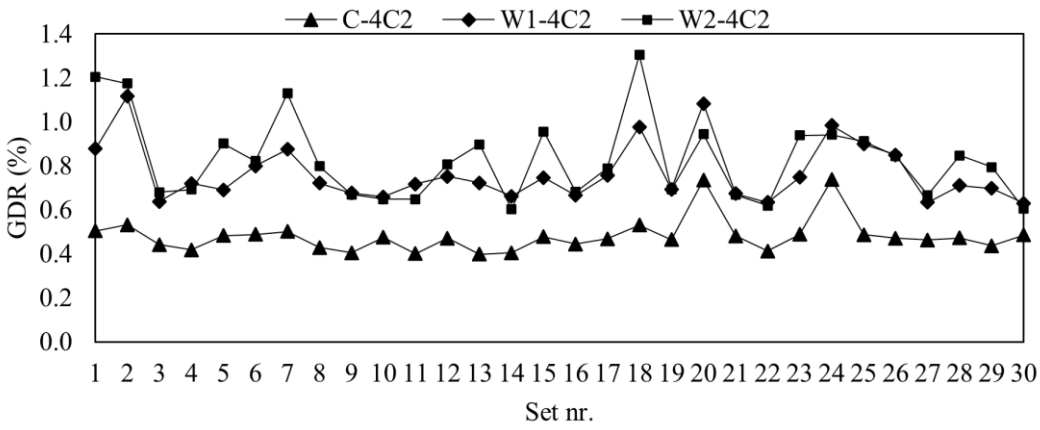

(a) 4C2

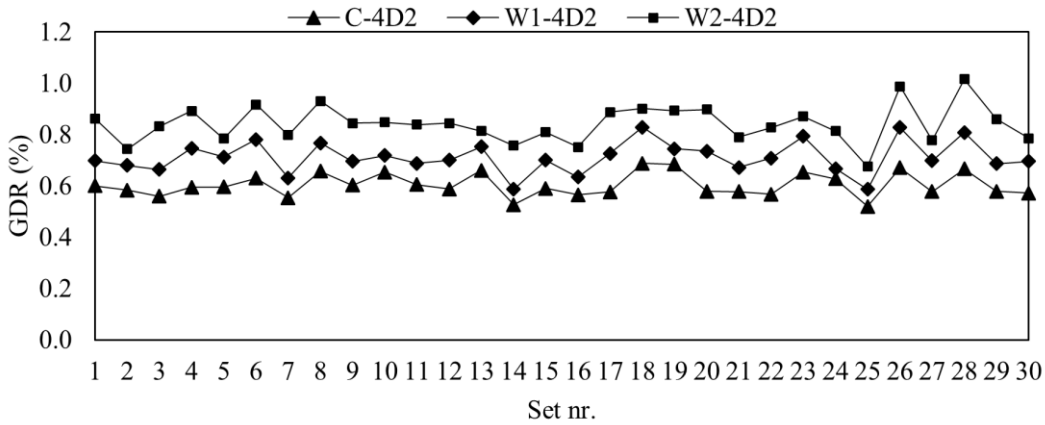

(b) 4D2

Figure 6.14: Set-to-set variation of m_{GDR} for frames 4C2 and 4D2

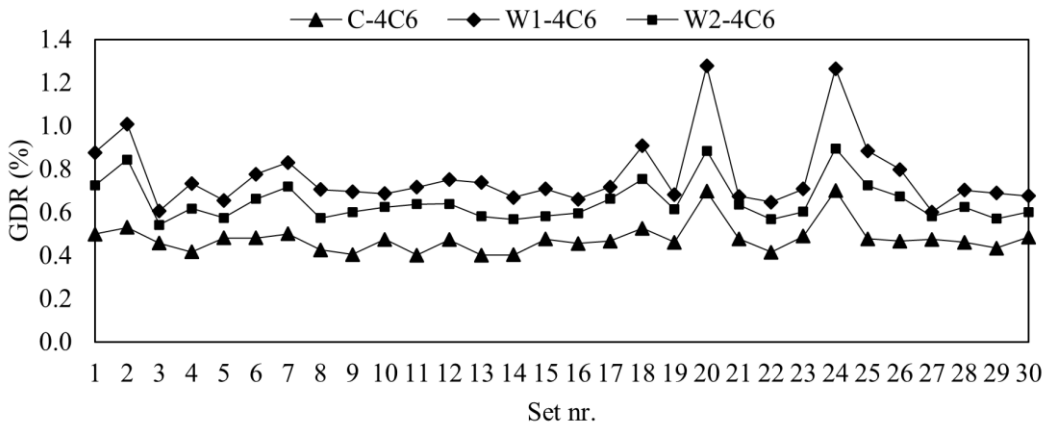

(a) 4C6

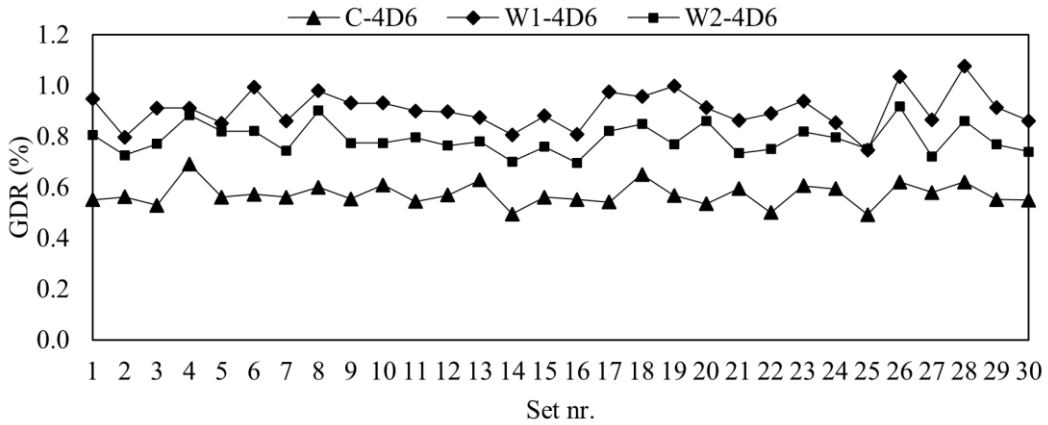

(b) 4D6

Figure 6.15: Set-to-set variation of m_{GDR} for frames 4C6 and 4D6

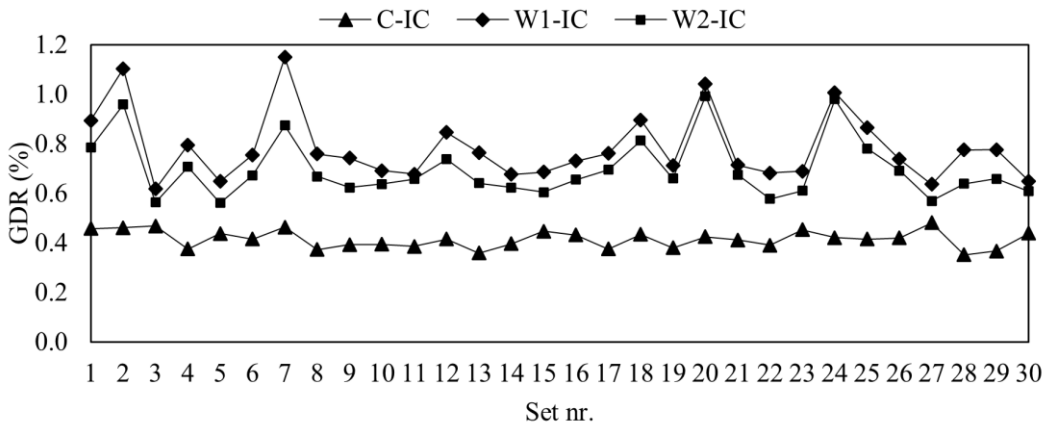

(a) IC

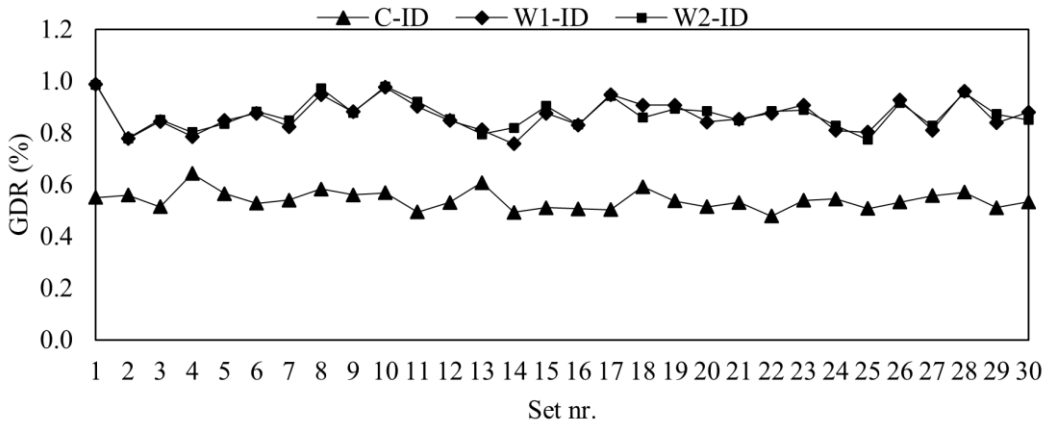

(b) ID

Figure 6.16: Set-to-set variation of m_{GDR} for frames IC and ID

6.2.3 Mean Global and Interstory Demand

The code-based assessment of displacement demand was completed by calculating the mean drift ratios from the data obtained from the 30 sets of analyses performed for each frame. To distinguish the mean drift ratios obtained from each set (m_{GDR}, $m_{IDR,k}$) from the mean drift ratios of the 30 sets of analyses (μ_{GDR}, $\mu_{IDR,k}$), the latter are denoted with the Greek letter μ and referred to as GDR demand and MIDR demand respectively. The GDR demand and MIDR demand were calculated using Equations (6.6) and (6.7) respectively. The CoV was computed using Equation (6.3), while the standard deviation for GDR and MIDR demands were computed using Equations (6.8) and (6.9) respectively. In these equations, N denotes the number of sets that were used

to calculate demand values and N=30, while *i* and *k* denote the number of set and the floor number, respectively.

$$\mu_{GDR} = \frac{\sum_{i=1}^{N} m_{GDR,i}}{N} \tag{6.6}$$

$$\mu_{IDR,k} = \frac{\sum_{i=1}^{N} m_{IDRk,i}}{N} \tag{6.7}$$

$$\sigma_{GDR} = \sqrt{\frac{\sum_{i=1}^{N} \left(m_{GDR,i} - \mu_{GDR} \right)^2}{N}} \tag{6.8}$$

$$\sigma_{IDRk} = \sqrt{\frac{\sum_{i=1}^{N} \left(m_{IDRk,i} - \mu_{IDRk} \right)^2}{N}} \tag{6.9}$$

The values of demand for GDR and MIDR calculated using the equations above are summarized in Table 6.1. The GDR demand values obtained from the time-history analyses using 30 sets of ground motion records are relatively small and do not exceed 1%. In each group of three similar frames (one CBF and two WBF), the GDR demand of the CBF is smaller than the demand imposed on the WBF. The trends of the MIDR vary, however this occurs because CBF and WBF experience maximum drift ratios in different floors. In overall, the MIDR demands imposed on the WBF are larger than the MIDR demands imposed on the CBF. The variances of the GDR and MIDR demands are listed in Table 6.2. The values of CoV were generally low for all the demand parameters that were computed in this section.

Table 6.1: Displacement demand calculated from 30 sets of time-history analyses

Frame	Demand						
	GDR (%)	MIDR1 (%)	MIDR2 (%)	MIDR3 (%)	MIDR4 (%)	MIDR5 (%)	MIDR6 (%)
C-4C4	0.475	0.846	0.655	0.389	0.219	-	-
W1-4C4	0.804	0.840	1.040	1.024	0.651	-	-
W2-4C4	0.813	1.223	1.263	0.718	0.366	-	-
C-4C2	0.481	0.749	0.711	0.401	0.216	-	-
W1-4C2	0.767	0.632	0.924	0.916	0.846	-	-
W2-4C2	0.830	1.094	1.230	0.885	0.397	-	-
C-4C6	0.477	0.719	0.693	0.400	0.260	-	-
W1-4C6	0.768	0.583	0.966	1.112	0.750	-	-
W2-4C6	0.649	0.557	0.876	0.961	0.505	-	-
C-6C4	0.476	0.830	0.869	0.608	0.406	0.346	0.196
W1-6C4	0.735	0.554	0.909	0.988	1.006	0.963	0.557
W2-6C4	0.711	0.688	1.018	1.112	1.007	0.702	0.343
C-IC	0.414	0.605	0.494	0.308	0.373	-	-
W1-IC	0.783	0.989	1.014	0.797	0.648	-	-
W2-IC	0.697	0.960	0.920	0.692	0.473	-	-
C-4D4	0.655	1.187	0.929	0.488	0.242	-	-
W1-4D4	0.841	0.823	1.090	1.012	0.702	-	-
W2-4D4	0.945	1.006	1.238	1.237	0.637	-	-
C-4D2	0.604	0.941	0.898	0.507	0.231	-	-
W1-4D2	0.711	0.701	0.830	0.776	0.688	-	-
W2-4D2	0.842	0.699	1.050	1.097	0.806	-	-
C-4D6	0.571	0.805	0.813	0.502	0.310	-	-
W1-4D6	0.905	0.695	1.065	1.128	1.009	-	-
W2-4D6	0.789	0.507	0.952	1.109	0.849	-	-
C-6D4	0.629	1.074	1.113	0.818	0.553	0.427	0.226
W1-6D4	0.792	0.592	0.937	1.008	1.022	0.951	0.709
W2-6D4	0.831	0.739	1.065	1.081	1.107	1.056	0.574
C-ID	0.540	0.819	0.653	0.386	0.403	-	-
W1-ID	0.868	1.083	0.968	0.989	0.836	-	-
W2-ID	0.872	1.071	1.058	1.082	0.650	-	-

Table 6.2: CoV of displacement demand calculated from 30 sets of time-history analyses

Frame	CoV						
	GDR (%)	MIDR1 (%)	MIDR2 (%)	MIDR3 (%)	MIDR4 (%)	MIDR5 (%)	MIDR6 (%)
C-4C4	0.143	0.201	0.186	0.113	0.116	-	-
W1-4C4	0.211	0.296	0.229	0.219	0.100	-	-
W2-4C4	0.220	0.295	0.254	0.130	0.071	-	-
C-4C2	0.161	0.230	0.203	0.091	0.074	-	-
W1-4C2	0.170	0.215	0.142	0.147	0.159	-	-
W2-4C2	0.223	0.299	0.232	0.203	0.075	-	-
C-4C6	0.144	0.205	0.183	0.084	0.074	-	-
W1-4C6	0.210	0.393	0.236	0.178	0.098	-	-
W2-4C6	0.141	0.237	0.151	0.125	0.090	-	-
C-6C4	0.165	0.297	0.226	0.115	0.092	0.085	0.095
W1-6C4	0.237	0.414	0.256	0.231	0.223	0.185	0.077
W2-6C4	0.249	0.551	0.338	0.237	0.177	0.128	0.092
C-IC	0.084	0.134	0.113	0.077	0.073	-	-
W1-IC	0.174	0.279	0.218	0.099	0.116	-	-
W2-IC	0.169	0.223	0.205	0.088	0.107	-	-
C-4D4	0.084	0.125	0.093	0.071	0.059	-	-
W1-4D4	0.065	0.098	0.071	0.064	0.094	-	-
W2-4D4	0.101	0.114	0.093	0.108	0.120	-	-
C-4D2	0.074	0.112	0.094	0.065	0.045	-	-
W1-4D2	0.085	0.097	0.076	0.086	0.102	-	-
W2-4D2	0.085	0.113	0.082	0.084	0.113	-	-
C-4D6	0.077	0.128	0.095	0.068	0.095	-	-
W1-4D6	0.078	0.097	0.070	0.074	0.103	-	-
W2-4D6	0.071	0.111	0.058	0.065	0.127	-	-
C-6D4	0.125	0.185	0.151	0.094	0.072	0.067	0.076
W1-6D4	0.109	0.168	0.102	0.094	0.081	0.075	0.106
W2-6D4	0.118	0.191	0.129	0.122	0.095	0.076	0.092
C-ID	0.066	0.097	0.083	0.052	0.068	-	-
W1-ID	0.068	0.085	0.072	0.073	0.098	-	-
W2-ID	0.064	0.082	0.070	0.086	0.073	-	-

6.3 Summary of Time-History Analyses

In this chapter, the procedure and results of time-history were presented. The time-history analyses were performed using real and unscaled earthquake record, which were selected according to the procedure presented in TBEC. These analyses produced a large amount of data, but this thesis was focused on the displacement demand of the frames expressed in terms of global and interstory drift ratios.

A considerable variation of was observed in the Δ_{max}/H values within each set. The set coefficients of variance could be as high as 2. This variance was a direct result of the variation and randomness of the ground motions that composed the record sets. The set means m_{GDR} and m_{IDRj} were less varied and displayed some clear trends. In general, the CBF had the lowest m_{GDR}, followed by the W1BF and then W2BF. The set variance however was almost not affected by the type of the frame. The same trends were observed among the mean of the set means μ_{GDR}. WBF experience larger GDR demands than the CBF. Consequently, the MIDR of the WBF were also generally greater than the MIDR of the CBF.

Chapter 7

Seismic Demand and Performance of the Frame Models

FEMA P-58 [147] is the next generation code for seismic design and assessment of structures [156-158]. It has been used to assess the performance of educational buildings in Venezuela [159], Tehran [160] and Beijing [161], to assess the damages of existing buildings [162] and the effectivity of energy dissipation devices in RC frames [163]. Cook et al. [164] performed a comparative study on various methods for the seismic risk assessment of structures and reported that while in general the results were similar, the procedure laid out in FEMA P-58 was more capable of capturing building-specific and site-specific mechanisms than the other methods considered.

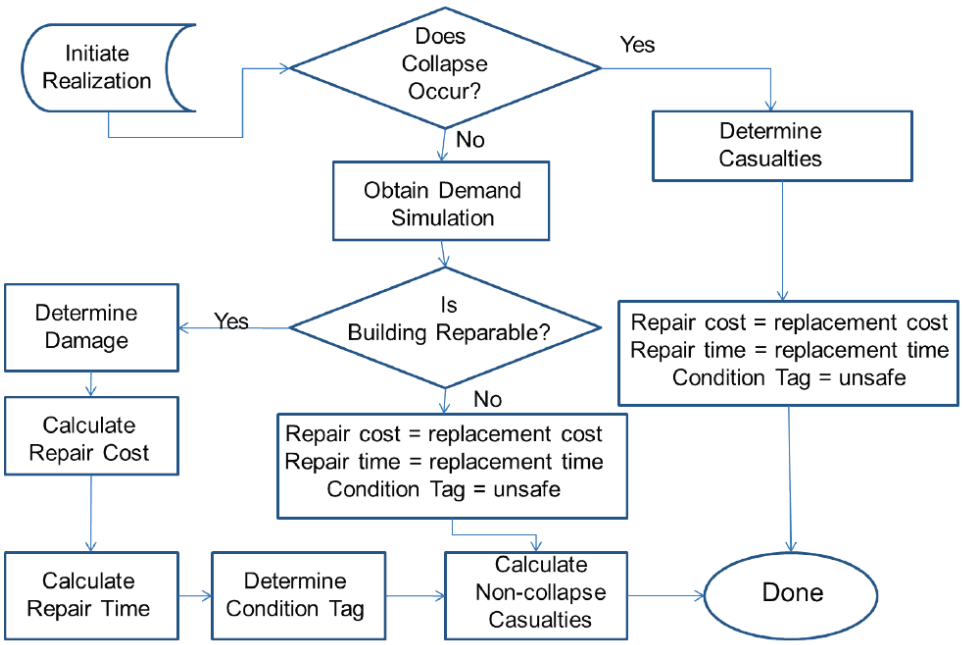

Figure 7.1: Flowchart of the assessment procedure presented in FEMA P-58 [147]

FEMA P-58 takes a probabilistic approach at performance assessment and includes parameters that are more understandable to parties such as shareholder, owners, contractors and public. The procedures described in FEMA P-58 aim to assess not only the construction cost or seismic performance in case of a seismic event, but costs of repair and/or replacement as well. These costs include dislocation costs, and financial effects of facilities that stop operating after seismic events. A flowchart detailing such assessment is presented in Figure 7.1. The first step is to assess the structural performance of a building.

FEMA P-58 takes a probabilistic approach to the performance assessment of structures. This approach is applied to detailed models which may include nonstructural elements as well. While simplified methods are also presented, performing limited or full suite time-history analyses for estimation of seismic demand is strongly suggested. Three assessment methods are introduced in this guideline, intensity based, scenario based and time based assessment. The three are briefly discussed below.

- **Intensity based assessment** is carried out when the probable performance of a structure subjected to earthquakes of a certain intensity is wanted. Ground motion records sets are defined at different intensity levels, and the analyses are performed. An output of such analyses are fragility curves.
- **Scenario based assessment** is carried out when the performance of a structure subjected to a certain earthquake scenario is wanted. The earthquake scenario can be defined by the magnitude (M), distance from fault and depth of the seismic event. The outcomes of such an assessment are presented in terms of demand parameter of choice versus probability of non-exceedance (PNE).
- **Time based assessment** is carried out when the probable performance of a structure over a desired period of time is wanted. Time based assessment can be carried out as a series of intensity based assessments. The results of time based assessment are presented in terms of time versus PNE.

Scenario based assessment was used in this thesis. The ground motion selection method of this assessment procedure is similar to the method suggested by TBEC and described in Section 6.1. A detailed model of the structure that is being assessed should be created. This model should include all structural elements that contribute to the load

carrying capacity system, and the nonstructural elements that might contribute to strength or stiffness, or that are susceptible to damage. All possible damage modes should be included in the model explicitly. If a damage mode is not included in the model explicitly, then the rationale behind it should be given. The model is subjected to time-history analyses suites and the output results are obtained in terms of the wanted parameters. The result of each analysis suite is termed a realization. Figure 7.2 describes the procedure to be followed after the realizations have been obtained. Consequences can be costs of repair or reaching a certain damage level.

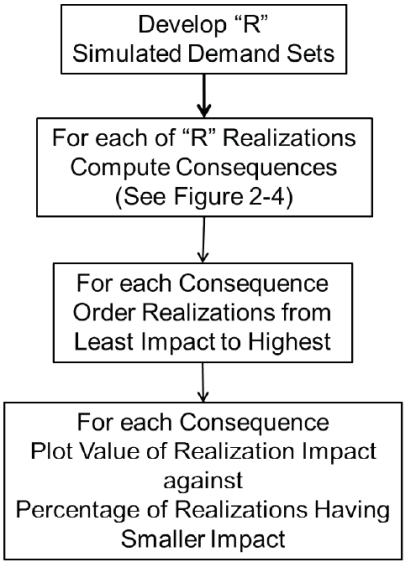

Figure 7.2: Flowchart for intensity and scenario based assessment procedures [147]

In this study, the nonlinear models of the frames were defined in such a way as to include all the damage mechanisms that code-complying structures are susceptible to. This procedure was described in detail in Chapter 4. Due to the hypothetical nature of the study, nonstructural elements were not included in the models. These models were subjected to time-history analyses using sets of ground motion records. The performance of the frame models was assessed in terms of global and interstory drift ratios. Therefore, for each realization the drift ratios are computed. Ideally thousands of realizations should be obtained from time-history analyses. Afterwards these realizations can be fit to a lognormal distribution, and PNE graphs can be plotted. A

sample of such an outcome is shown in Figure 7.3 . Since performing thousands of analyses sets of time-history analyses is difficult and requires considerable time, limited suite analyses can be performed and then a Monte Carlo simulation which modifies the input to take into account uncertainties that come with small samples is suggested.

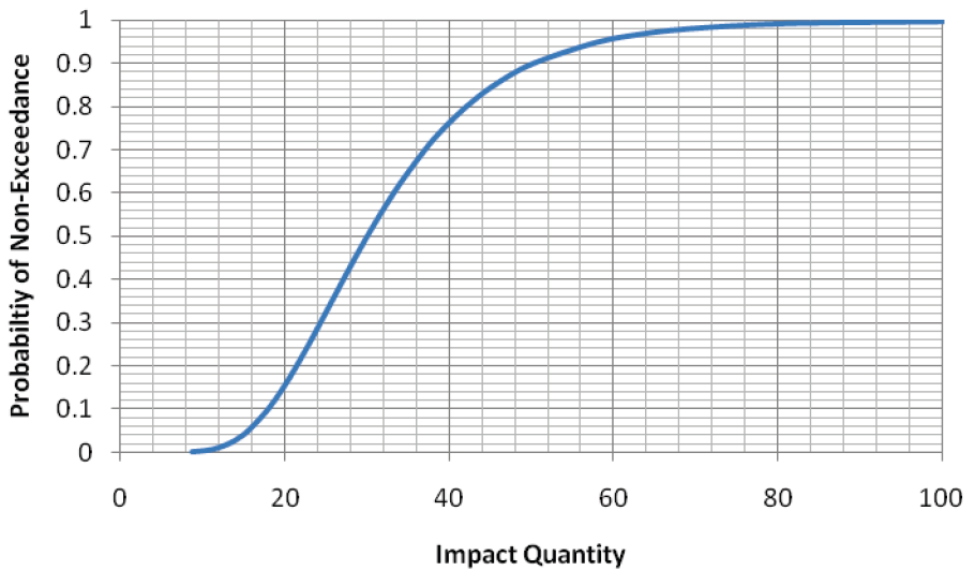

Figure 7.3: PNE graph, as obtained for scenario based assessments [147]

7.1 Including Uncertainties in the Estimation of the Seismic Demand

Even if a considerable amount of time-history analyses is performed, the use of simple models may ignore the variability of other parameters, such as material properties, loads acting on the structure and cross sections of the structural elements. These parameters should ideally be represented by distributions rather than single values, in order to account for the potential variation that may occur. For instance, while the concrete quality is defined by its characteristic strength, taking samples from actual structures may show some variability. Jalayer et al. [165] investigated the effect of the uncertainties of the structural parameters, while Celarek and Dolsek [166] investigated

the effect of modeling uncertainties. FEMA P-58 defines a dispersion β_m that stands for modeling dispersion and is to be added to the dispersion of the results of time-history analyses. β_m has three components, β_c, β_q and β_{gm}.

The dispersion for construction quality assurance β_c is related to the building definition and construction quality assurance. The values of β_c range from 0.1 to 0.4, for the following situations:

- β_c=0.10 for new and existing buildings of superior quality.
- β_c=0.25 for new and existing buildings of average quality.
- β_c=0.40 for new and existing buildings of limited quality.

The dispersion for quality of the analytical model β_q describes the quality and completeness of the analytical model. The values of β_q range from 0.1 to 0.4, for the following situations:

- β_q=0.10 for numerical models of superior quality that include all structural and nonstructural components that contribute to the strength and stiffness of the structures.
- β_q=0.25 for numerical models of average quality that include most of the structural and nonstructural components that contribute to the strength and stiffness of the structures.
- β_q=0.40 for numerical models of limited quality that include the contribution of the structural components in the strength and stiffness of the structures.

The dispersion due to ground motion variability β_{gm} is associated with the uncertainty of the predictive ability of attenuation relationships used to derive the target spectrum. Since in this thesis code-based spectra were used for the selection of ground motion records β_{gm} was not taken into consideration.

Two values were considered for each of the β_c and β_q dispersion parameters. The frame models represent code-compliant construction; therefore, the buildings were assumed to be new buildings of superior or average quality. On the other hand, since the models were simple, the numerical models were assumed to be of average or limited quality

and completeness. The scenarios that were considered for the dispersion parameters β_c and β_q are presented in Table 7.1.

Table 7.1: Values of dispersion considered for the added uncertainties of the models

Dispersion parameter	**Uncertainty description**	**Value of dispersion**
β_c	New building of superior quality	0.10
	New building of average quality	0.25
β_q	Numerical model of average quality and completeness	0.25
	Numerical modeling of limited quality and completeness	0.40

$$\beta_m = \sqrt{\beta_c^2 + \beta_q^2} \leq 0.5 \tag{7.1}$$

Table 7.2: Combination scenarios for the construction and model quality dispersions

Scenario	β_c	β_q	β_m	**Weight**
1	0.10	0.25	0.27	0.25
2	0.10	0.40	0.41	0.25
3	0.25	0.25	0.35	0.25
4	0.25	0.40	0.47	0.25
Weighted scenario			**0.38**	

The modeling dispersion β_m is calculated using Equation (7.1) and should not exceed 0.5. There are four possible combinations of pairs (β_c, β_q) which have equal chance of occurring. These scenarios are listed in Table 7.2, alongside with the average modeling dispersion β_m. This value of dispersion was added to the results of the time-history analyses to account for the uncertainties related to construction and modeling.

7.2 Code-based Assessment of Demand

The procedures for selecting ground motion records and performing time-history analyses were based on TBEC [63]. In Chapter 6 it was observed that there is some set-to-set variance for GDR and MIDR due to the random nature of the ground motion records that were used to perform the time-history analyses. As this variance did not account for the variances due to design, construction and modeling, an additional measure of variance (β_m) was calculated in Section 7.1. The distributions of the demand parameters (GDR and MIDR) were reevaluated using μ_{GDR} and μ_{IDRk} and the modified variances that included β_m.

7.2.1 Code-based Fragility for GDR

Code-based fragility functions relating GDR to PNE were developed for all the frames. The distributions of set means (m_{GDR}) were used to generate the code-based fragility functions. For instance, the set distribution of m_{GDR} for frame C-4C4 is shown in Table 7.3. This set is characterized by the mean μ_{GDR}=0.475%, standard deviation σ_{GDR}=0.068, and variance CoV=0.143. The inherent variance of the sets was enhanced using the modeling dispersion β_m computed in Section 7.1. The fragility function was generated as a cumulative lognormal distribution of this data set. Such a function can be used to determine the probability that for any given frame, a certain level of deformation will be exceeded or not. The fragility functions were used to compute the PNE for the performance levels for each frame, thus providing an idea of the actual performance of the frames.

The fragility functions of frames 4C4 are shown in Figure 7.4a while Figure 7.4b shows the fragility functions of frames 4D4. In both cases, the CBF have steeper fragility functions than WBF. This means that for the same level of GDR, the PNE for the CBF is higher than the PNE of WBF. The PNE for LD was calculated as 14.2%, 4.2% and 0.2% for frames C-4C4, W1-4C4 and W2-4C4 respectively, while the PNE for CD and CP was practically 100% for all three frames. The PNE for LD was calculated as 0.3%, 3.8% and 0.1% for frames C-4D4, W1-4D4 and W2-4D4 respectively, while the PNE for CD and CP was practically 100% for all three frames.

Table 7.3: Distribution of m_{GDR} for frame C-4C4 and its mean, standard deviation and variance

μ_{GDR} (%)			0.475		
σ_{GDR}			0.068		
CoV			0.143		
Set 1-5	**Set 6-10**	**Set 11-15**	**Set 16-20**	**Set 21-25**	**Set 26-30**
0.441	0.536	0.470	0.461	0.456	0.506
0.374	0.456	0.428	0.428	0.443	0.421
0.392	0.448	0.397	0.527	0.515	0.477
0.463	0.456	0.425	0.520	0.685	0.442
0.501	0.426	0.499	0.665	0.541	0.449

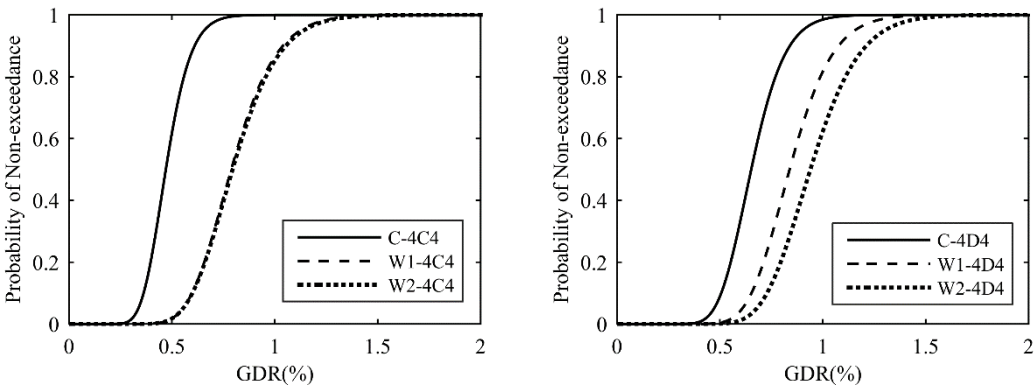

(a) 4C4 (b) 4D4

Figure 7.4: Fragility functions of regular frames with four stories and four bays based on the sets of m_{GDR}

The fragility functions of frames 4C2 and 4D2 are shown in Figure 7.5a and Figure 7.5b respectively. In both cases, the CBF have steeper fragility functions than WBF. This means that for the same level of GDR, the PNE for the CBF is higher than the PNE of WBF. The PNE for LD was calculated as 0.0% for frames C-4C2 and W2-4C2, and 0.6% for frame W1-4C2, while the PNE for CD and CP was practically 100% for all three frames. The PNE for LD was calculated as 0.0%, 1.4% and 0.1% for frames C-4D2, W1-4D2 and W2-4D2 respectively, while the PNE for CD and CP was practically 100% for all three frames.

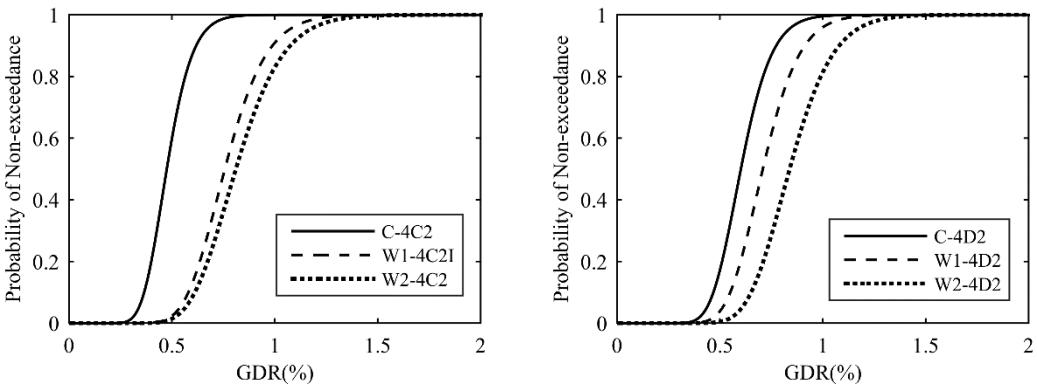

(a) 4C2 (b) 4D2

Figure 7.5: Fragility functions of regular frames with four stories and two bays based on the sets of m_{GDR}

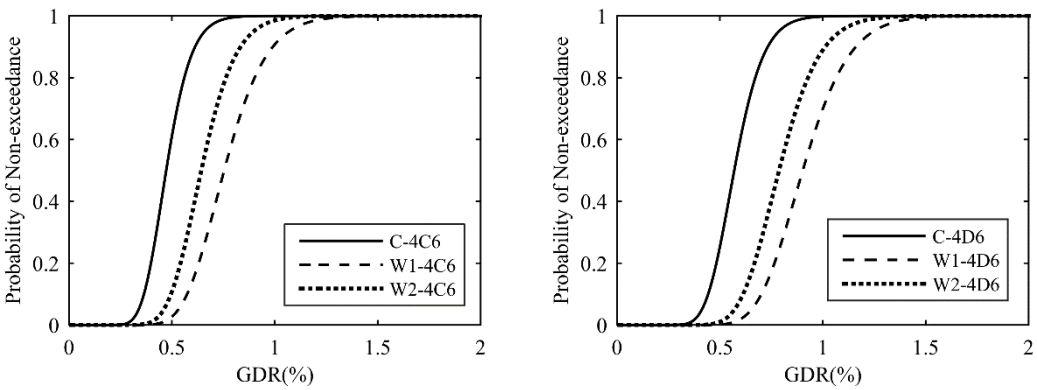

(a) 4C6 (b) 4D6

Figure 7.6: Fragility functions of regular frames with four stories and six bays based on the sets of m_{GDR}

Figure 7.6a and b display the fragility functions for 4C6 and 4D6 frames respectively. In both cases, the CBF have steeper fragility functions than WBF. This means that for the same level of GDR, the PNE for the CBF is higher than the PNE of WBF. The PNE for LD was calculated as 2.4%, 0.7% and 0.0% for frames C-4C6, W1-4C6 and W2-4C6 respectively, while the PNE for CD and CP was practically 100% for all three frames. The PNE for LD was calculated as 0.0% for all three frames, while the PNE for CD and CP was practically 100% for all three frames.

Figure 7.7a and b display the fragility functions for 6C4 and 6D4 frames respectively. In both cases, the CBF have steeper fragility functions than WBF. This means that for the same level of GDR, the PNE for the CBF is higher than the PNE of WBF. The

PNE for LD was calculated as 2.5%, 2.7% and 2.4% for frames C-6C4, W1-6C4 and W2-6C4 respectively, while the PNE for CD and CP was practically 100% for all three frames. The PNE for LD was calculated as 0.04%, 0.4% and 0.7% for frames C-6D4, W1-6D4 and W2-6D4 respectively, while the PNE for CD and CP was practically 100% for all three frames.

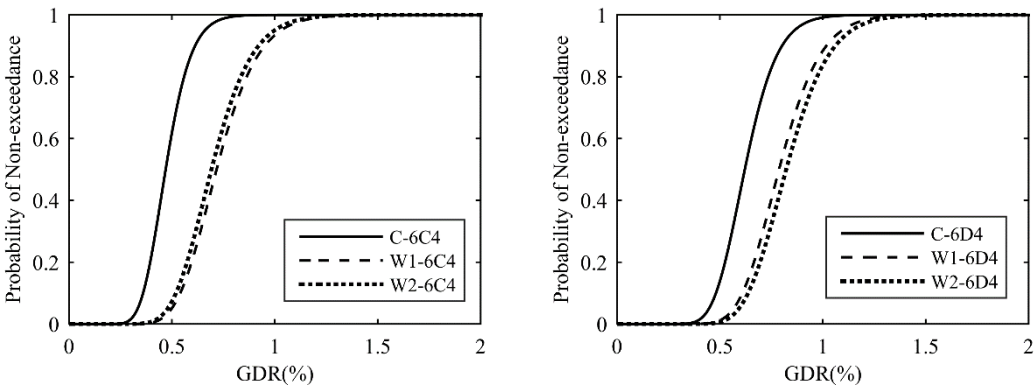

(a) 6C4 (b) 6D4

Figure 7.7: Fragility functions of regular frames with six stories and four bays based on the sets of m_{GDR}

The fragility functions of frames IC and ID are shown in Figure 7.8a and b respectively. In both cases, the CBF have steeper fragility functions than WBF. This means that for the same level of GDR, the PNE for the CBF is higher than the PNE of WBF. The PNE for LD was calculated as 33.1%, 4.6% and 0.8% for frames C-IC, W1-IC and W2-IC respectively, while the PNE for CD and CP was practically 100% for all three frames. The PNE for LD was calculated as 0.1%, 10.9% and 0.3% for frames C-ID, W1-ID and W2-ID respectively, while the PNE for CD and CP was practically 100% for all three frames.

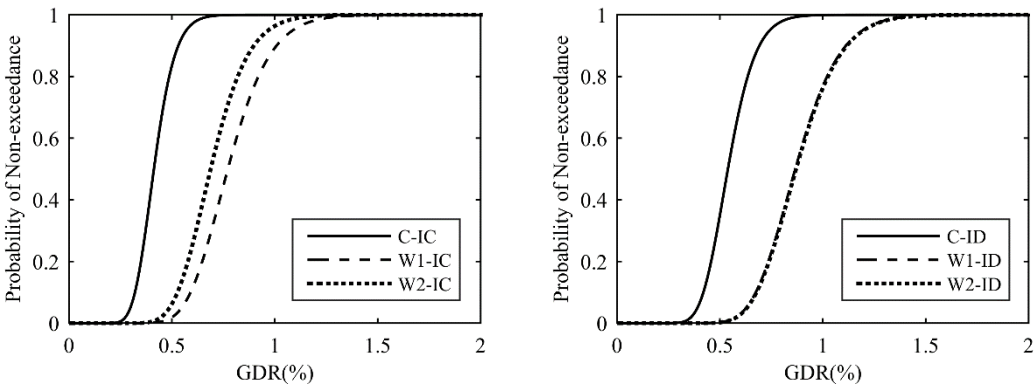

(a) IC (b) ID

Figure 7.8: Fragility functions of irregular frames

In overall, the fragility functions of the CBF are steeper than the fragility functions of the WBF. The values of PNE for the LD performance level were low, at most around 85%, therefore all the frames likely exceeded the LD threshold. Typically, WBF had lower PNE for LD than CBF. All the frames had virtually 100% PNE for the CD and CP performance levels. Therefore, it is unlikely that any of the frames exceeded the CD and CP thresholds. The performance of the all the frames is likely to CD, however this was assessed in more detail in the following section.

7.2.2 Demand Ranges vs Capacity

Considering the drift ratios that were obtained from the time-history analyses as distributions, it is possible to determine ranges of drift ratios for desired confidence intervals. These ranges are defined by the lower bound (LB) and upper bound (UB), as shown schematically in Figure 7.9.

In this thesis the GDR ranges were calculated for a confidence interval of 90%. Therefore, if the frame models were to be subjected to time-history analysis using a new set of ground motion records compatible with the design elastic spectrum, the probability that the result obtained from this 31st set would fall in the defined range is 90%.

It is possible to compute the drift ratio ranges for any of the desired drift parameters. However, since the performance levels were also expressed in terms of GDR, GDR ranges were calculated only. These GDR ranges were compared with the damage

regions defined by the performance levels. A generalized example is shown in Figure 7.10. In this example, the mean demand μ_{GDR} is represented by a rhombus shaped dot, while the GDR range is represented by the oblique line pattern box. The damage regions defined by the performance levels are represented by monochromatic stacked columns, with hues ranging from white to dark grey. The collapse region begins after the CP limit, and virtually has no upper limit. However, for sake of representation, collapse regions were shown only until 6% GDR. The location of the GDR range defines the performance of the frame model itself.

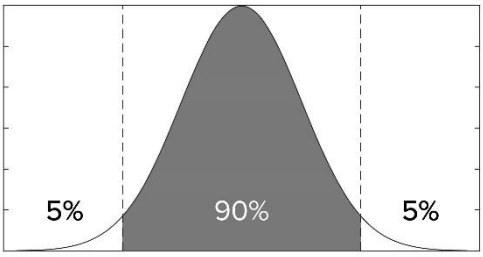

Figure 7.9: Graphical description of LB and UB for a normal distribution for a confidence interval of 90%

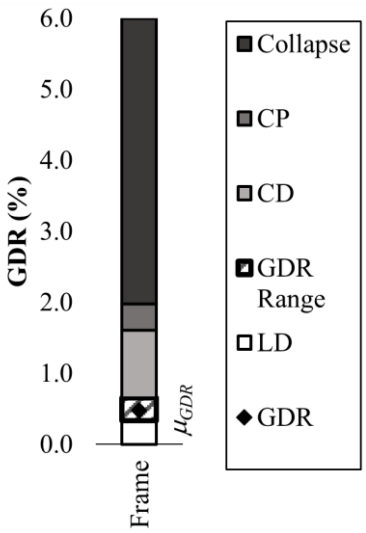

Figure 7.10: Example of the comparison of GDR ranges with the damage regions defined by the performance levels.

Figure 7.11 shows the comparison of demand and capacity for the regular frames with four bays and four and six stories. From this graph it is obvious that the WBF have higher GDR capacities for CD and CP. The GDR ranges are also wider for the WBF than the CBF. Nonetheless, in all the four bay frames the GDR range falls within the CD damage level. Typically, the frames designed for soil class D have greater μ_{GDR} and GDR wider ranges, regardless of the type of beam. W2 type frames have slightly higher μ_{GDR} and slightly wider GDR ranges than W1 type frames.

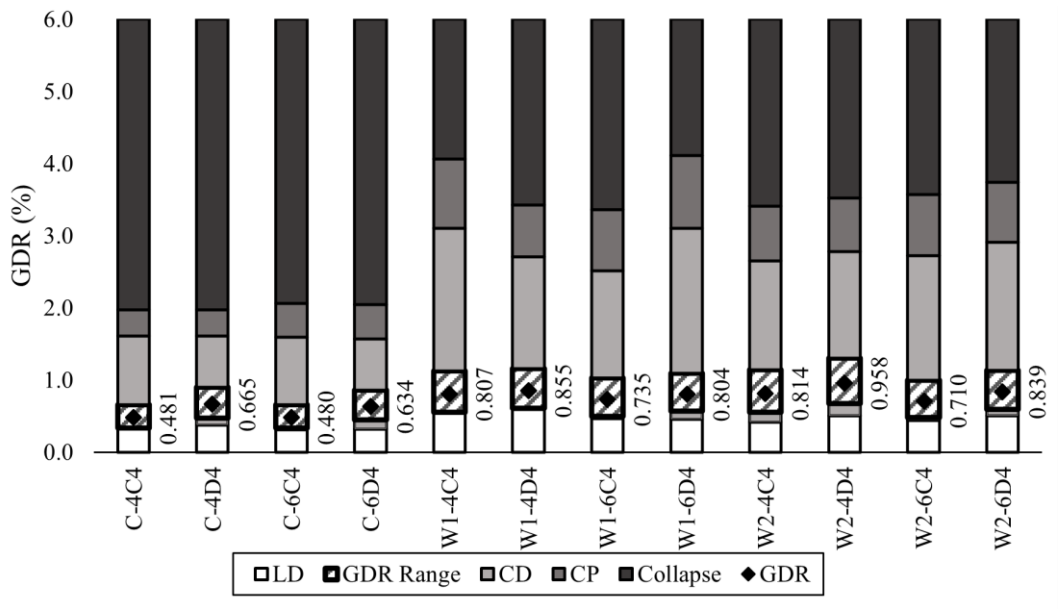

Figure 7.11: Demand vs. Capacity of the four bay and four and six story frames based on the sets of m_{GDR}

Figure 7.12 shows the comparison of demand and capacity for the regular frames with four bays and four and six stories. Again, the WBF have higher GDR capacities for CD and CP and even collapse than the CBF. The GDR ranges are also wider for the WBF than the CBF. However, the GDR range of 4C2, 4D2, 4C6 and 4D6 frames falls within the CD damage level. Similarly, to the four bay frames, 4D2 and 4D6 frames have higher μ_{GDR} and wider GDR ranges than frames 4C2 and 4C6 respectively.

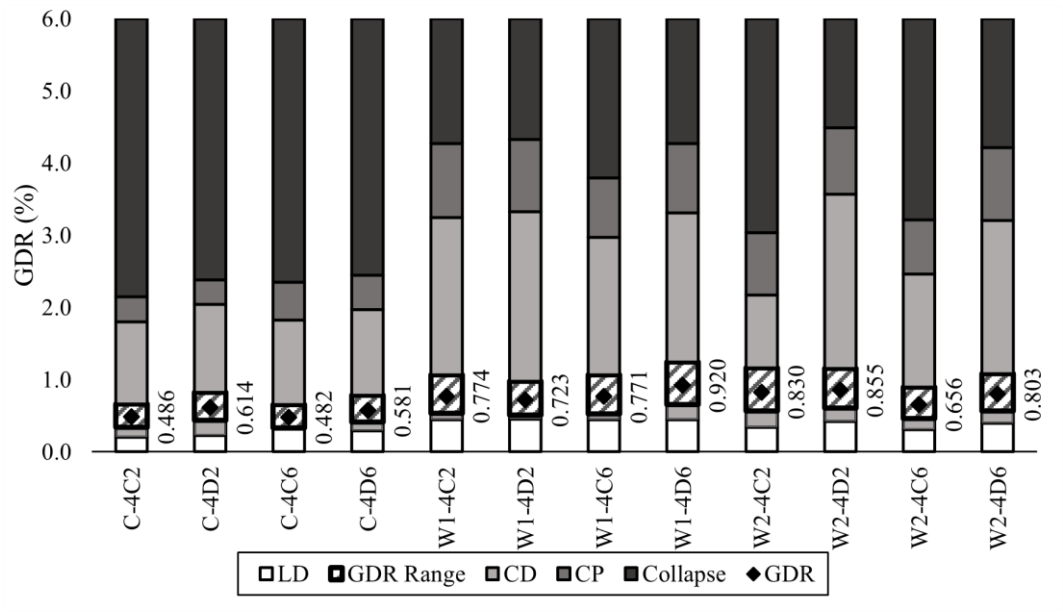

Figure 7.12: Demand vs. Capacity of the four story and four and six bay frames based on the sets of m_{GDR}

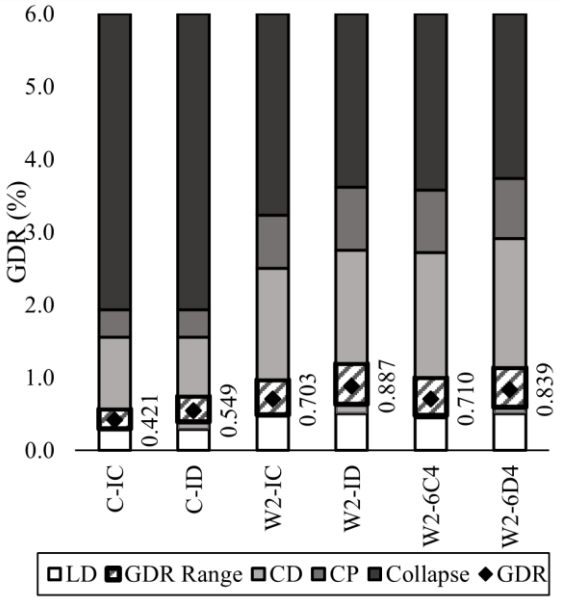

Figure 7.13: Demand vs. Capacity of the irregular frames based on the sets of m_{GDR}

Figure 7.13 shows the comparison of demand and capacity for the irregular frames IC and ID. It is obvious that the WBF have higher GDR capacities for CD and CP and even collapse than the CBF. The GDR ranges are also wider for the WBF than the

CBF. Similarly, to the regular frames, the GDR range falls within the CD damage level.

In overall, the GDR range was situated within the CD region for all the frames, CBF and WBF. Therefore, it can be stated with a 90% confidence level that the performance of all the frames is CD. This is the performance level mandated by TBEC for residential construction. While parameters such as soil class, number of stories and bays, and beam type affected the values of μ_{GDR} and GDR ranges, they did not affect the overall performance of the frames.

7.2.3 Interstory Drift Ratio Profiles

Interstory drift ratios were also obtained as an outcome of the time-history analyses. μ_{IDR} were estimated and fragility functions of the MIDR were generated as well. MIDR profiles were plotted for each frame using μ_{IDR}. From these graphs observations about damage distributions among the floors can be made.

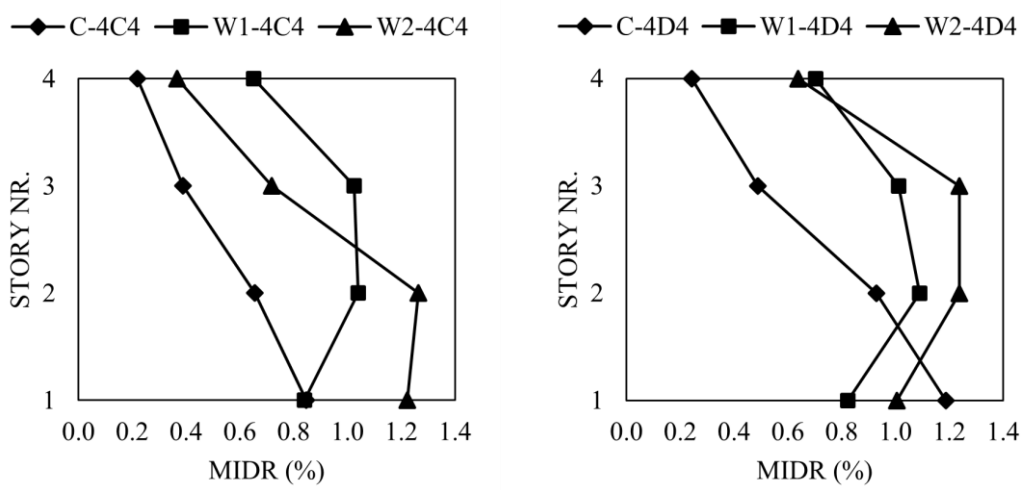

(a) 4C4 (b) 4D4

Figure 7.14: MIDR profiles for the four story and four bay frames

An observation of the MIDR profile for the 4C4 and 4D4 frames (Figure 7.14) showed that regardless of the soil type, the CBF reached the highest MIDR value in the first

story. The MIDR profile of the C-4C4 and C-4D4 frames showed a steady decrease in the values of MIDR on the upper stories. The situation is different for the WBF. W1-4C4, W1-4D4 and W2-4D4 displayed very similar MIDR profiles. The highest values of MIDR were observed in the second and third stories, while the MIDR of the first and fourth stories were almost the same. The only exception to this pattern was frame W2-4C4, in which the highest values of MIDR were observed in the first and second stories.

The two bay CBF had higher MIDR in the first and second stories, while the values of MIDR3 and MIDR4 steadily decreased, as shown in Figure 7.15. Frames W1-4D2 and W2-4D2 showed similar MIDR patterns to frames W1-4C4, W1-4D4 and W2-4D4. They displayed higher MIDR in the second and third stories, while the MIDR of the first and fourth stories were similar (Figure 7.15b). Frame W1-4C2 was characterized by a lower MIDR1, while MIDR2, MIDR3 and MIDR4 were almost the same (Figure 7.15a). Frame W2-4C2 was characterized by higher MIDR1 and MIDR2, that were followed by decreasing MIDR for the third and fourth stories.

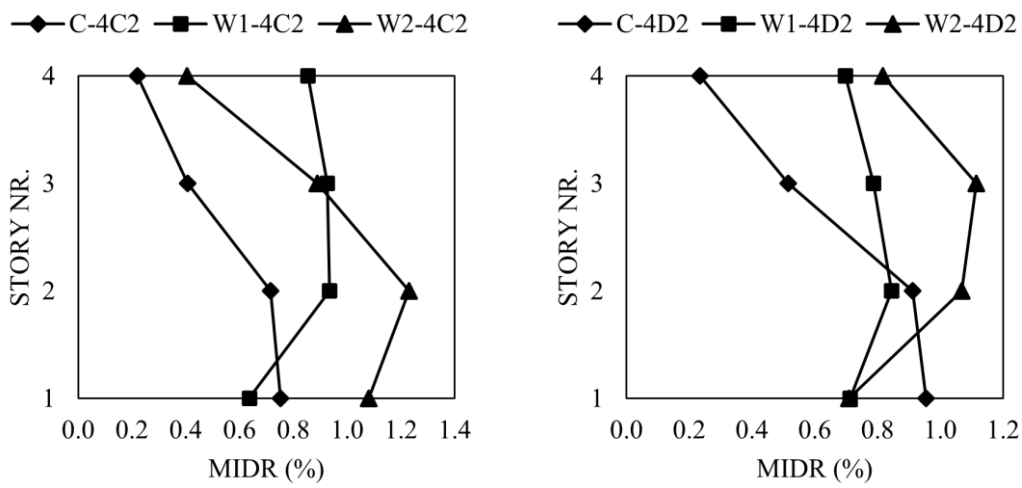

(a) 4C2 (b) 4D2

Figure 7.15: MIDR profiles for the four story and two bay frames

The MIDR profiles of the six bay CBF (Figure 7.16) were similar to the MIDR profiles of C-4C2 and C-4D2 frames (Figure 7.15). All the six bay WBF displayed very similar

MIDR profiles. The greatest values of MIDR were observed in the second and third stories. MIDR1 was almost the same as MIDR4 for frame W1-4C6 (Figure 7.16a), while for the rest of the WBF, MIDR4 was greater than MIDR1.

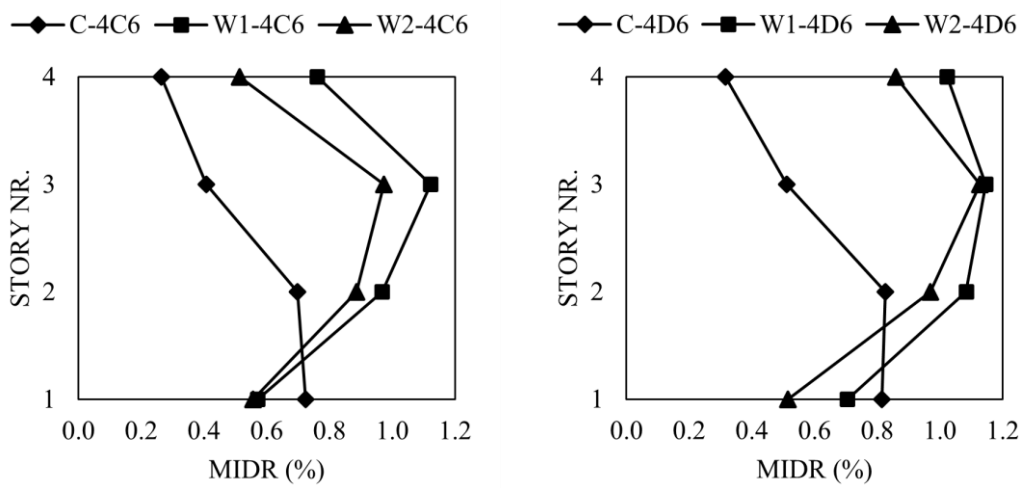

(a) 4C6 (b) 4D6

Figure 7.16: MIDR profiles for the four story and six bay frames

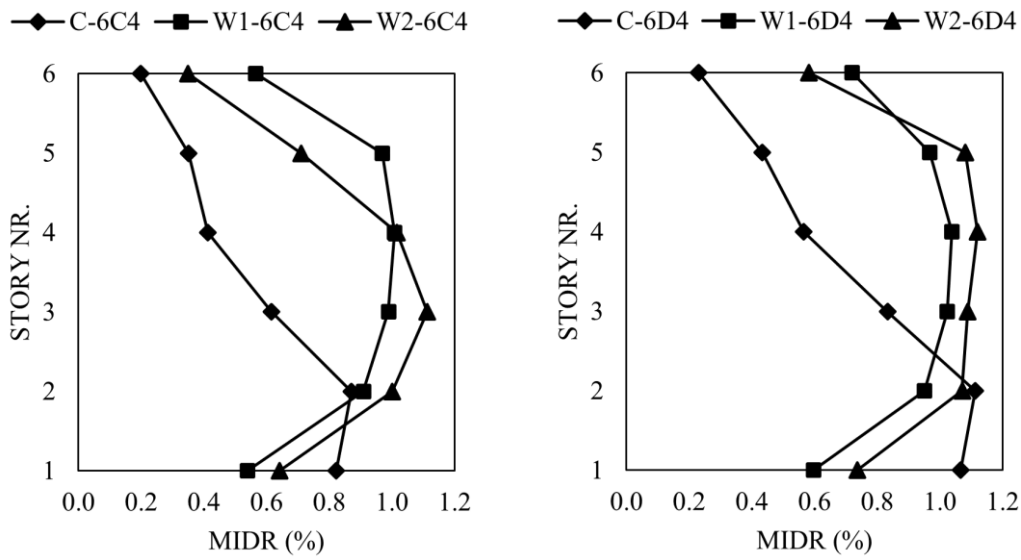

(a) 6C4 (b) 6D4

Figure 7.17: MIDR profiles for the six story and four bay frames

The six story frames displayed somewhat different MIDR profiles than the four story frames that were discussed above. Regardless of the soil class, the six story CBF reached their greatest values of MIDR in the first and second stories (Figure 7.17). Afterwards the values of MIDR almost linearly declined up to the sixth story. Frames W1-6C4 (Figure 7.17a), W1-6D4 and W2-6D4 (Figure 7.17b) displayed similar MIDR profiles. They reached the highest values of MIDR in second to fifth stories, in which MIDR was almost constant, while MIDR1 were similar in value to MIDR6. Frame W2-6C4 displayed a slightly different profile from the rest of the six story WBF. MIDR values peaked in second, third and fourth stories for frame W2-6C4 (Figure 7.17a).

The irregular frames displayed different MIDR profiles (Figure 7.18) than the regular frames that were discussed above. The MIDR profile of the irregular CBF was declining from the first to the third story, however MIDR3 and MIDR4 were almost the same for the C-IC and C-ID frames. In frames W1-IC and W2-IC the greatest values of MIDR were observed in the first and second stories. The MIDR profile linearly declined through the upper stories of these two frames (Figure 7.18a). The WBF designed for soil class D on the other hand showed an almost constant MIDR profile in stories one through three, while MIDR4 was lower for both W1-ID and W2-ID frames (Figure 7.18b).

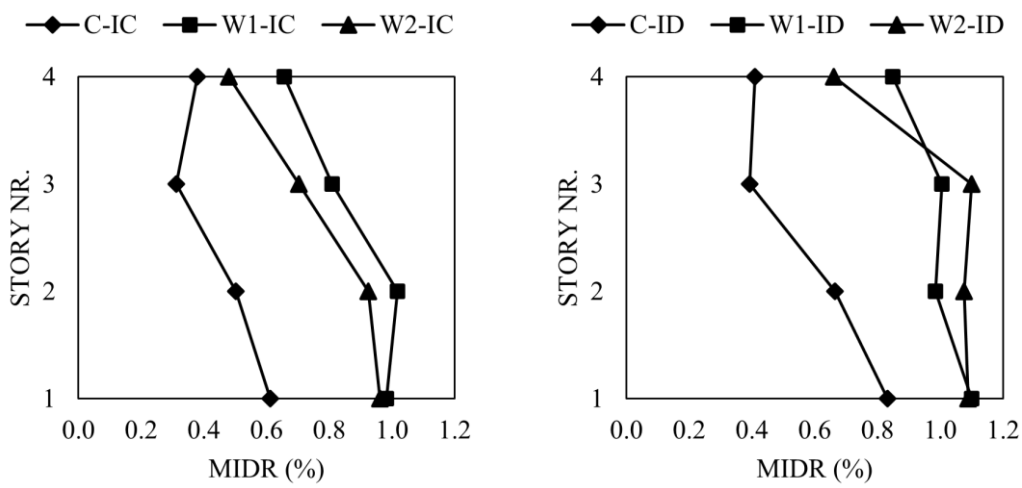

(a) IC (b) ID

Figure 7.18: MIDR profiles for the irregular frames

While the MIDR profiles can be affected by the story stiffness and therefore the sizing of the structural members, it was observed to better correlate with the plastic mechanisms that were shown in Figure 5.8 to Figure 5.14. The location of the maximum MIDR in the frames typically matched the location of the highest damage indicated by the formation of full plastic hinges. The formation of multiple story mechanisms observed in Figure 5.8 to Figure 5.14 also matched the location of higher and almost constant MIDR values in the WBF. The MIDR profiles of the irregular frames were more affected by the change in story stiffness than the MIDR profiles of the regular frames, since alongside reduction of the size of columns, the number of columns in the upper floors of the irregular frames was also reduced. This caused a considerable change in stiffness among the stories, and therefore relatively higher MIDR were observed in the fourth stories.

7.3 Analysis of Variance

The variance of the results of the time-history analyses between the sets is small as observed from the graphs of m_{GDR} and m_{IDR} in Figure 6.6, Figure 6.8, Figure 6.9, Figure 6.10, Figure 6.11, Figure 6.12, Figure 6.13, Figure 6.14, Figure 6.15, and Figure 6.16. Upon examination of the CoV plots shown in Figure 6.7, as well as in Appendix C, it was observed that the variance was independent of the frames, therefore was related to the random nature of the process that was used to select the ground motion records for the sets.

Therefore, it could be possible to consider the data obtained from each of the analysis sets as part of a larger population, containing 330 datapoints, instead of 30 datapoints for each frame. To test this hypothesis, one-way ANOVA was performed for all demand parameters that were evaluated, GDR and MIDRs. The critical F for this hypothesis is 1.505. Table 7.4 summarizes the F parameter for all the demand sets for all the frames. All the values presented in Table 7.4 are less than the critical F=1.505; therefore, the statistical parameters of the samples were considered representative of the statistical parameters of the respective population. Thus, for each frame, the results obtained from each set are not significantly different, and all the result sets can be grouped into a larger data pool that can be considered a single population. For each

frame GDR demands form populations with 330 data. Similarly, for each frame, each MIDR demands form populations with 330 data.

Table 7.4: The F parameter calculated from one-way ANOVA for the GDR and MIDR demand parameters for all the frames

Frame	**F-parameter** $F_{critical}$ **= 1.505**						
	GDR	**MIDR1**	**MIDR2**	**MIDR3**	**MIDR4**	**MIDR5**	**MIDR6**
C-4C4	0.195	0.218	0.268	0.516	0.604	-	-
W1-4C4	0.258	0.313	0.269	0.332	0.152	-	-
W2-4C4	0.277	0.320	0.292	0.255	0.174	-	-
C-4C2	0.196	0.245	0.243	0.152	0.189	-	-
W1-4C2	0.184	0.235	0.161	0.172	0.180	-	-
W2-4C2	0.245	0.293	0.245	0.306	0.129	-	-
C-4C6	0.170	0.208	0.211	0.128	0.176	-	-
W1-4C6	0.260	0.466	0.293	0.211	0.127	-	-
W2-4C6	0.161	0.266	0.170	0.145	0.174	-	-
C-6C4	0.200	0.309	0.247	0.134	0.156	0.278	0.381
W1-6C4	0.287	0.526	0.346	0.278	0.260	0.249	0.097
W2-6C4	0.311	0.558	0.417	0.289	0.269	0.212	0.289
C-IC	0.087	0.123	0.122	0.161	0.117	-	-
W1-IC	0.222	0.311	0.269	0.142	0.239	-	-
W2-IC	0.219	0.241	0.247	0.108	0.258	-	-
C-4D4	0.120	0.167	0.127	0.187	0.225	-	-
W1-4D4	0.079	0.116	0.101	0.087	0.188	-	-
W2-4D4	0.151	0.158	0.128	0.170	0.273	-	-
C-4D2	0.086	0.138	0.118	0.096	0.131	-	-
W1-4D2	0.111	0.120	0.102	0.128	0.165	-	-
W2-4D2	0.112	0.165	0.115	0.118	0.200	-	-
C-4D6	0.098	0.161	0.128	0.146	0.481	-	-
W1-4D6	0.096	0.134	0.087	0.095	0.156	-	-
W2-4D6	0.084	0.200	0.066	0.079	0.207	-	-
C-6D4	0.229	0.283	0.244	0.142	0.121	0.258	0.437
W1-6D4	0.168	0.264	0.163	0.141	0.108	0.096	0.156
W2-6D4	0.195	0.306	0.209	0.186	0.130	0.122	0.246
C-ID	0.088	0.118	0.114	0.121	0.208	-	-
W1-ID	0.098	0.107	0.091	0.144	0.322	-	-
W2-ID	0.081	0.109	0.095	0.131	0.179	-	-

7.4 Probabilistic Assessment of Demand

Based on the ANOVA analysis of the data obtained from the time-history analyses for each of the frames, it was concluded that it was appropriate to consider the populations containing the results of each individual time-history analysis (Δ_{max}/H) equivalent to the populations of the set means (m_{GDR}). The new sets containing 330 entries of Δ_{max}/H have the same mean as the sets containing 30 m_{GDR}, but the dispersion changes. Comparing the data from Table 7.3 and Table 7.5, it can be observed that while the mean μ_{GDR} is the same, the standard deviation and CoV vary significantly. The variance calculated using the population of 330 entries is higher.

Table 7.5: Distribution of 330 values of Δ_{max}/H (%) for frame C-4C4 and its mean (%), standard deviation and variance

μ_{GDR} (%)				0.475			
σ_{GDR}				0.499			
CoV				1.050			
				Δ_{max}/H			
0.152	0.694	0.060	0.303	0.291	0.882	0.582	0.727
0.329	0.303	0.514	0.079	0.329	0.280	0.388	0.199
0.401	0.482	0.291	0.198	0.319	0.408	0.061	0.976
1.134	0.607	0.754	0.656	0.065	0.082	0.731	0.052
0.084	0.088	0.221	0.722	0.468	0.071	0.141	0.414
0.676	0.343	0.287	0.530	0.379	2.455	0.071	0.693
0.731	0.782	0.548	0.075	0.361	0.214	0.060	0.842
0.615	0.488	0.119	0.359	0.726	0.046	0.359	0.653
0.374	0.319	0.069	0.326	0.104	0.803	0.537	0.531
0.669	0.205	0.284	0.709	1.411	0.494	0.374	0.547
0.273	0.143	0.238	0.169	0.664	0.638	0.759	0.381
0.706	0.453	0.167	0.248	0.097	0.588	0.457	0.328
0.513	0.081	0.494	0.268	0.109	0.603	2.455	0.217
0.971	0.569	0.715	0.096	0.585	1.101	0.081	0.094
0.504	0.077	0.341	0.828	0.066	0.055	0.403	0.298

Table 7.5 (continued)

Δ_{max}/H							
0.642	0.273	0.290	0.741	0.309	0.066	0.341	0.396
1.080	0.486	0.373	0.454	0.182	0.155	0.174	0.485
0.555	1.546	0.429	0.430	0.155	0.104	0.547	0.552
0.319	0.271	0.427	0.170	0.111	1.043	0.181	0.060
0.177	0.293	0.130	0.213	0.846	0.529	0.554	0.151
0.379	0.468	2.674	0.477	0.659	0.462	0.291	0.240
0.550	0.498	0.214	0.064	0.234	0.722	0.513	0.753
2.674	0.466	0.801	0.358	0.413	0.059	2.674	0.607
0.123	0.057	0.461	0.453	0.343	0.175	0.278	0.339
0.180	0.075	1.080	1.080	0.190	1.308	1.762	0.487
0.430	1.099	0.413	0.379	0.220	0.074	0.463	0.366
0.130	0.273	0.055	0.782	0.287	0.517	0.413	1.043
0.632	0.451	0.327	0.401	0.375	0.060	0.313	0.412
0.468	0.485	0.503	0.480	0.407	0.259	0.707	0.048
0.304	0.300	0.421	0.554	0.362	0.498	0.229	0.278
0.356	0.302	0.233	0.381	0.471	0.304	0.193	0.221
0.287	0.297	0.238	0.120	4.138	0.186	0.256	0.071
0.080	0.478	0.273	0.539	0.535	0.237	0.297	0.488
0.971	0.547	0.581	0.498	0.473	0.121	0.153	0.803
0.411	0.676	0.693	0.546	0.179	0.108	0.466	0.801
0.607	0.485	0.186	0.206	0.251	0.379	2.455	0.189
0.521	0.488	0.127	0.727	0.152	0.208	0.428	
0.443	0.233	0.448	0.499	2.455	0.412	0.189	
0.591	0.488	0.976	0.085	0.891	0.528	0.046	
0.549	0.250	0.232	0.269	0.272	0.137	0.753	
0.360	0.206	0.417	0.120	0.329	0.163	0.175	
0.393	4.138	0.243	0.374	0.143	0.430	0.428	

7.4.1 Probabilistic Fragility Functions of GDR

The fragility functions for GDR were computed again, this time using the full populations of 330 entries of Δ_{max}/H for each of the frames. The PNE for the performance levels were also computed using the new distributions as well, since the results are sensitive to the variance.

The fragility functions of the frames are shown in Figure 7.19, Figure 7.20, Figure 7.21, Figure 7.22 and Figure 7.23. In general, the CBF have steeper fragility functions than WBF. This means that for the same level of GDR, the PNE for the CBF is higher than the PNE of WBF.

The PNE for the performance levels of the frames with four stories and four bays were estimated from the fragility functions shown in Figure 7.19. The PNE for LD was calculated as 60.1%, 59.4% and 39.8% for frames C-4C4, W1-4C4 and W2-4C4 respectively, the PNE for CD was 100% for frame C-4C4 and 99.9% for frames W1-4C4 and W2-4C4, and CP was practically 100% for all three frames. The PNE for LD was calculated as 36.9%, 42.0% and 25.1% for frames C-4D4, W1-4D4 and W2-4D4 respectively, the PNE for CD was calculated as 97.3%, 100.0% and 99.9% for frames C-4D4, W1-4D4 and W2-4D4 respectively, and CP was 98.8% for frame C-4D4 and practically 100% for the other two frames.

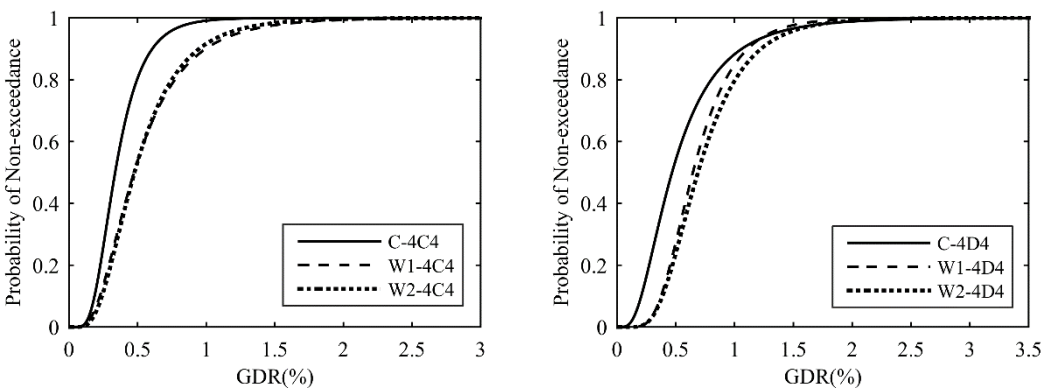

(a) 4C4 (b) 4D4

Figure 7.19: Fragility functions of regular frames with four stories and four bays based on the sets of Δ_{max}/H

The PNE for the performance levels of the frames with four stories and two bays were estimated from the fragility functions shown in Figure 7.20. The PNE for LD was calculated as 18.0%, 47.1% and 27.5% for frames C-4C2, W1-4C2 and W2-4C2 respectively, the PNE for CD was 100% for frames C-4C2 and W1-4C2 and 99.8% for frame W2-4C2, and CP was practically 100% for all three frames. The PNE for LD was calculated as 5.2%, 35.1% and 17.8% for frames C-4D2, W1-4D2 and W2-4D2 respectively, while the PNE for performance levels CD and CP was practically 100% for all three frames.

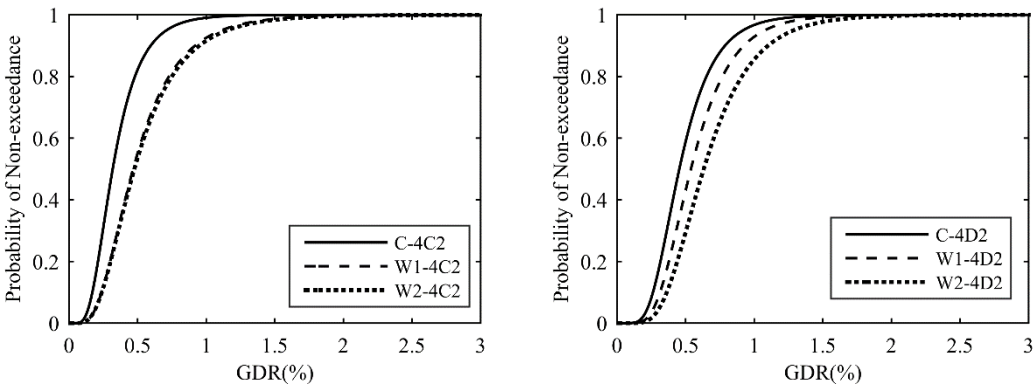

(a) 4C2 (b) 4D2

Figure 7.20: Fragility functions of regular frames with four stories and two bays based on the sets of Δ_{max}/H

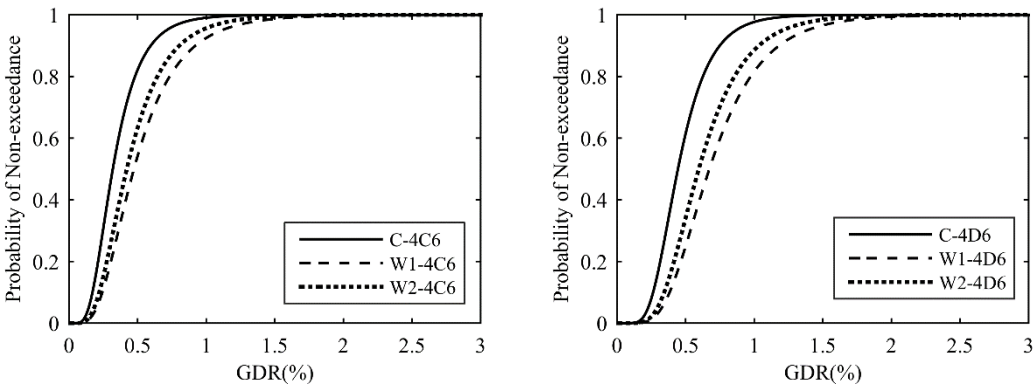

(a) 4C6 (b) 4D6

Figure 7.21: Fragility functions of regular frames with four stories and six bays based on the sets of Δ_{max}/H

The PNE for the performance levels of the frames with four stories and six bays were estimated from the fragility functions shown in Figure 7.21. The PNE for LD was calculated as 49.1%, 45.9% and 26.5% for frames C-4C6, W1-4C6 and W2-4C6 respectively, while the PNE for performance levels CD and CP was practically 100% for all three frames. The PNE for LD was calculated as 15.6%, 17.8% and 17.2% for frames C-4D6, W1-4D6 and W2-4D6 respectively, while the PNE for performance levels CD and CP was practically 100% for all three frames.

The PNE for the performance levels of the frames with six stories and four bays were estimated from the fragility functions shown in Figure 7.22. The PNE for LD was calculated as 51.9%, 56.1% and 55.8% for frames C-6C4, W1-6C4 and W2-6C4 respectively, the PNE for CD was 99.9% for frames C-6C4 and W1-6C4 and 100% for frame W2-6C4, and CP was practically 100% for all three frames. The PNE for LD was calculated as 19.7%, 33.4% and 37.2% for frames C-6D4, W1-6D4 and W2-6D4 respectively, the PNE for CD was calculated as 97.3% for frame C-6D4 and 100.0% frames W1-4D4 and W2-4D4, and CP was practically 100% for all three frames.

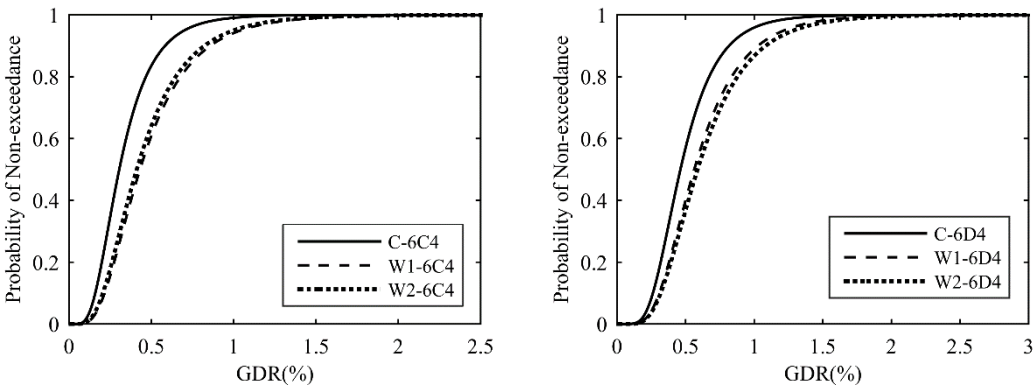

(a) 6C4 (b) 6D4

Figure 7.22: Fragility functions of regular frames with six stories and four bays based on the sets of Δ_{max}/H

The PNE for the performance levels of the irregular frames were estimated from the fragility functions shown in Figure 7.23. The PNE for LD was calculated as 48.1%, 46.5% and 50.0% for frames C-IC, W1- IC and W2- IC respectively, the PNE for CD was 100% for frames C- IC and W2-IC and 99.9% for frame W1- IC, while CP was

practically 100% for all three frames. The PNE for LD was calculated as 15.3%, 23.6% and 24.7% for frames C-ID, W1- ID and W2- ID respectively, the PNE for CD was calculated as 99.9% for frame C-ID and 100.0% for frames W1-ID and W2-ID, while CP was practically 100% for all three frames.

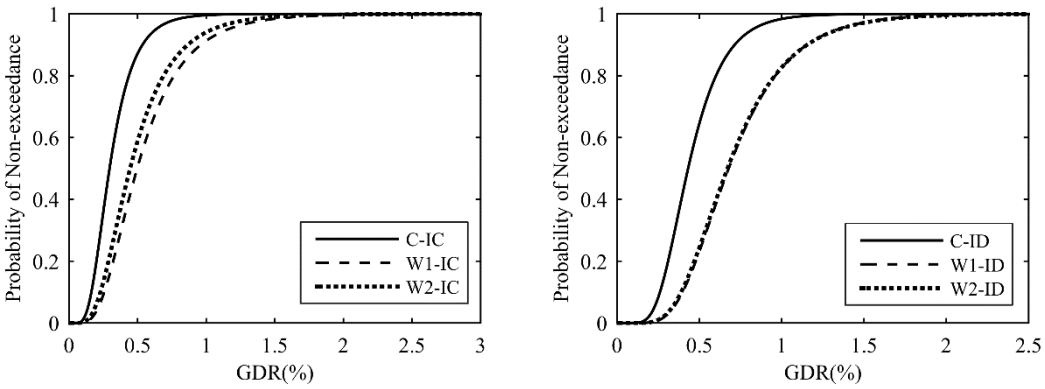

(a) IC (b) ID

Figure 7.23: Fragility functions of the irregular frames based on the sets of Δ_{max}/H

In general, it was observed that the frames designed for soil class C had higher values of PNE than the frames designed for soil class D, regardless of the elevation configuration. This means that the frames designed for soil class D are more likely to exceed the CD performance level than their soil class C counterparts. It was also noted that the PNE for the LD performance level calculated in this section are higher than the values of PNE calculated in Section 7.2.1 for the same frames. Based on the code-based approach it is almost certain that all the frames will exceed the CD performance threshold, while the likelyhood that this will happen are smaller based on probabilistic approach. In this aspect, the code-based approach provides more conservative estimations of the probabilities that each frame will exceed or not a certain performance level.

7.4.2 Demand vs. Capacity – Probabilistic Approach

Using the populations of Δ_{max}/H, the GDR ranges were computed, using the same procedure as in Section 7.2.2 for each of the frames. Figure 7.24 shows the comparison

of demand and capacity for the regular frames with four bays and four and six stories. From this graph it is obvious that the WBF have higher GDR capacities for CD and CP and even collapse than the CBF. The GDR ranges are also wider for the WBF than the CBF. Nonetheless, in all the four bay frames the GDR range falls within the CD damage level. Typically, the frames designed for soil class D have greater μ_{GDR} and GDR wider ranges, particularly the CBF. The difference is less pronounced in the case of the four bay WBF. W2 type frames have slightly higher μ_{GDR} and slightly wider GDR ranges than W1 type frames.

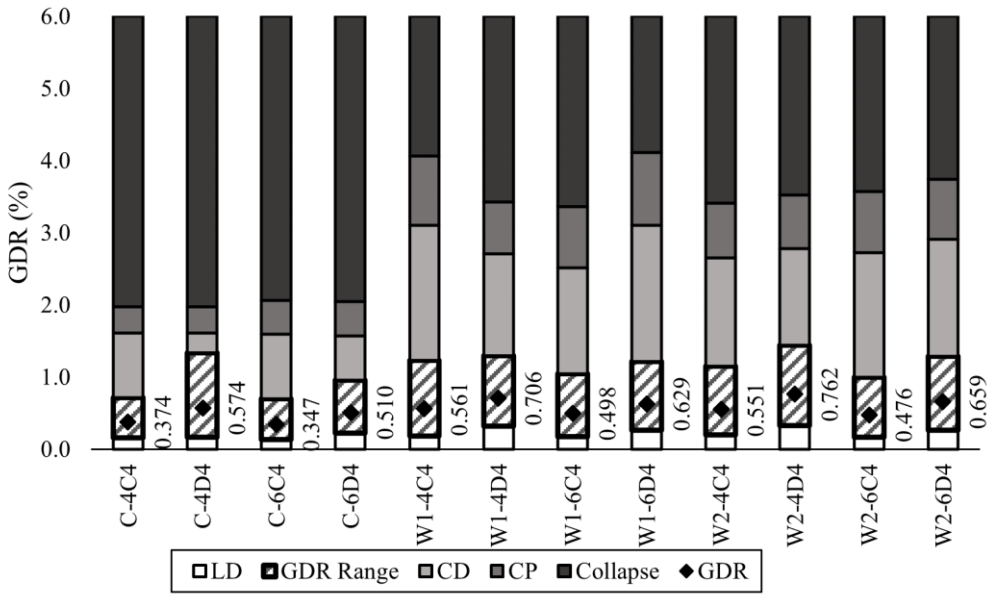

Figure 7.24: Demand vs. Capacity of the four bay and four and six story frames based on the sets of Δ_{max}/H

Figure 7.25 shows the comparison of demand and capacity for the regular frames with four stories and two and six bays. Again, the WBF have higher GDR capacities for CD and CP and even collapse than the CBF. The GDR ranges are also wider for the WBF than the CBF. However, the GDR range of 4C2, 4D2, 4C6 and 4D6 frames falls within the CD damage level. Similarly to the four bay frames, 4D2 and 4D6 frames have higher μ_{GDR} and wider GDR ranges than frames 4C2 and 4C6 respectively.

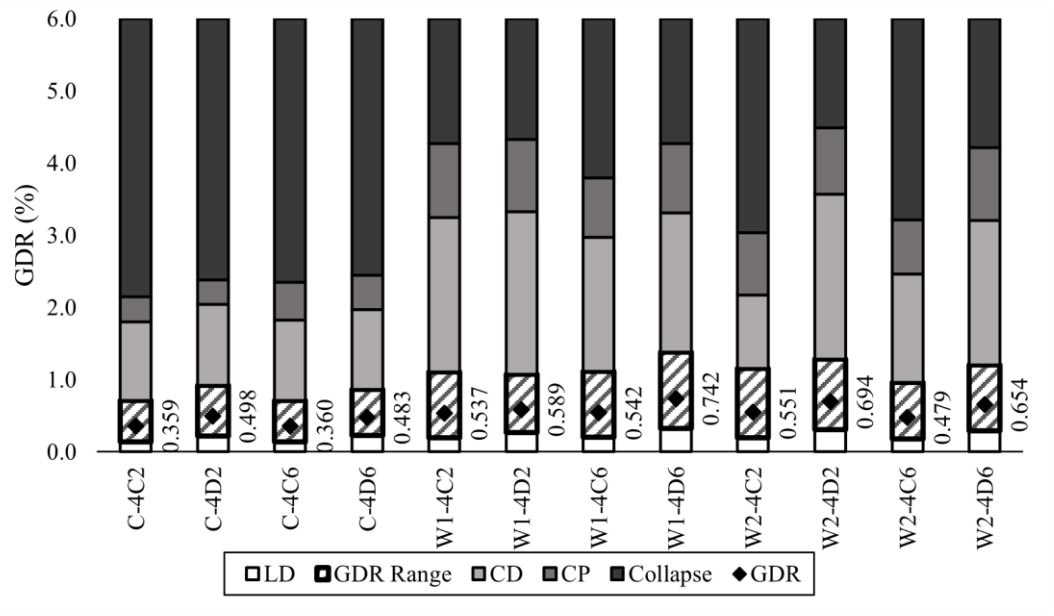

Figure 7.25: Demand vs. Capacity of the four story and two and six bay frames based on the sets of Δ_{max}/H

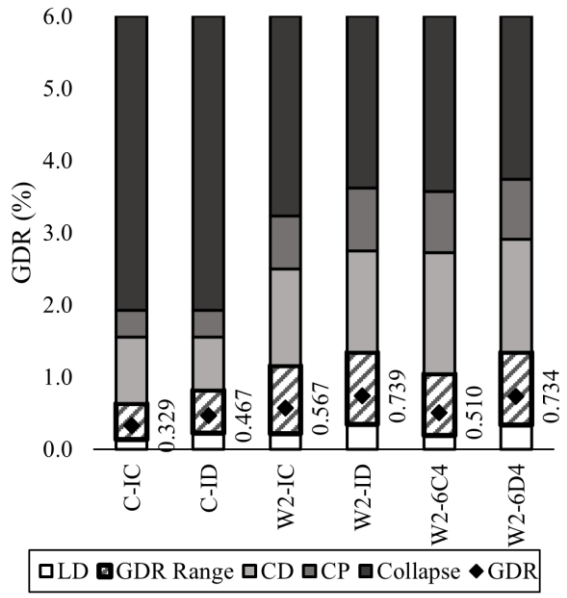

Figure 7.26: Demand vs. Capacity of the irregular frames based on the sets of Δ_{max}/H

Figure 7.26 shows the comparison of demand and capacity for the irregular frames IC and ID. It is obvious that the WBF have higher GDR capacities for CD and CP and even collapse than the CBF. The GDR ranges are also wider for the WBF than for the

CBF. Similarly, to the regular frames, the GDR range falls within the CD damage level. Again, the frames designed for soil class D have greater μ_{GDR} and GDR wider ranges, regardless of the type of beam.

It should be noted that while the use of sets of 330 entries of Δ_{max}/H does not affect the μ_{GDR}, the computed GDR ranges change considerably for all the frames. The GDR ranges computed using the probabilistic approach are wider than the ranges computed using the code-based approach. The probabilistic LB are smaller than the code-based LB, while the UB are greater. In overall, the GDR ranges computed using the probabilistic approach were also situated within the CD region for all the frames, CBF and WBF. Therefore, it can be stated with a 90% confidence level that the performance of all the frames is CD. This is the performance level mandated by TBEC for residential construction. While parameters such as soil class, number of stories and bays, and beam type affected the values of μ_{GDR} and GDR ranges, they did not affect the overall performance of the frames.

7.5 Analyzing 4D4 Frames for Higher Seismic Hazard

The fragility functions of the GDR show that the WBF presented in this thesis are highly likely to display the performance expected by design. Their mechanisms are satisfactory, and the comparison of GDR ranges to the damage regions shows a code-compliant behavior. Therefore, the following question is posed:

What would happen if the WBF designed as LD class for a maximum SDC of 3 (S_{DS}=0.5) were to be subjected to seismic hazard of SDC2 (S_{DS}=0.75)?

To answer this question, some of the frames that were analyzed previously, were subjected to new sets of ground motion records, that were compatible with the response spectrum for SDC2. Since it was observed that the number of stories and bays had very little effect on the results of the time-history analyses, the four story and four bay frames were selected for these analyses. Generally, frames designed for soil class D displayed higher displacement demand, therefore frames 4D4 were used in this section.

The target spectrum used to select the sets of ground motion records for these analyses is shown in Figure 7.27. The spectrum used to select the ground motion records for SDC3 was added for reference. The results of the time-history analyses were also presented together with the results obtained when the same frames were subjected to the design seismic hazard, for sake of comparison. The frames C-4D4, W1-4D4 and W2-4D4 were renamed as C-SDC2, W1-SDC2 and W2-SDC2 to avoid confusion, and to denote that they were subjected to seismic hazard corresponding to the target spectrum generated for SDC2.

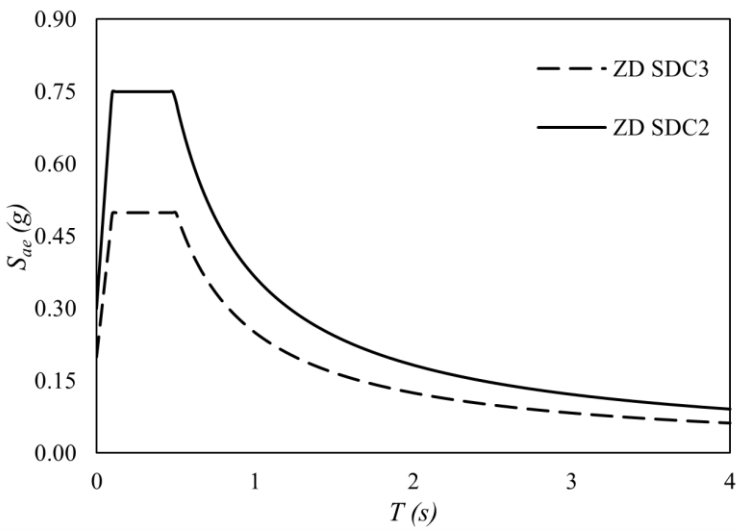

Figure 7.27: Elastic target spectra for soil class D and SDC 2 and 3 used for the selection of the ground motion records sets

7.5.1 Set-Based Results

The 4D4 frames were subjected to time-history analyses using sets of ground motion records compatible with the response spectrum for SDC2. The GDR set means (m_{GDR}) for these frames are shown in Figure 7.28, together with the results obtained previously for SDC3. When the 4D4 frames were subjected to higher-than-design seismic hazard, the obtained displacement demands were also considerably higher. The WBF experienced higher displacement demand than the CBF in both cases.

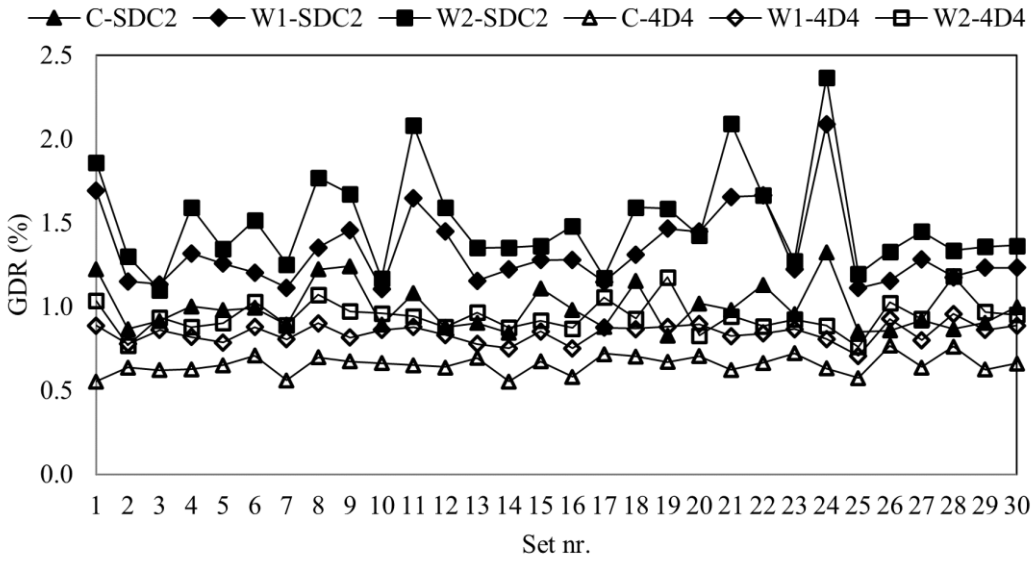

Figure 7.28: Set-to-set variation of m_{GDR} for frames 4D4, analyzed for seismic hazards SDC2 and SDC3

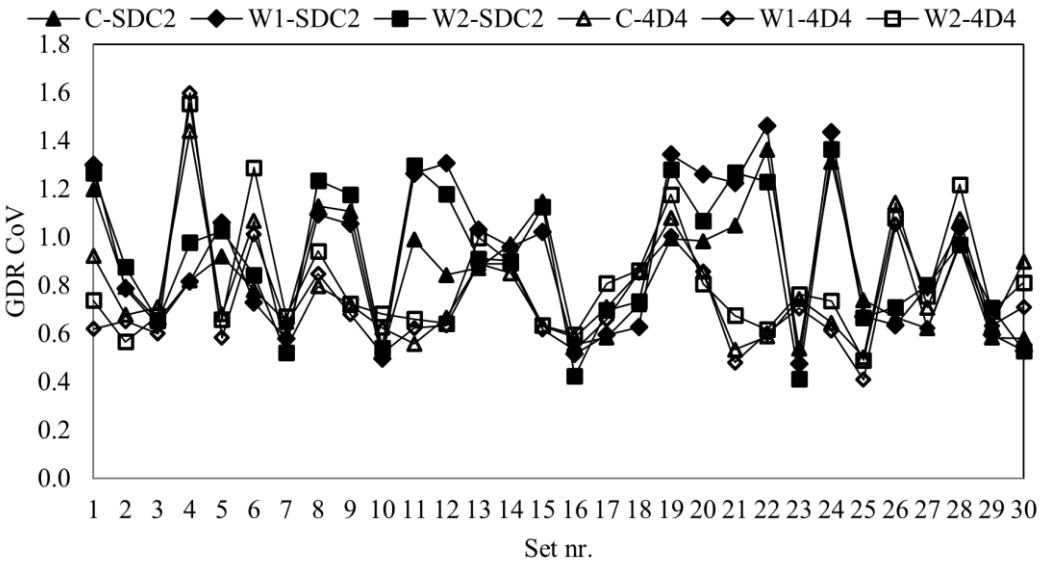

Figure 7.29: Set-to-set CoV of m_{GDR} for frames 4D4, analyzed for seismic hazards SDC2 and SDC3

The values of CoV for each set are shown in Figure 7.29. There are no clear distinctions between the values of CoV for the frames subjected to the same sets of ground motion records, both for records compatible with the SDC2 and SDC3 spectra.

The variance is therefore independent of the frames and almost entirely related to the variance of the ground motion records within sets and random nature of the selection of these sets. The IDR were also computed but are not presented here in detail.

The mean GDR and IDR calculated from all 30 sets of ground motion records μ_{GDR} are presented in Table 7.6. The increase in seismic hazard caused an increase of approximately 50% in μ_{GDR} but the set variance was not considerably affected. The WBF displayed higher μ_{GDR}.

Table 7.6: Displacement demand μ_{GDR} and its variance calculated for frames 4D4 subjected to seismic hazard SDC2 and SDC3

Frame	μ_{GDR} **(%)**	**GDR CoV**
C-4D4	0.655	0.324
W1-4D4	0.841	0.272
W2-4D4	0.945	0.250
C-SDC2	0.990	0.136
W1-SDC2	1.333	0.167
W2-SDC2	1.501	0.194

7.5.2 Code-Based Approach for Fragility Functions and Demand vs. Capacity

The fragility functions were generated for the frames analyzed for SDC2 using the code-based approach that was explained in Section 7.2.1 and are shown in Figure 7.30. Frame C-SDC2 has steeper curve than the WBF. From these functions, the PNE of the performance levels were also computed. The PNE for LD is 0% for all three frames. The PNE for CD are 99.3%, 100% and 99.9% for frames C-SDC2, W1-SDC2 and W2-SDC2 respectively. Finally, the PNE for CP is 100% for all three frames. From these values it can be stated that while all the frames will certainly exceed the LD threshold, they are unlikely to reach any of the limits of the other two performance levels.

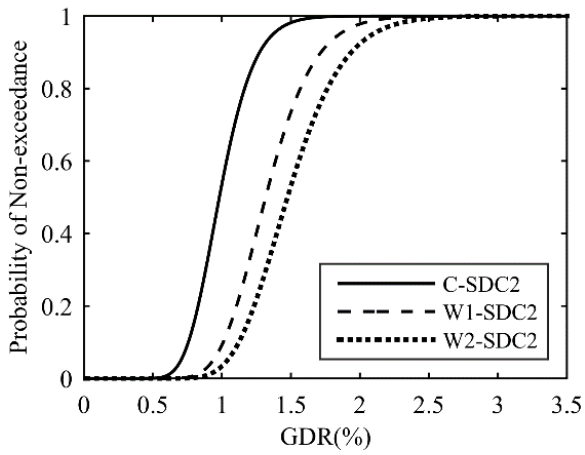

Figure 7.30: Fragility functions of the frames analyzed for SDC2 seismic hazard based on the sets of m_{GDR}

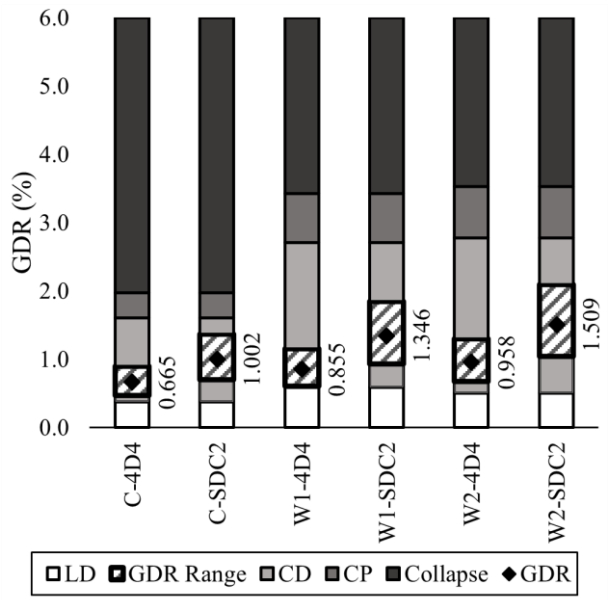

Figure 7.31: Demand vs. Capacity of the frames analyzed for SDC2 seismic hazard based on the sets of m_{GDR}

Using the distributions of m_{GDR} the LB,UB and GDR ranges were computed for a 90% confidence level. Figure 7.31 shows the comparison of the demand expressed as μ_{GDR} and GDR range to the capacity expressed as the performance regions. The results of the frames 4D4 that were previously shown in Figure 7.11 were also added for comparison. The frames that were subjected to ground motion records compatible with

the SDC2 spectrum display higher μ_{GDR} and wider GDR ranges. The WBF display higher μ_{GDR} and wider GDR ranges than the CBF as well. However, both μ_{GDR} and the GDR ranges are within the CD performance region. Therefore, the 4D4 frames that were designed for seismic hazard SDC3 but were analyzed for seismic hazard SDC2 still displayed code-conforming performance.

7.5.3 Probabilistic Approach for Fragility Functions and Demand vs. Capacity

The fragility functions were generated for the frames analyzed for SDC2 using the probabilistic approach that was explained in Section 7.4.1 as well and are shown in Figure 7.32. Frame C-SDC2 has steeper curve than the WBF. From these functions, the PNE of the performance levels were also computed. The PNE for LD are 9.4%, 18.4% and 9.2% for frames C-SDC2, W1-SDC2 and W2-SDC2 respectively. The PNE for CD are 96.2%, 98.9% and 98.0% for frames C-SDC2, W1-SDC2 and W2-SDC2 respectively. Finally, the PNE for CP are 98.7%, 99.7% and 99.4% for frames C-SDC2, W1-SDC2 and W2-SDC2 respectively. From these values it can be stated that while all the frames will certainly exceed the LD threshold, they are unlikely to reach any of the limits of the other two performance levels.

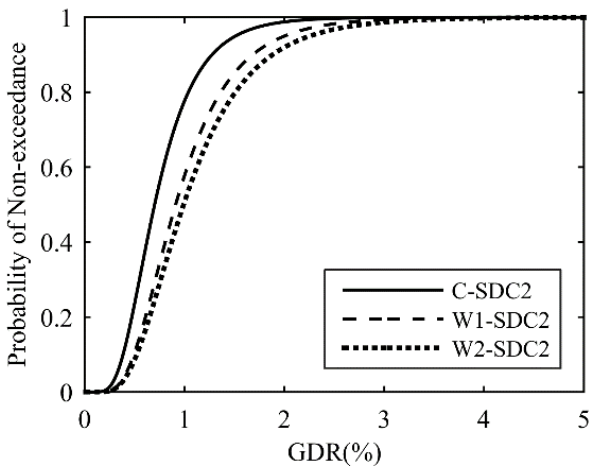

Figure 7.32: Fragility functions of the frames analyzed for SDC2 seismic hazard based on the sets of Δ_{max}/H

The comparison of the demand and capacity is shown in Figure 7.33. The GDR ranges of the frames subjected to SDC2 seismic hazard and computed using the sets of 330 values of Δ_{max}/H are considerably wider than their SDC3 counterparts. The μ_{GDR} and GDR ranges of the WBF are also considerably larger than those of the CBF. However, the whole GDR ranges are within the CD performance region, therefore the performance of the 4D4 frames that were designed for SDC3 but analyzed for SDC2 still displayed the code-required CD performance.

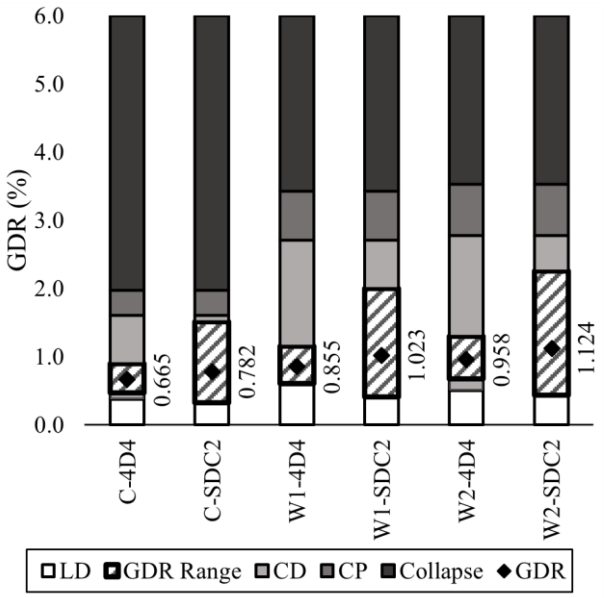

Figure 7.33: Demand vs. Capacity of the frames analyzed for SDC2 seismic hazard based on the sets of Δ_{max}/H

7.5.4 Interstory Drift Ratio Profiles

The interstory drift ratio profiles were previously generated for the 4D4 frames and shown in Figure 7.14b. Figure 7.34 presents both the previously plotted MIDR profiles and the MIDR profiles of the 4D4 frames when subjected to seismic hazard of SDC2. Similar markers were used for the frames, the difference being the MIDR profiles of frames analyzed for SDC3 hazard are shown in dotted lines, while their counterparts analyzed for SDC2 are shown in solid lines. This was done to help observe the effect of the seismic hazard level on the MIDR profiles.

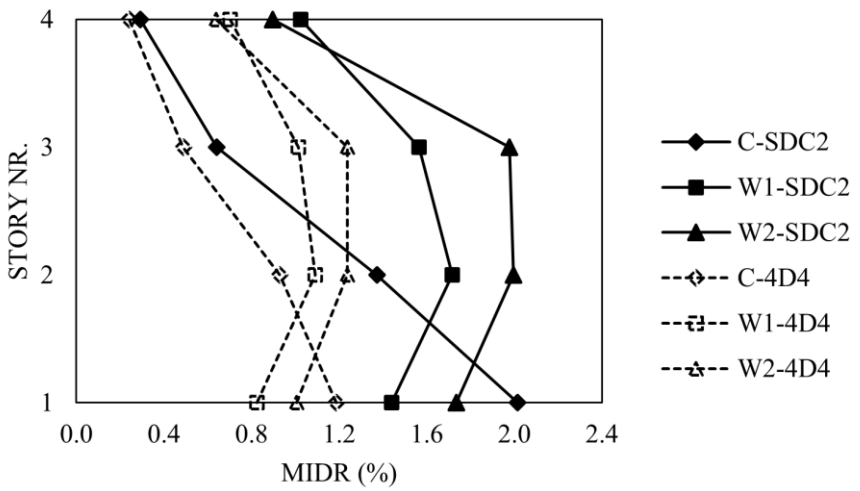

Figure 7.34: MIDR profiles for the 4D4 frames derived for SDC2 and SDC3

SDC2 amplified the values of MIDR but did not change the shape of the MIDR profiles for the 4D4 frames. On both cases, the highest MIDR for the CBF is MIDR1, while the WBF reach the highest MIDR at the second and third stories. In Section 7.2.3 it was noted that the MIDR profiles were compatible with the plastic mechanisms observed from the pushover analyses. The higher seismic hazard only amplified the values of the MIDR without affecting the shape of the MIDR profiles, it can be stated that the similar plastic mechanisms were formed in frames C-SDC2, W1-SDC2 and W2-SDC2 as in frames C-4D4, W1-4D4 and W2-4D4 respectively.

7.6 Summary

In this chapter, the results obtained from the time-history analyses presented in the previous chapter were processed using two approaches, a code-based approach and a probabilistic approach. The code-based approach makes use of populations of demand parameters that are the mean values (m_{GDR} and m_{IDRi}) obtained from each set of time-history analyses. The population of each demand parameter for each frame contains 30 elements. The probabilistic approach makes use of populations of demand parameters that are obtained from each individual time-history analysis (Δ_{max}/H and δ_{max}/h). The population of each demand parameter for each frame contains 330 elements. Fragility functions were generated by using these populations as data sets

and focusing mostly on the GDR. The GDR ranges were also calculated for a desired confidence level (90%) and were compared to the performance regions obtained from the pushover analyses.

From these analyses it was observed that the WBF in general display higher values of demand (m_{GDR}) and wider GDR range than the CBF. This conclusion was consistent and independent of the number of stories, bays, soil class or computation approach. However, both m_{GDR} and GDR ranges were within the CD region for both CBF and WBF, therefore the performance of all the frames was CD. So, while the WBF are considerably more flexible than the CBF, they also have greater deformation capacities that make up for the excess flexibility without affecting the performance. The PNE for the LD obtained from the fragility functions were very small for all the frames, therefore all the analyzed frames were highly likely to exceed the LD threshold. On the other hand, the PNE for CD and CP was practically 100% for all the frames, therefore none of the frames is expected to exceed the limits of any of these regions.

No clear trend was observed when comparing frames based on the number of stories or bays, while the soil class affected the trends of the demand parameters in an expected form. The frames designed for soil class D displayed higher demand m_{GDR} and wider GDR ranges. Soil class D is softer than soil class C and its plateau of the response spectrum is longer. Therefore, the spectral accelerations that frames designed for soil class D were higher than the spectral accelerations that frames designed for soil class C. Since the sets of ground motion records are compatible with the response spectra, the frames designed for soil class D were expected to be subjected to higher accelerations than the frames designed for soil class C.

The probabilistic approach of data processing provided higher PNE for the LD performance level. So, the code-based approach is more conservative when assessing the PNE of LD. On the other hand, the GDR ranges obtained from the probabilistic approach are wider than those obtained from the code-based approach. In this case, using the GDR ranges obtained from the probabilistic approach yields more conservative results.

MIDR profiles were generated for all the frames that were analyzed. The most important observation from the MIDR profiles was that they were compatible with the plastic damages observed from the pushover analyses.

In the last part of this chapter the performance of the frames that were designed for SDC3 was assessed for a higher seismic hazard (SDC2). Since parameters such as number of stories, bays and soil class were assessed previously, only frames 4D4 were used for this part of the study. The frames 4D4 which had been previously analyzed using 30 sets of ground motion records compatible with the response spectrum of soil class D and SDC3, were subjected to time-history analyses using 30 sets of ground motion records compatible with the response spectrum of soil class D and SDC2. The fragility functions and the demand vs. capacity comparison were carried out using both code-based and probabilistic approaches for these frames.

The demand parameters of the frames when subjected to the higher seismic hazard were greater than the demand parameters calculated previously. The GDR ranges were also wider. However, the trends observed previously did not change. The WBF experienced larger m_{GDR} and GDR ranges than the CBF. The PNE of CD and CP regions were practically 100%, therefore frames 4D4 were not expected to exceed the CD limit even when subjected to higher seismic hazard than their design hazard. The GDR ranges were well within the CD region for frames C-SDC2, W1-SDC2 and W2-SDC2, so their performance level was CD. The fact that the SDC2 frames still displayed CD performance level means that the original frames have adequate overstrength. The MIDR profiles of the frames analyzed for SDC2 were similar to the original 4D4 frames, however the MIDR values were greater. This means that the damage mechanisms were not changed by the higher seismic hazard, and the frames still displayed the ductile mechanisms that were shown in Chapter 5, Section 5.5.

Chapter 8

Conclusions

This thesis has presented an analytical study on wide beam frames that are designed according to the requirements of the up-to-date seismic code of Turkey, TBEC. The thesis aims to address the main concerns that are associated with wide beam construction, such as excessive flexibility, limited ductility and energy dissipation capacity and this type of structures being unsuitable for construction in zone of high seismic risk. A considerable importance is given to the quantification of the displacement demand of wide beam frames. The wide beam frames were compared to conventional beam frames that were designed for similar geometry and loading conditions.

Two-dimensional frames were used throughout this study. Different elevation configurations were considered in order to obtain a varied sample of models. These included regular frames with different number of stories and different number of bays, and frames that were not simple and symmetric in elevation. The frame models were designed for two soil classes, C and D. Three beam type sections were considered as well, one conventional beam section type and two wide beam sections.

A series of analyses were carried out to answer the questions that were set in the scope of this work. Nonlinear static analyses were used to obtain insight into the load, deformation and energy dissipation capacity of the frames, as well as their damage mechanisms. Time-history analyses were used to obtain the displacement demands, using real ground motion records. Furthermore, the results of the time-history analyses were statistically processed to obtain the probabilities that various scenarios would take place or not. The last part of the study was based on FEMA P-58, which is deemed the next generation standard for seismic design and assessment.

Initially, the effect of the frame geometry was assessed. It was observed that:

- The number of bays does not affect the results of either pushover or time-history analyses in a significant or unexpected form.
- The number of floors somewhat affects both the capacity and demand, as well as story mechanisms. The frames with six stories display higher values of demand than the frames with four stories. Also, the six story frames display multistory mechanisms comprising more stories than the four story frames.
- The irregular frames displayed higher capacities than the regular and symmetric frames. This was particularly true for the irregular frames with conventional beams.
- Therefore, the geometry of the frames had a small and predictable impact on the performance and behavior of the frame models that were discussed in this thesis.

The effect of soil class was also assessed, and the following observations were made:

- The soil class affected both the capacity and seismic demand for all the frames.
- Frames designed for soil class D displayed higher capacities and greater displacement demands than the frames designed for soil class C.

The beam type was the most important parameter that was assessed during this study. The following observations were made:

- Typically frames with conventional beams displayed higher lateral load capacities, higher initial stiffness, lower displacement capacities and lower displacement demands than frames with wide beams.
- These were related to the larger inherent stiffness of the conventional beam frames.
- The wide beam frames on the other hand were more flexible, displayed higher displacement capacities and experience larger displacement demands.
- Wide beam frames also displayed higher energy capacities than the conventional beams frames, and more extended plastic mechanisms.
- Wide beam frames displayed favorable mechanisms and ductile behavior similar to the behavior of the conventional beam frames, even though the first ones were designed as limited ductility class, while the latter were designed as high ductility class.

- The ranges of the global drift ratio estimated for a 90% confidence factor were wider for the wide beam frames as well.
- The entire GDR range was within the Controlled Damage region for both conventional and wide beam frames.
- Regardless of the type of beam, the performance of all the frames was Controlled Damage, which is the performance level required by TBEC for residential construction.
- The code-based approach of the assessment of seismic demand gave more conservative results when the probabilities of non-exceedance were estimated for various damage levels, while the probabilistic approach gave more conservative results in the estimation of the GDR ranges.
- The GDR demand was estimated for all the frames. The mean GDR demand did not exceed 1% for any of the frames, whether it had wide or conventional beam.
- The interstory drift ratio profiles were generated using the IDR demands from time-history analyses. The largest MIDR in these profiles matched the observed location where most plastic damage had occurred from the pushover analyses.
- The type of wide beam used made the most significant difference in terms of capacity and behavior. Frames with beam type W1 displayed a slightly more ductile behavior than frames with beam type W2.
- If the column size is not limited, the use of narrower wide beams (type W1) can be beneficial in terms of ductility.
- If columns size is limited, wide beams of type W2 yield a satisfactory performance without compromising the safety of the structures.

An important observation that was made regarding the beam type, is that they form an integral part of the framing system, and considerably affect the strength and stiffness of the frames.

In the final part of this thesis, some of the frames were subjected to higher seismic hazard than their design seismic hazard. Since the effect of parameters such as geometry and soil conditions were previously assessed, the regular four story and four bay frames, designed for soil class D were used during this part of the study. The frames were designed for Seismic Design Class 3 (S_{DS}=0.5) but were subjected to

ground motion records compatible with a new spectrum generated for Seismic Design Class 2 (S_{DS}=0.75). The following observations were made:

- The displacement demand of the frames subjected to SDC2 hazard was greater than the displacement of the original frames by 50-60%.
- The GDR ranges were wider than the GDR ranges of the original frames.
- The same trends were observed in these frames as well. The wide beam frames experienced larger displacement demands than the conventional beam frame. The GDR ranges of the wide beam frames were wider than the GDR range of the conventional beam frame.
- However, both the conventional and the wide beam frames that were designed for SDC3 but subjected to SDC2 still remained in the Control Damage region, as required by TBEC.

The wide beam frames not only were capable to perform satisfactorily under the seismic hazard for which they were designed, but they could also withstand a seismic hazard higher than their design level. This conclusion does not infer that wide beam frames can be under designed and still perform satisfactorily. It rather should be taken as an indication that future code revisions may consider removing either the ductility limitations or the limitations of the seismic zone in which wide beam frames can be constructed. Since this part of the conclusion was based on the results of three frames only, more detailed study would be required and recommended in order to bring about such a change in code provisions.

References

[1] ACI 318. Building code requirements for structural concrete (ACI 318-08) and commentary. American Concrete Institute; 2008.

[2] European Committee for Standardization. Eurocode 2: Design of concrete structures-part 1-1: General rules and rules for buildings. The European Union Per Regulation; 2004.

[3] Augenti N, Cosenza E, Dolce M, Manfredi G, Masi A, Samela L. Performance of school buildings during the 2002 Molise, Italy, earthquake. Earthquake Spectra. 2004;20(S1):S257-S70.

[4] Goretti A, Di Pasquale G. Building inspection and damage data for the 2002 Molise, Italy, earthquake. Earthquake Spectra. 2004;20(S1):S167-S90.

[5] Alexander DE. The L'Aquila earthquake of 6 April 2009 and Italian Government policy on disaster response. Journal of Natural Resources Policy Research. 2010;2(4):325-42.

[6] Ricci P, De Luca F, Verderame GM. 6th April 2009 L'Aquila earthquake, Italy: reinforced concrete building performance. Bulletin of Earthquake Engineering. 2011;9(1):285-305.

[7] Verderame GM, Iervolino I, Ricci P. Report on the damages on buildings following the seismic event of 6th of April 2009 time 1: 32 (UTC)-L'Aquila M= 5.8, V1. 20. 2009.

[8] Formisano A. Seismic damage assessment of school buildings after 2012 Emilia Romagna earthquake. Ingegneria Sismica. 2012;29(2-3):72-86.

[9] Rossi L, Holtschoppen B, Butenweg C. Official data on the economic consequences of the 2012 Emilia-Romagna earthquake: a first analysis of database SFINGE. Bulletin of Earthquake Engineering. 2019;17(9):4855-84.

[10] Romão X, Costa A, Paupério E, Rodrigues H, Vicente R, Varum H, et al. Field observations and interpretation of the structural performance of constructions after the 11 May 2011 Lorca earthquake. Engineering Failure Analysis. 2013;34:670-92.

[11] Feriche M, Vidal F, Alguacil G, Navarro M, Aranda C. Vulnerabilidad y Daño en el Terremoto de Lorca de 2011.

[12] Hermanns L, Fraile A, Alarcón E, Álvarez R. Performance of buildings with masonry infill walls during the 2011 Lorca earthquake. Bulletin of Earthquake Engineering. 2014;12(5):1977-97.

[13] Buforn E, Pro C, Cesca S, Udías A, Del Fresno C. The 2010 Granada, Spain, deep earthquake. Bulletin of the Seismological Society of America. 2011;101(5):2418-30.

[14] Casado CL, Garrido J, Delgado J, Peláez JA, Henares J. HVSR estimation of site effects in Melilla (Spain) and the damage pattern from the 01/25/2016 Mw 6.3 Alborán Sea earthquake. Natural Hazards. 2018;93(1):153-67.

[15] Lekidis V, Karakostas C, Dimitriu P, Margaris B, Kalogeras I, Theodulidis N. The Aigio (Greece) seismic sequence of June 1995: seismological, strong motion data and effects of the earthquakes on structures. Journal of earthquake engineering. 1999;3(03):349-80.

[16] Decanini L, Liberatore L, Mollaioli F, De Sortis A. Estimation of near-source ground motion and seismic behaviour of RC framed structures damaged by the 1999 Athens earthquake. Journal of earthquake engineering. 2005;9(05):609-35.

[17] Kotsovos M, Pavlovic M. The 1999 Athens earthquake: causes of damage not predicted by structural design methods. Structural Engineer. 2001;79(15):23-9.

[18] Lekkas E, Carydis P, Skourtsos E, Mavroulis S, Andreadakis E, Antoniou V, et al., editors. Factors controlling the distribution of building damage in the traditional Vrissa settlement induced by the 2017 June 12, Mw 6.3 Lesvos (Northeastern Aegean Sea, Greece) earthquake. 8th International INQUA Meeting on Paleoseismology, Active Tectonics and Archeoseismology (PATA); 2017.

[19] Mavroulis S, Andreadakis E, Spyrou N-I, Antoniou V, Skourtsos E, Papadimitriou P, et al. UAV and GIS based rapid earthquake-induced building damage assessment and methodology for EMS-98 isoseismal map drawing: The June 12, 2017 Mw 6.3 Lesvos (Northeastern Aegean, Greece) earthquake. International Journal of Disaster Risk Reduction. 2019;37:101169.

[20] Papathanassiou G, Valkaniotis S, Pavlides S. The July 20, 2017 Bodrum-Kos, Aegean Sea Mw= 6.6 earthquake; preliminary field observations and image-based survey on a lateral spreading site. Soil Dynamics and Earthquake Engineering. 2019;116:668-80.

[21] Yalçıner A, Annunziato A, Papadopoulos G, Dogan G, Guler H, Cakir T, et al. The 20th July 2017 (22: 31 UTC) Bodrum-Kos Earthquake and Tsunami: Post Tsunami Field Survey Report. Online report at: http://usersmetuedutr/yalciner/july-21-2017-tsunami-report/Report-Field-Survey-of-July-20-2017-Bodrum-Kos-Tsunamipdf. 2017.

[22] Sucuoğlu H. The 1999 Kocaeli and Düzce-Turkey Earthquakes. Middle East Technical University. 2000.

[23] Sezen H, Whittaker AS, Elwood KJ, Mosalam KM. Performance of reinforced concrete buildings during the August 17, 1999 Kocaeli, Turkey earthquake, and seismic design and construction practise in Turkey. Engineering Structures. 2003;25(1):103-14.

[24] Ministy of Environment and Urban Planning DOND, Earthquake Research Department. Turkish Seismic Regulations for Structures to be Built in Seismic Regions 2007.

[25] Doğangün A. Performance of reinforced concrete buildings during the May 1, 2003 Bingöl Earthquake in Turkey. Engineering Structures. 2004;26(6):841-56.

[26] Calayır Y, Sayın E, Yön B. Performance of structures in the rural area during the March 8, 2010 Elazığ-Kovancılar earthquake. Natural hazards. 2012;61(2):703-17.

[27] Celep Z, Erken A, Taskin B, Ilki A. Failures of masonry and concrete buildings during the March 8, 2010 Kovancılar and Palu (Elazığ) earthquakes in Turkey. Engineering Failure Analysis. 2011;18(3):868-89.

[28] Tapan M, Comert M, Demir C, Sayan Y, Orakcal K, Ilki A. Failures of structures during the October 23, 2011 Tabanlı (Van) and November 9, 2011 Edremit (Van) earthquakes in Turkey. Engineering Failure Analysis. 2013;34:606-28.

[29] Ates S, Kahya V, Yurdakul M, Adanur S. Damages on reinforced concrete buildings due to consecutive earthquakes in Van. Soil Dynamics and Earthquake Engineering. 2013;53:109-18.

[30] Çelebi E, Aktas M, Çağlar N, Özocak A, Kutanis M, Mert N, et al. October 23, 2011 Turkey/Van–Ercis earthquake: structural damages in the residential buildings. Natural Hazards. 2013;65(3):2287-310.

[31] Bikçe M, Çelik TB. Failure analysis of newly constructed RC buildings designed according to 2007 Turkish Seismic Code during the October 23, 2011 Van earthquake. Engineering Failure Analysis. 2016;64:67-84.

[32] Yalvaç S. Determining the Effects of the 2020 Elazığ-Sivrice/Turkey (Mw 6.7) Earthquake from the Surrounding CORS-TR GNSS Stations. Turkish Journal of Geosciences.1(1):15-20.

[33] Eyidoğan H, Hobbs TE. Recovery Underway Following Damaging 24 January 2020 Elazığ Earthquake in Eastern Turkey, Temblor. 2020.

[34] K. Onder Cetin GM, Anastasios Sextos, Jonathan P. Stewart. Seismological and Engineering Effects of the M 7.0 Samos Island (Aegean Sea) Earthquake. 2020.

[35] Carydis P. The Tirana, Albania, earthquake of January 9, 1988. 1988.

[36] Papadopoulos GA, Agalos A, Carydis P, Lekkas E, Mavroulis S, Triantafyllou I. The 26 November 2019 Mw 6.4 Albania Destructive Earthquake. Seismological Research Letters. 2020.

[37] Duni L, Theodoulidis N. Short note on the November 26, 2019, Durres (Albania) M6. 4 earthquake: Strong ground motion with emphasis in Durres city. EMSC on Line Report Available online: https://wwwgooglecomhk/url. 2019.

[38] Vesho N, Marku A, Andrew C, editors. Structural engineering observations from the 26 November 2019 M6. 4 Albanian earthquake. NZSEE 2020 Webinar Series; 2020: New Zealand Society for Earthquake Engineering, PO Box 2193.

[39] Beck JL, Hall JF. Factors contributing to the catastrophe in Mexico City during the earthquake of September 19, 1985. Geophysical Research Letters. 1986;13(6):593-6.

[40] Villaverde R. Investigation on the cause of numerous upper floor failures during the 1985 Mexico City earthquake: Department of Engineering, University of California; 1989.

[41] Verde RV. Explanation for the numerous upper floor collapses during the 1985 Mexico City earthquake. Earthquake engineering & structural dynamics. 1991;20(3):223-41.

[42] Mitchell D, Tinawi R, Redwood RG. Damage to buildings due to the 1989 Loma Prieta earthquake—a Canadian code perspective. Canadian Journal of Civil Engineering. 1990;17(5):813-34.

[43] Kasai K, Maison BF. Building pounding damage during the 1989 Loma Prieta earthquake. Engineering structures. 1997;19(3):195-207.

[44] Jones L, Aki K, Boore D, Celebi M, Donnellan A, Hall J, et al. The magnitude-6.7 Northridge, California, earthquake of 17-January-1994. Science. 1994;266(5184):389-97.

[45] Mitchell D, Devall RH, Saatcioglu M, Simpson R, Tinawi R, Tremblay R. Damage to concrete structures due to the 1994 Northridge earthquake. Canadian Journal of Civil Engineering. 1995;22(2):361-77.

[46] Eberhard MO, Baldridge S, Marshall J, Mooney W, Rix GJ. The mw 7.0 Haiti earthquake of January 12, 2010: USGS/EERI advance reconnaissance team report. US Geological Survey Open-File Report. 2010;1048:58.

[47] Kato H, Tajiri S, Mukai T. Preliminary reconnaissance report of the Chile Earthquake 2010. Building Research Institute Japan. 2010.

[48] Bonelli P, Restrepo JI, Boroschek R, Carvallo JF, editors. The 2010 Great Chile Earthquake–Changes to Design Codes. Proceedings of the International Symposium on Engineering Lessons Learned from the 2011 Great East Japan Earthquake; 2012.

[49] Ingham JM, Griffith MC. The performance of unreinforced masonry buildings in the 2010/2011 Canterbury earthquake swarm. Report to the Royal Commission of Inquiry. 2011.

[50] Dhakal RP. Damage to non-structural components and contents in 2010 Darfield earthquake. Bulletin of the New Zealand Society for Earthquake Engineering. 2010;43(4):404-11.

[51] Kaiser A, Holden C, Beavan J, Beetham D, Benites R, Celentano A, et al. The Mw 6.2 Christchurch earthquake of February 2011: preliminary report. New Zealand journal of geology and geophysics. 2012;55(1):67-90.

[52] Dizhur D, Ingham J, Moon L, Griffith M, Schultz A, Senaldi I, et al. Performance of masonry buildings and churches in the 22 February 2011 Christchurch earthquake. Bulletin of the New Zealand Society for Earthquake Engineering. 2011;44(4):279-96.

[53] Kam WY, Pampanin S. The seismic performance of RC buildings in the 22 February 2011 Christchurch earthquake. Structural Concrete. 2011;12(4):223-33.

[54] Esteva L. Earthquake engineering research and practice in Mexico after the 1985 earthquakes. Bulletin of the New Zealand Society for Earthquake Engineering. 1987;20(3):159-200.

[55] Meli R, Avila J. The Mexico earthquake of September 19, 1985—Analysis of building response. Earthquake Spectra. 1989;5(1):1-17.

[56] Esteva L. The Mexico earthquake of September 19, 1985—Consequences, lessons, and impact on research and practice. Earthquake Spectra. 1988;4(3):413-26.

[57] Sordo E, Terán A, Guerrero J, Juárez H, Iglesias J. The Mexico Earthquake of September 19, 1985—Ductility and Resistance Requirements Imposed on a Concrete Building. Earthquake spectra. 1989;5(1):41-50.

[58] Scholl RE. Observations of the performance of buildings during the 1985 Mexico earthquake, and structural design implications. International Journal of Mining and Geological Engineering. 1989;7(1):69-99.

[59] Domínguez D, López-Almansa F, Benavent-Climent A. Would RC wide-beam buildings in Spain have survived Lorca earthquake (11-05-2011)? Engineering Structures. 2016;108:134-54.

[60] Ersin Arıoğlu KA, A. Ülkü Arıoğlu. Uluslararası Deprem Mühendisliği Açısından Önemli Bir Olgu ve Kayıp: “Güçlendirilmiş Adapazarı Vilayet Binası”. Tarihi Eserlerin Güçlendirilmesi ve Geleceğe Güvenle Devredilmesi Sempozyumu-1; Ankara2007. p. 241-53.

[61] Wenk T, editor The Adana-Ceyhan Earthquake of June 27, 1998: Report on the Reconnaissance Mission from July 6-12, 1998 of the Swiss Society of Earthquake Engineering and Structural Dynamics (SGEB). Reconnaissance Mission of the Swiss Society of Earthquake Engineering and Structural Dynamics; 1998: ETH Zurich.

[62] Malley JO, Celebi M, Bruneau M, Saaticioglu M, Erdik M, Gulkan P. Buildings. Earthquake Spectra. 1993;9(1):49-85.

[63] Başkanlığı AVaDY. Türkiye Bina Deprem Yönetmeliği - Deprem Etkisi Altında Binaların Tasarımı için Esaslar. Çevre, Şehircilik ve İklim Değişikliği Bakanlığı; 2018.

[64] NCSE. Real Decreto 997/2002, de 27 de septiembre, por el que se aprueba la norma de construcción sismorresistente: parte general y edificación (NCSR-02). Boletín Oficial del Estado; 2002.

[65] Minister of the Infrastructures. Norme tecniche per le Costruzioni. Decree of the Minister of the Infrastructures. 2008;14.

[66] Turkish Institute of Standard. TS 500 Design and Construction Guidelines for Reinforced Concrete Structures. 2000.

[67] Ministero delle Infrastrutture e dei Trasporti. Norme tecniche per le costruzioni. Ministero delle Infrastrutture e dei Trasporti; 2008.

[68] Bonacci J, Alcocer S, Cagley J, Lafave J, Paultre P, Criswell M, editors. Recommendations for Design of Beam–Column Connections in Monolithic Reinforced Concrete Structures. American Concrete Institute; 2002.

[69] Code P. Eurocode 8: Design of structures for earthquake resistance. Brussels: European Committee for Standardization; 2005.

[70] Standards NZ. Concrete structure standard-the design of concrete structures (NZS 3101: Part 1: 1995). SNZ Wellington; 1995.

[71] Code GS. EAK 2000. Technical Chamber of Greece, Greek Government Journal—FEK; 2000.

[72] Association CS. Design of concrete structures: Mississauga, Ont.: Canadian Standards Association; 2004.

[73] Hatamoto H, Bessho S, Matsuzaki Y. Reinforced concrete wide-beam-to-column subassemblages subjected to lateral load. Special Publication. 1991;123:291-316.

[74] Popov EP, Cohen JM, Koso-Thomas K, Kasai K. Behavior of interior narrow and wide beams. Structural Journal. 1992;89(6):607-16.

[75] Gentry TR, Wight JK. Wide beam-column connections under earthquake-type loading. Earthquake Spectra. 1994;10(4):675-703.

[76] Lafave JM, Wight JK. Reinforced concrete exterior wide beam-column-slab connections subjected to lateral earthquake loading. Structural Journal. 1999;96(4):577-85.

[77] Lafave JM, Wight JK. Reinforced concrete wide-beam construction vs. conventional construction: resistance to lateral earthquake loads. Earthquake Spectra. 2001;17(3):479-505.

[78] Quintero-Febres CG, Wight JK. Experimental study of reinforced concrete interior wide beam-column connections subjected to lateral loading. Structural Journal. 2001;98(4):572-82.

[79] Lafave JM. Behavior and design of reinforced concrete beam-column connections with wide beams. Structures 2001: A Structural Engineering Odyssey2001. p. 1-2.

[80] Stehle J, Abdouka K, Goldsworthy H, Mendis P. The seismic performance of reinforced concrete frames with wide band beams. WIT Transactions on The Built Environment. 1998;41.

[81] Stehle JS, Abdouka K, Goldsworthy H, Mendis P, editors. The seismic performance of reinforced concrete wide band beam construction. Twelfth World Conference on Earthquake Engineering; 2000.

[82] Stehle JS, Goldsworthy H, Mendis P. Reinforced Concrete interior wide-band beam-column connections subjected to lateral earthquake loading. Structural Journal. 2001;98(3):270-9.

[83] Siah W, Stehle J, Mendis P, Goldsworthy H. Interior wide beam connections subjected to lateral earthquake loading. Engineering structures. 2003;25(3):281-91.

[84] Goldsworthy HM, Abdouka K. Displacement-based assessment of non ductile exterior wide band beam-column connections. Journal of Earthquake Engineering. 2012;16(1):61-82.

[85] Kulkarni SA, Li B. Seismic behavior of reinforced concrete interior wide-beam column joints. Journal of Earthquake Engineering. 2008;13(1):80-99.

[86] Li B, Kulkarni SA. Seismic behavior of reinforced concrete exterior wide beam-column joints. Journal of structural engineering. 2010;136(1):26-36.

[87] Masi A, Santarsiero G, Mossucca A, Nigro D. Seismic behaviour of RC beam-column subassemblages with flat beam. Proceedings of XV Convegno della Associazione Nazionale Italiana di Ingegneria Sismica, ANIDIS Padova, Italy. 2013.

[88] Masi A, Santarsiero G, editors. Seismic tests on RC building exterior joints with wide beams. Advanced Materials Research; 2013: Trans Tech Publ.

[89] Benavent-Climent A. Seismic behavior of RC wide beam-column connections under dynamic loading. Journal of earthquake engineering. 2007;11(4):493-511.

[90] Benavent-Climent A, Cahís X, Vico J. Interior wide beam-column connections in existing RC frames subjected to lateral earthquake loading. Bulletin of Earthquake Engineering. 2010;8(2):401-20.

[91] Benavent-Climent A, Cahís X, Zahran R. Exterior wide beam–column connections in existing RC frames subjected to lateral earthquake loads. Engineering Structures. 2009;31(7):1414-24.

[92] Elsouri A, Harajli M. Interior RC wide beam-narrow column joints: Potential for improving seismic resistance. Engineering structures. 2015;99:42-55.

[93] Elsouri AM, Harajli MH. Seismic response of exterior RC wide beam–narrow column joints: Earthquake-resistant versus as-built joints. Engineering Structures. 2013;57:394-405.

[94] Fadwa I, Ali TA, Nazih E, Sara M. Reinforced concrete wide and conventional beam–column connections subjected to lateral load. Engineering Structures. 2014;76:34-48.

[95] Mirzabagheri S, Tasnimi AA. Reinforced concrete roof exterior wide and conventional beam–column joints under lateral load. The Structural Design of Tall and Special Buildings. 2016;25(9):397-411.

[96] Mirzabagheri S, Tasnimi AA, Issa F. Experimental and numerical study of reinforced concrete interior wide beam-column joints subjected to lateral load. Canadian Journal of Civil Engineering. 2018;45(11):947-57.

[97] Pakzad A, Khanmohammadi M. Experimental cyclic behavior of code-conforming exterior wide beam-column connections. Engineering Structures. 2020;214:110613.

[98] Huang RY, Kuang J, Behnam H. Cyclic behaviour of wide beam-column joints with shear strength ratios of 1.0 and 1.7. International Journal of Civil and Environmental Engineering. 2017;11(4):399-405.

[99] Behnam H, Kuang J, Huang RY. Exterior RC wide beam-column connections: Effect of beam width ratio on seismic behaviour. Engineering Structures. 2017;147:27-44.

[100] Behnam H, Kuang J. Exterior RC wide beam–column connections: effect of spandrel beam on seismic behavior. Journal of Structural Engineering. 2018;144(4):04018013.

[101] Huang RY, Kuang JS, Behnam H. Shear strength of exterior wide beam-column joints with different beam reinforcement ratios. Journal of Earthquake Engineering. 2018:1-23.

[102] Serna-Ros P, Fernandez-Prada M, Miguel-Sosa P, Debb O. Influence of stirrup distribution and support width on the shear strength of reinforced concrete wide beams. Magazine of concrete research. 2002;54(3):181-91.

[103] Shuraim AB. Transverse stirrup configurations in RC wide shallow beams supported on narrow columns. Journal of Structural Engineering. 2012;138(3):416-24.

[104] Donaire-Avila J, Benavent-Climent A, Escobedo A, Oliver-Saiz E, Ramírez-Márquez A, Feriche M, editors. Damage assessment on building structures subjected to the recent near-fault earthquake in Lorca (Spain). 15 World Conference on Earthquake Engineering Lisbon, Portugal; 2012.

[105] Benavent-Climent A, Escobedo A, Donaire-Avila J, Oliver-Saiz E, Ramírez-Márquez AL. Assessment of expected damage on buildings subjected to Lorca earthquake through an energy-based seismic index method and nonlinear dynamic response analyses. Bulletin of Earthquake Engineering. 2013;12(5):2049-73.

[106] López-Almansa F, Domínguez D, Benavent-Climent A. Vulnerability analysis of RC buildings with wide beams located in moderate seismicity regions. Engineering Structures. 2013;46:687-702.

[107] Domínguez D, López-Almansa F, Benavent Climent A. Comportamiento, para el terremoto de Lorca de 11-05-2011, de edificios de vigas planas proyectados sin tener en cuenta la acción sísmica. 2014.

[108] Vielma JC, Barbat AH, Oller S. Seismic safety of low ductility structures used in Spain. Bulletin of Earthquake Engineering. 2009;8(1):135-55.

[109] Gómez-Martínez F, Verderame GM, De Luca F, Pérez-García A, Alonso-Durá A. High ductility seismic performances of wide-beam RC frames. XVI Convegno ANIDIS September. 2015:13-7.

[110] Gómez-Martínez F, Alonso-Durá A, De Luca F, Verderame GM. Seismic performances and behaviour factor of wide-beam and deep-beam RC frames. Engineering Structures. 2016;125:107-23.

[111] Gómez-Martínez F, Alonso-Durá A, De Luca F, Verderame GM. Ductility of wide-beam RC frames as lateral resisting system. Bulletin of Earthquake Engineering. 2016;14(6):1545-69.

[112] Dönmez C. Seismic Performance of Wide-Beam Infill-Joist Block RC Frames in Turkey. Journal of Performance of Constructed Facilities. 2015;29(1):04014026.

[113] Afad. Turkish Earthquake Hazard Map (in Turkish) 2018

[114] Council IC. International Building Code. Cengage Learning; 2009.

[115] Lubkowski Z, Aluisi B, editors. Deriving Ss and S1 parameters from PGA maps. Proc 15th world conference earthquake engineering Lisboa, Portugal; 2012.

[116] Zaslavsky Y, Rabinovich M, Perelman N, Avirav V. Seismic hazard maps in terms of spectral acceleration at periods of 0.2 sec and 1 sec for the design response spectrum (two-point method) in the new version of the Israel building code (SI 413). The National Steering Committee for Earthquake Preparedness, Report. 2009(522/474):09.

[117] Booth E. The estimation of peak ground-motion parameters from spectral ordinates. Journal of Earthquake Engineering. 2007;11(1):13-32.

[118] Standartları T. TS498 Yapı Elemanlarının Boyutlandırılmasında Alınacak Yüklerin Hesap Değerleri. Türk Standartları Enstitüsü.

[119] Bal İE, Crowley H, Pinho R, Gülay FG. Detailed assessment of structural characteristics of Turkish RC building stock for loss assessment models. Soil Dynamics and Earthquake Engineering. 2008;28(10-11):914-32.

[120] Structures CA. SAP2000, V. 20.0.0 CSI analysis reference manual. Berkeley, California; 2017.

[121] Mander JB, Priestley MJ, Park R. Theoretical stress-strain model for confined concrete. Journal of structural engineering. 1988;114(8):1804-26.

[122] Chadwell C, Imbsen R. XTRACT: A tool for axial force-ultimate curvature interactions. Structures 2004: Building on the past, securing the future2004. p. 1-9.

[123] Paulay T, Priestley MN. Seismic design of reinforced concrete and masonry buildings. 1992.

[124] Takeda T, Sozen MA, Nielsen NN. Reinforced concrete response to simulated earthquakes. Journal of the structural division. 1970;96(12):2557-73.

[125] Al-Chaar G, Issa M, Sweeney S. Behavior of masonry-infilled nonductile reinforced concrete frames. Journal of Structural Engineering. 2002;128(8):1055-63.

[126] Lee HS, Woo SW. Effect of masonry infills on seismic performance of a 3-storey R/C frame with non-seismic detailing. Earthquake engineering & structural dynamics. 2002;31(2):353-78.

[127] Dolšek M, Fajfar P. Soft storey effects in uniformly infilled reinforced concrete frames. Journal of Earthquake Engineering. 2001;5(01):1-12.

[128] Yuen YP, Kuang J. Nonlinear seismic responses and lateral force transfer mechanisms of RC frames with different infill configurations. Engineering Structures. 2015;91:125-40.

[129] Uva G, Porco F, Fiore A. Appraisal of masonry infill walls effect in the seismic response of RC framed buildings: A case study. Engineering Structures. 2012;34:514-26.

[130] Jalaeefar A, Zargar A, editors. Effect of infill walls on behavior of reinforced concrete special moment frames under seismic sequences. Structures; 2020: Elsevier.

[131] Su L, Shi J. Displacement-based earthquake loss assessment methodology for RC frames infilled with masonry panels. Engineering structures. 2013;48:430-41.

[132] Dolšek M, Fajfar P. The effect of masonry infills on the seismic response of a four-storey reinforced concrete frame—a deterministic assessment. Engineering Structures. 2008;30(7):1991-2001.

[133] Panagiotakos T, Fardis M, editors. Seismic response of infilled RC frames structures. 11th world conference on earthquake engineering; 1996.

[134] Bertoldi S, Decanini L, Gavarini C. Telai tamponati soggetti ad azioni sismiche, un modello semplificato: confronto sperimentale e numerico. Atti del. 1993;6:815-24.

[135] Uva G, Raffaele D, Porco F, Fiore A. On the role of equivalent strut models in the seismic assessment of infilled RC buildings. Engineering Structures. 2012;42:83-94.

[136] Žarnić R, Gostič S. Masonry infilled frames as an effective structural sub-assemblage: Routledge; 2019.

[137] Dolšek M, Fajfar P. Simplified non-linear seismic analysis of infilled reinforced concrete frames. Earthquake engineering & structural dynamics. 2005;34(1):49-66.

[138] Park R, Paulay T. Reinforced concrete structures: John Wiley & Sons; 1975.

[139] Priestley MN, Seible F, Calvi GM. Seismic design and retrofit of bridges: John Wiley & Sons; 1996.

[140] Inel M, Ozmen HB. Effects of plastic hinge properties in nonlinear analysis of reinforced concrete buildings. Engineering structures. 2006;28(11):1494-502.

[141] Committee ASSRS. Seismic rehabilitation of existing buildings (ASCE/SEI 41-06). American Society of Civil Engineers; 2007.

[142] Council BSS. Prestandard and commentary for the seismic rehabilitation of buildings. Report FEMA-356, Washington, DC. 2000.

[143] Akkar S, Sucuoğlu H, Yakut A. Displacement-based fragility functions for low- and mid-rise ordinary concrete buildings. Earthquake Spectra. 2005;21(4):901-27.

[144] Zarfam P, Mofid M. On the modal incremental dynamic analysis of reinforced concrete structures, using a trilinear idealization model. Engineering Structures. 2011;33(4):1117-22.

[145] Chopra AK. Dynamics of structures: theory and applications to earthquake engineering: Prentice-Hall; 2001.

[146] Shome N. Probabilistic seismic demand analysis of nonlinear structures: Stanford University; 1999.

[147] Council AT. FEMA P-58: Seismic Performance Assessment of Buildings: Vol. 1–Methodology. Federal Emergency Management Agency; 2012.

[148] Reyes JC, Kalkan E. How many records should be used in an ASCE/SEI-7 ground motion scaling procedure? Earthquake Spectra. 2012;28(3):1223-42.

[149] Mehmet Palanci AHK, Ahmet Demir. A statistical assessment on global drift ratio demands of mid-rise RC buildings using code-compatible real ground motion records. Bulletin of Earthquake Engineering. 2018.

[150] Huang Y, Whittaker A, Luco N. Performance Assessment of Conventional and Base-Isolated Nuclear Power Plants for Earthquake and Blast Loadings. MCEER Report 08-0019. Multidisciplinary Center for Earthquake Engineering Research, University at Buffalo, State University of New, Buffalo, NY. 2008.

[151] Ambraseys N, Smit P, Douglas J, Margaris B, Sigbjörnsson R, Olafsson S, et al. Internet site for European strong-motion data. Bollettino di geofisica teorica ed applicata. 2004;45(3):113-29.

[152] Akkar S, Sandıkkaya M, Şenyurt M, Sisi AA, Ay B, Traversa P, et al. Reference database for seismic ground-motion in Europe (RESORCE). Bulletin of earthquake engineering. 2014;12(1):311-39.

[153] Ancheta TD, Darragh RB, Stewart JP, Seyhan E, Silva WJ, Chiou BS-J, et al. NGA-West2 database. Earthquake Spectra. 2014;30(3):989-1005.

[154] Kayhan AH. Scaled and unscaled ground motion sets for uni-directional and bi-directional dynamic analysis. Earthquakes and Structures. 2016;10(3):563-88.

[155] Kayhan AH. Selection and scaling of ground motion records using harmony search. Teknik Dergi. 2012;23(1):5751-75.

[156] Hamburger R, Rojahn C, Heintz J, Mahoney M, editors. FEMA P58: Next-generation building seismic performance assessment methodology. 15th world conference on earthquake engineering; 2012.

[157] Hamburger RO. FEMA P-58-Next-generation performance assessment of buildings. AEI 2011: Building Integration Solutions2011. p. 211-8.

[158] Heintz JA. The Horizon For Next-Generation Performance Assessment Of Buildings Is Here: FEMA P-58.

[159] Vielma J, Angulo C, Díaz K, Prado A, Gutiérrez J, Pannillo G, et al. SEISMIC ASSESSMENT OF EDUCATIONAL BUILDINGS ACCORDING TO FEMA P-58.

[160] Yekrangnia M, Bakhshi A, Ghannad MA, Panahi M. Risk assessment of confined unreinforced masonry buildings based on FEMA P-58 methodology: a case study—school buildings in Tehran. Bulletin of Earthquake Engineering. 2021;19(2):1079-120.

[161] Zeng X, Lu X, Yang T, Xu Z. Application of the FEMA-P58 methodology for regional earthquake loss prediction. Natural Hazards. 2016;83(1):177-92.

[162] Cardone D, Perrone G. Damage and loss assessment of pre-70 RC frame buildings with FEMA P-58. Journal of Earthquake Engineering. 2017;21(1):23-61.

[163] Du K, Bai W, Bai J, Yan D, Gong M, Sun J. Comparative Seismic Performance Assessment of Reinforced Concrete Frame Structures with and without Structural Enhancements Using the FEMA P-58 Methodology. ASCE-ASME Journal of Risk and Uncertainty in Engineering Systems, Part A: Civil Engineering. 2021;7(4):04021047.

[164] Cook D, Fitzgerald K, Chrupalo T, Haselton C. Comparison of FEMA P-58 with other building seismic risk assessment methods. Chico, California, available at: http://static-setshbrisk.com/reports/RiskAssessmentComparisonReport_FEMA-P-58-to-OtherMethods_2017_03_08 pdf. 2017.

[165] Jalayer F, Iervolino I, Manfredi G. Structural modeling uncertainties and their influence on seismic assessment of existing RC structures. Structural safety. 2010;32(3):220-8.

[166] Celarec D, Dolšek M. The impact of modelling uncertainties on the seismic performance assessment of reinforced concrete frame buildings. Engineering Structures. 2013;52:340-54.

Appendices

Appendix A
Loading and Geometric Details of the Frame Models

In this appendix the figures presenting the loading and geometric details of the all the frames are given. In Section A1 the distribution of the gravity loads is presented. In Sections A2 to A4 the section sizes and reinforcement details of the frame members are presented.

A.1 Gravity load details

The gravity load distribution on the frame models is presented graphically in the figures from Figure A.1 to Figure A.10. Three types of gravity loads were applied on the frame models, the weight of the structure itself, including coating layers, the weight of the infill walls and the live loads, denoted as g, g_w and q respectively. These load distributions are based on the values of g, g_w and q, given in Chapter 3, and the slab load distribution shown in Figure 3.11, Figure 3.12, Figure 3.13, Figure 3.14, Figure 3.17, Figure 3.18, Figure 3.19, and Figure 3.20.

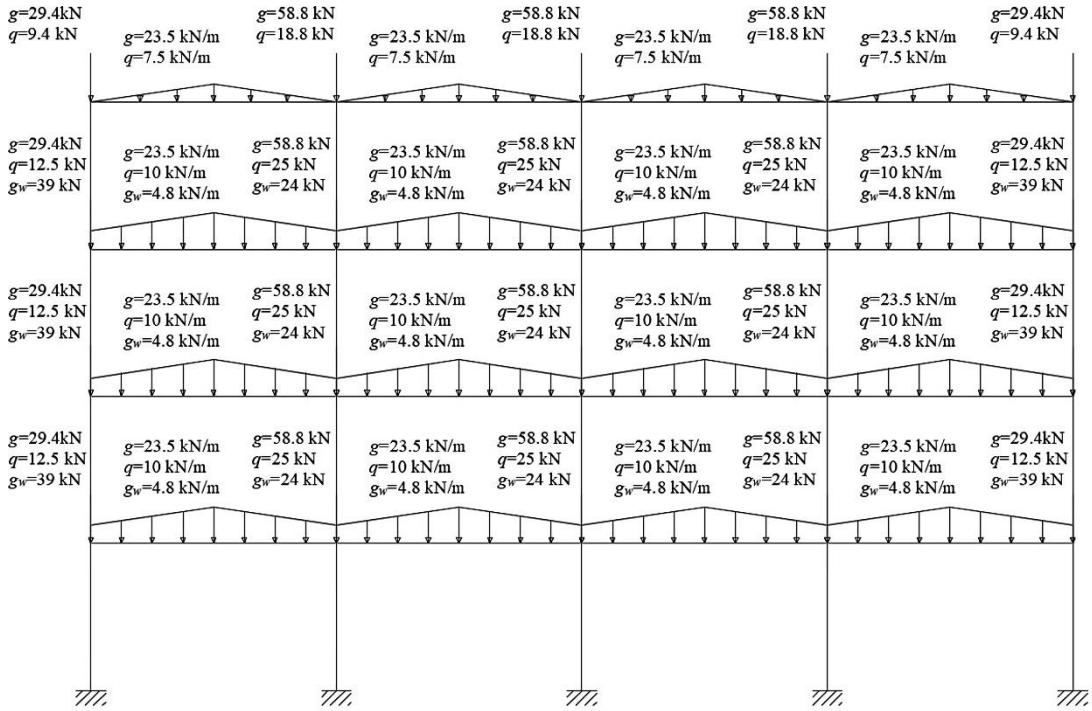

Figure A.1: Gravity load configuration of regular frames with 4 stories and 4 bays and conventional beams

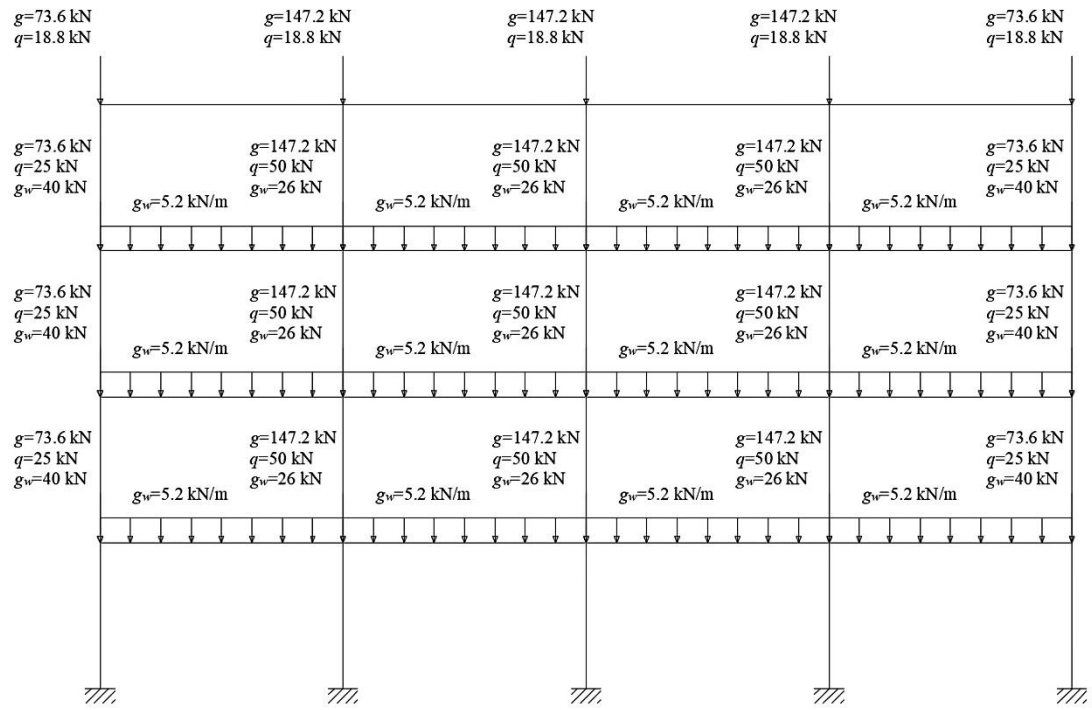

Figure A.2: Gravity load configuration of regular frames with 4 stories and 4 bays and wide beams

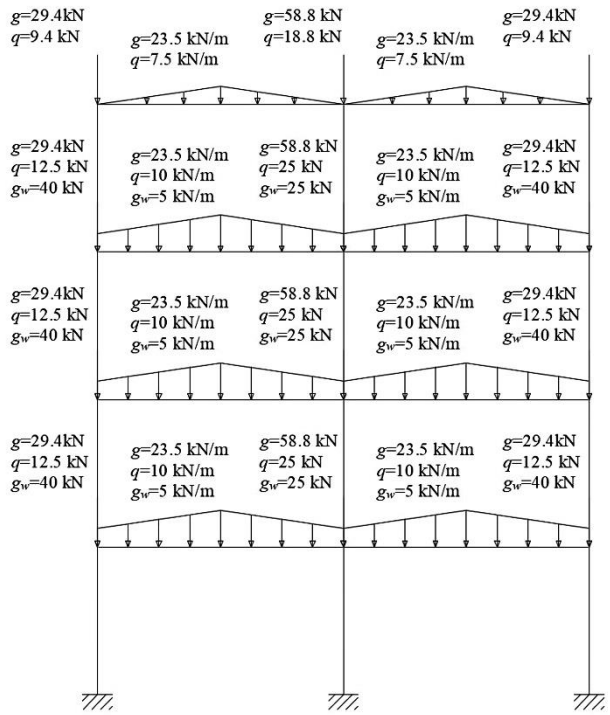

Figure A.3: Gravity load configuration of regular frames with 4 stories and 2 bays and conventional beams

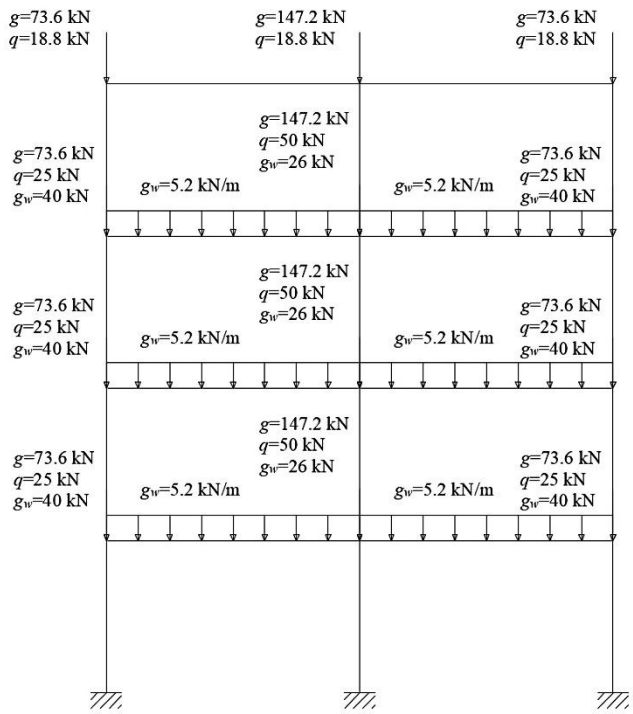

Figure A.4: Gravity load configuration of regular frames with 4 stories and 2 bays and wide beams

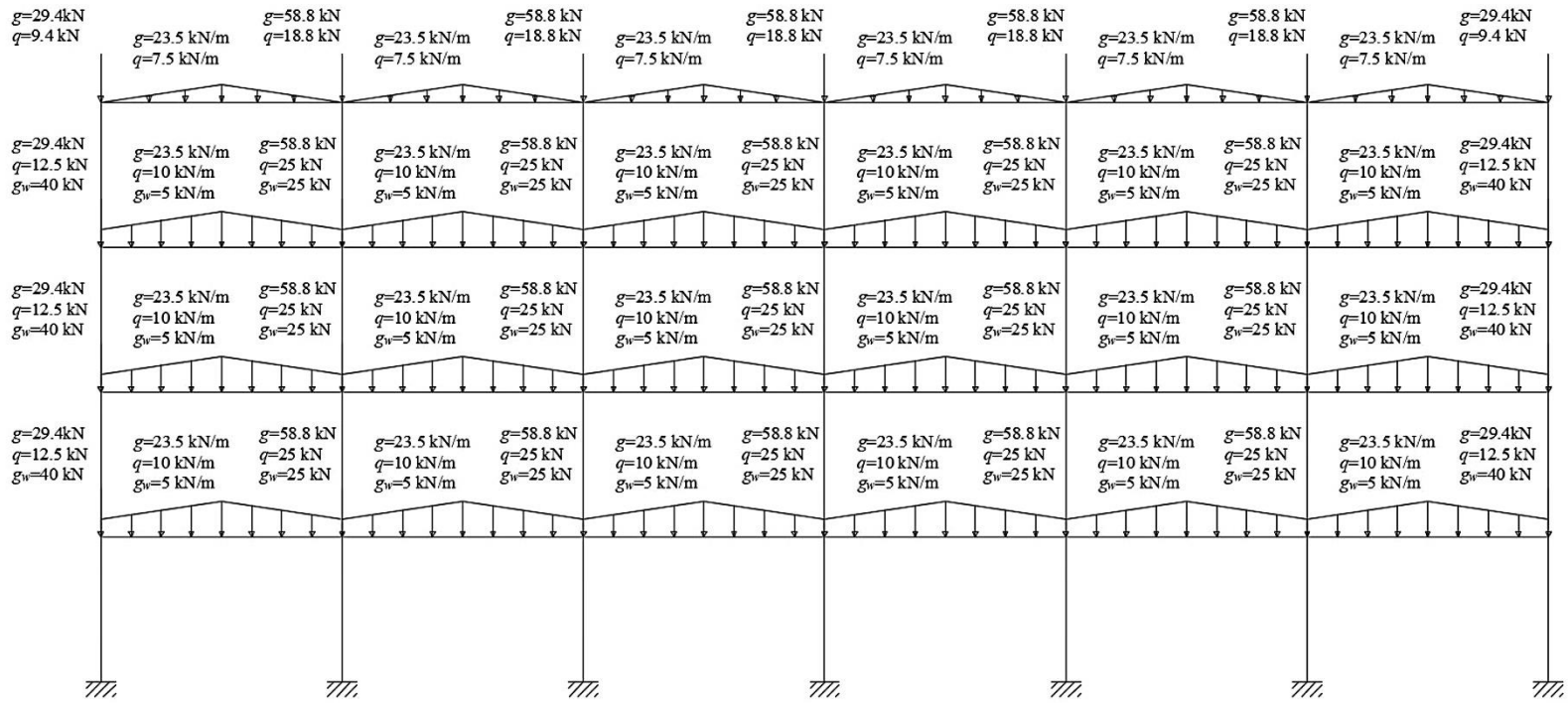

Figure A.5: Gravity load configuration of regular frames with 4 stories and 6 bays and conventional beams

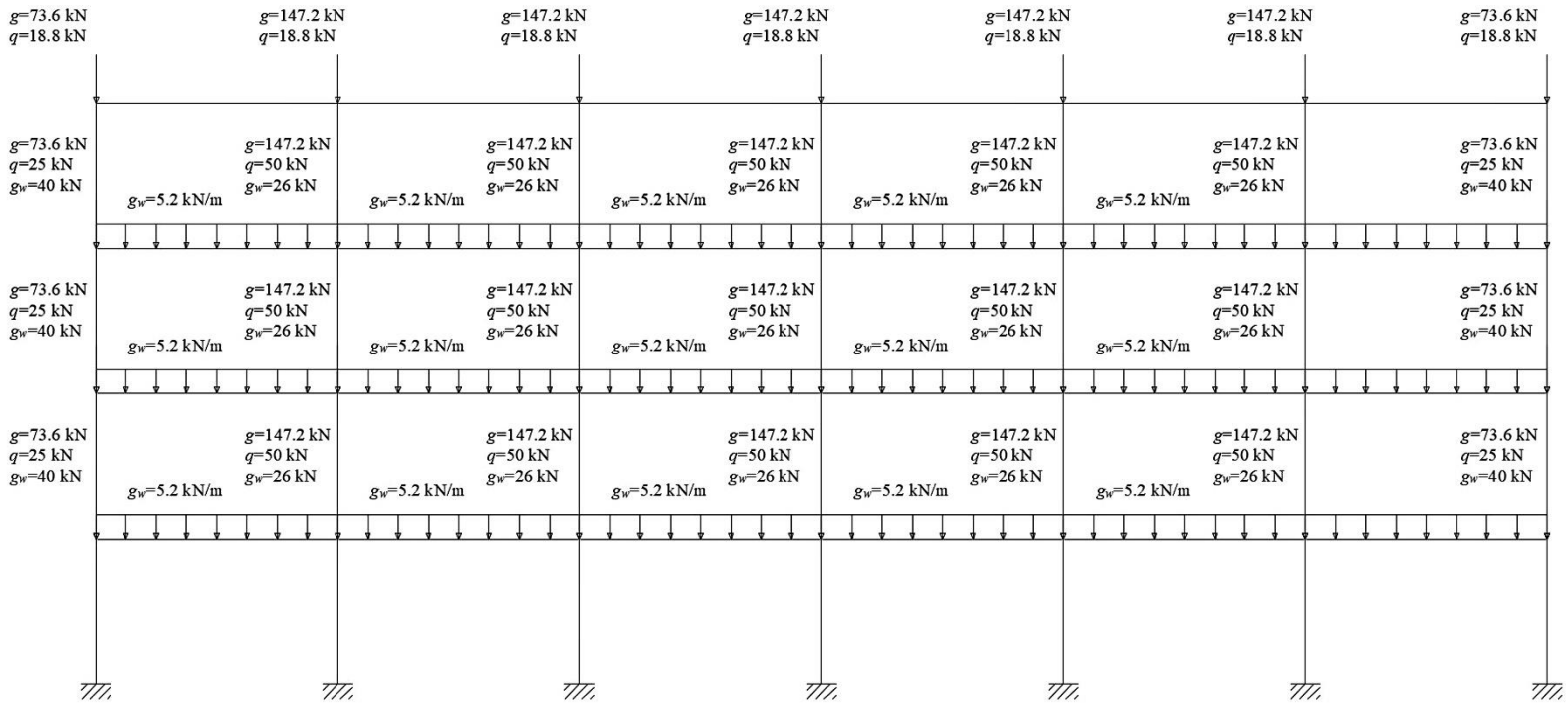

Figure A.6: Gravity load configuration of regular frames with 4 stories and 6 bays and wide beams

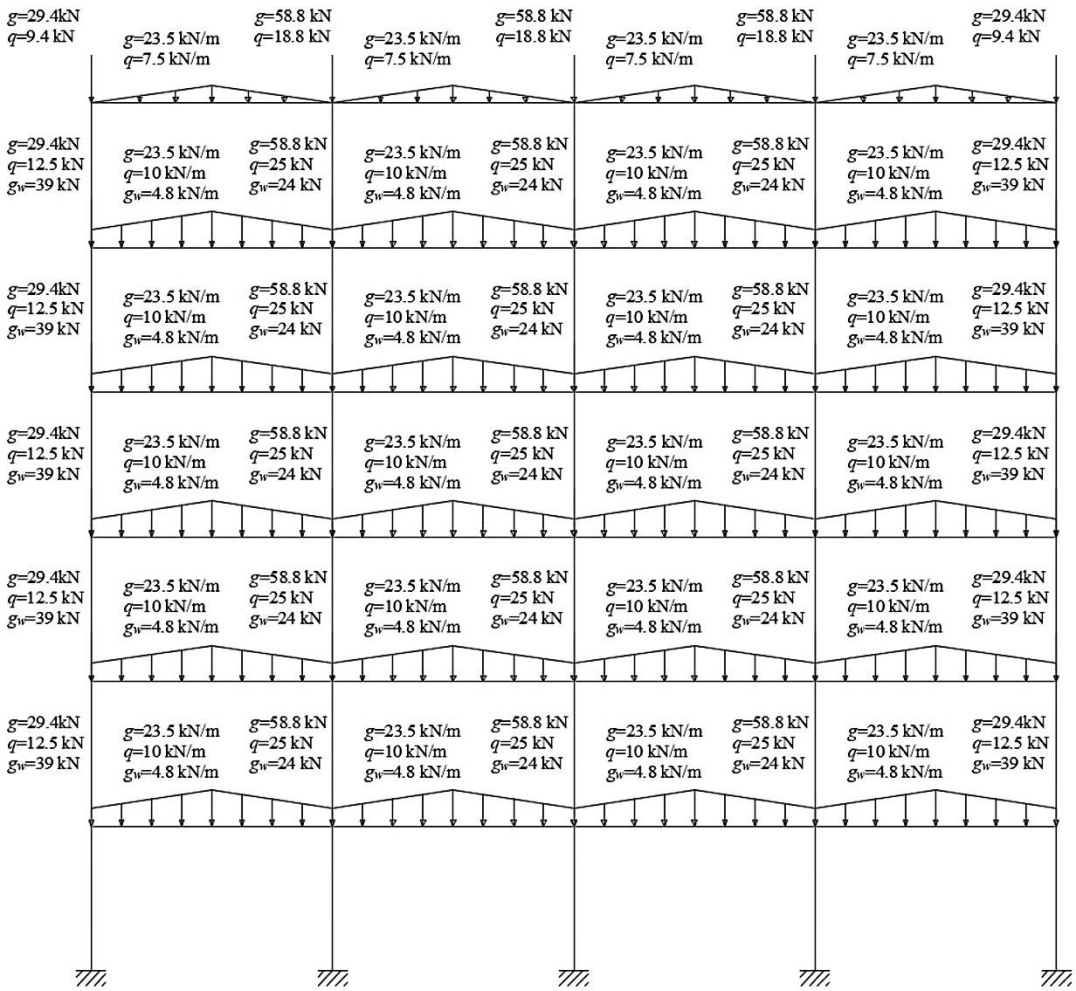

Figure A.7: Gravity load configuration of regular frames with 6 stories and4 bays and conventional beams

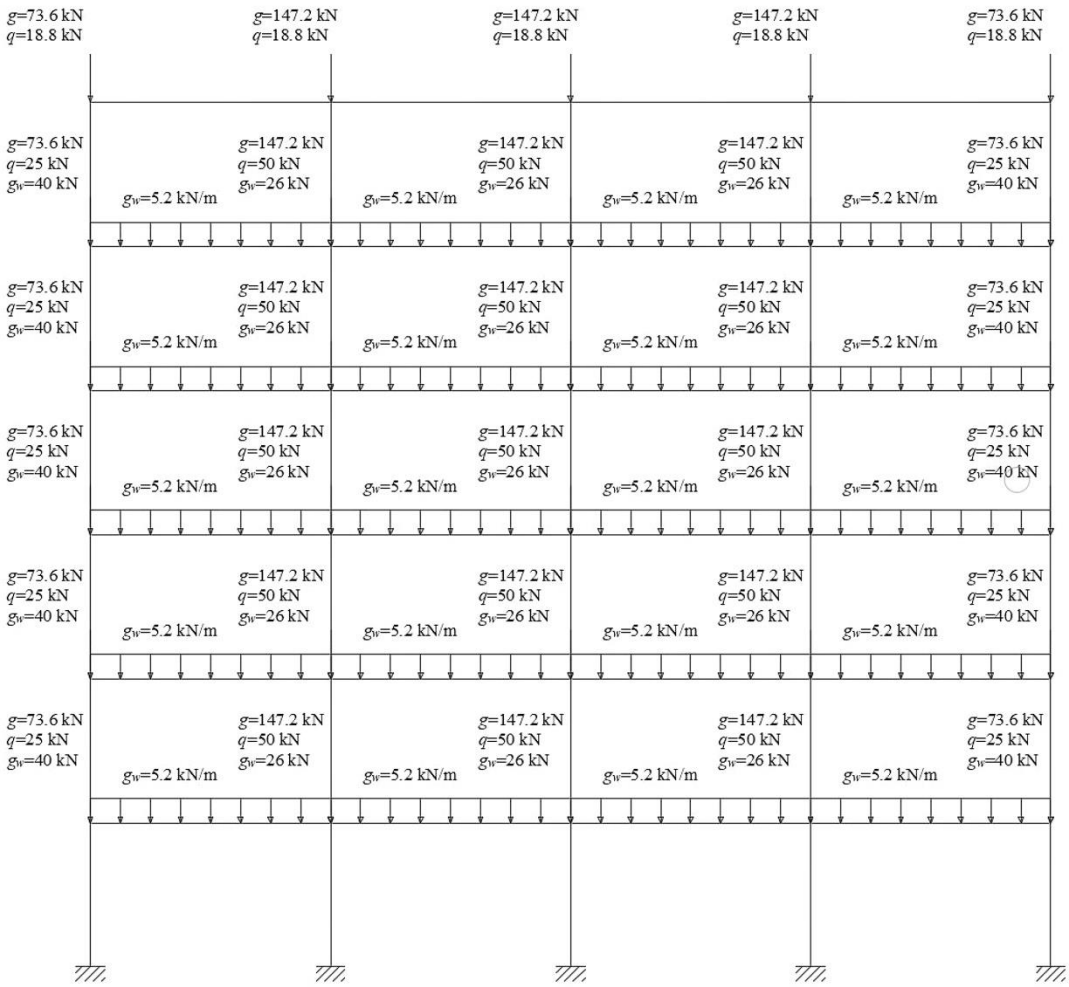

Figure A.8: Gravity load configuration of regular frames with 6 stories and4 bays and wide beams

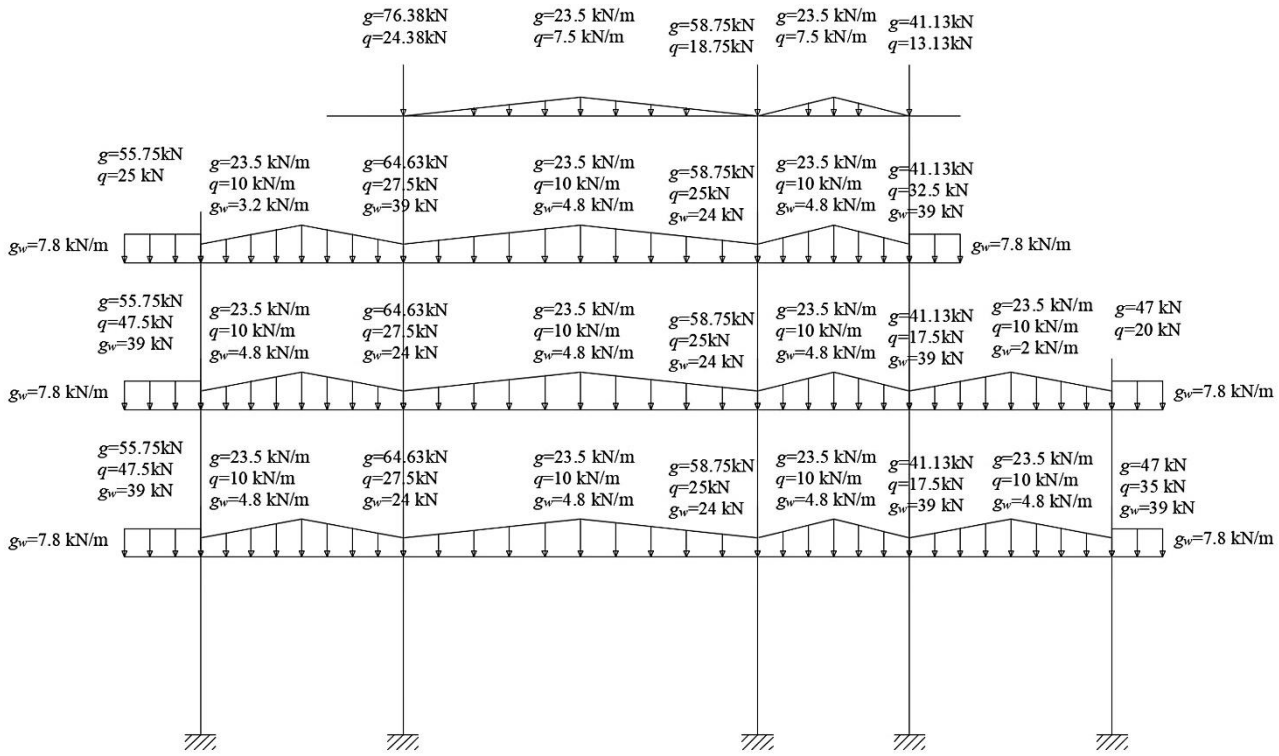

Figure A.9: Gravity load configuration of regular frames with 4 stories and 6 bays and conventional beams

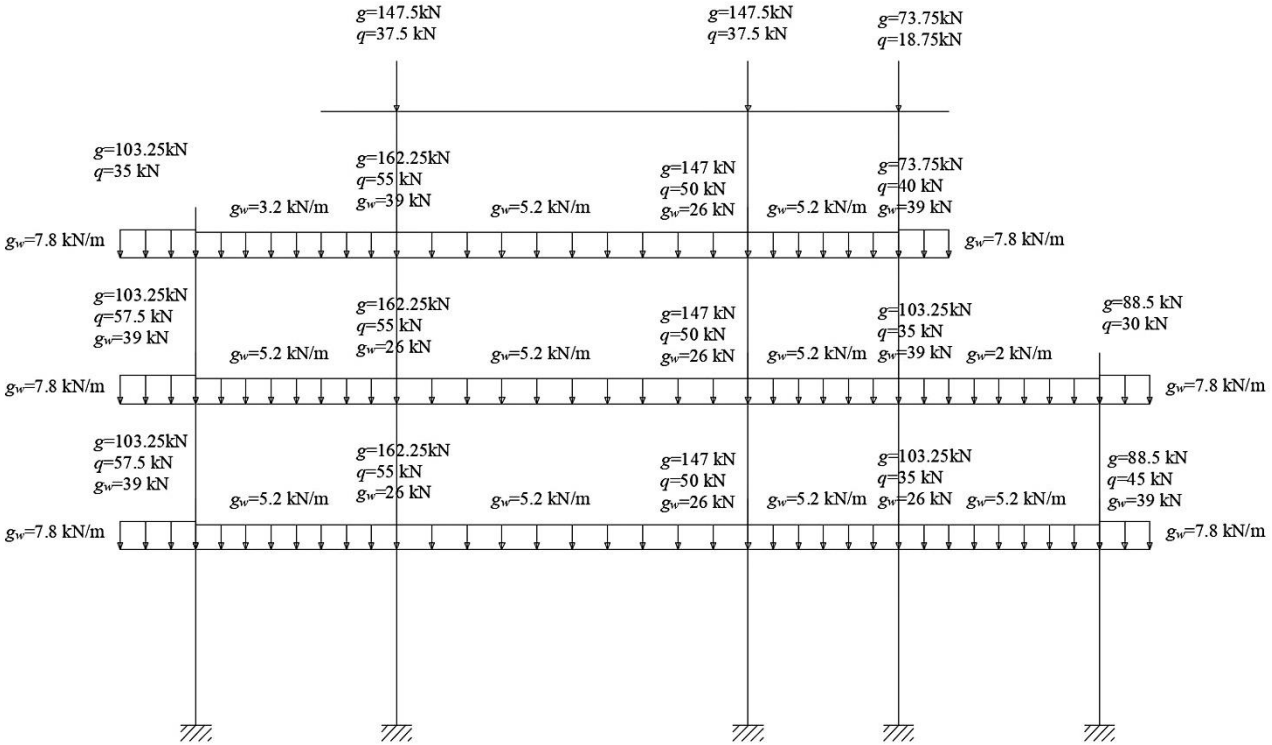

Figure A.10: Gravity load configuration of regular frames with 4 stories and 6 bays and wide beams

A.2 Section and reinforcement details for CBF

The section and reinforcement details of the CBF are given in Figure A.11 to Figure A.20. The section sizes are given in cm, while the longitudinal reinforcement ratios are given in percentages.

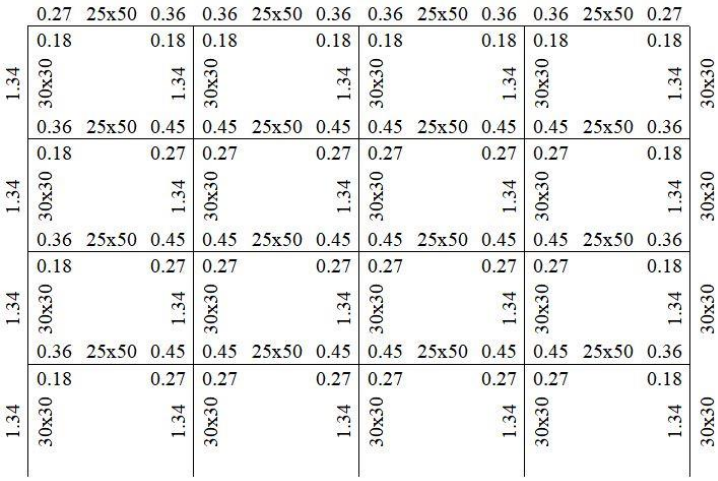

Figure A.11: Section sizes and reinforcement ratios of members of frame C-4C4

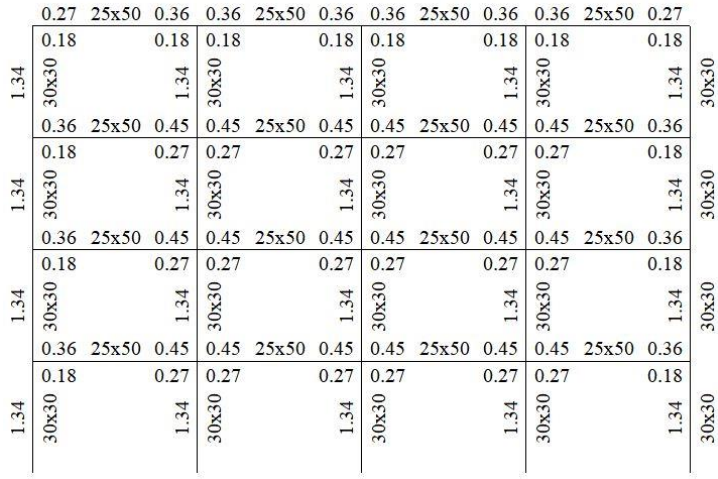

Figure A.12: Section sizes and reinforcement ratios of members of frame C-4D4

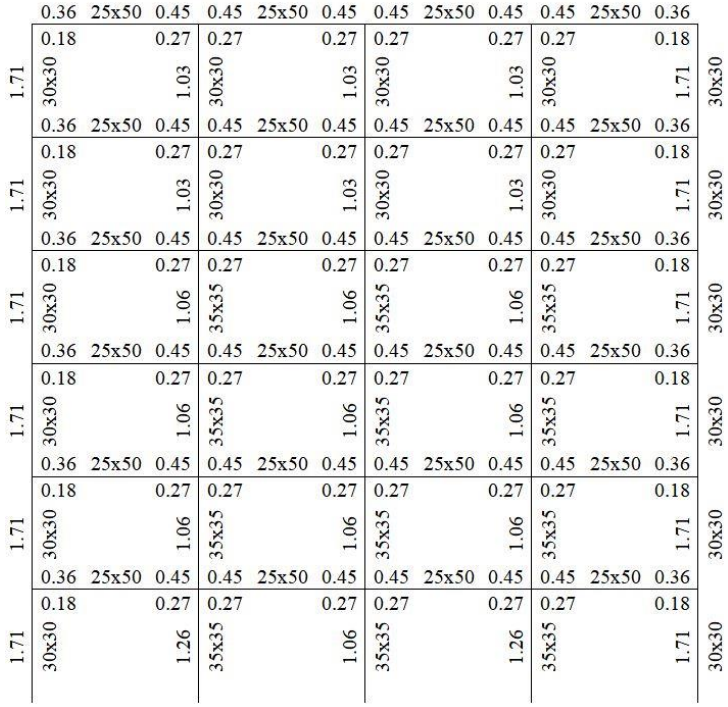

Figure A.13: Section sizes and reinforcement ratios of members of frame C-6C4

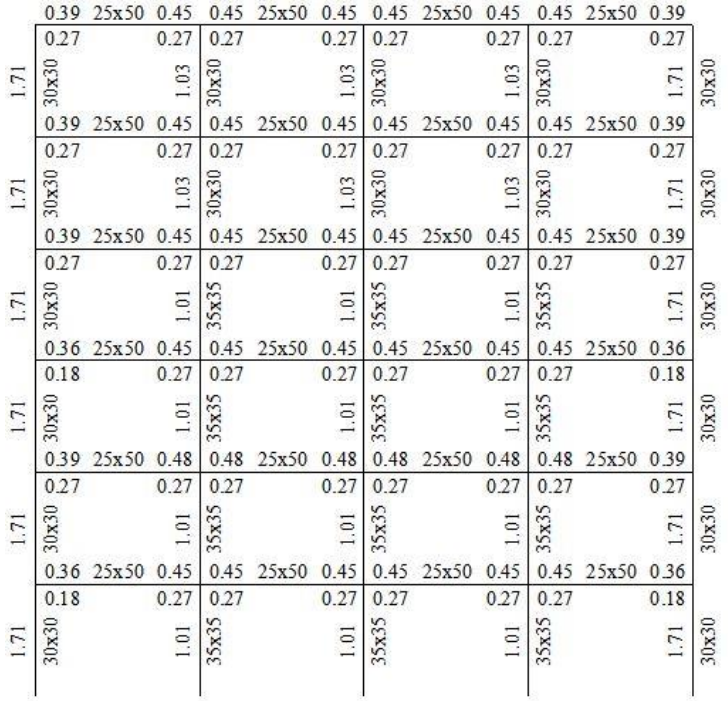

Figure A.14: Section sizes and reinforcement ratios of members of frame C-6D4

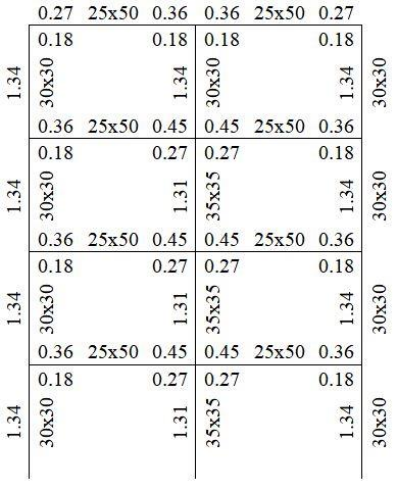

Figure A.15: Section sizes and reinforcement ratios of members of frame C-4C2

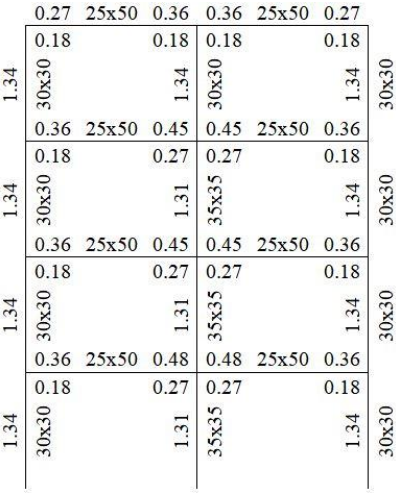

Figure A.16: Section sizes and reinforcement ratios of members of frame C-4D2

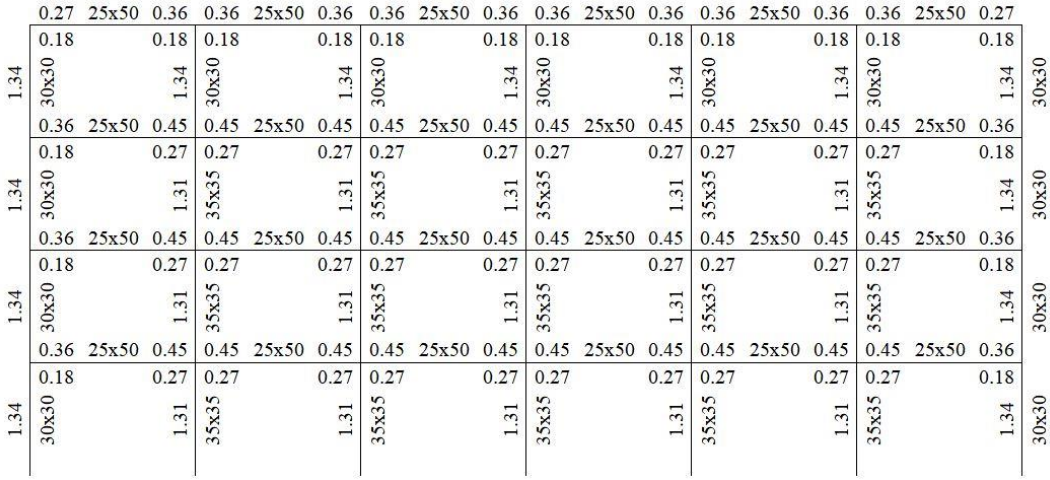

Figure A.17: Section sizes and reinforcement ratios of members of frame C-4C6

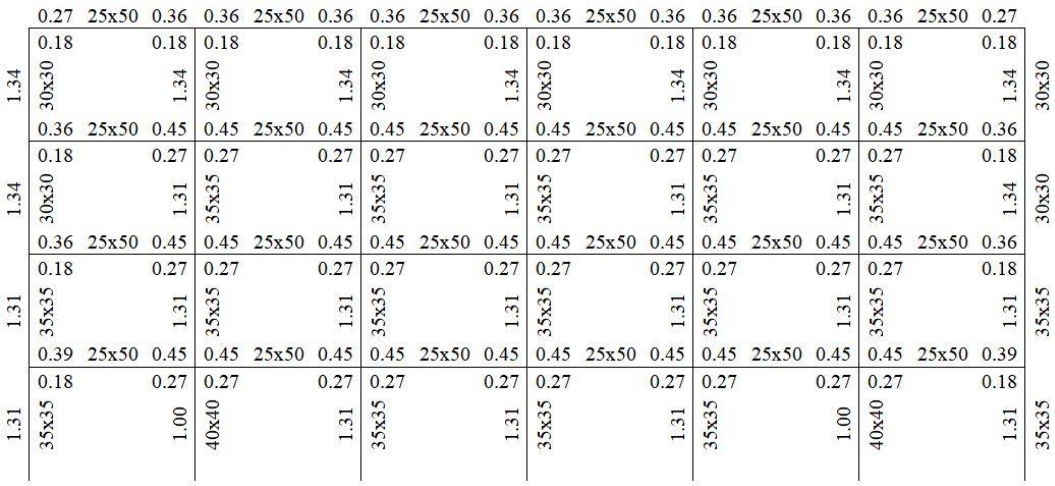

Figure A.18: Section sizes and reinforcement ratios of members of frame C-4D6

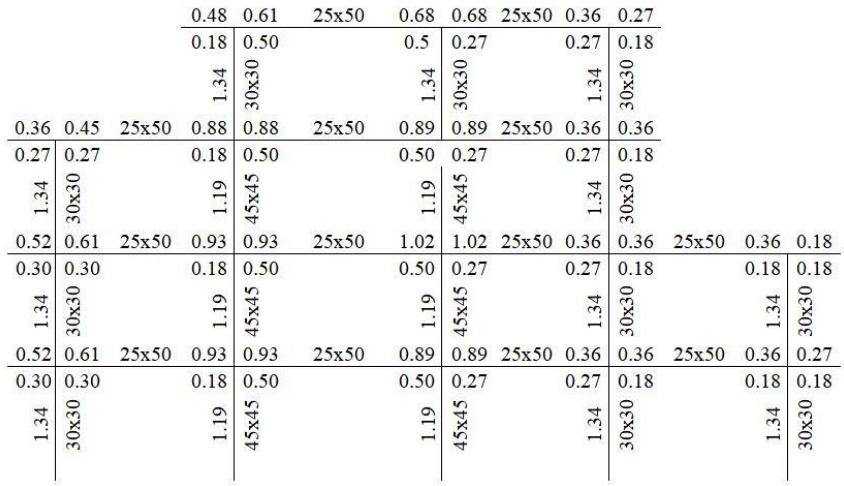

Figure A.19: Section sizes and reinforcement ratios of members of frame C-IC

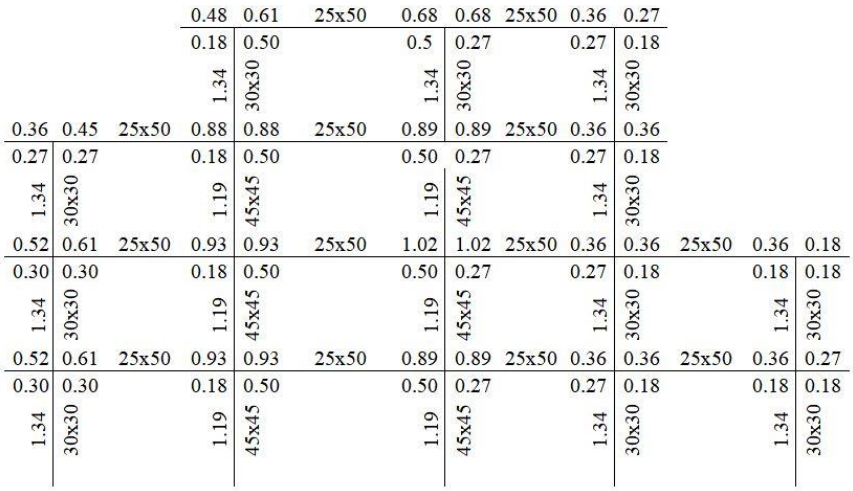

Figure A.20: Section sizes and reinforcement ratios of members of frame C-ID

A.3 Section and reinforcement details for W1BF

The section and reinforcement details of the W1BF are given in Figure A.21 to Figure A.30. The section sizes are given in cm, while the longitudinal reinforcement ratios are given in percentages.

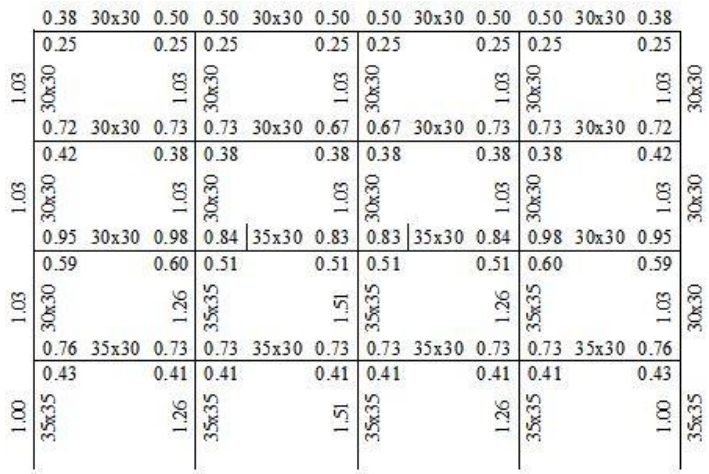

Figure A.21: Section sizes and reinforcement ratios of members of frame W1-4C4

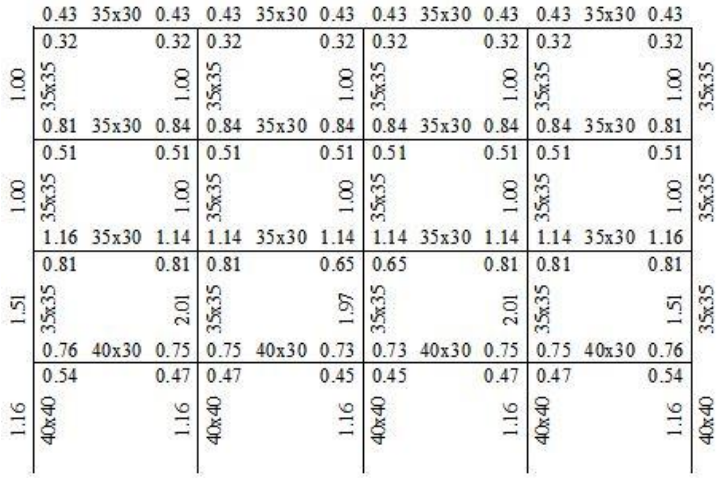

Figure A.22: Section sizes and reinforcement ratios of members of frame W1-4D4

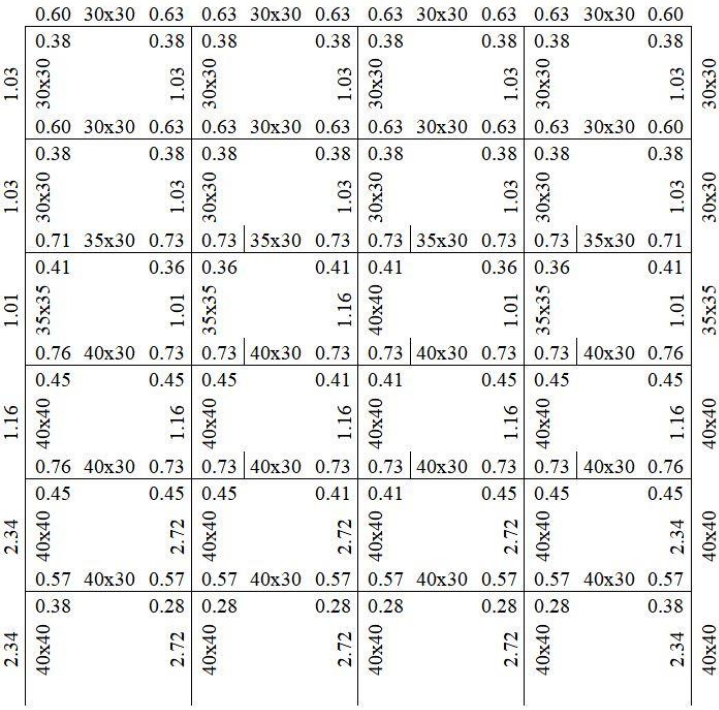

Figure A.23: Section sizes and reinforcement ratios of members of frame W1-6C4

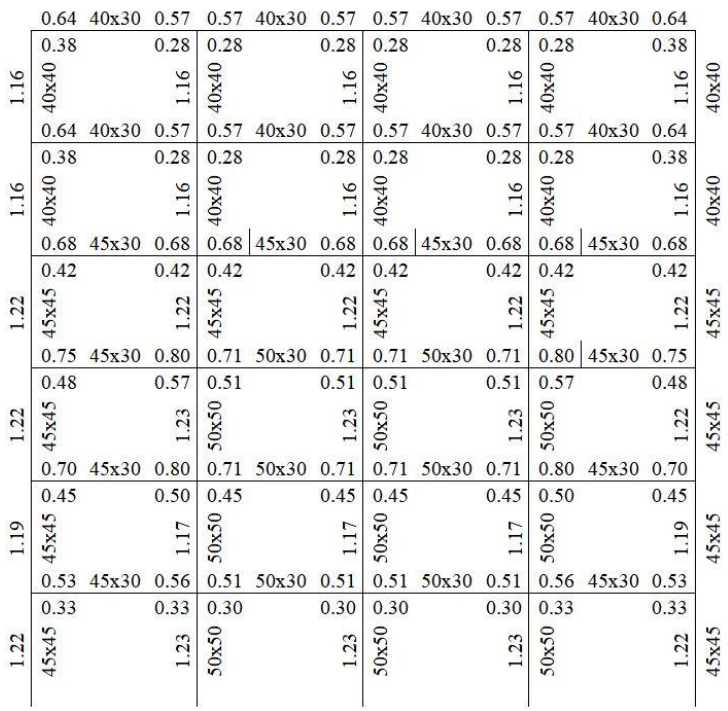

Figure A.24: Section sizes and reinforcement ratios of members of frame W1-6D4

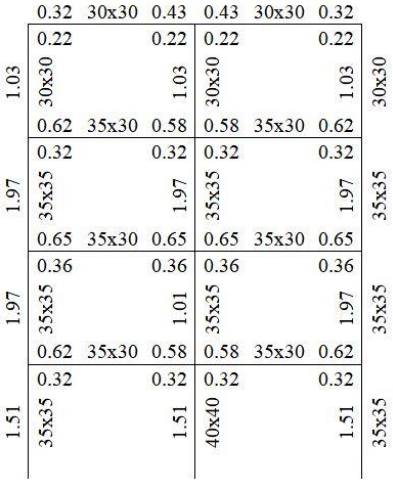

Figure A.25: Section sizes and reinforcement ratios of members of frame W1-4C2

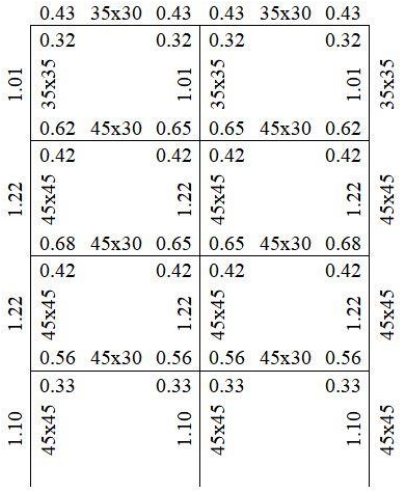

Figure A.26: Section sizes and reinforcement ratios of members of frame W1-4D2

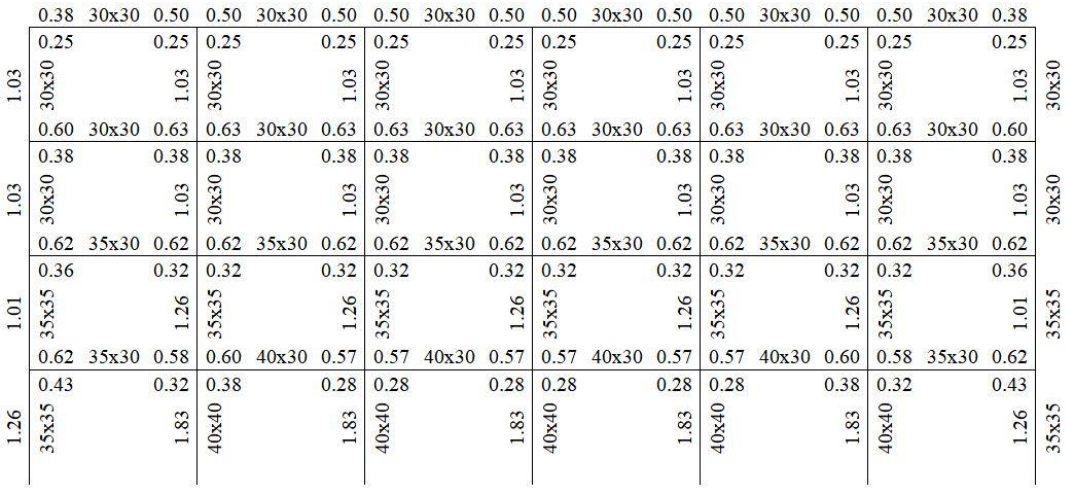

Figure A.27: Section sizes and reinforcement ratios of members of frame W1-4C6

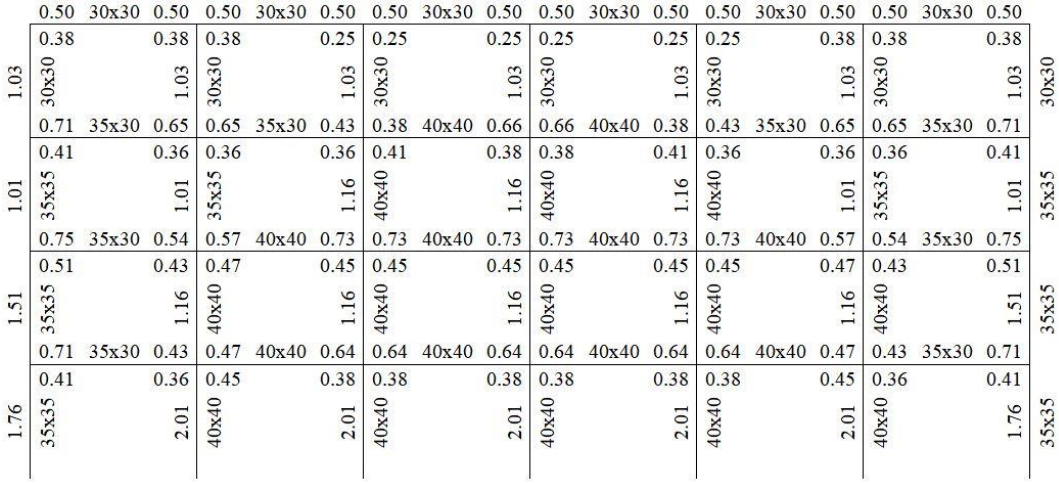

Figure A.28: Section sizes and reinforcement ratios of members of frame W1-4D6

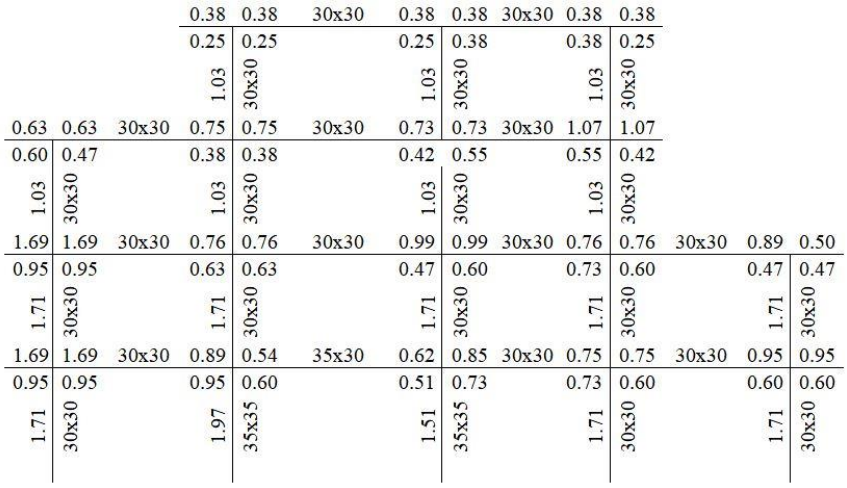

Figure A.29: Section sizes and reinforcement ratios of members of frame W1-IC

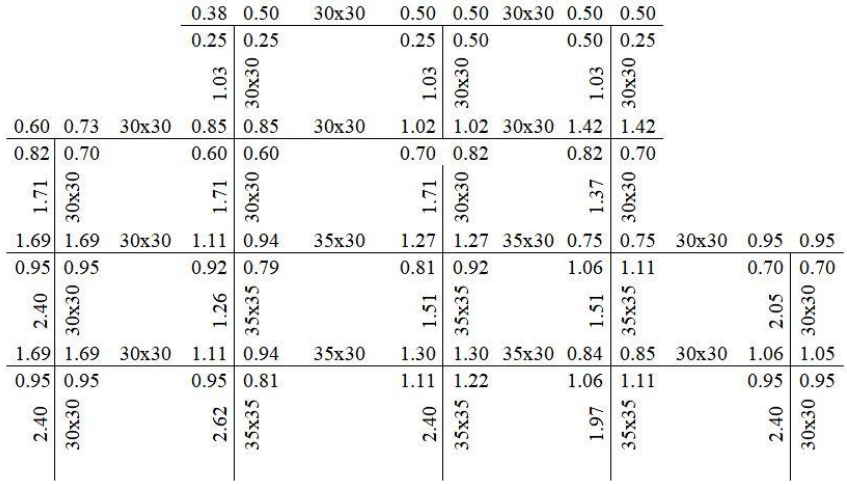

Figure A.30: Section sizes and reinforcement ratios of members of frame W1-ID

A.4 Section and reinforcement details for W2BF

The section and reinforcement details of the W2BF are given in Figure A.31 to Figure A.40. The section sizes are given in cm, while the longitudinal reinforcement ratios are given in percentages.

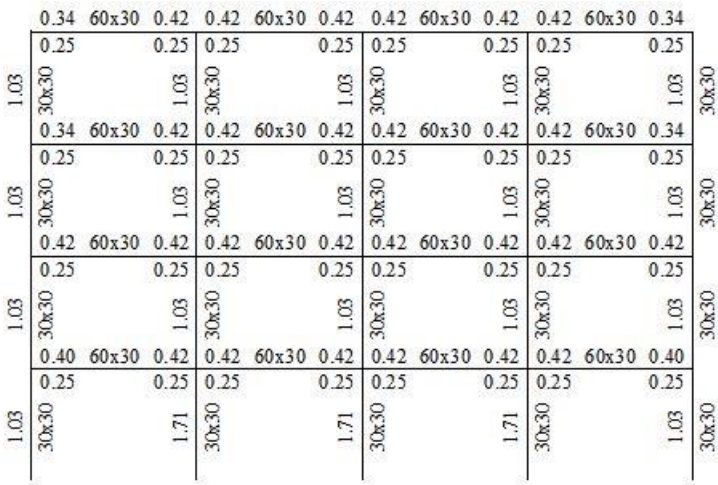

Figure A.31: Section sizes and reinforcement ratios of members of frame W2-4C4

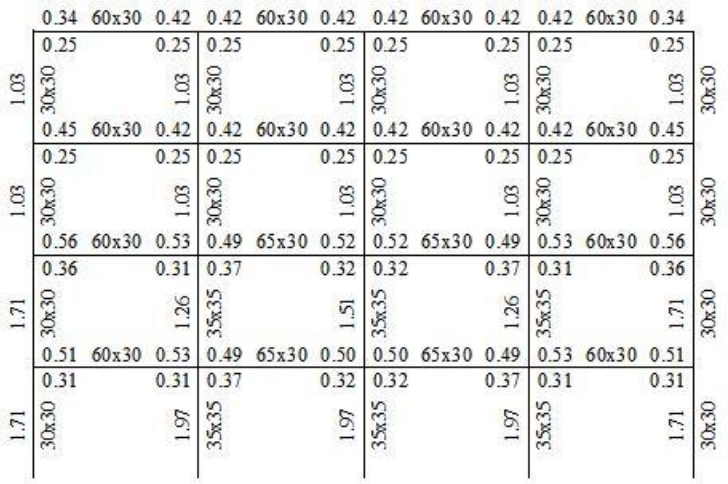

Figure A.32: Section sizes and reinforcement ratios of members of frame W2-4D4

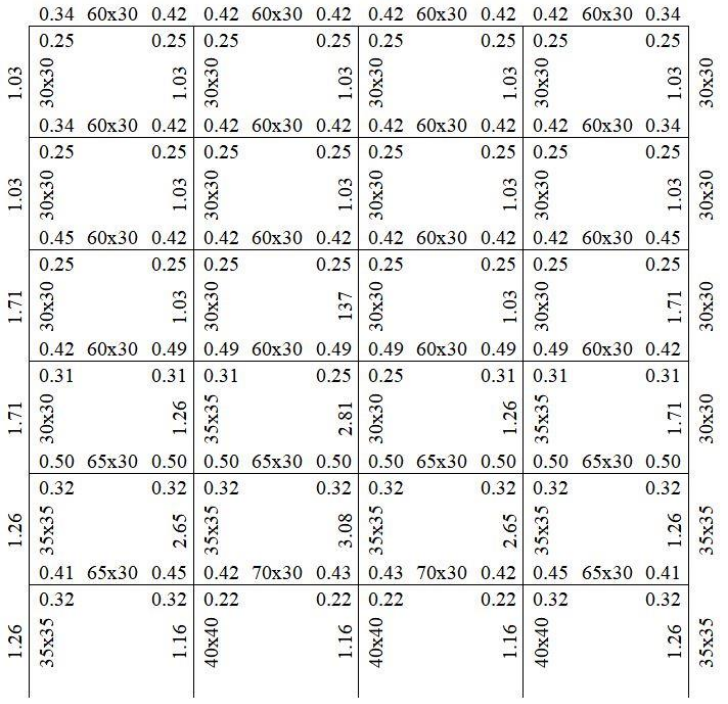

Figure A.33: Section sizes and reinforcement ratios of members of frame W2-6C4

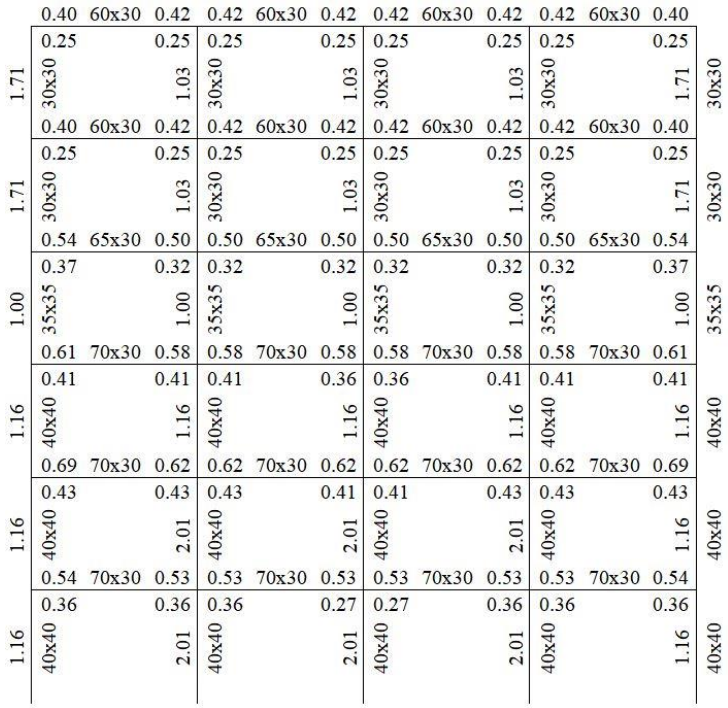

Figure A.34: Section sizes and reinforcement ratios of members of frame W2-6D4

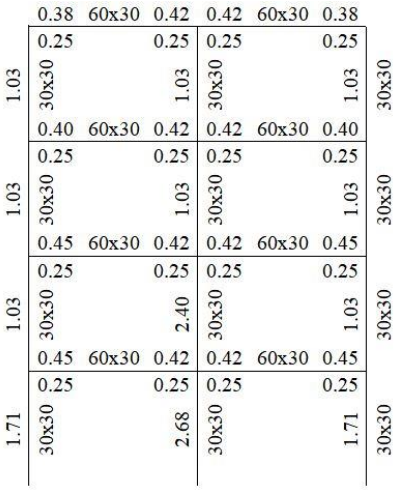

Figure A.35: Section sizes and reinforcement ratios of members of frame W2-4C2

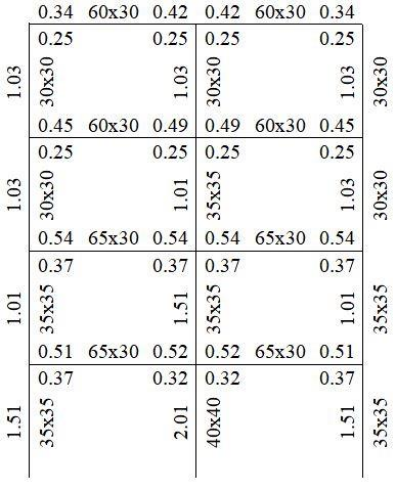

Figure A.36: Section sizes and reinforcement ratios of members of frame W2-4D2

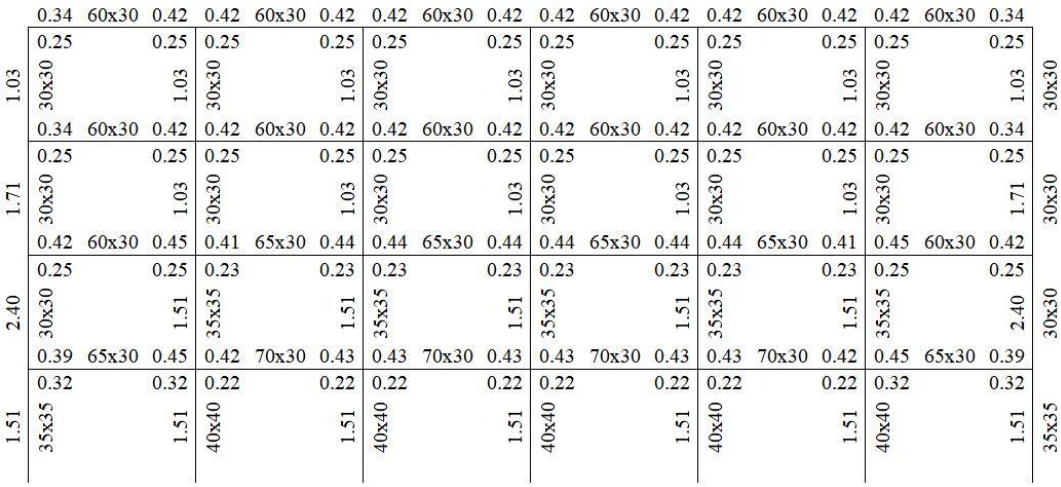

Figure A.37: Section sizes and reinforcement ratios of members of frame W2-4C6

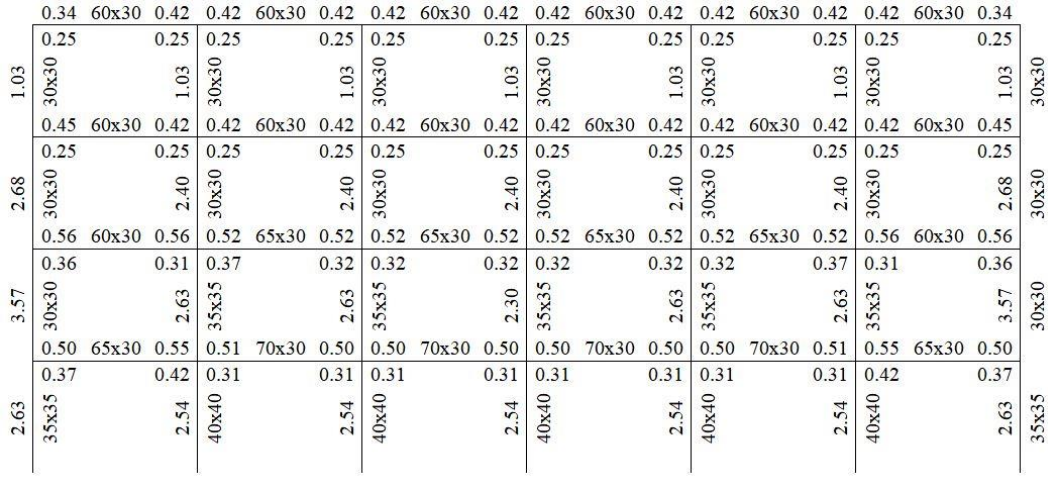

Figure A.38: Section sizes and reinforcement ratios of members of frame W2-4D6

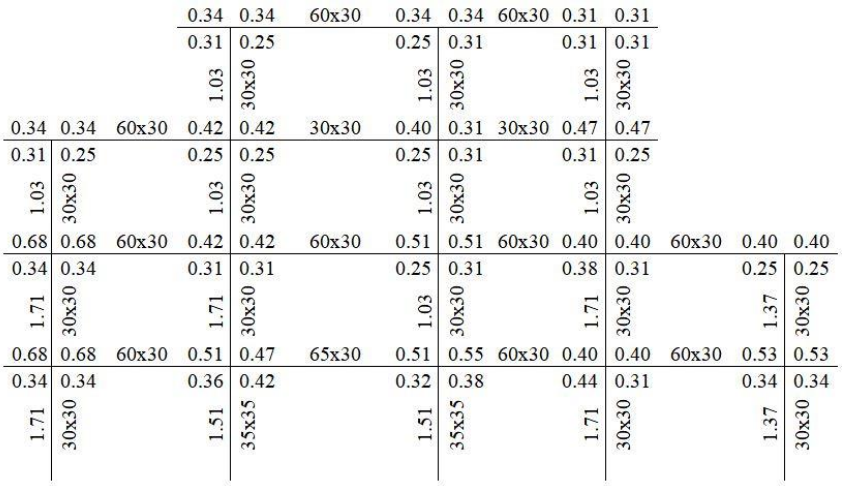

Figure A.39: Section sizes and reinforcement ratios of members of frame W2-IC

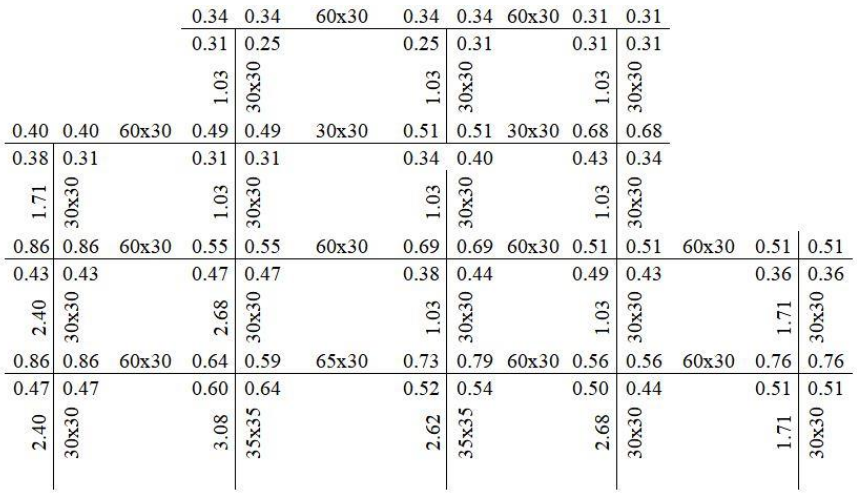

Figure A.40: Section sizes and reinforcement ratios of members of frame W2-ID

Appendix B

List of Ground Motion Records

The selection of the ground motion record sets was discussed in Chapter 6. In this Appendix, the ground motion records that were used to perform time-history analyses are listed in tabular form. Their compatibility with the target spectra is shown in figures containing the acceleration spectra of the individual records, their mean and the corresponding code spectrum.

B.1 Soil Class C and SDC3

Table B.1, Table B.2 and Table B.3 list the records selected for Soil Class C and SDC3.

Table B.1: Ground motion record sets 1-10 for Soil Class C and SDC3

Set 1	**Set 2**	**Set 3**	**Set 4**	**Set 5**	**Set 6**	**Set 7**	**Set 8**	**Set 9**	**Set 10**
247y	4101x	212y	963y	698x	1515x	4228x	4872y	1520y	4219y
4873x	1055x	2935y	4228y	2739y	139y	1510y	8166x	4031y	5775x
222y	216y	5478y	4858y	812x	4377x	3689x	1013x	4133y	5800x
1511y	3472y	4086x	4383y	4508x	2935x	2661y	1494y	2616x	5804x
2612x	3966x	3748y	5275y	3966y	3468x	2654y	1734x	318y	313y
825y	954x	5818y	4169y	2714y	989y	952x	3778y	1527x	1488y
4206y	3748x	3871x	5681y	4546x	2623y	4547y	2734y	292x	8110x
1198y	2645y	1519x	4037x	3955y	825x	288y	3871y	4130y	352x
4869y	4009x	4316y	1626y	4867y	5810y	3776x	1028x	1184y	4124x
3018y	1546x	354y	5813x	1086x	5472x	1545x	739y	6891x	410y
5265x	1510x	4101y	1533y	1053x	347x	4477y	5637y	8896x	2893y

Table B.2: Ground motion record sets 11-20 for Soil Class C and SDC3

Set 11	**Set 12**	**Set 13**	**Set 14**	**Set 15**	**Set 16**	**Set 17**	**Set 18**	**Set 19**	**Set 20**
5678x	4218y	3865y	4228y	8166y	4858x	825y	369x	814x	2379x
4140x	6059y	787y	3470x	1493y	952y	2393y	1611x	5818y	5678y
5807x	590x	249x	4137x	265y	410x	779y	5284x	812y	3343x
57x	4871y	3753y	3023y	1086x	3859y	1515y	1535x	825y	3979y
4213y	5806x	3884x	5656x	3345x	2655x	237x	1614x	4392x	600x
4846x	1642y	4864x	223x	454y	4331y	476x	3472x	514x	4101x
2650x	1148y	133y	4016x	1520x	5804y	6915y	2465y	8164y	1505y
5656y	1551x	4071y	1633y	830x	497y	2892y	4336y	3744x	3268x
4314x	5775y	1193x	352y	3029x	4228x	2625x	4475y	3884y	5656x
1208y	5274y	974x	4227y	2490x	3760y	1083x	825x	5284y	1643y
5284x	1546y	5662x	4870y	3495y	3744y	139y	3964x	3274y	448y

Table B.3: Ground motion record sets 21-30 for Soil Class C and SDC3

Set 21	**Set 22**	**Set 23**	**Set 24**	**Set 25**	**Set 26**	**Set 27**	**Set 28**	**Set 29**	**Set 30**
5265y	763y	1086x	5819y	553y	5775y	3220x	4882x	5478y	1058y
1005y	215y	4096y	4142x	5282y	3751x	5636y	4133y	1762y	4040y
5678y	3349x	601y	1505y	3884y	4147y	514x	1489x	997x	1520x
830x	5472y	1762x	79y	5494y	2470x	4133y	3845y	787x	5280y
2626x	1202y	1531y	5775y	220y	4392y	1532y	5285y	5809x	4142x
3507x	830y	6891y	5265y	1532x	1534y	4336y	1182y	6971x	3175x
1489y	4848y	50x	3760x	3459y	825x	1633x	164x	4101x	3455y
1545y	4213y	5654y	4285x	292y	550y	1488x	3884y	2385x	4858y
755x	1520y	4103y	4842x	825x	935y	4141x	6060x	3017x	1533y
3871y	1530x	4227x	5284y	4864x	4277y	3748y	5662y	4882y	787x
3744x	4071x	4170y	5472x	997x	891x	5678y	4130y	1515y	243y

Figure B.1 to Figure B.30 present the plots of the acceleration spectra of the individual records, their mean and the target spectrum for Soil Class C and SDC3.

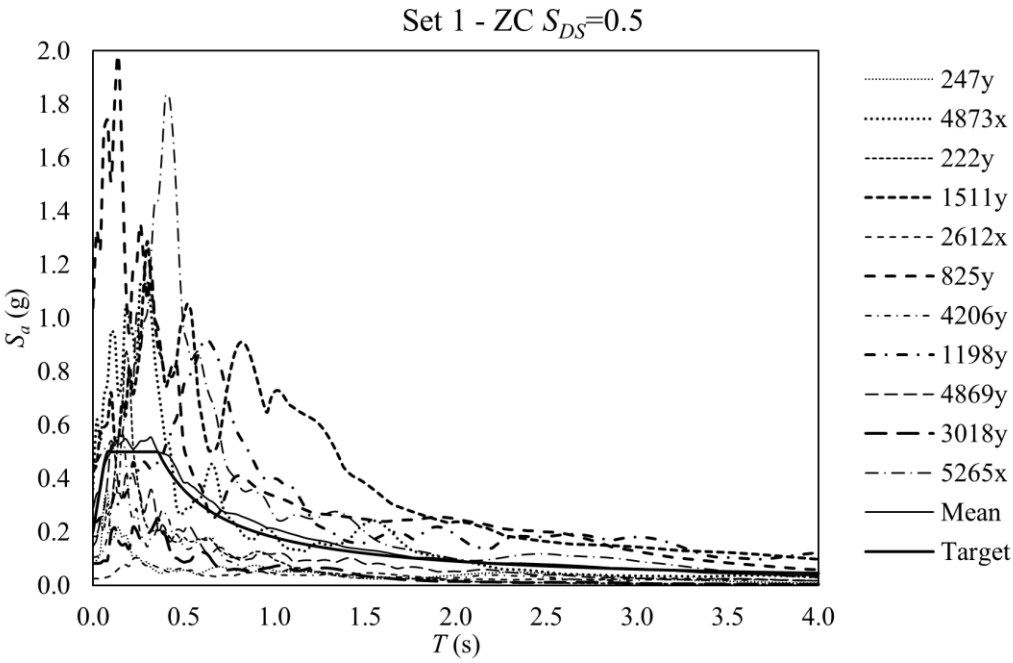

Figure B.1: Spectral acceleration of the ground motion records of Set 1 and their mean and target spectrum

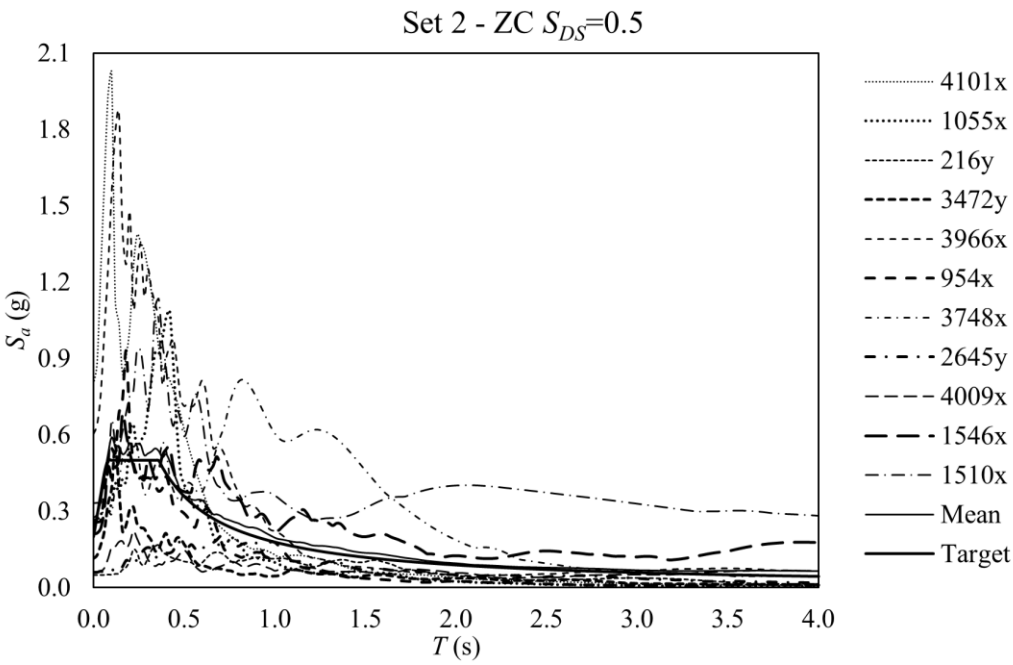

Figure B.2: Spectral acceleration of the ground motion records of Set 2 and their mean and target spectrum

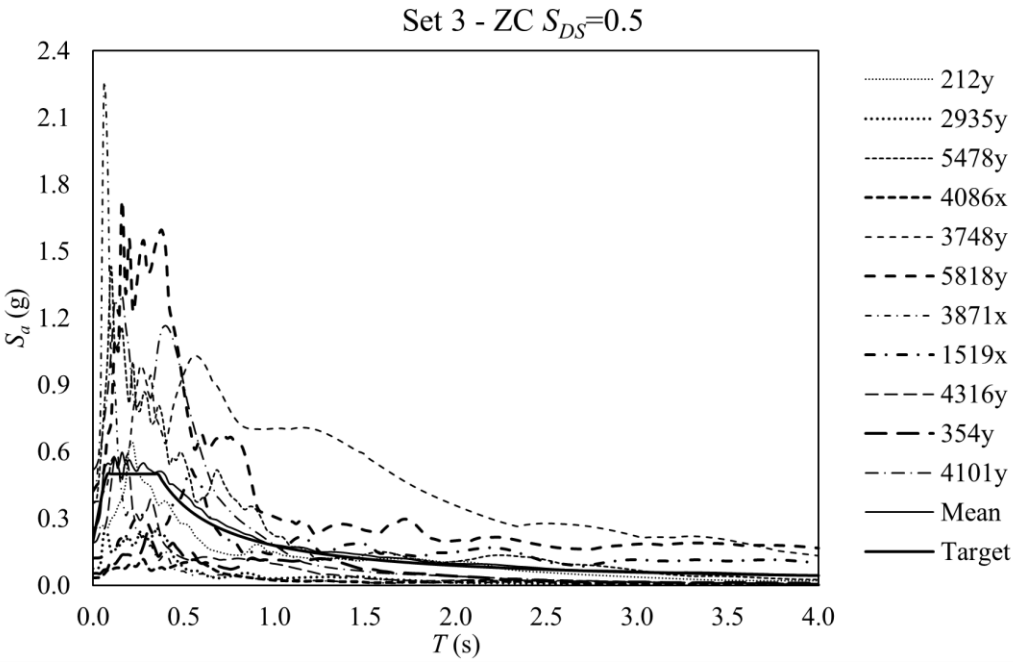

Figure B.3: Spectral acceleration of the ground motion records of Set 3 and their mean and target spectrum

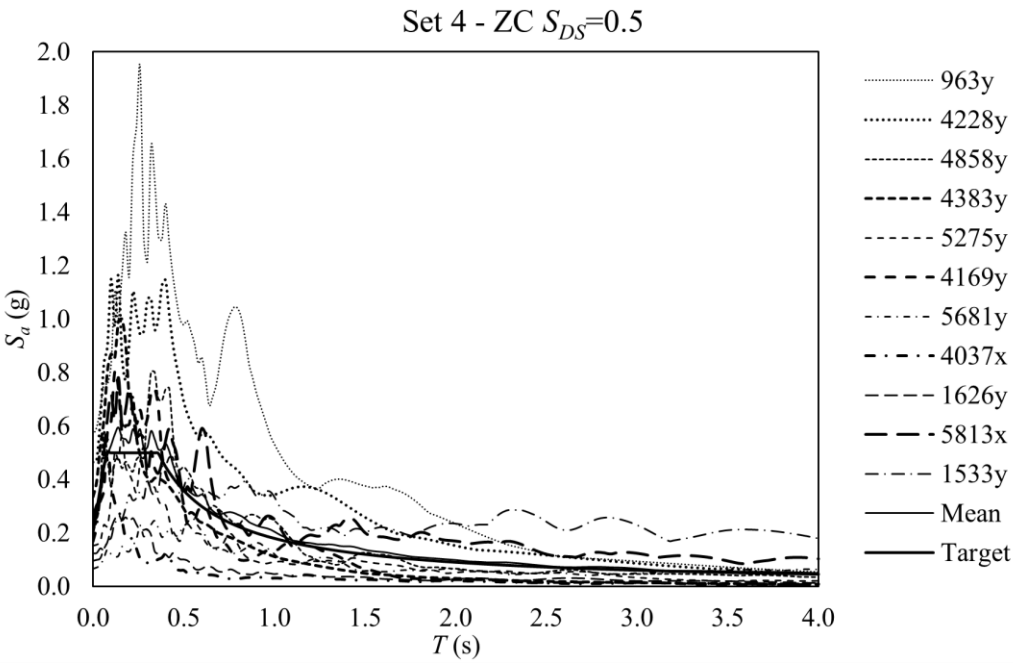

Figure B.4: Spectral acceleration of the ground motion records of Set 4 and their mean and target spectrum

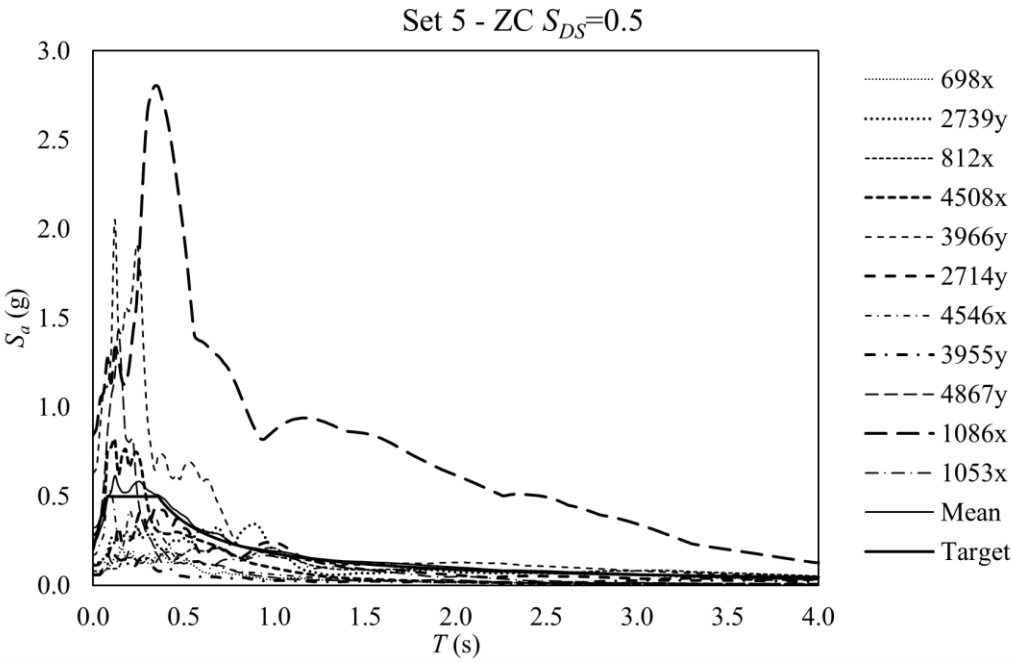

Figure B.5: Spectral acceleration of the ground motion records of Set 5 and their mean and target spectrum

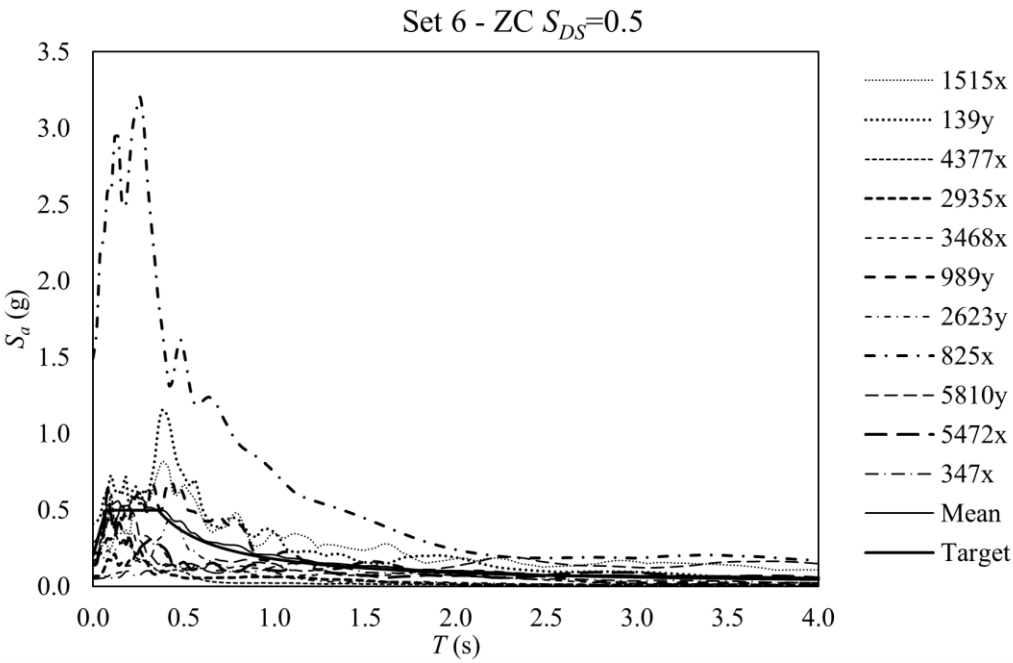

Figure B.6: Spectral acceleration of the ground motion records of Set 6 and their mean and target spectrum

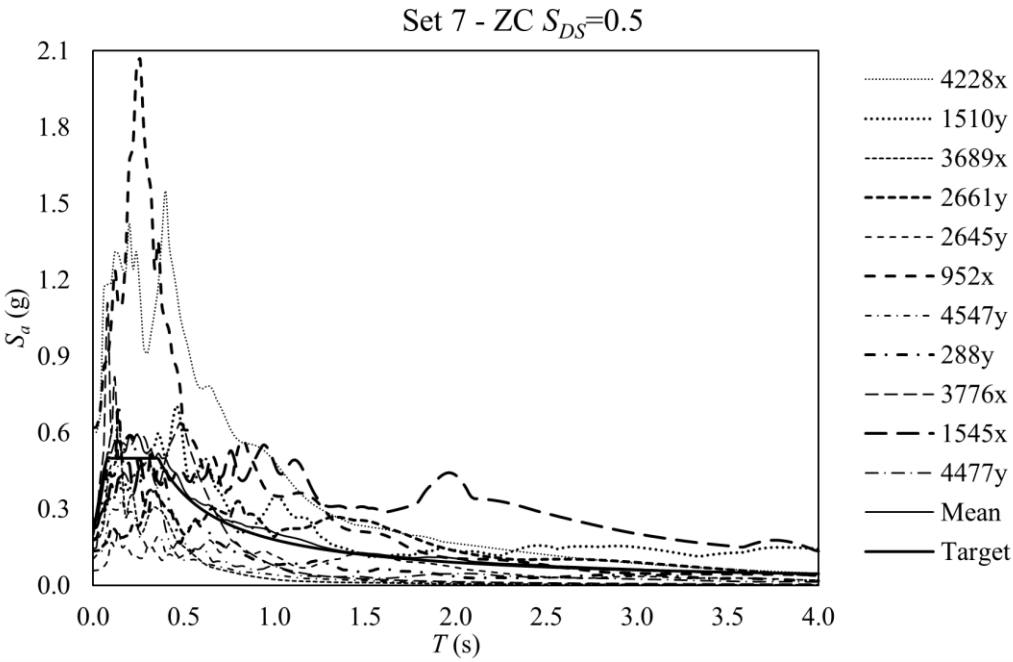

Figure B.7: Spectral acceleration of the ground motion records of Set 7 and their mean and target spectrum

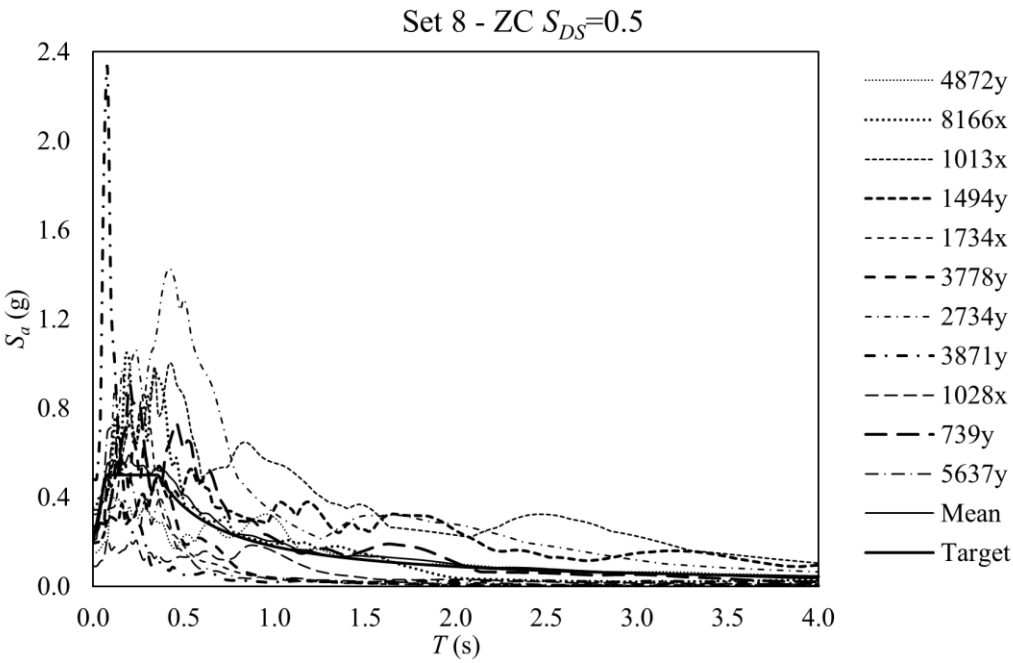

Figure B.8: Spectral acceleration of the ground motion records of Set 8 and their mean and target spectrum

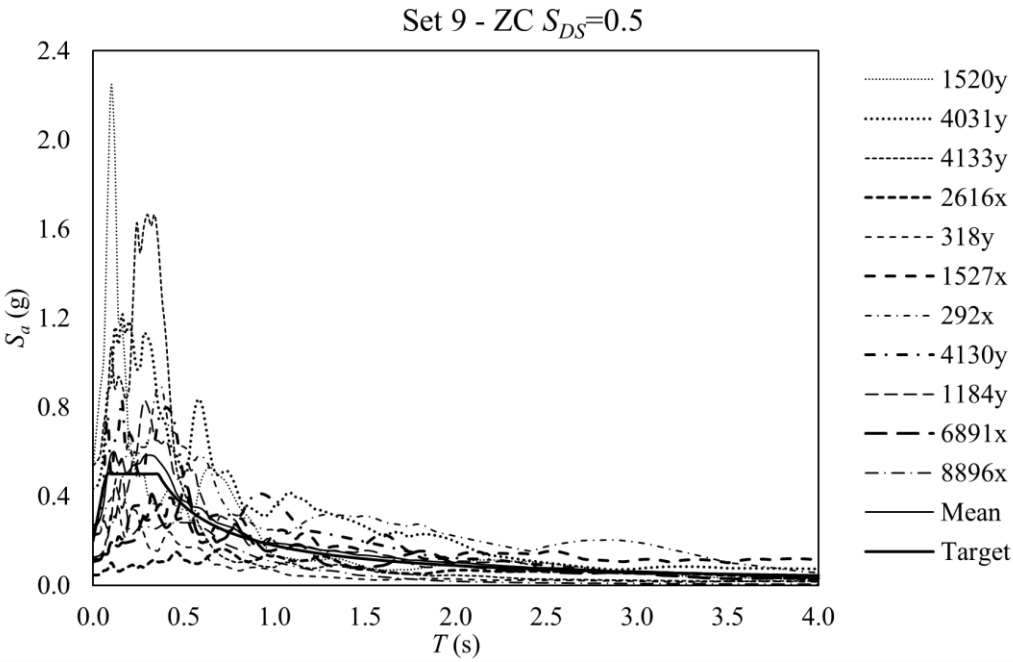

Figure B.9: Spectral acceleration of the ground motion records of Set 9 and their mean and target spectrum

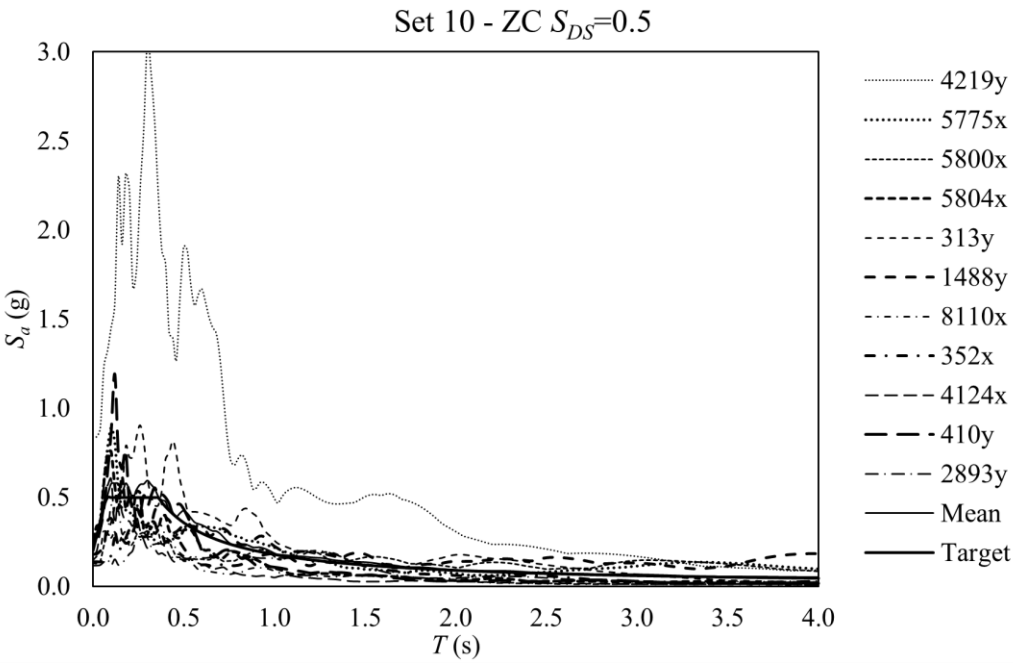

Figure B.10: Spectral acceleration of the ground motion records of Set 10 and their mean and target spectrum

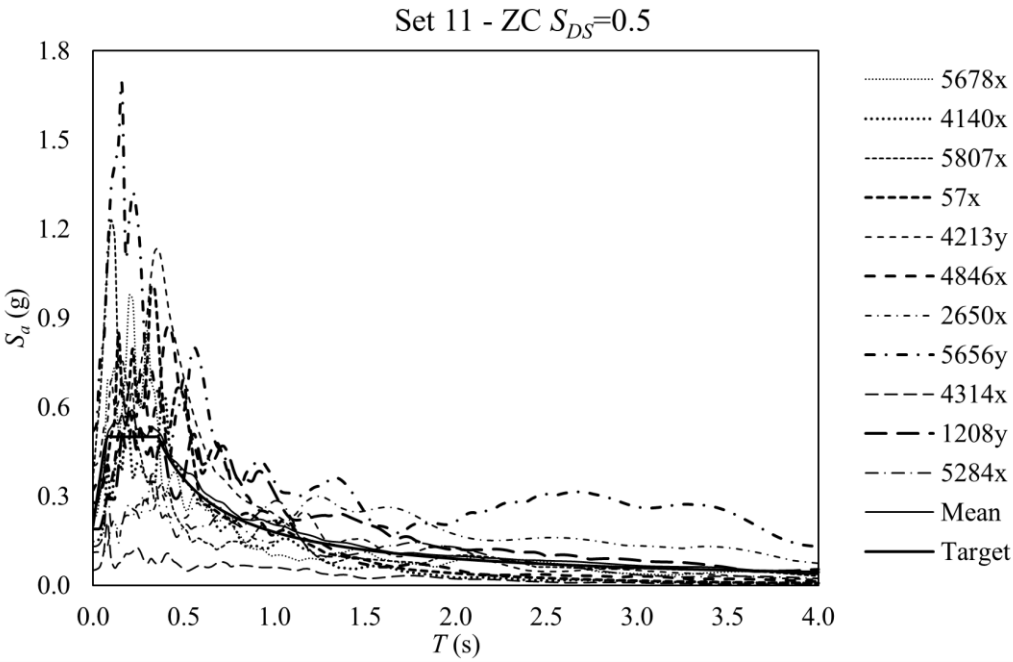

Figure B.11: Spectral acceleration of the ground motion records of Set 11 and their mean and target spectrum

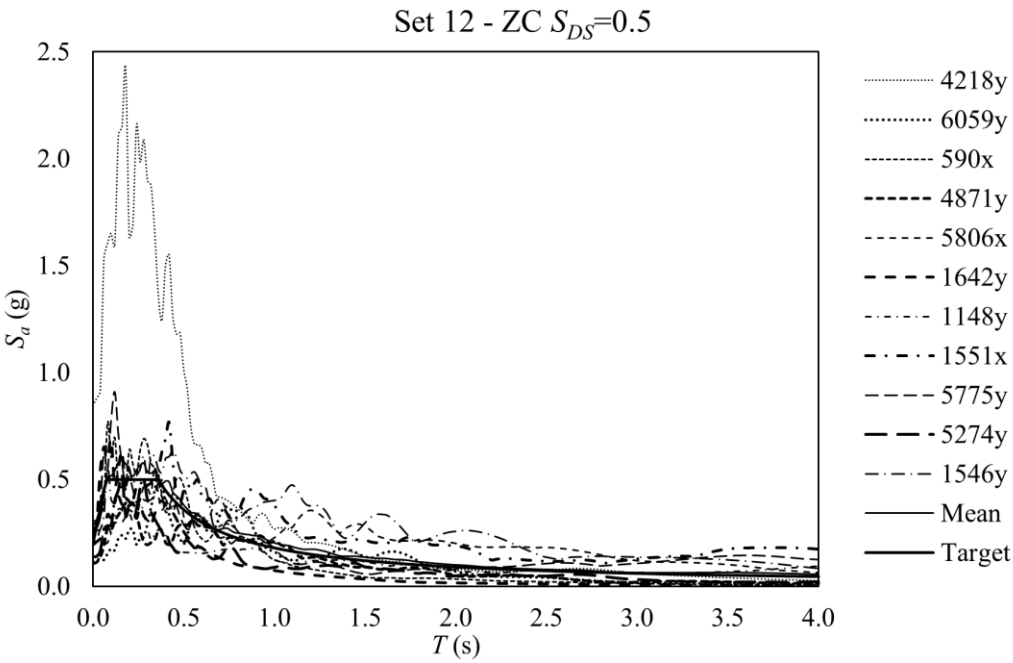

Figure B.12: Spectral acceleration of the ground motion records of Set 12 and their mean and target spectrum

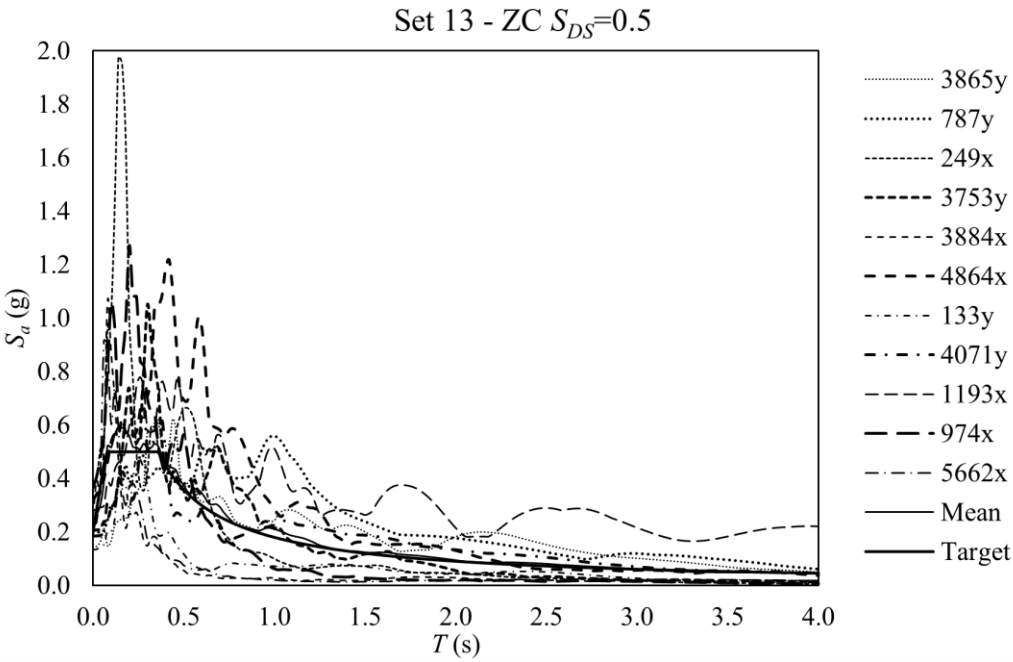

Figure B.13: Spectral acceleration of the ground motion records of Set 13 and their mean and target spectrum

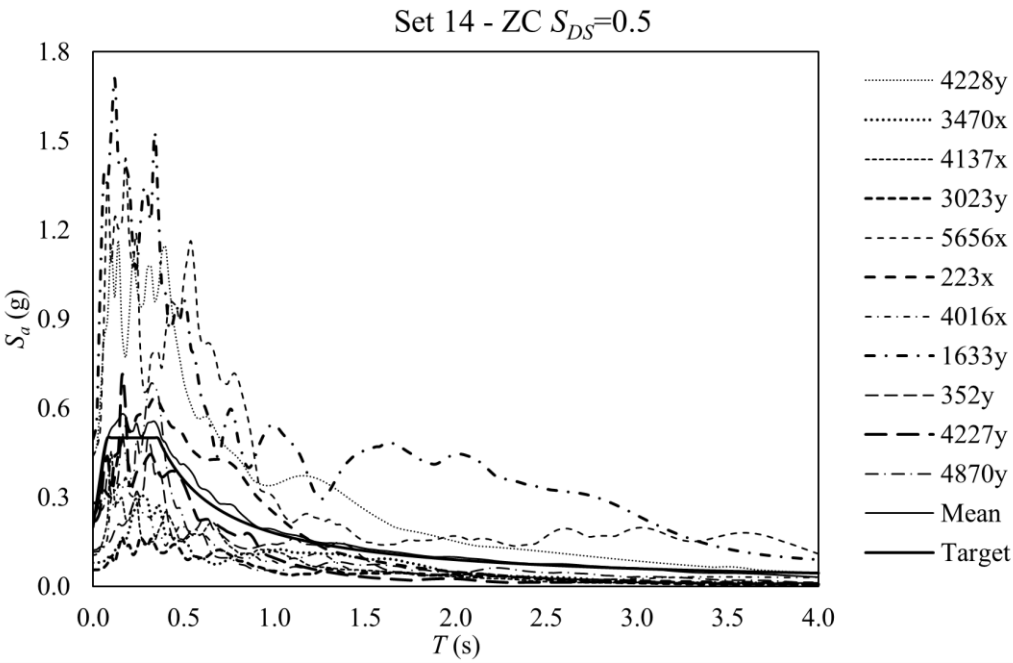

Figure B.14: Spectral acceleration of the ground motion records of Set 14 and their mean and target spectrum

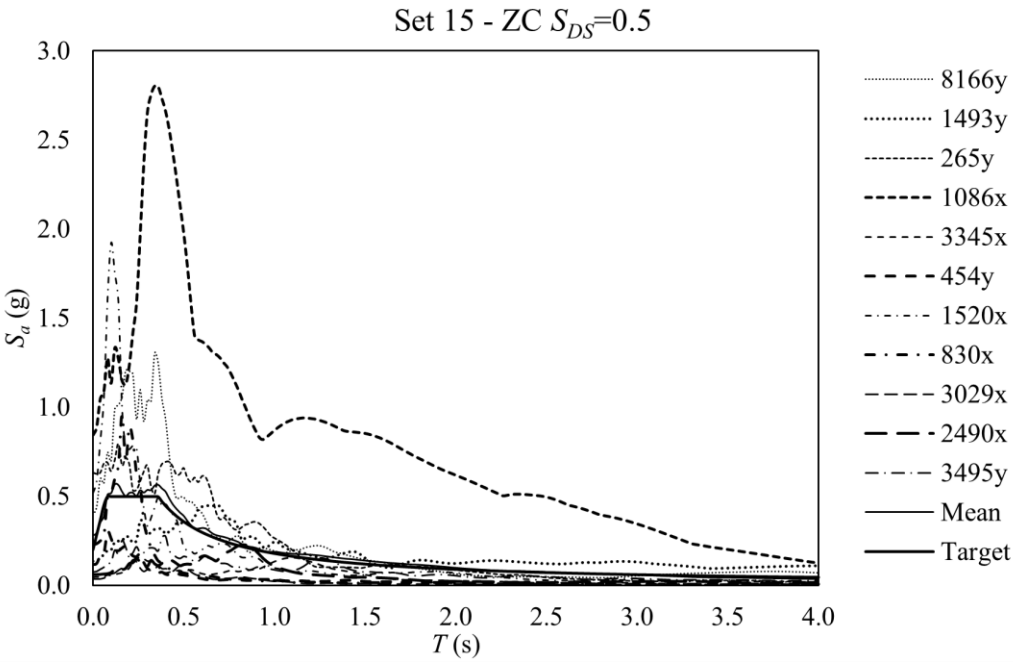

Figure B.15: Spectral acceleration of the ground motion records of Set 15 and their mean and target spectrum

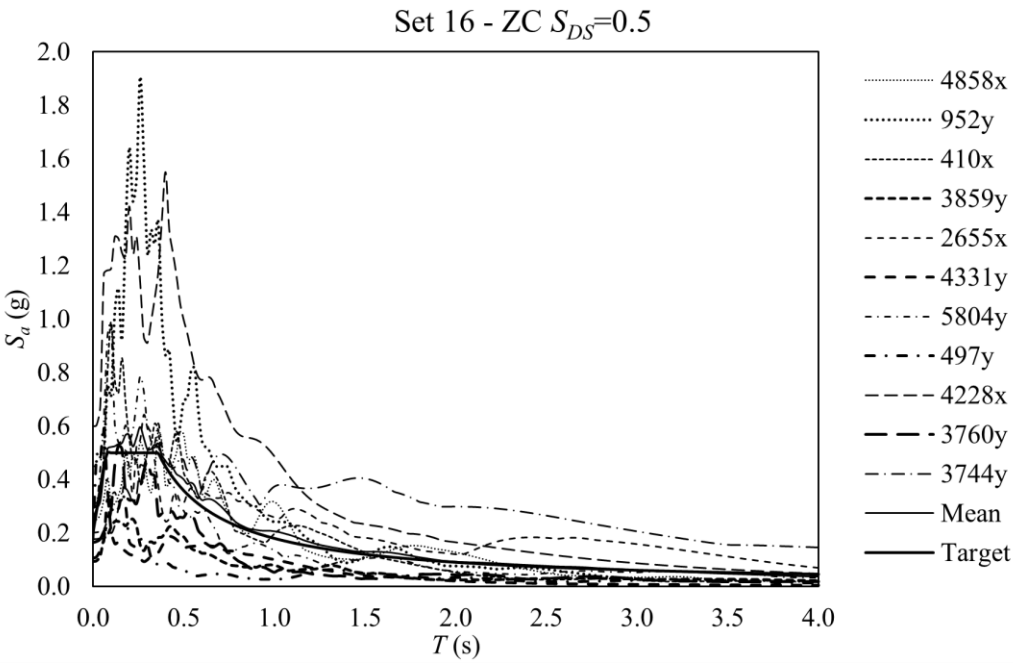

Figure B.16: Spectral acceleration of the ground motion records of Set 16 and their mean and target spectrum

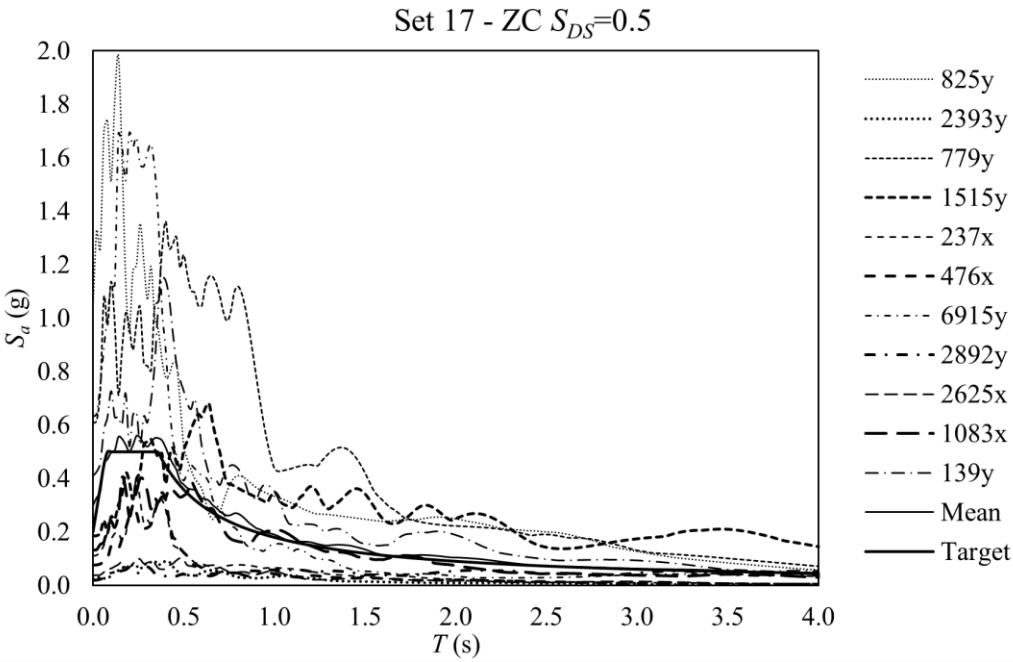

Figure B.17: Spectral acceleration of the ground motion records of Set 17 and their mean and target spectrum

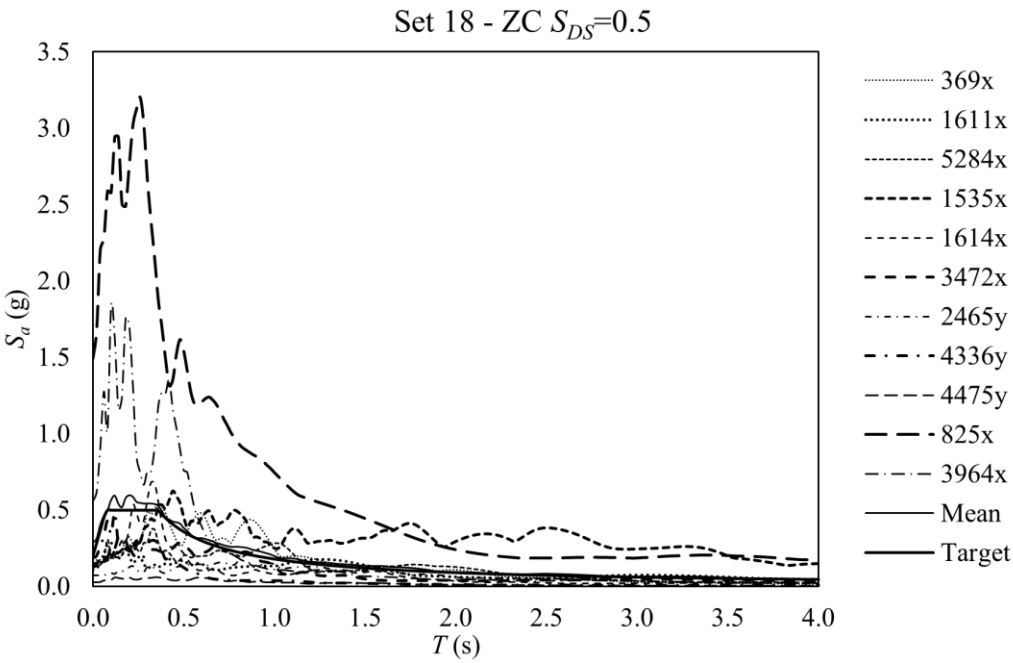

Figure B.18: Spectral acceleration of the ground motion records of Set 18 and their mean and target spectrum

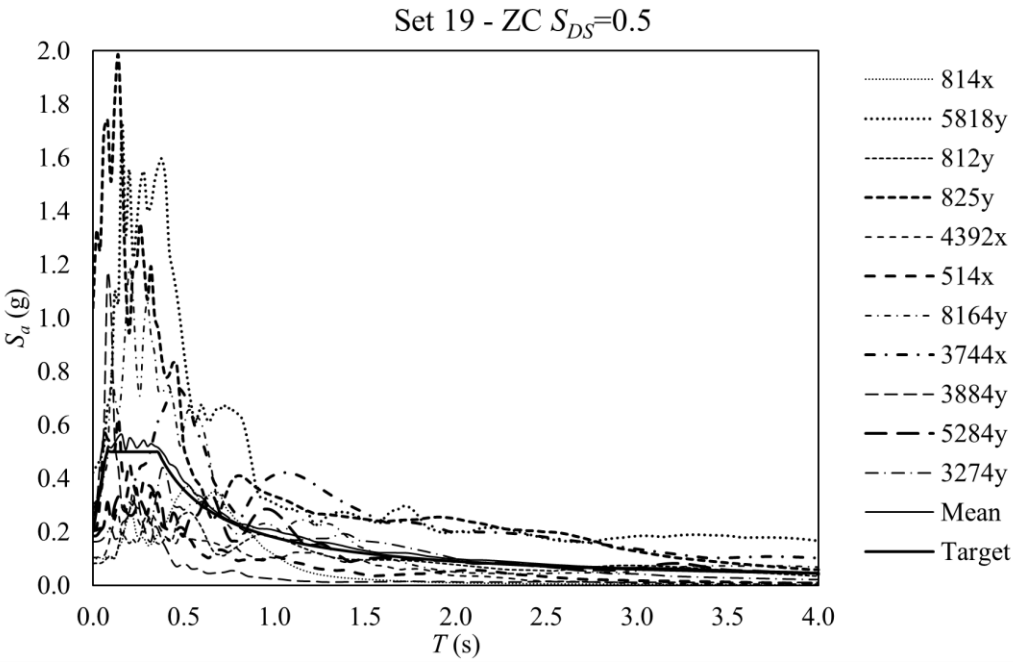

Figure B.19: Spectral acceleration of the ground motion records of Set 19 and their mean and target spectrum

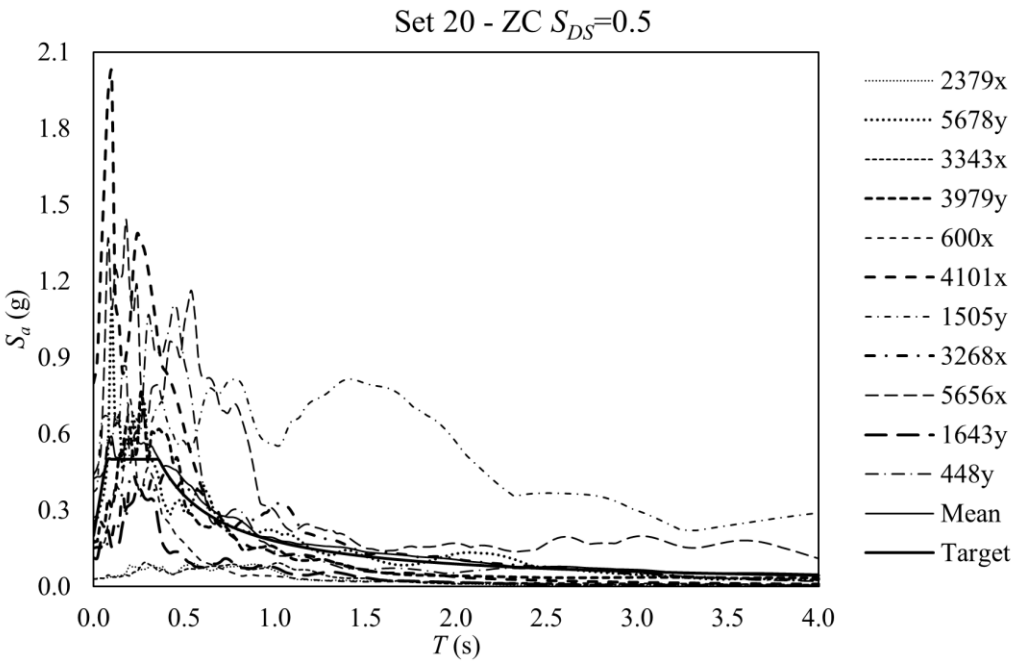

Figure B.20: Spectral acceleration of the ground motion records of Set 20 and their mean and target spectrum

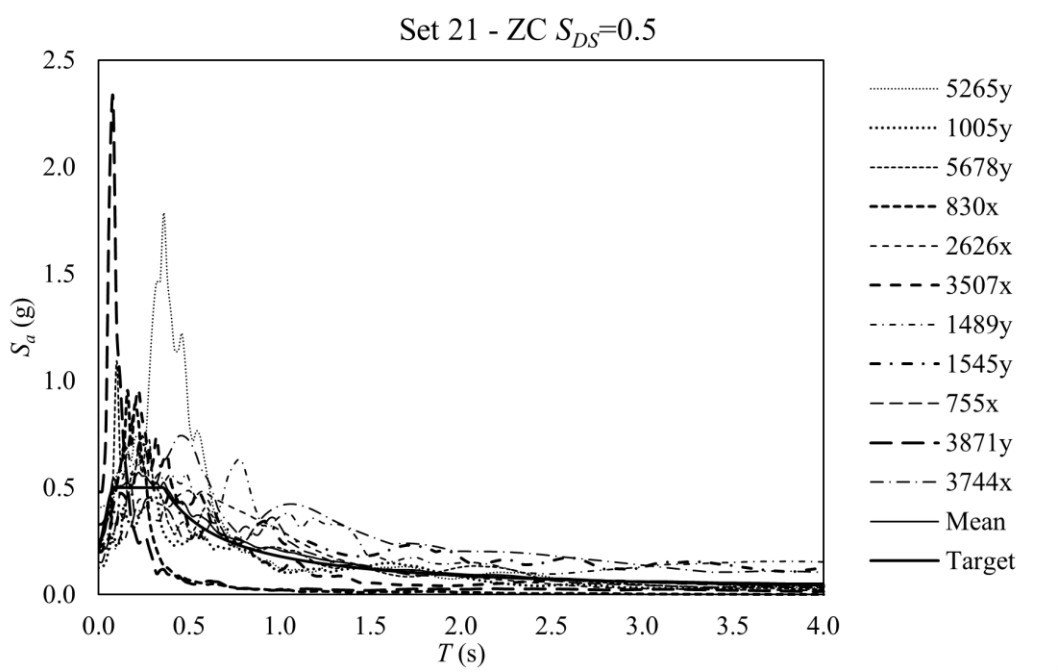

Figure B.21: Spectral acceleration of the ground motion records of Set 21 and their mean and target spectrum

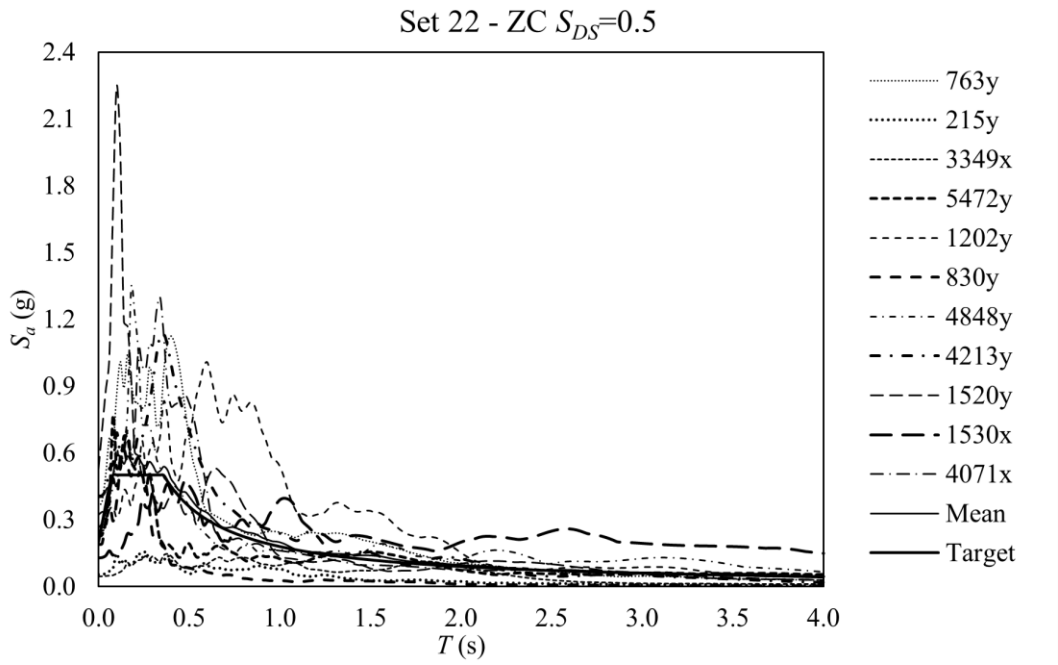

Figure B.22: Spectral acceleration of the ground motion records of Set 22 and their mean and target spectrum

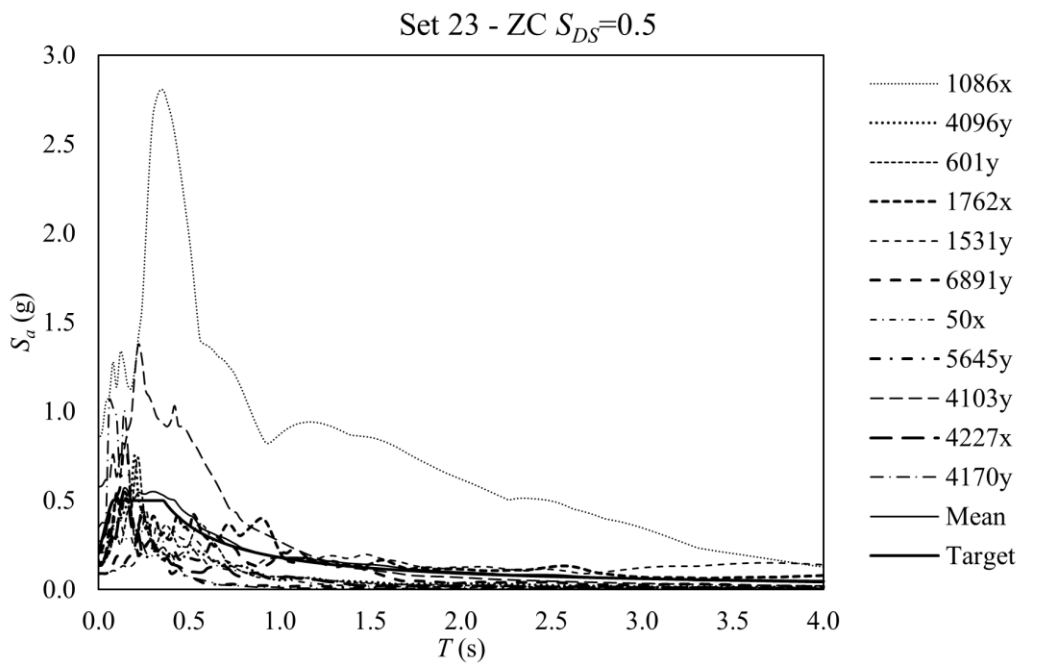

Figure B.23: Spectral acceleration of the ground motion records of Set 23 and their mean and target spectrum

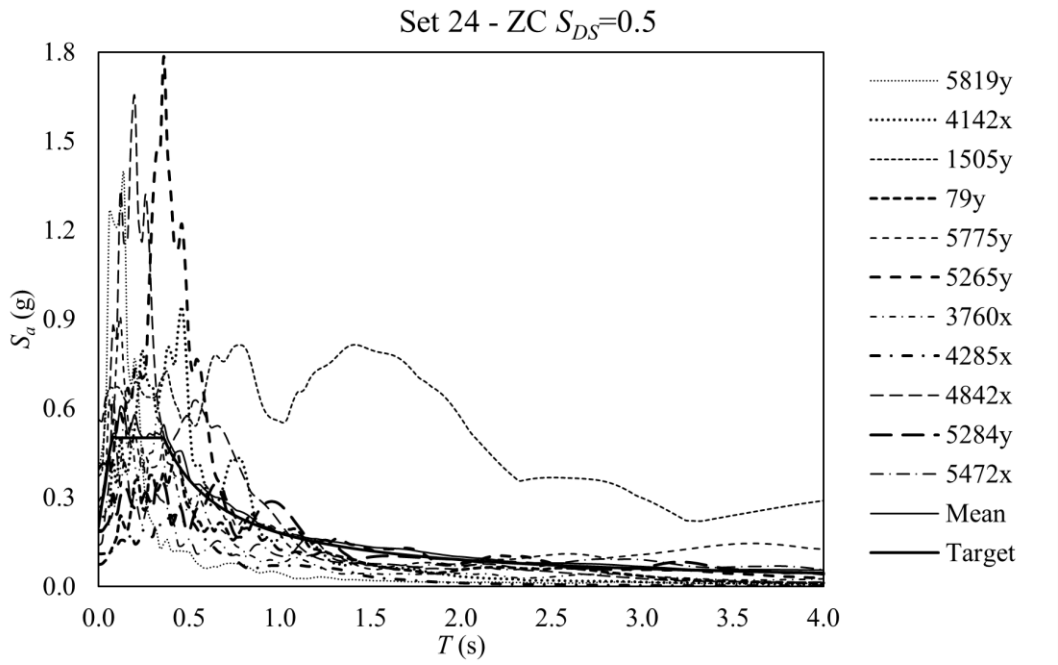

Figure B.24: Spectral acceleration of the ground motion records of Set 24 and their mean and target spectrum

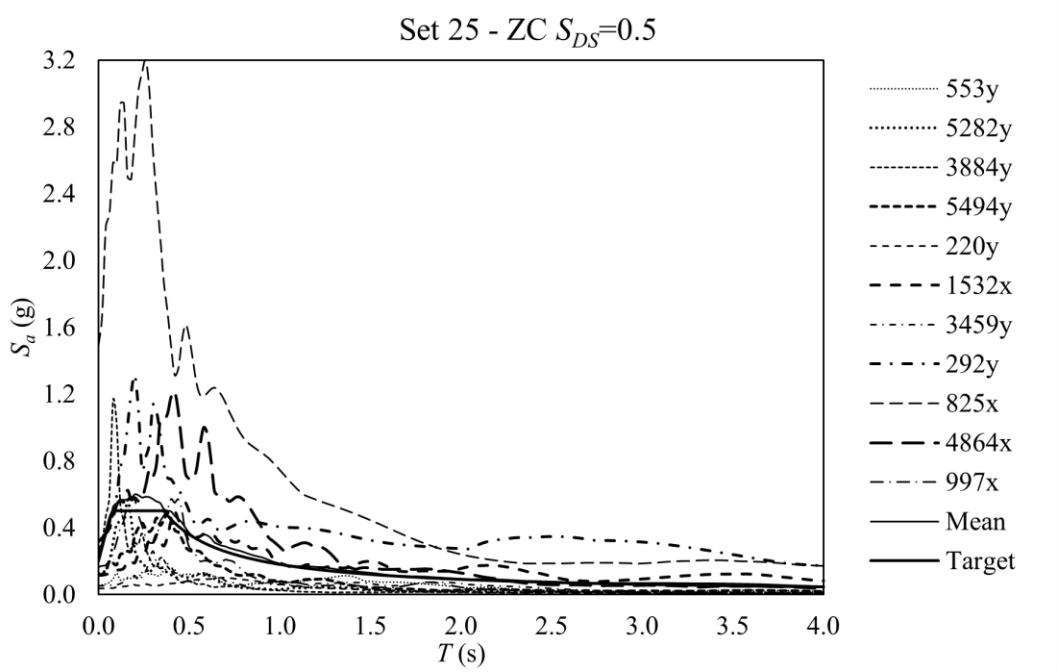

Figure B.25: Spectral acceleration of the ground motion records of Set 25 and their mean and target spectrum

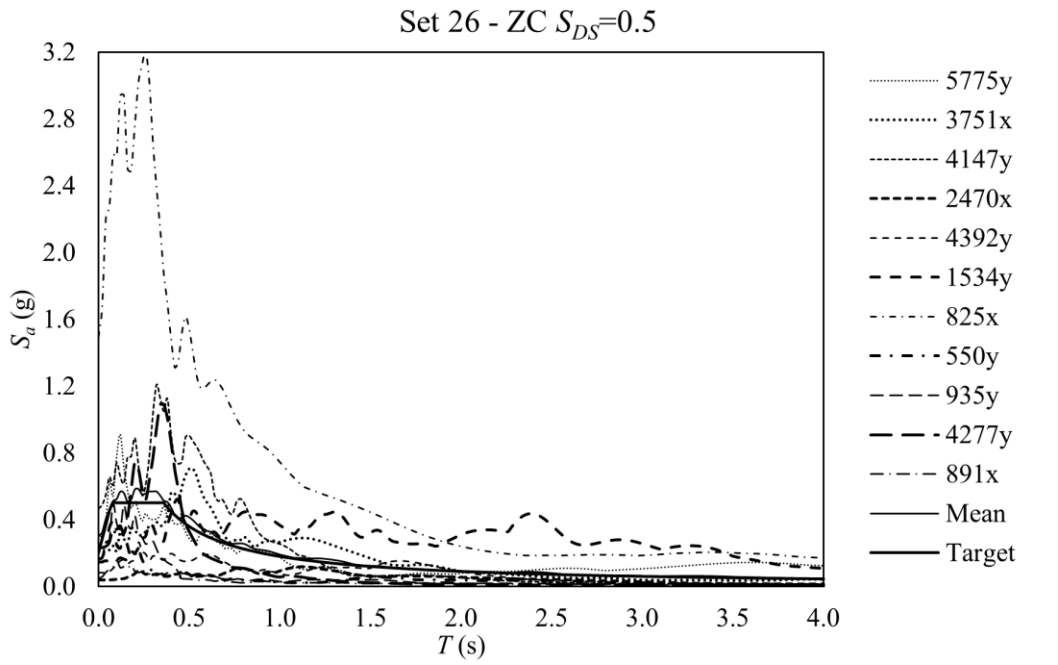

Figure B.26: Spectral acceleration of the ground motion records of Set 26 and their mean and target spectrum

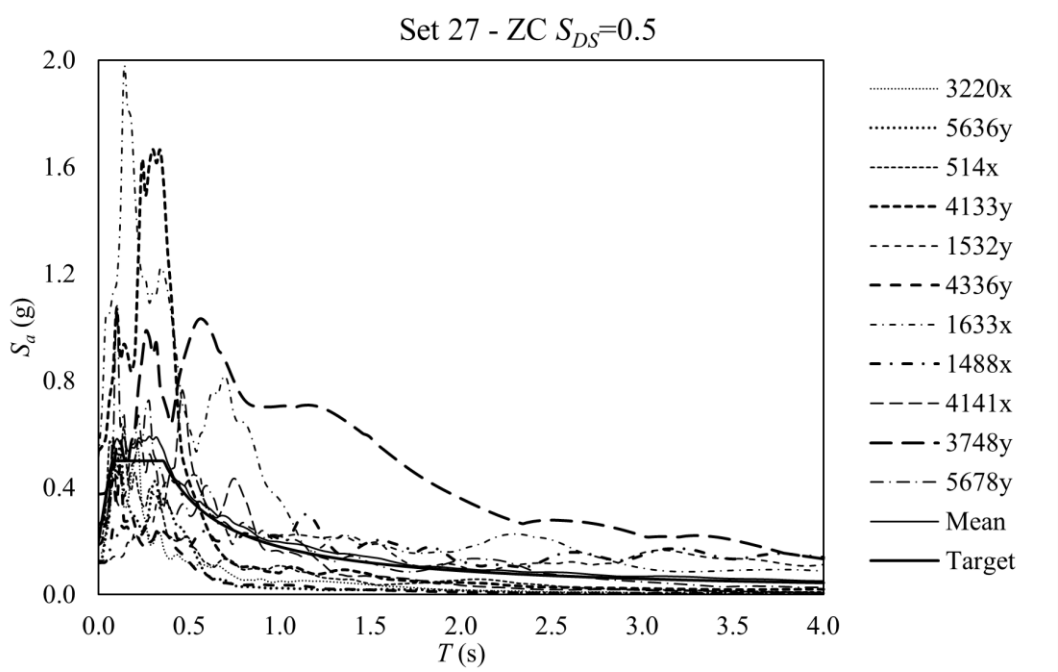

Figure B.27: Spectral acceleration of the ground motion records of Set 27 and their mean and target spectrum

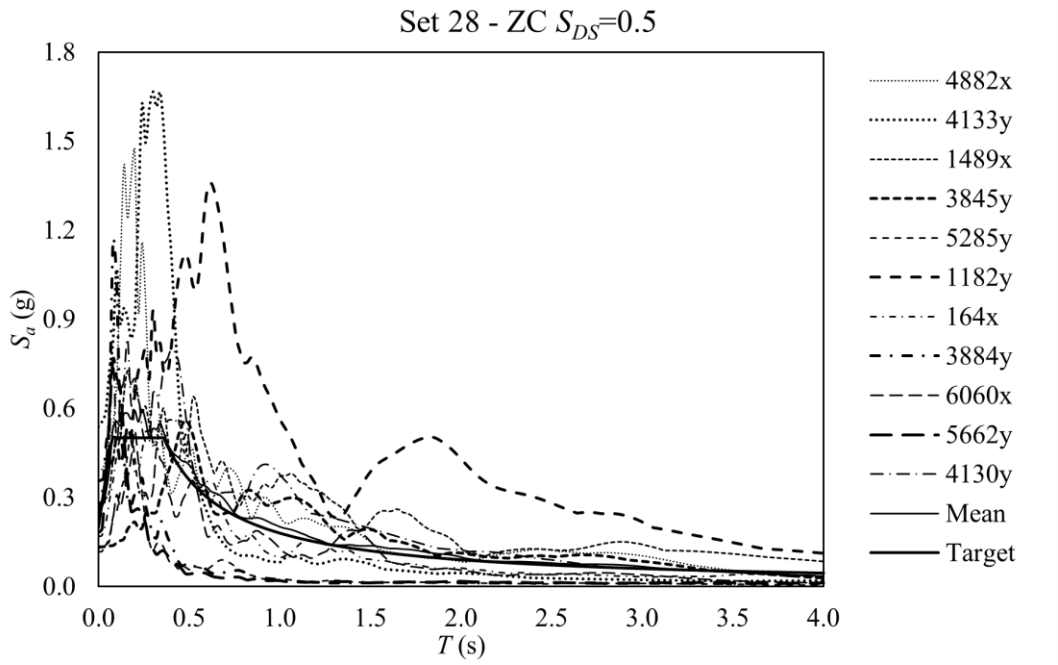

Figure B.28: Spectral acceleration of the ground motion records of Set 28 and their mean and target spectrum

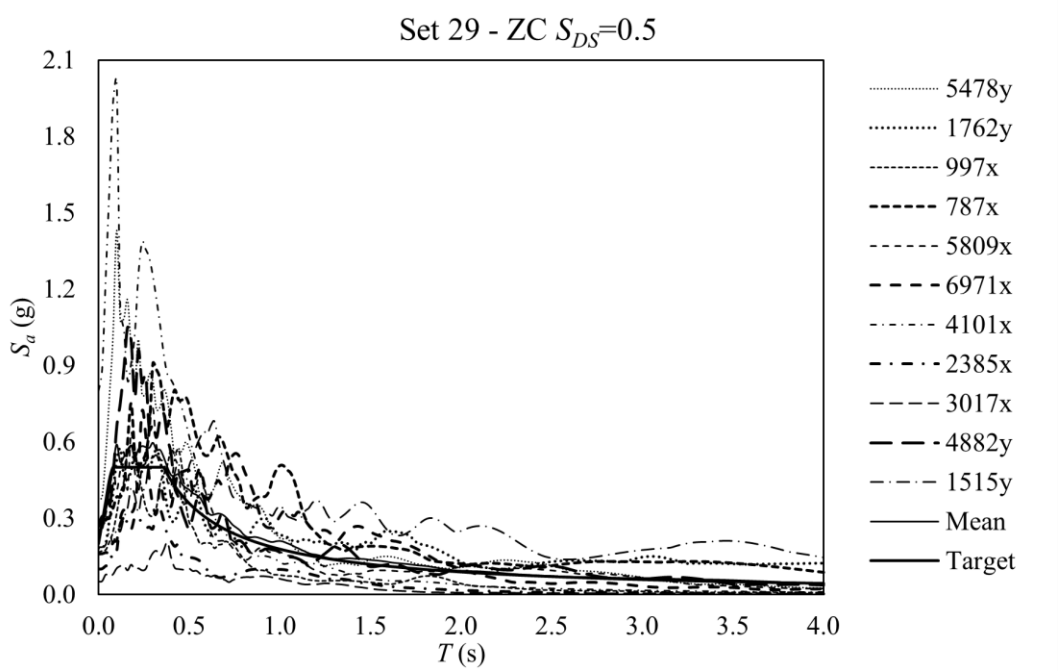

Figure B.29: Spectral acceleration of the ground motion records of Set 29 and their mean and target spectrum

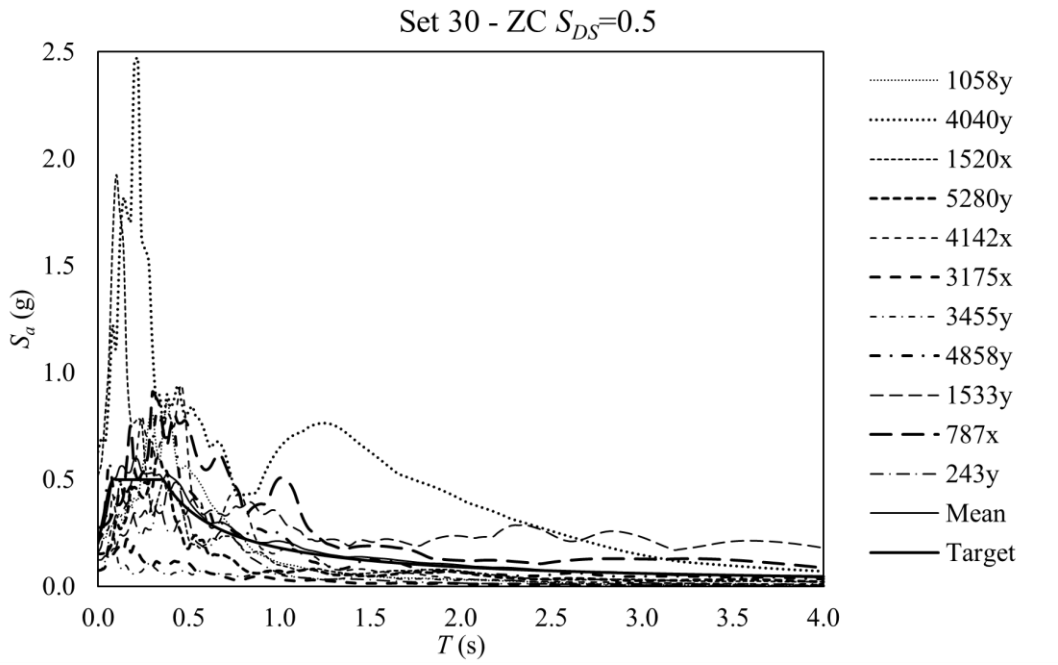

Figure B.30: Spectral acceleration of the ground motion records of Set 30 and their mean and target spectrum

B.2 Soil Class D and SDC3

Table B.6 list the records selected for Soil Class D and SDC3.

Table B.4: Ground motion record sets 1-10 for Soil Class D and SDC3

Set 1	**Set 2**	**Set 3**	**Set 4**	**Set 5**	**Set 6**	**Set 7**	**Set 8**	**Set 9**	**Set 10**
1110y	3850y	1602x	126y	5823y	634x	2507y	5780x	209x	412y
2752x	167y	126y	8755y	4115x	4881x	180y	126y	179y	5825x
3467x	4879y	4880x	5777y	5969y	68x	1552x	6962y	1543y	4081x
6893y	316y	3724y	599y	5652y	34y	412x	2411y	8118x	5829y
5827x	778y	343x	3856x	8843x	953y	200y	949x	633y	561x
171x	1003x	180y	1538x	5774y	5777y	4889x	202x	1077x	4102y
725y	126x	3467y	68x	646x	1540x	165x	5827x	3362y	1045x
547y	770y	1240x	3032y	730y	406y	723x	2998x	411x	993y
4208y	737x	523x	1063y	126y	1000x	803x	8771x	725y	757y
3963y	5825x	8118x	406y	182y	757x	984x	30x	2618x	1110y
1000x	2899x	4136x	8075y	167x	1063x	183x	3566y	126y	8102x

Table B.5: Ground motion record sets 11-20 for Soil Class D and SDC3

Set 11	**Set 12**	**Set 13**	**Set 14**	**Set 15**	**Set 16**	**Set 17**	**Set 18**	**Set 19**	**Set 20**
3692x	754y	547x	5825x	4889y	3936y	312x	171y	308x	1119y
4458x	6975x	5798x	606y	3969y	165y	602x	2754y	625x	8133x
175y	4136x	6927x	1106y	350x	167x	1003y	561y	664y	1003x
613y	8755y	397x	412x	1077y	1118y	1547x	728y	3749y	181y
6013y	2254x	6879x	173y	5836y	6927y	187x	4104x	561x	4106y
985y	1003x	1001x	8060y	1498y	5823y	171x	1101x	730y	1740y
767x	170x	5827x	341x	3754y	1203x	167x	183x	1540y	4849y
5785x	1233y	183y	2467x	4861y	3570y	5827y	31y	1646y	6874x
1176y	3467x	1101x	180y	5249x	1107y	1498x	993y	4894y	5805y
4102y	1602x	1754x	625x	5969y	3830y	692y	558y	181y	5836y
6927x	6927y	1035y	724x	6966x	5836y	3963y	411x	1491x	355x

Table B.6: Ground motion record sets 21-30 for Soil Class D and SDC3

Set 21	**Set 22**	**Set 23**	**Set 24**	**Set 25**	**Set 26**	**Set 27**	**Set 28**	**Set 29**	**Set 30**
5975y	611x	11x	502y	4134y	5838x	611y	1119x	1602x	30y
5805y	1203y	4861y	517y	725y	3749y	4074x	668x	93y	597x
764y	767x	767y	800y	4861x	5836y	777x	1543y	180y	1039x
668x	764x	978y	654x	30y	629x	310y	308y	754y	1100y
5780x	187x	2375x	4853x	183y	678y	6965x	130y	3969x	776x
170x	5969y	183x	458x	1491y	5266x	721y	8771x	462y	999y
1077x	1116y	6966x	184x	3499x	2998x	674y	3963y	147y	6952y
2943x	8692y	184x	5780x	984x	4861y	6927x	180x	5780x	862x
529y	5786y	173y	719x	4889x	180y	412y	949x	169x	6927x
880y	68x	611x	1034x	958y	165x	1100y	882y	343y	645y
2752x	5825x	199x	180y	2752x	6911y	768x	406y	2744y	4134y

Figure B.30 to Figure B.60 present the plots of the acceleration spectra of the individual records, their mean and the target spectrum for Soil Class D and SDC3.

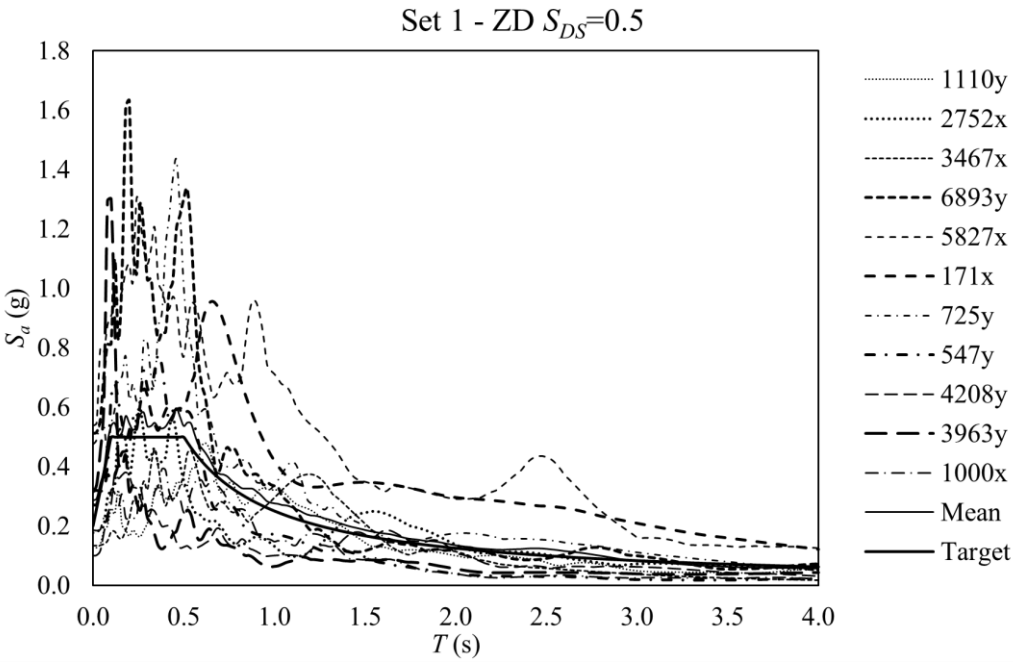

Figure B.31: Spectral acceleration of the ground motion records of Set 1 and their mean and target spectrum

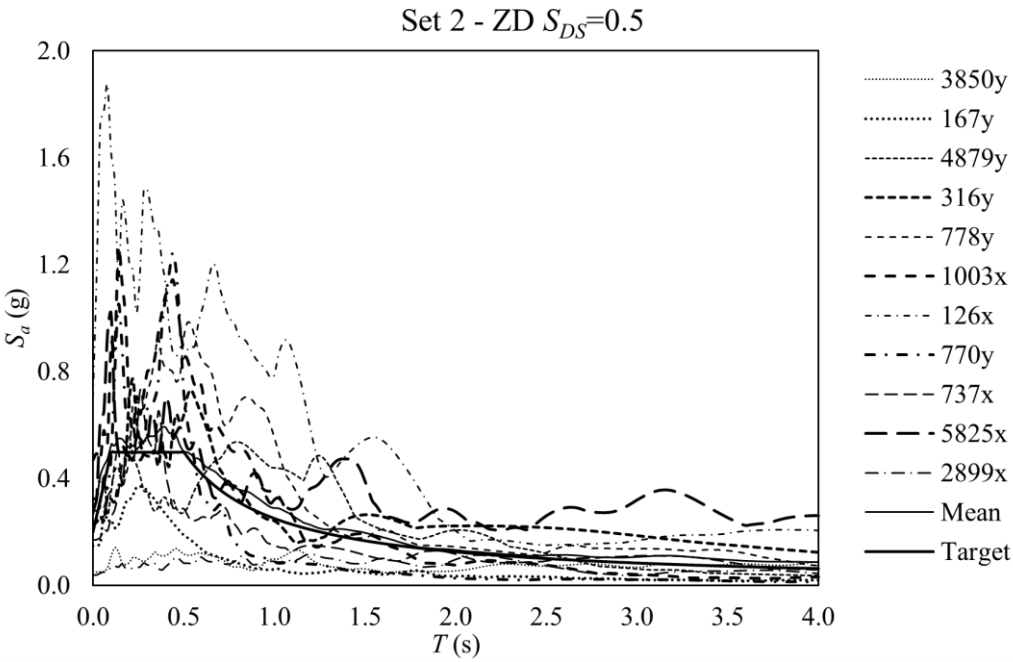

Figure B.32: Spectral acceleration of the ground motion records of Set 2 and their mean and target spectrum

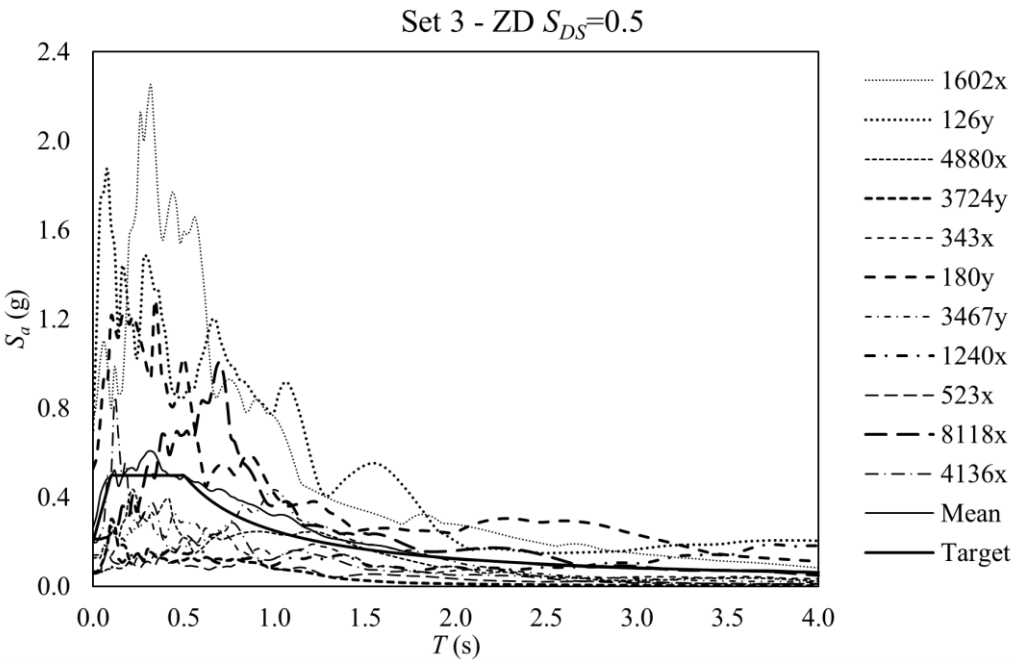

Figure B.33: Spectral acceleration of the ground motion records of Set 3 and their mean and target spectrum

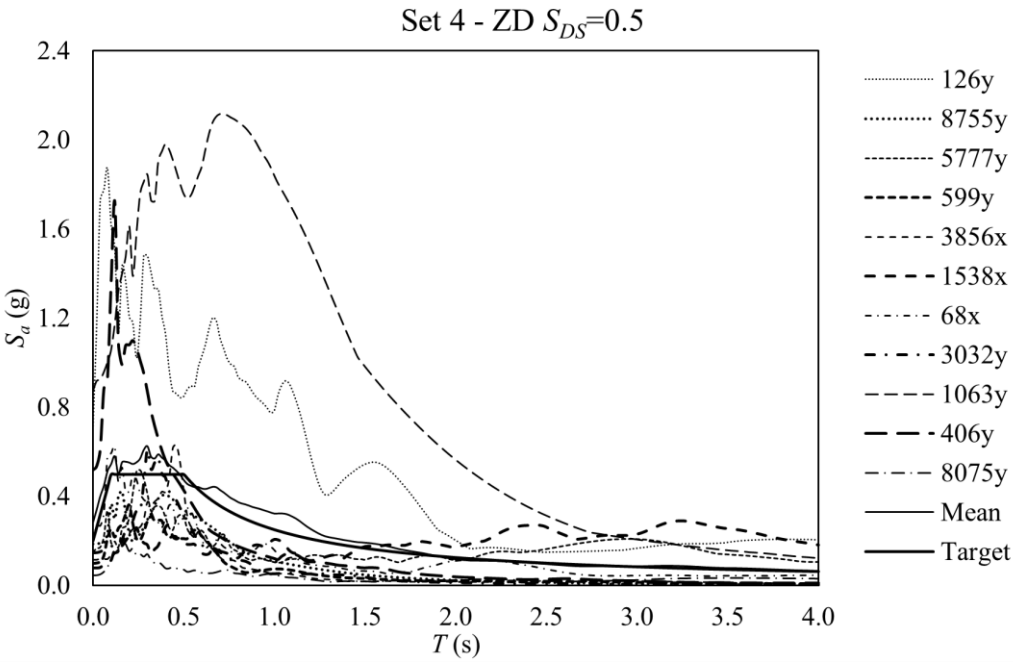

Figure B.34: Spectral acceleration of the ground motion records of Set 4 and their mean and target spectrum

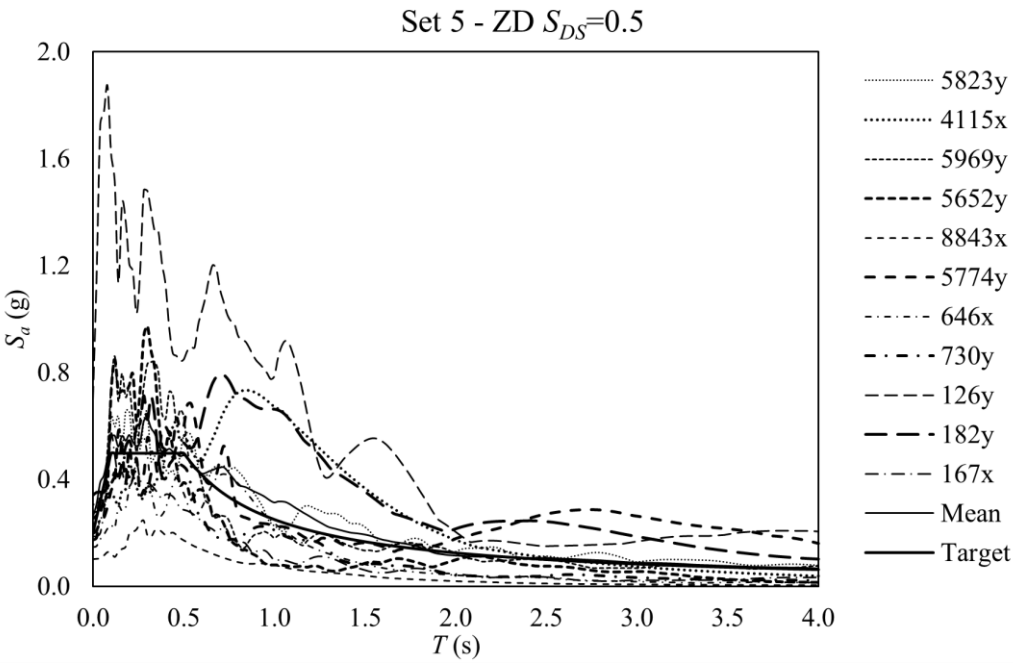

Figure B.35: Spectral acceleration of the ground motion records of Set 5 and their mean and target spectrum

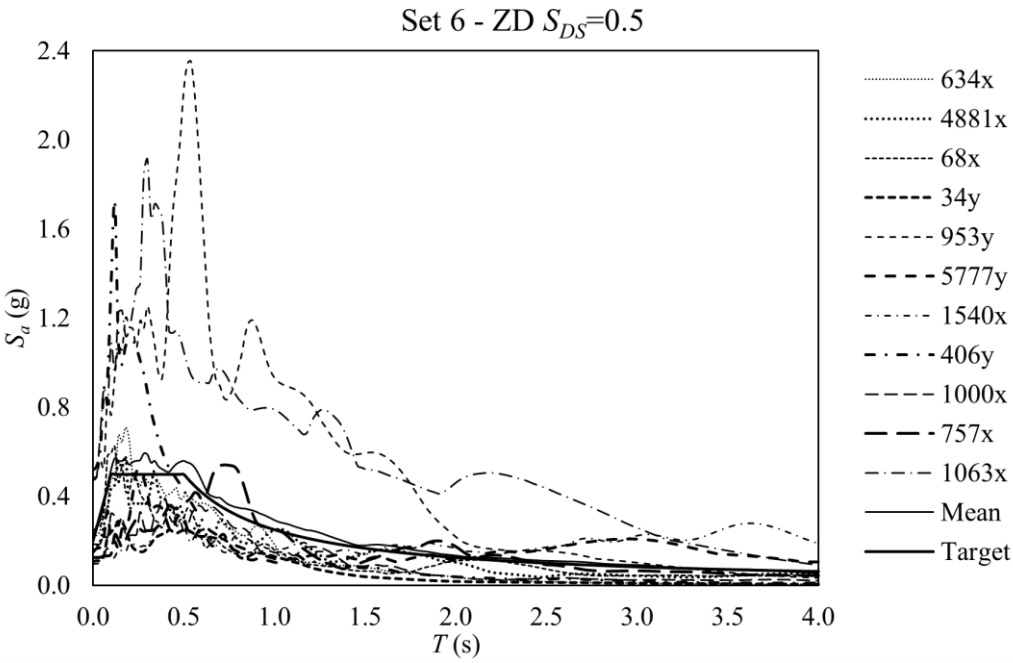

Figure B.36: Spectral acceleration of the ground motion records of Set 6 and their mean and target spectrum

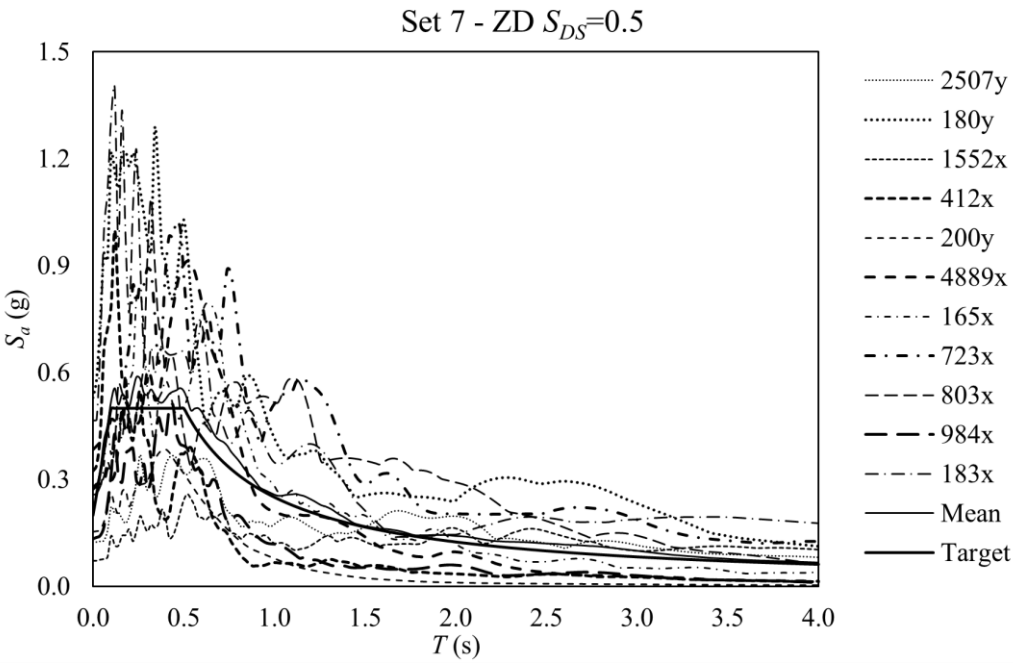

Figure B.37: Spectral acceleration of the ground motion records of Set 7 and their mean and target spectrum

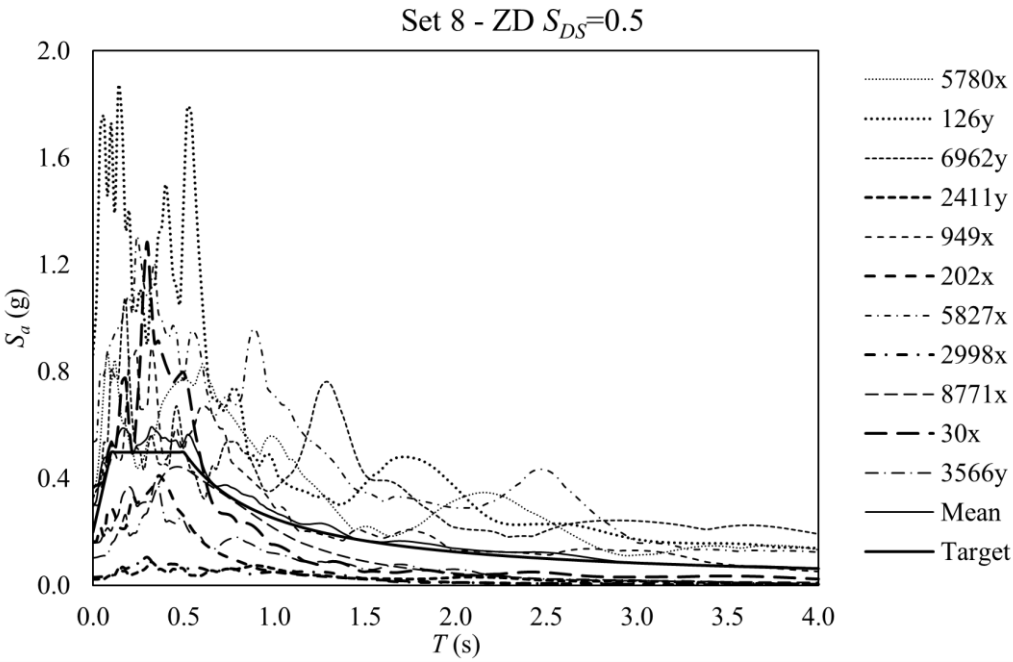

Figure B.38: Spectral acceleration of the ground motion records of Set 8 and their mean and target spectrum

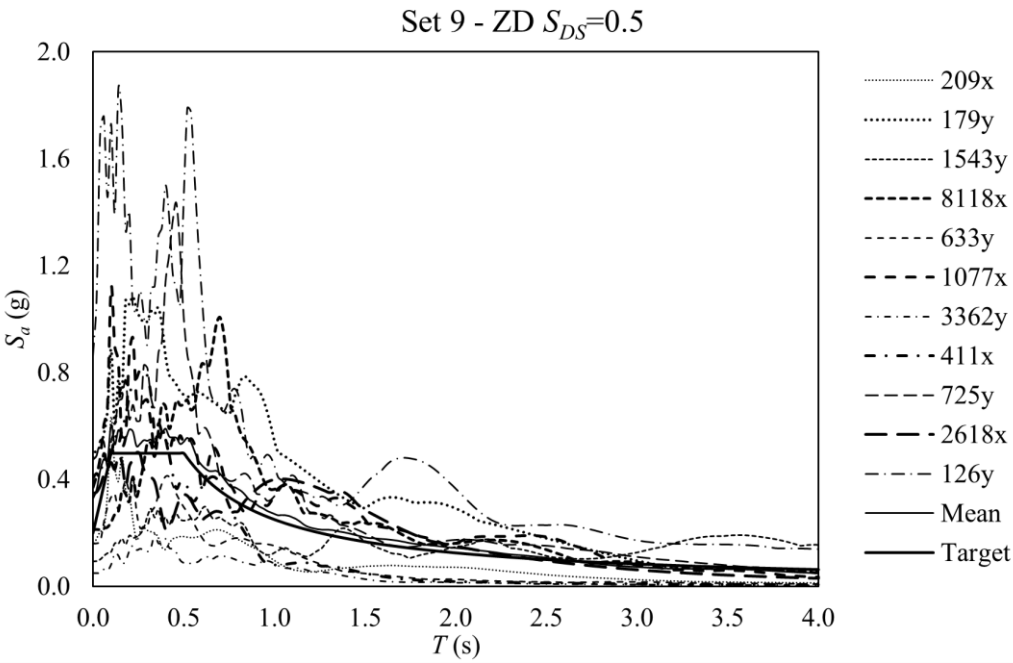

Figure B.39: Spectral acceleration of the ground motion records of Set 9 and their mean and target spectrum

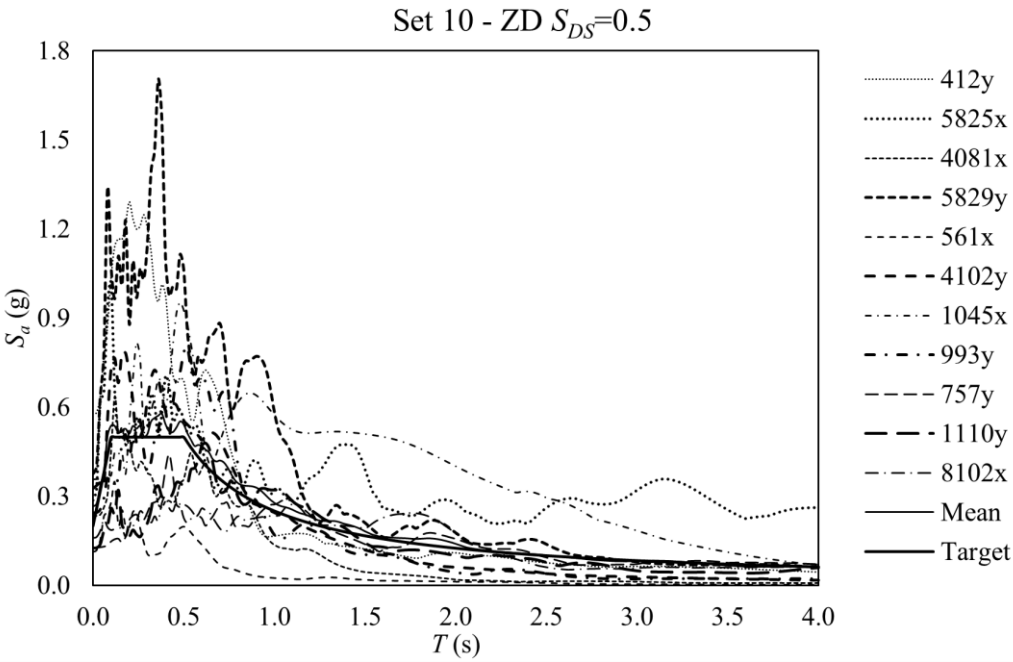

Figure B.40: Spectral acceleration of the ground motion records of Set 10 and their mean and target spectrum

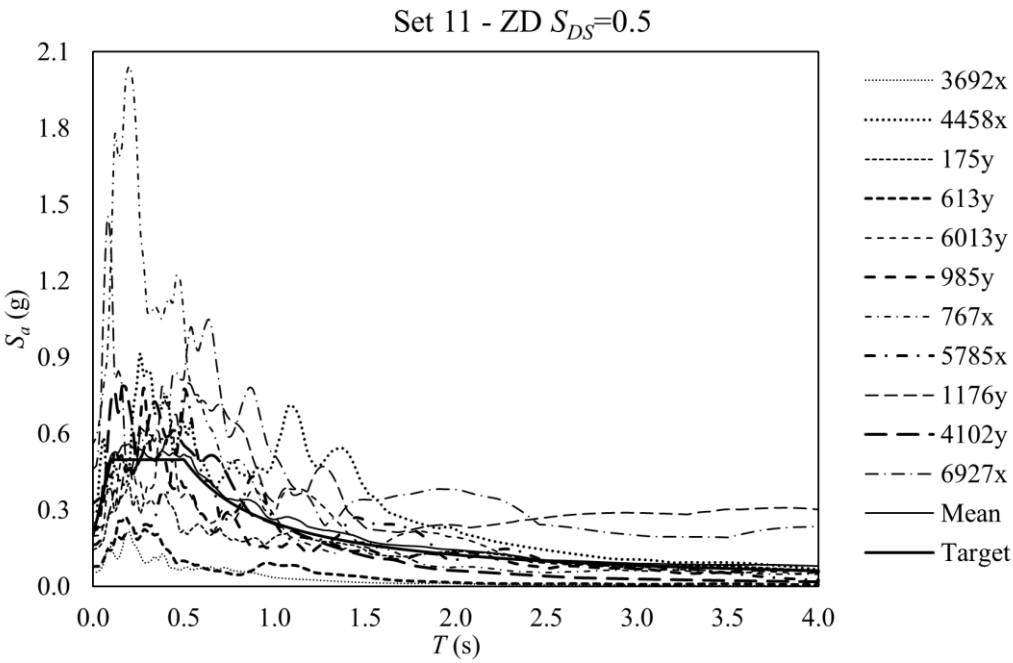

Figure B.41: Spectral acceleration of the ground motion records of Set 11 and their mean and target spectrum

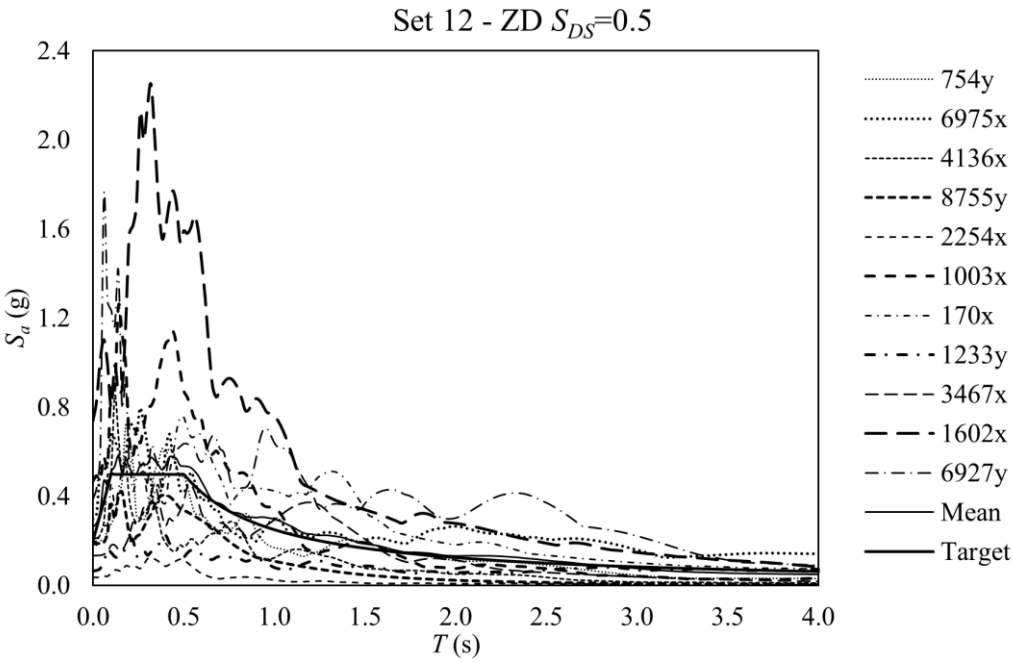

Figure B.42: Spectral acceleration of the ground motion records of Set 12 and their mean and target spectrum

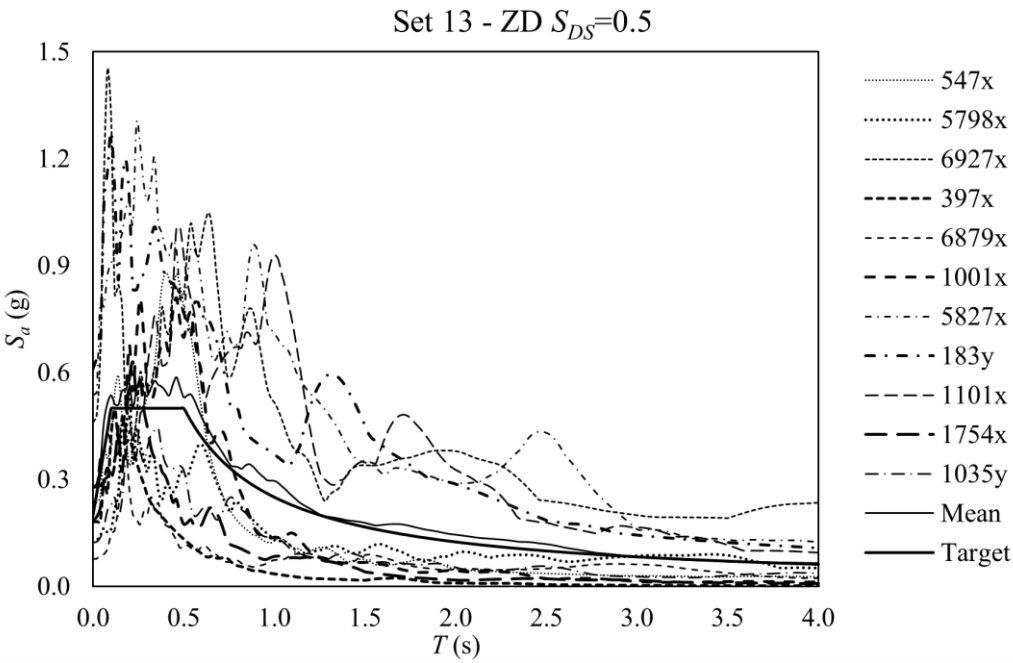

Figure B.43: Spectral acceleration of the ground motion records of Set 13 and their mean and target spectrum

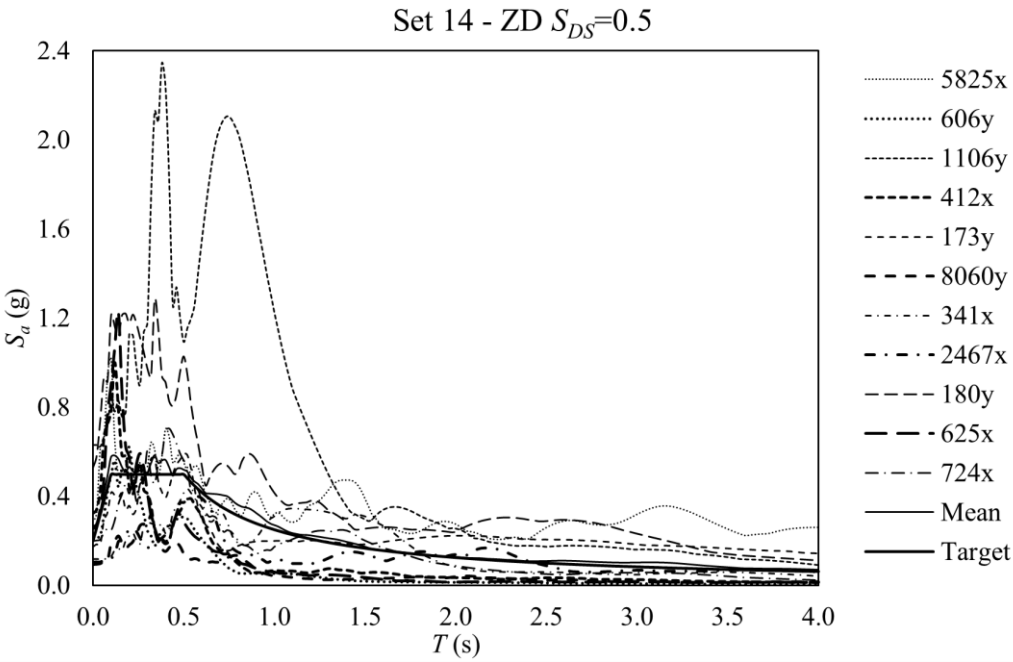

Figure B.44: Spectral acceleration of the ground motion records of Set 14 and their mean and target spectrum

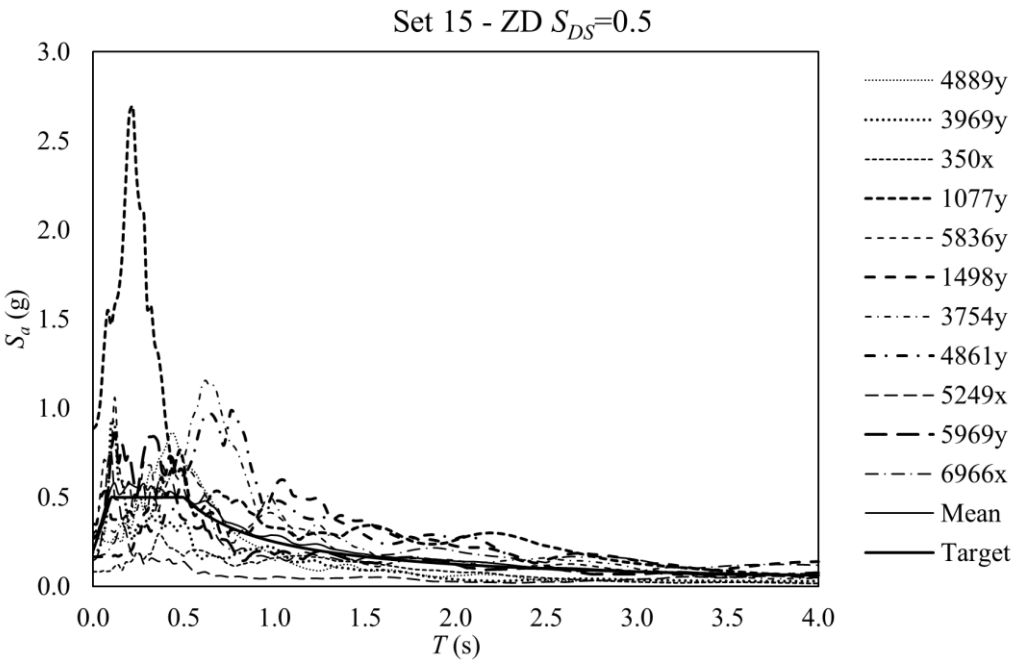

Figure B.45: Spectral acceleration of the ground motion records of Set 15 and their mean and target spectrum

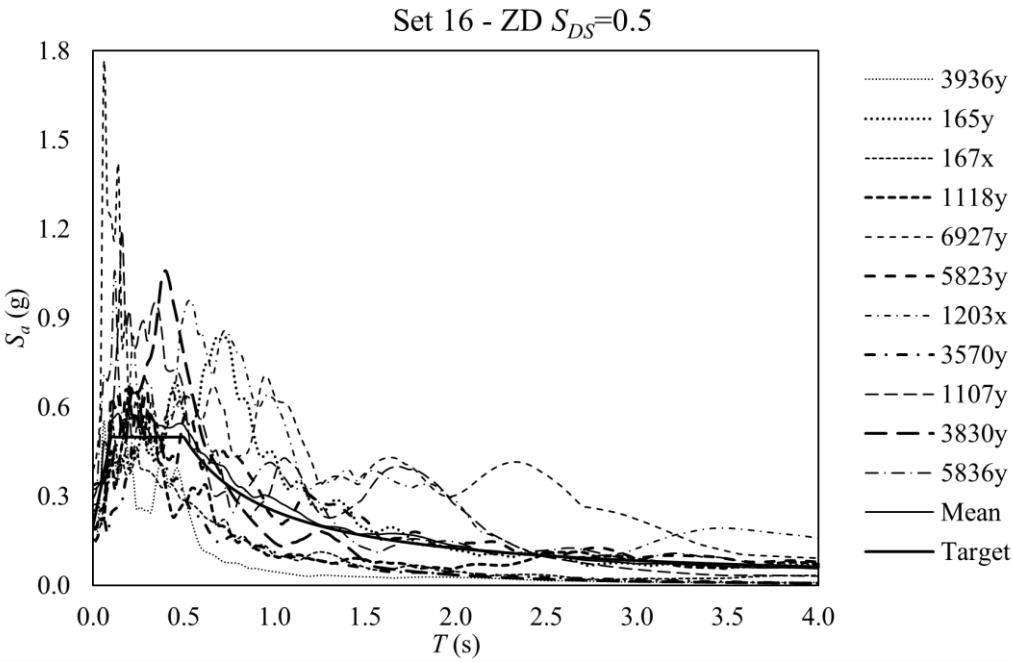

Figure B.46: Spectral acceleration of the ground motion records of Set 16 and their mean and target spectrum

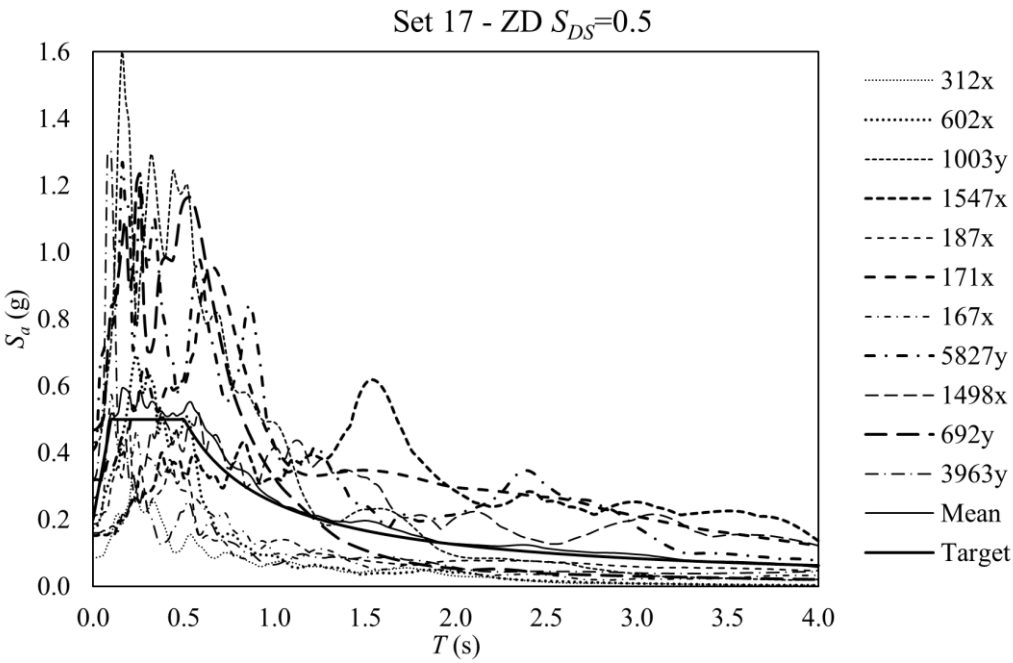

Figure B.47: Spectral acceleration of the ground motion records of Set 17 and their mean and target spectrum

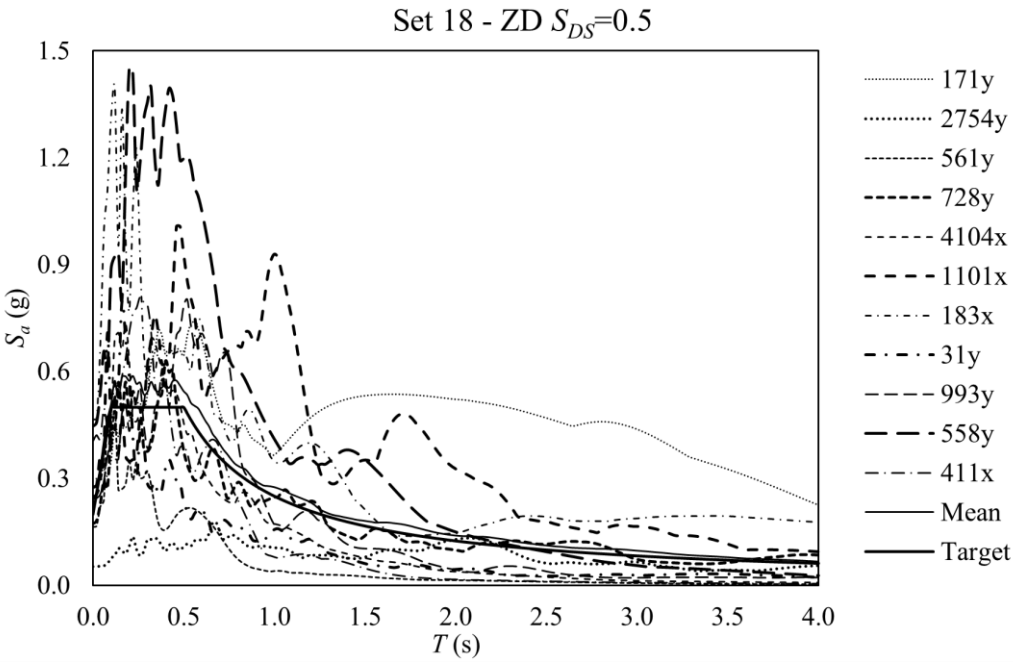

Figure B.48: Spectral acceleration of the ground motion records of Set 18 and their mean and target spectrum

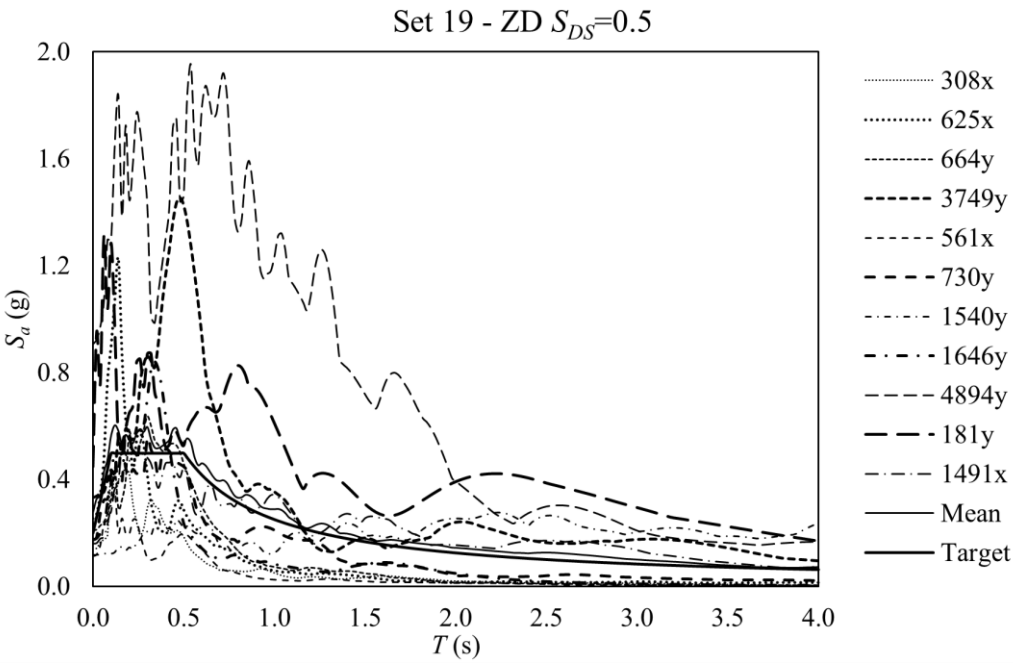

Figure B.49: Spectral acceleration of the ground motion records of Set 19 and their mean and target spectrum

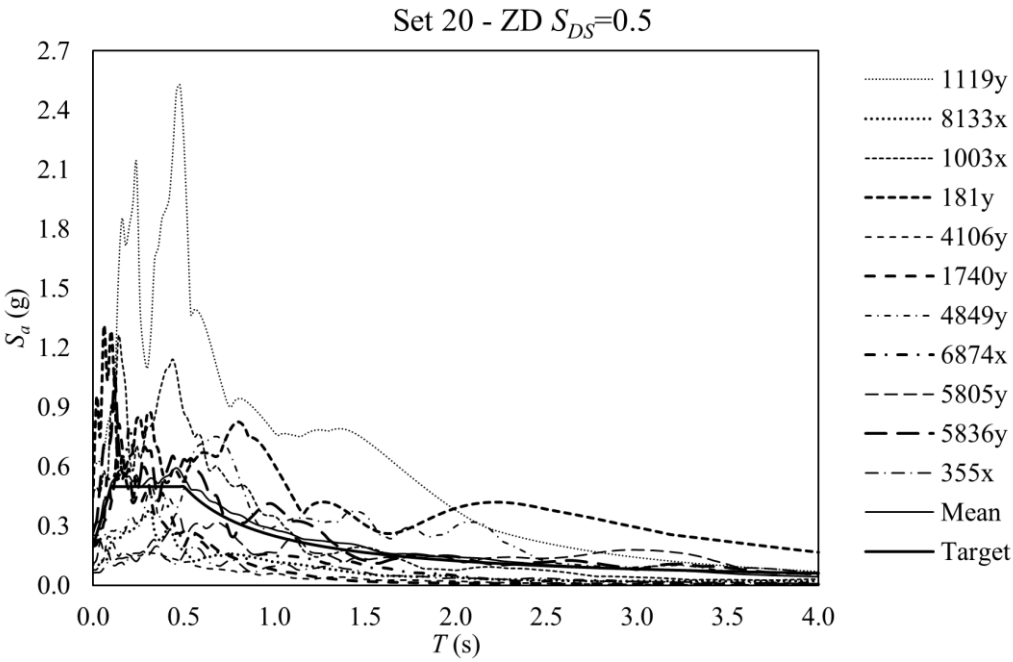

Figure B.50: Spectral acceleration of the ground motion records of Set 20 and their mean and target spectrum

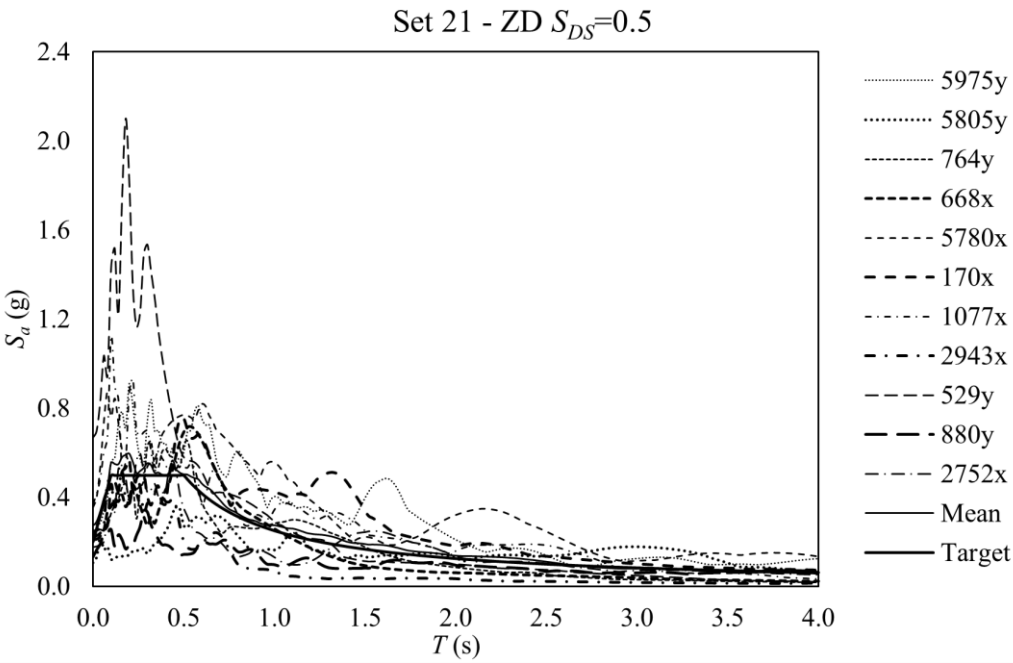

Figure B.51: Spectral acceleration of the ground motion records of Set 21 and their mean and target spectrum

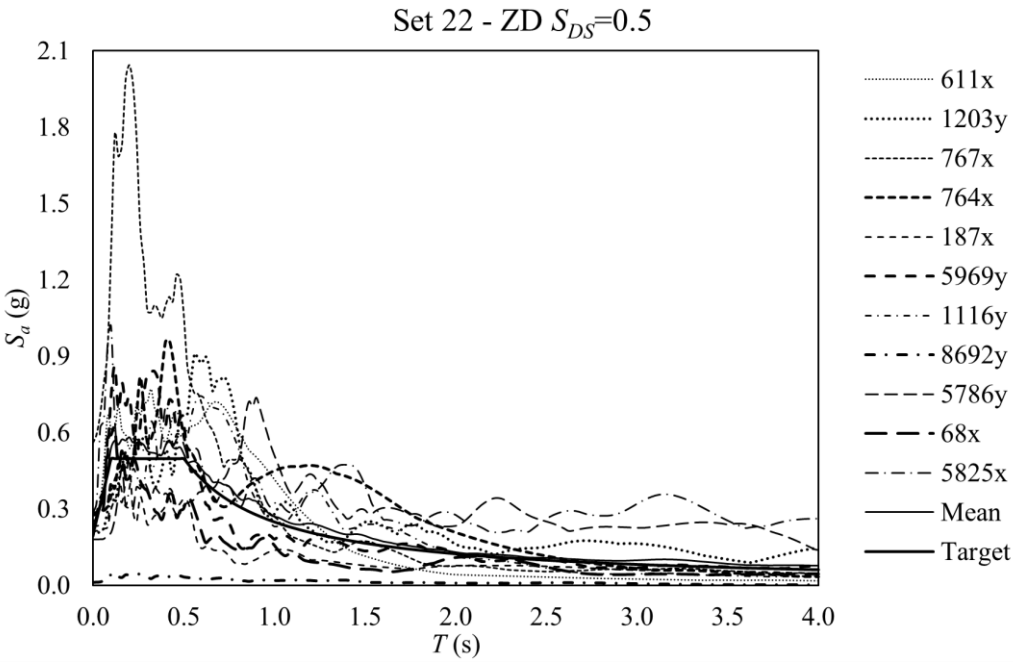

Figure B.52: Spectral acceleration of the ground motion records of Set 22 and their mean and target spectrum

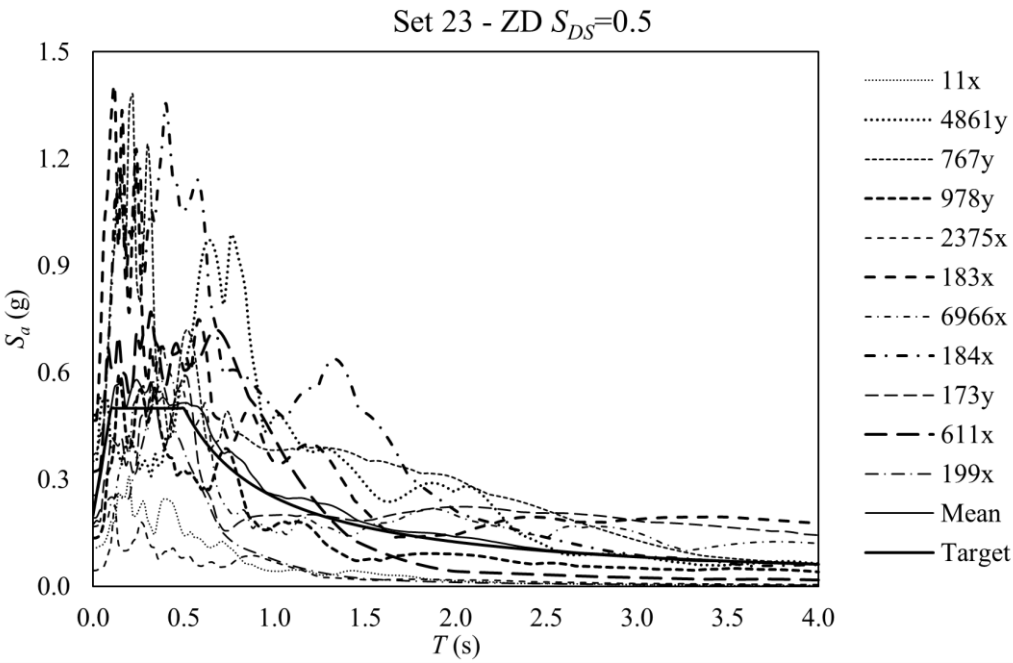

Figure B.53: Spectral acceleration of the ground motion records of Set 23 and their mean and target spectrum

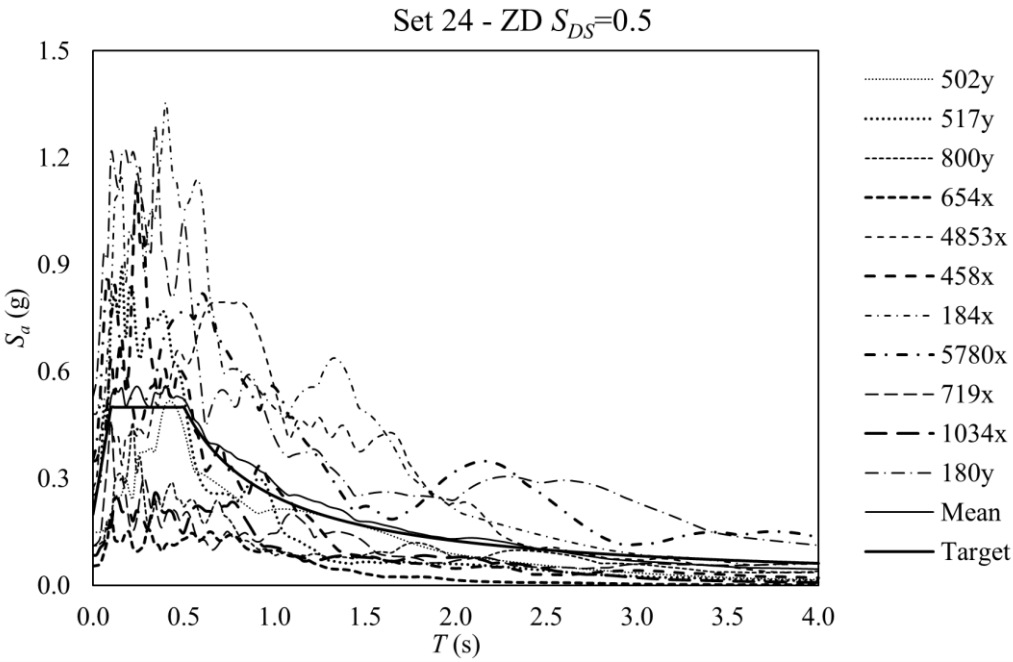

Figure B.54: Spectral acceleration of the ground motion records of Set 24 and their mean and target spectrum

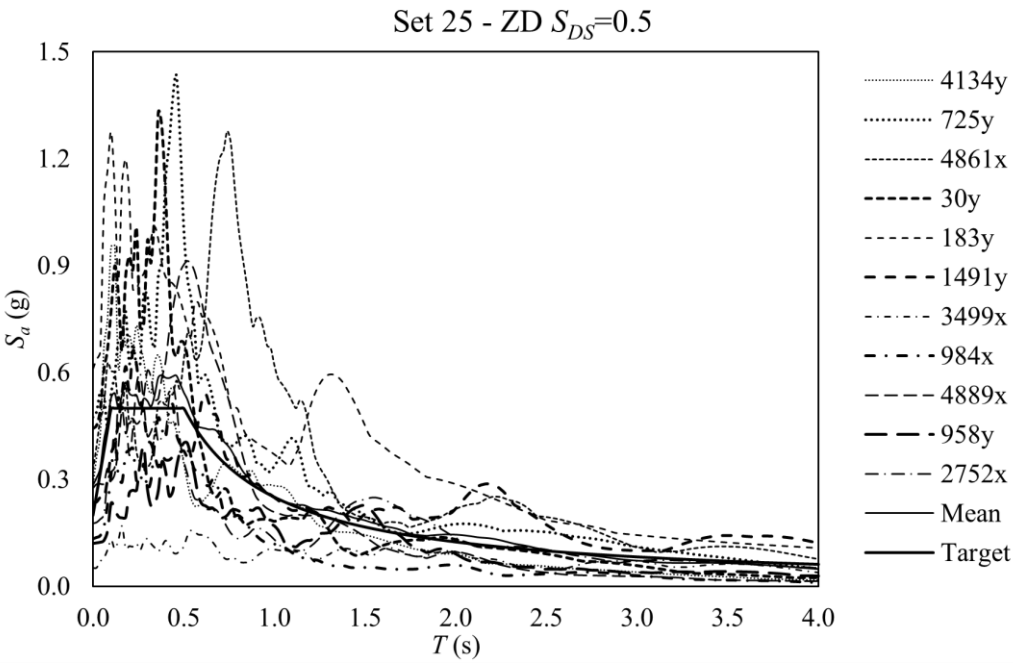

Figure B.55: Spectral acceleration of the ground motion records of Set 25 and their mean and target spectrum

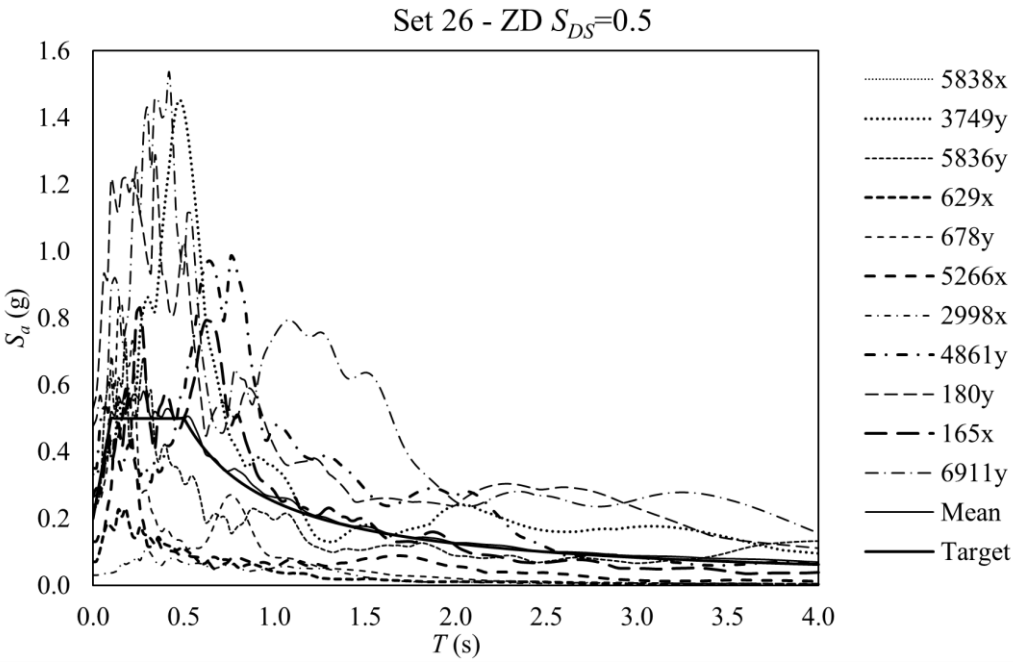

Figure B.56: Spectral acceleration of the ground motion records of Set 26 and their mean and target spectrum

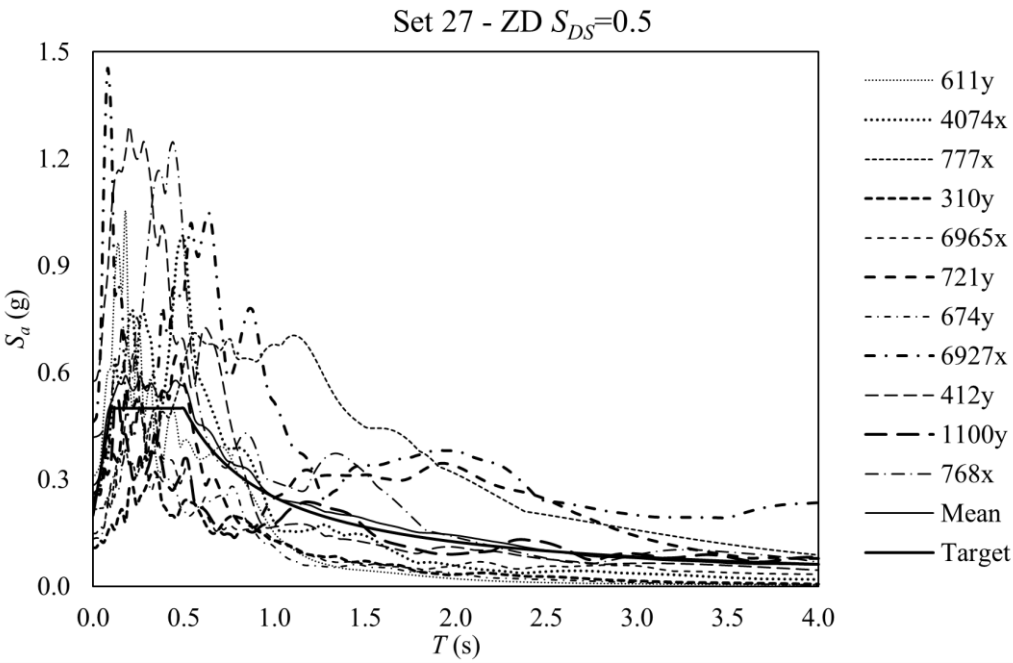

Figure B.57: Spectral acceleration of the ground motion records of Set 27 and their mean and target spectrum

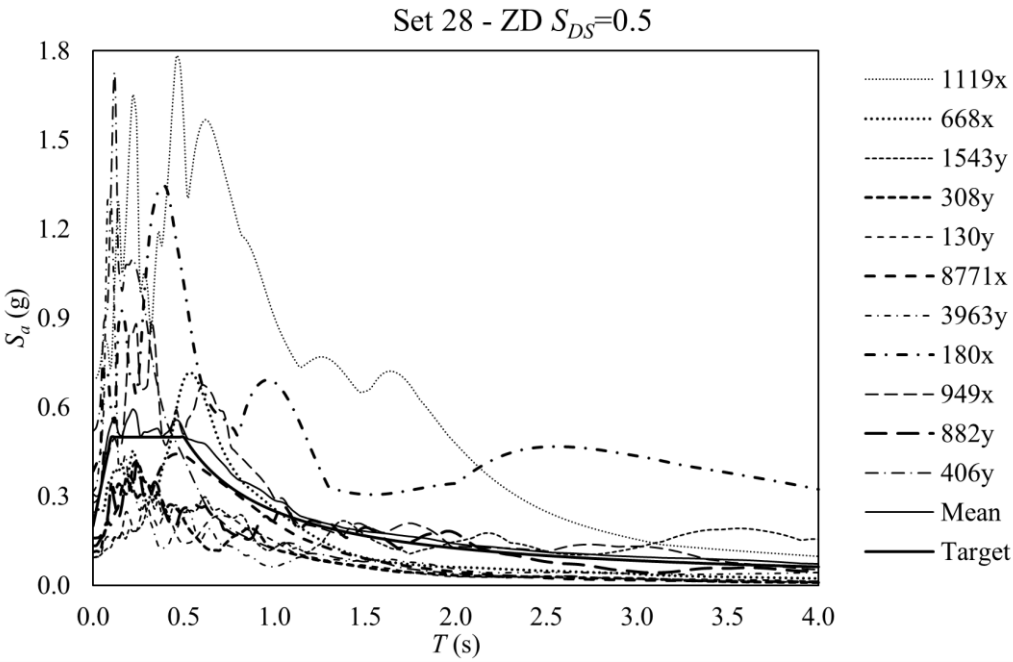

Figure B.58: Spectral acceleration of the ground motion records of Set 28 and their mean and target spectrum

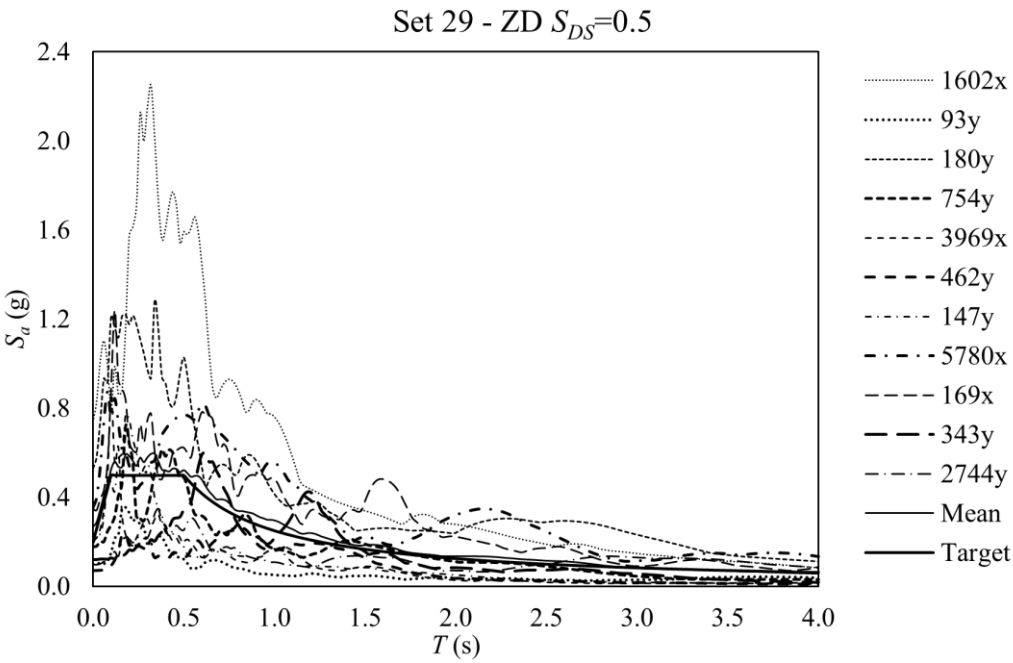

Figure B.59: Spectral acceleration of the ground motion records of Set 29 and their mean and target spectrum

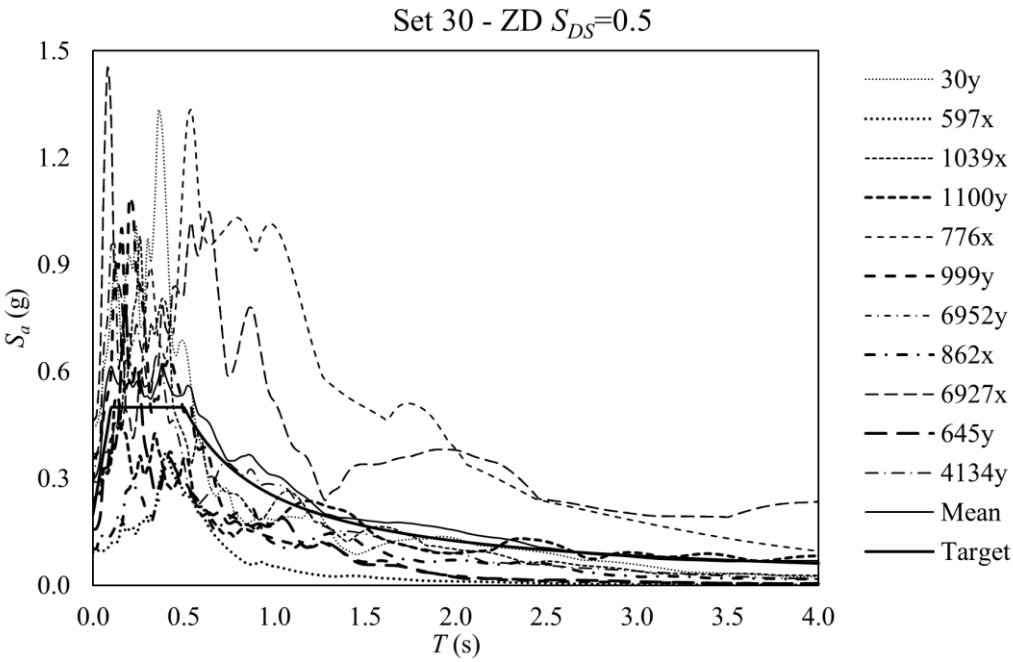

Figure B.60: Spectral acceleration of the ground motion records of Set 30 and their mean and target spectrum

B.3 Soil Class D and SDC2

Table B.8 and Table B.9 list the records selected for Soil Class D and SDC2.

Table B.7: Ground motion record sets 1-10 for Soil Class D and SDC2

Set 1	**Set 2**	**Set 3**	**Set 4**	**Set 5**	**Set 6**	**Set 7**	**Set 8**	**Set 9**	**Set 10**
767x	1118x	1003x	1100y	322x	1602x	165y	4207y	6911y	126y
1045x	174x	6927y	3512y	5829y	4066y	995y	154x	406y	172y
987x	2458x	692x	547x	171y	3935y	1077y	5825x	203x	184x
3963x	1119x	1646x	322x	1003x	5825y	5780x	5831y	529x	1491y
5831y	126y	4138y	1119x	184x	3830y	5825x	209x	723y	806y
4159x	2421y	1119y	406y	1077y	6927x	3032y	1602x	635x	5829y
5825x	3935y	6896x	126x	329y	642y	266x	3935y	4134x	6975x
681y	6927x	953y	5827x	3963y	558x	679y	595x	5829y	1119y
4146y	1106x	6y	1063x	1063y	1063x	126y	3749y	8118x	5992y
4894x	8062y	181y	5823y	6005y	1101x	180y	4894y	6893y	530x
182x	4081y	183y	169y	561y	1495x	1106x	1063x	3749y	4136x

Table B.8: Ground motion record sets 11-20 for Soil Class D and SDC2

Set 11	**Set 12**	**Set 13**	**Set 14**	**Set 15**	**Set 16**	**Set 17**	**Set 18**	**Set 19**	**Set 20**
4894x	562x	4066y	998x	4098x	692y	3963y	5827x	4894x	692x
6927y	3504x	6927y	6927y	184x	3735y	682x	406y	183x	1866x
1038x	6893x	8755y	4889x	4081y	529x	949y	1203x	5988y	5992x
126y	4081y	1077y	547x	126x	725y	5836x	179x	4881y	1003x
613y	6927x	1063y	995y	3963x	768x	996x	681x	1615x	1503x
1740y	183x	4102y	1063y	960y	5801y	4849y	5992y	5780y	5827y
6962x	1057x	3749y	126y	4856x	169x	1119y	342y	3963y	2746x
1082y	180y	1003x	1540x	770y	5992x	5774y	8937x	316y	183y
5825x	682y	770x	1100y	5969y	6927x	5827x	960x	1119x	993y
681x	767y	722x	30y	1035y	721x	1602x	126y	754x	960y
559y	4894x	5825y	180y	558y	181y	183y	183x	3935x	6927x

Table B.9: Ground motion record sets 21-30 for Soil Class D and SDC2

Set 21	**Set 22**	**Set 23**	**Set 24**	**Set 25**	**Set 26**	**Set 27**	**Set 28**	**Set 29**	**Set 30**
770x	1045y	1602x	5249y	3890x	1044y	767x	985y	766x	721x
412x	692x	721y	4894x	3908x	768x	1077x	1063y	5827y	558y
4104y	5817y	184x	681y	3181x	3963y	6877y	174y	5969y	6927x
5988y	3830y	595x	6962x	6893y	126y	5992y	126y	547y	692y
4134y	721y	766x	3963x	5803x	1748x	6927x	1495x	5836x	126y
3317y	126y	181y	406y	8161y	1119y	6893y	309x	5780x	1076y
6962x	558x	767x	3843x	6927x	4861x	721y	5829x	1119x	348y
4894x	324x	5836y	1084y	184y	6927y	3969y	6927x	721y	5992y
180y	1602y	985x	960x	126y	447y	4102y	692y	558y	181y
6927x	700y	6927y	5652x	1106x	3570y	5969x	2710y	3003y	1538y
5831y	6927y	5823y	1748y	723x	5827x	6911x	68x	126x	767y

Figure B.61 to Figure B.90 present the plots of the acceleration spectra of the individual records, their mean and the target spectrum for Soil Class D and SDC2.

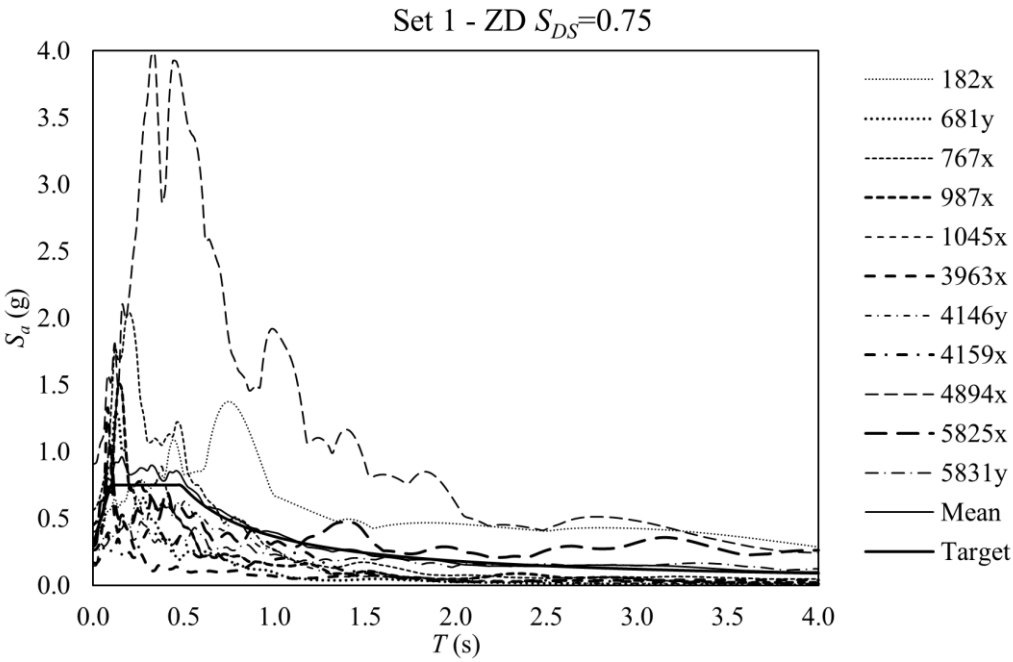

Figure B.61: Spectral acceleration of the ground motion records of Set 1 and their mean and target spectrum

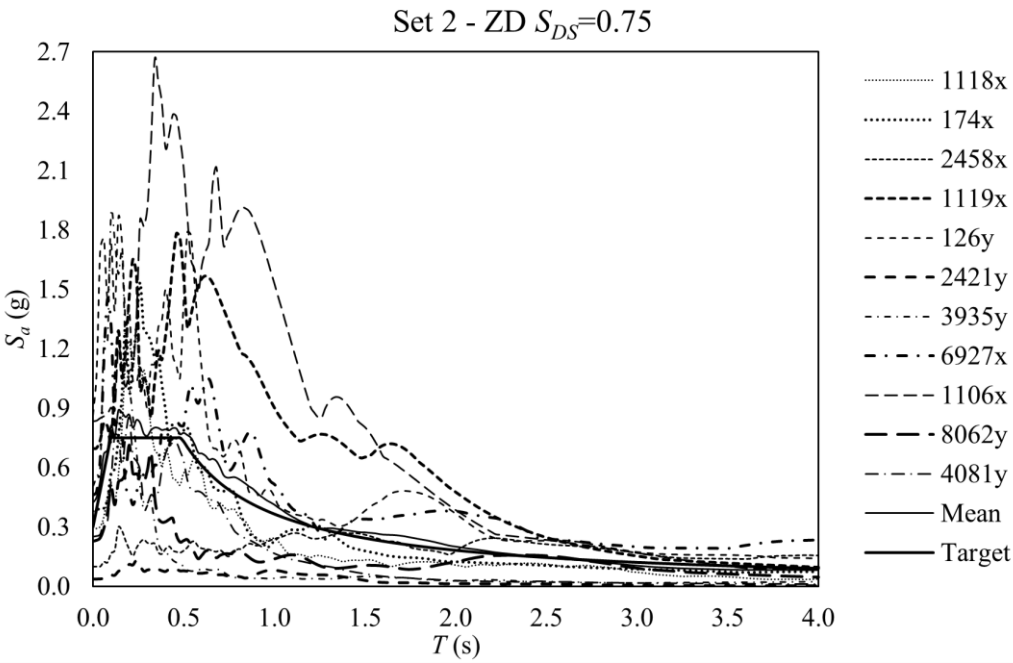

Figure B.62: Spectral acceleration of the ground motion records of Set 2 and their mean and target spectrum

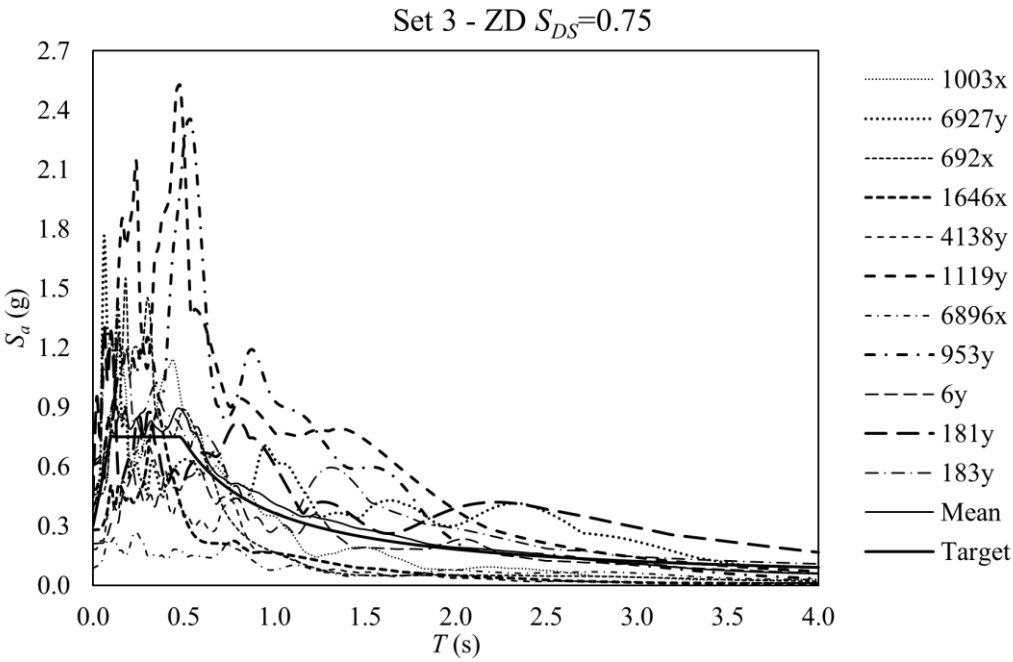

Figure B.63: Spectral acceleration of the ground motion records of Set 3 and their mean and target spectrum

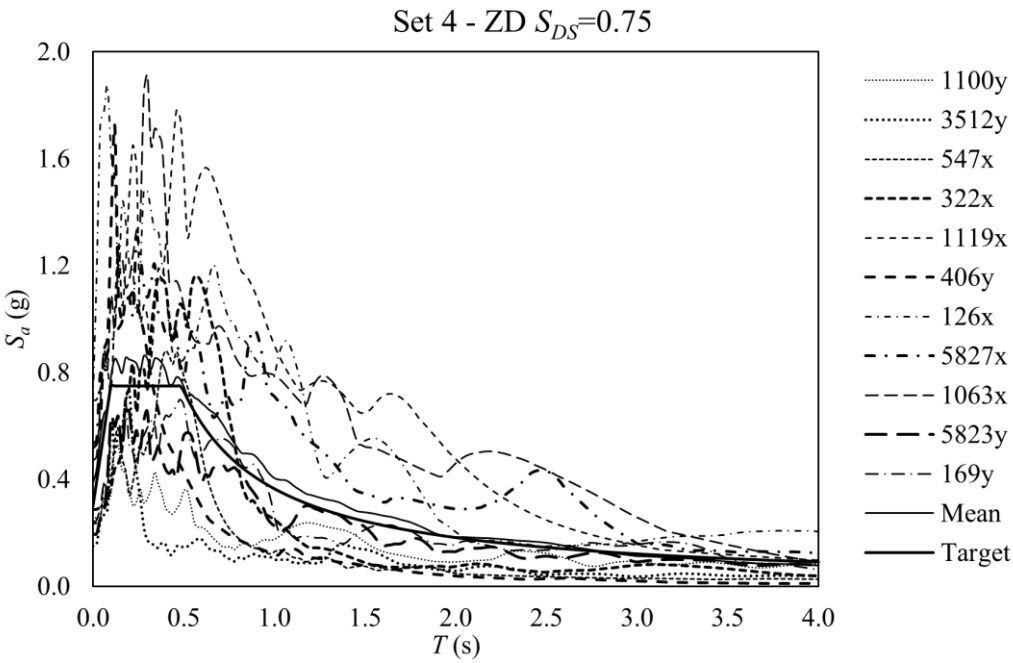

Figure B.64: Spectral acceleration of the ground motion records of Set 4 and their mean and target spectrum

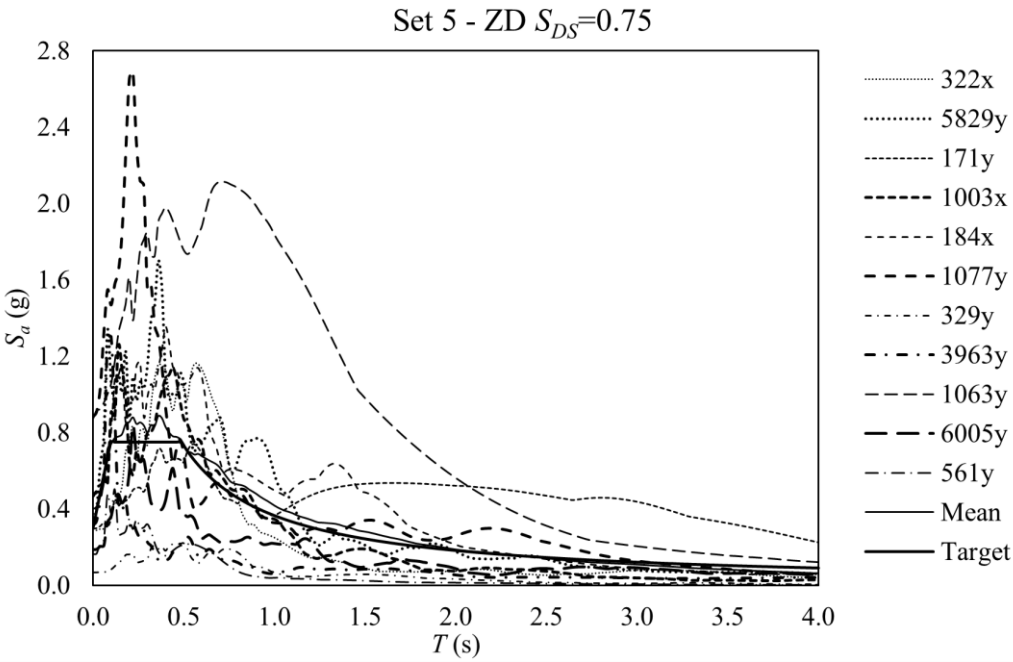

Figure B.65: Spectral acceleration of the ground motion records of Set 5 and their mean and target spectrum

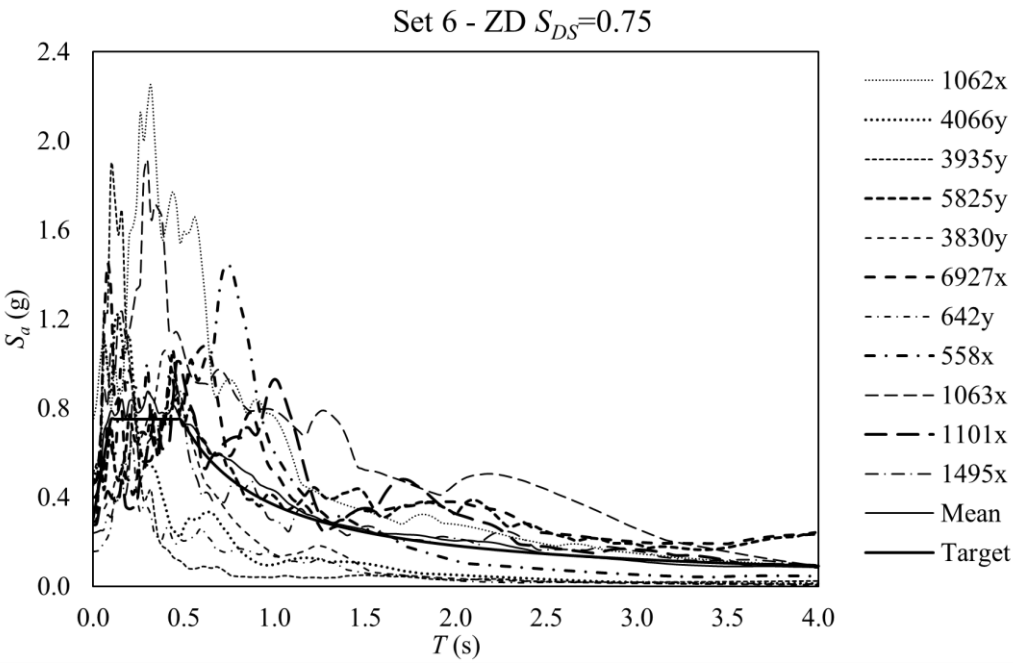

Figure B.66: Spectral acceleration of the ground motion records of Set 6 and their mean and target spectrum

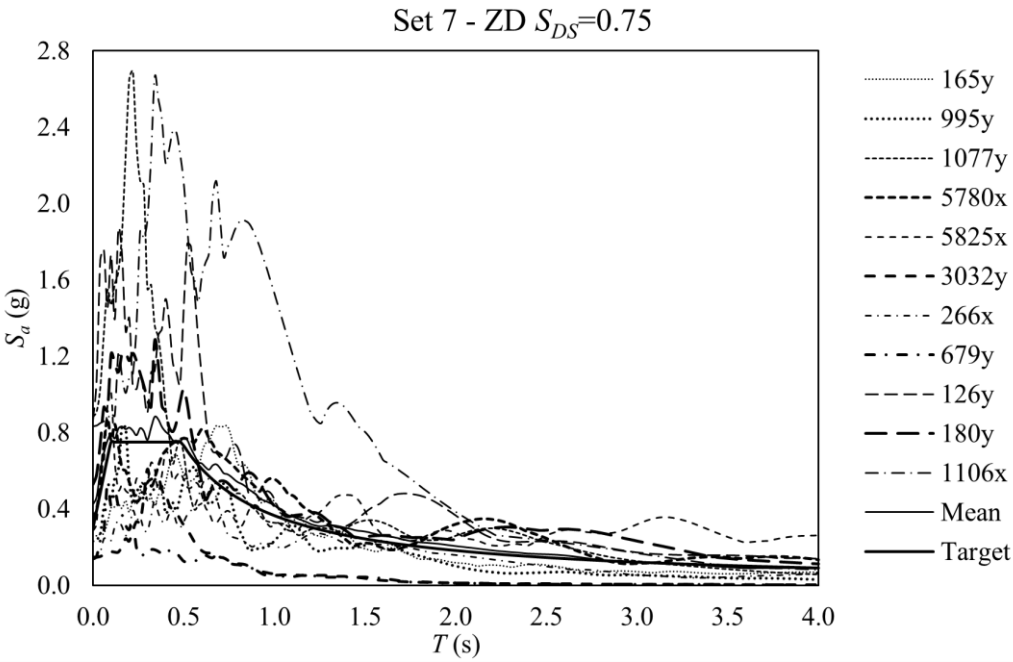

Figure B.67: Spectral acceleration of the ground motion records of Set 7 and their mean and target spectrum

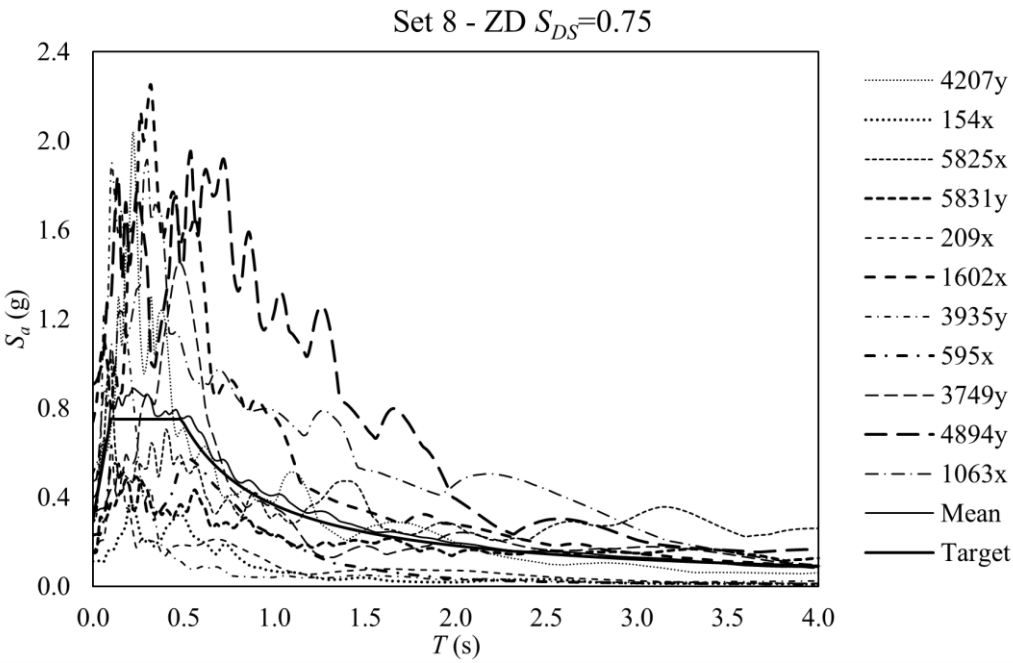

Figure B.68: Spectral acceleration of the ground motion records of Set 8 and their mean and target spectrum

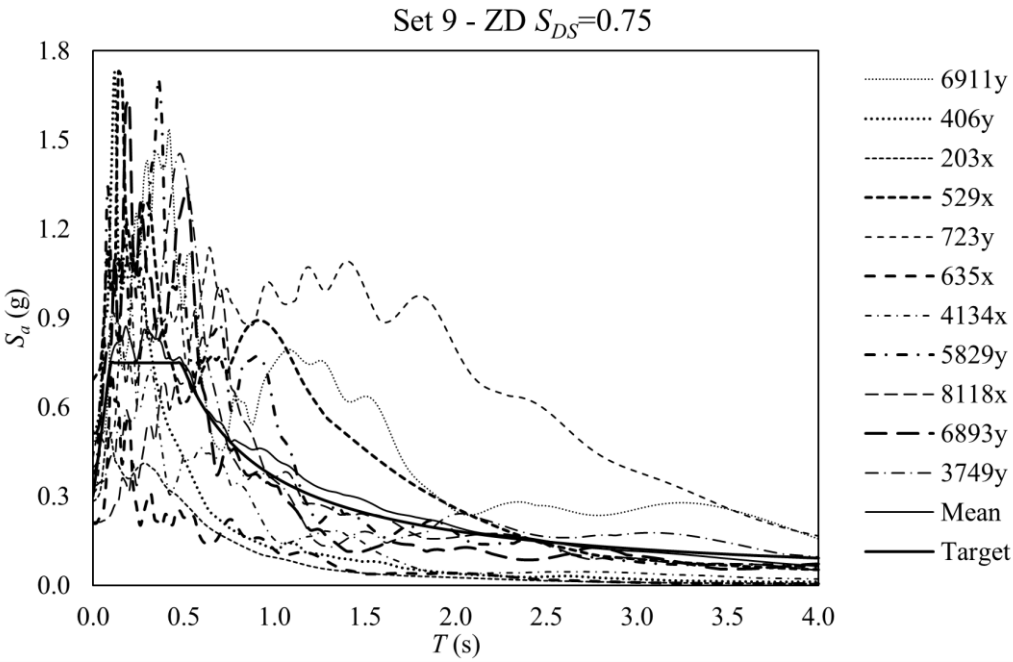

Figure B.69: Spectral acceleration of the ground motion records of Set 9 and their mean and target spectrum

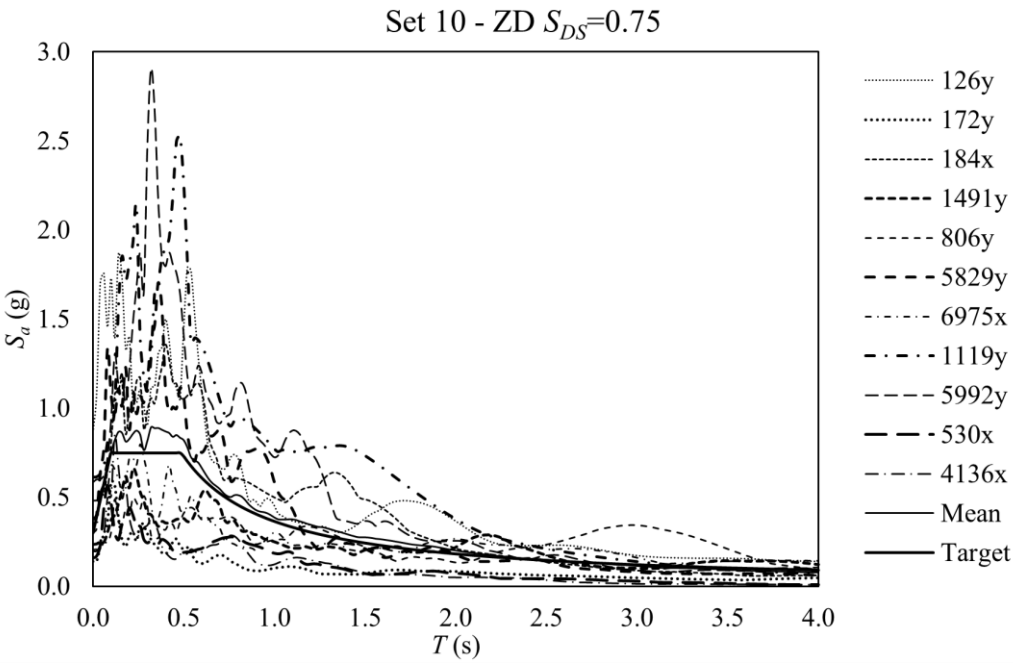

Figure B.70: Spectral acceleration of the ground motion records of Set 10 and their mean and target spectrum

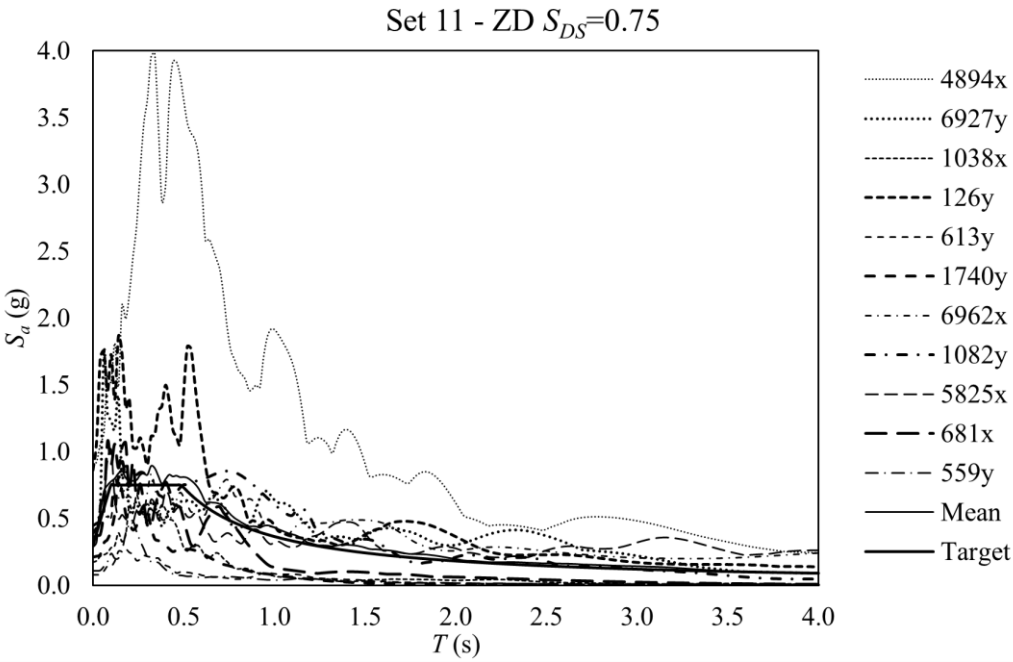

Figure B.71: Spectral acceleration of the ground motion records of Set 11 and their mean and target spectrum

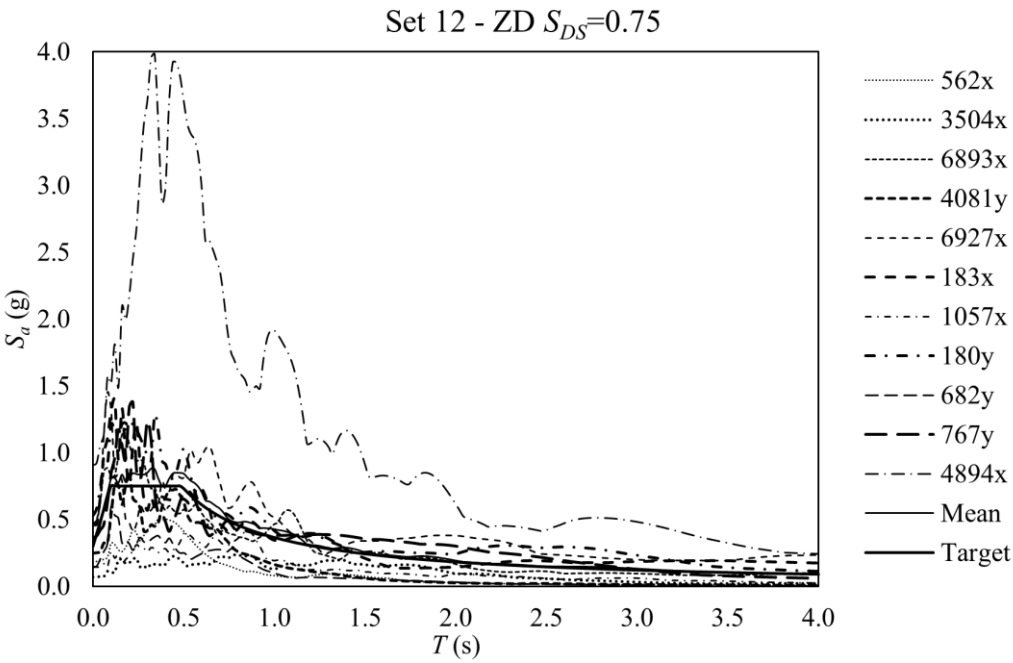

Figure B.72: Spectral acceleration of the ground motion records of Set 12 and their mean and target spectrum

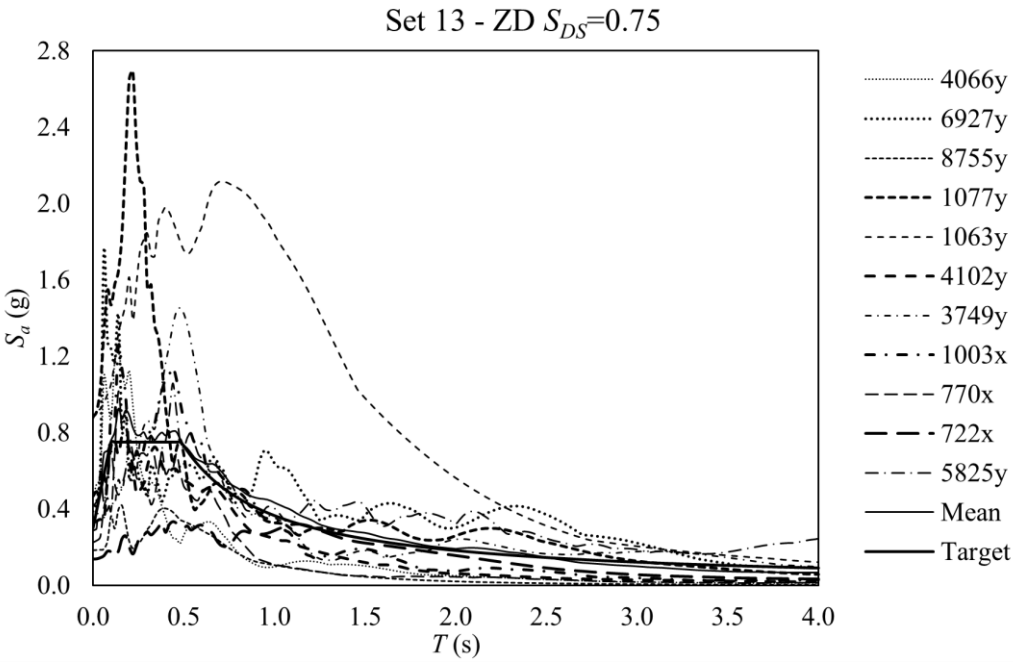

Figure B.73: Spectral acceleration of the ground motion records of Set 13 and their mean and target spectrum

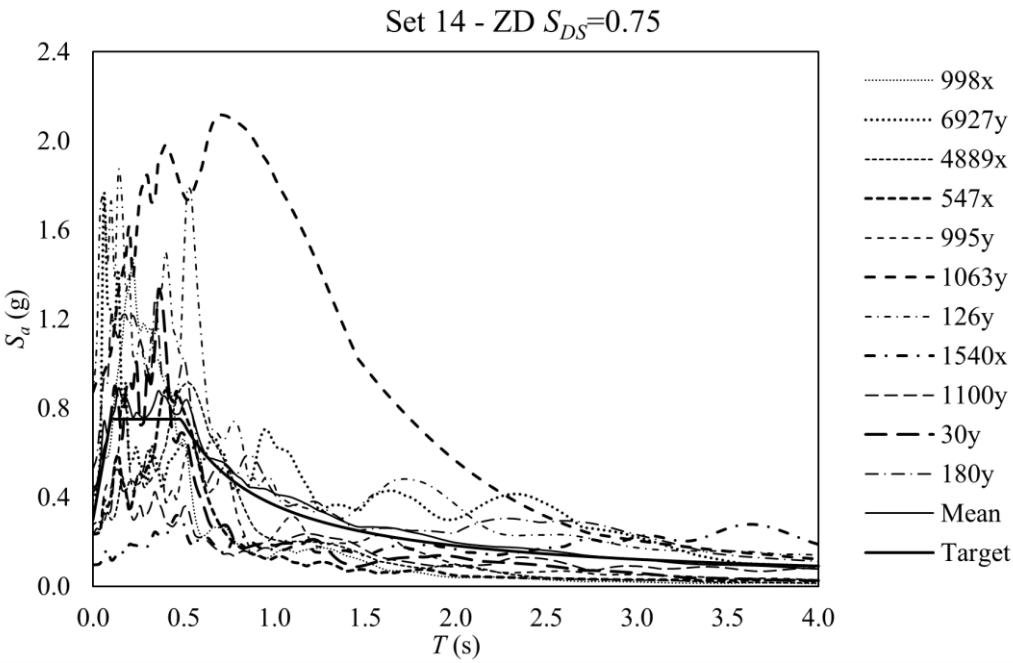

Figure B.74: Spectral acceleration of the ground motion records of Set 14 and their mean and target spectrum

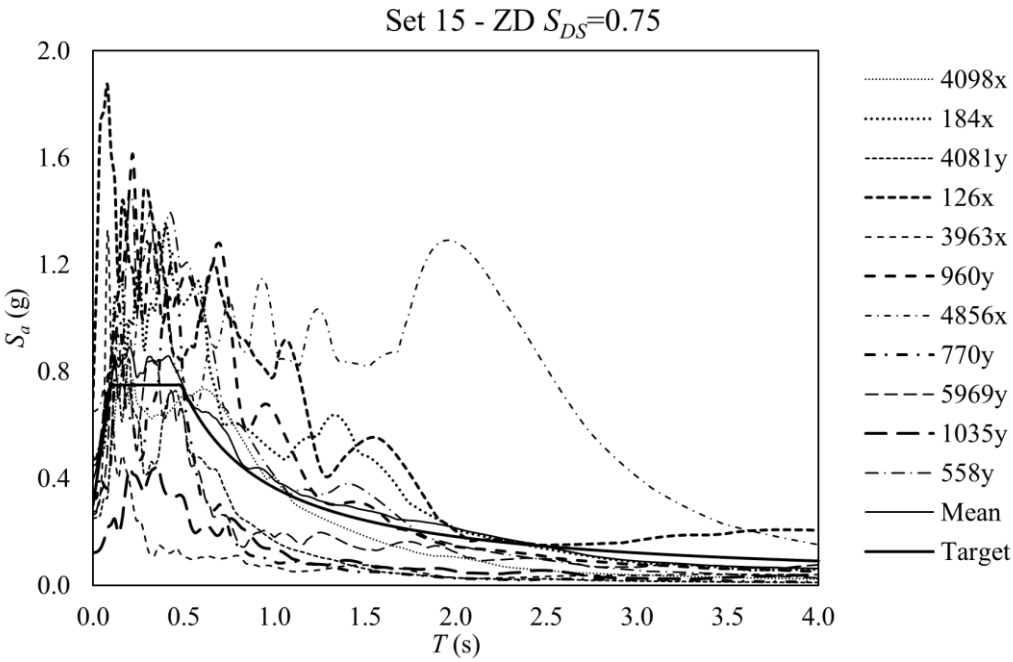

Figure B.75: Spectral acceleration of the ground motion records of Set 15 and their mean and target spectrum

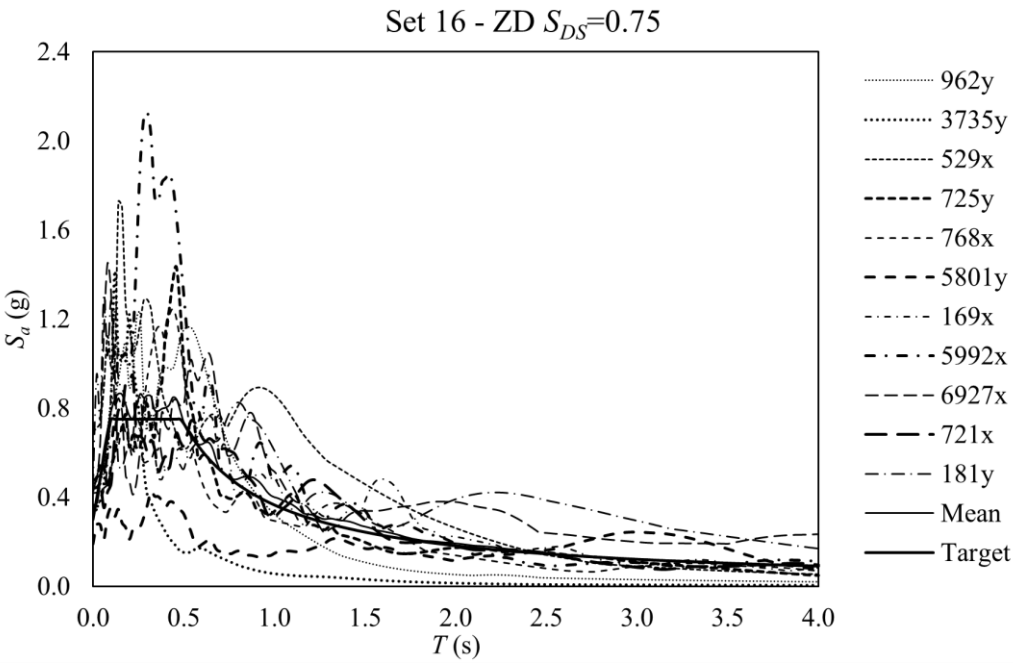

Figure B.76: Spectral acceleration of the ground motion records of Set 16 and their mean and target spectrum

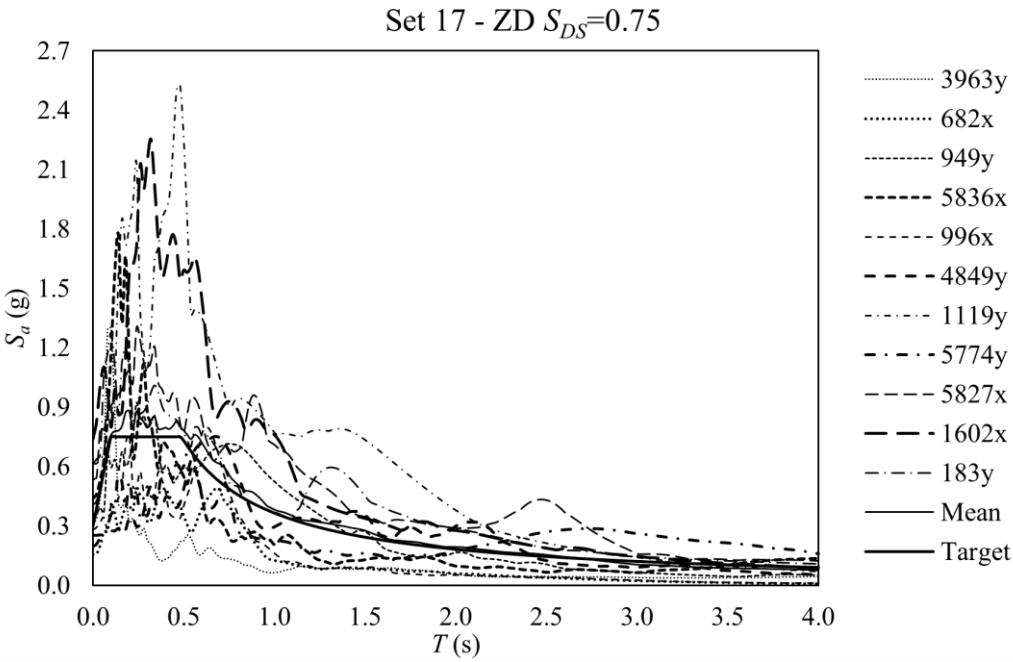

Figure B.77: Spectral acceleration of the ground motion records of Set 17 and their mean and target spectrum

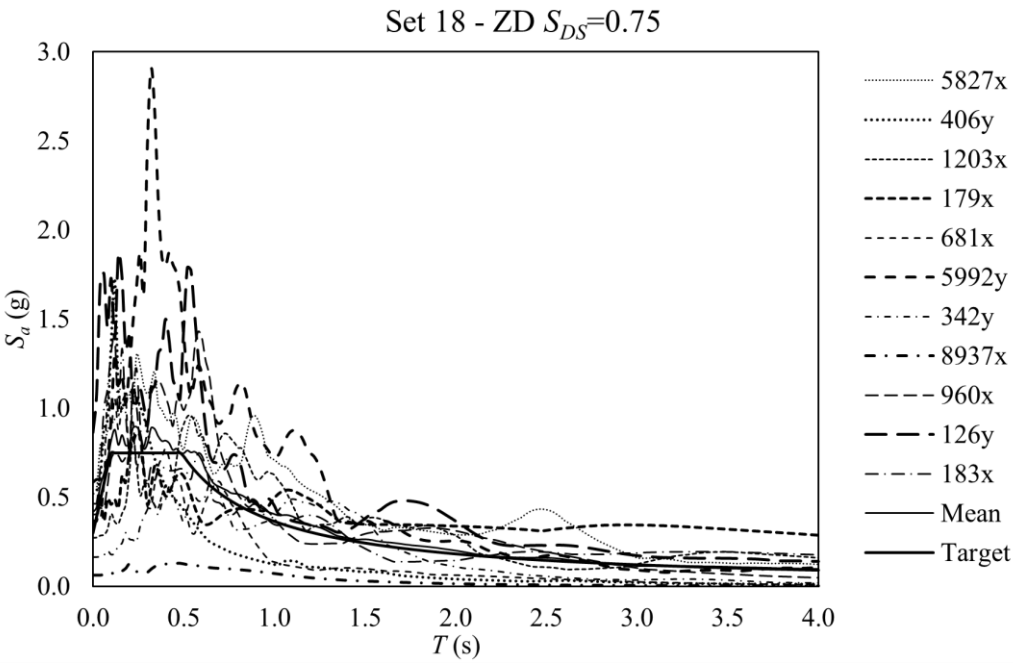

Figure B.78: Spectral acceleration of the ground motion records of Set 18 and their mean and target spectrum

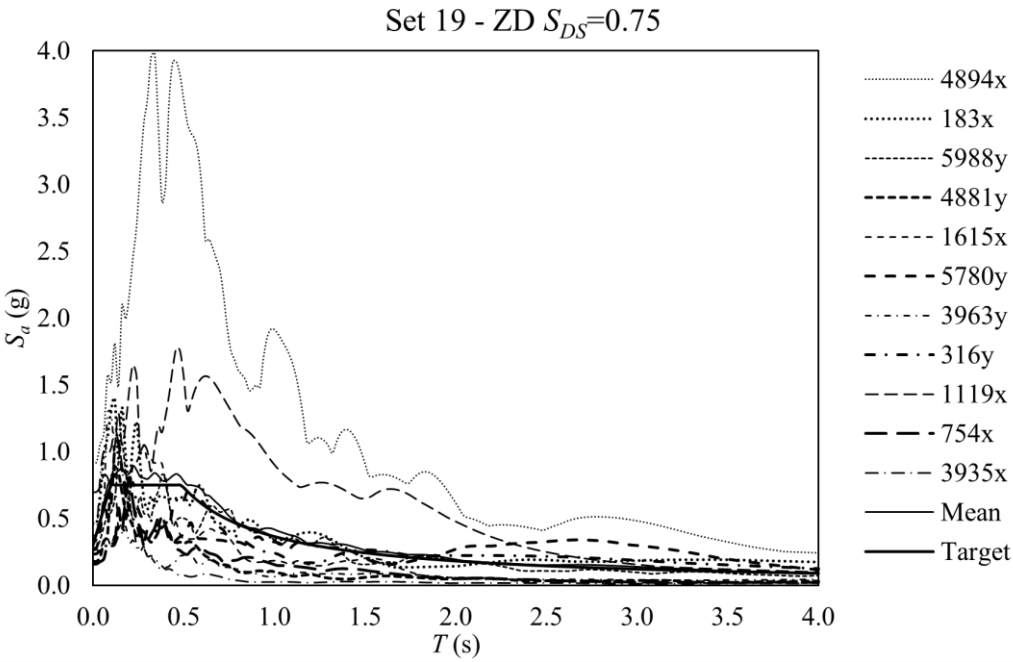

Figure B.79: Spectral acceleration of the ground motion records of Set 19 and their mean and target spectrum

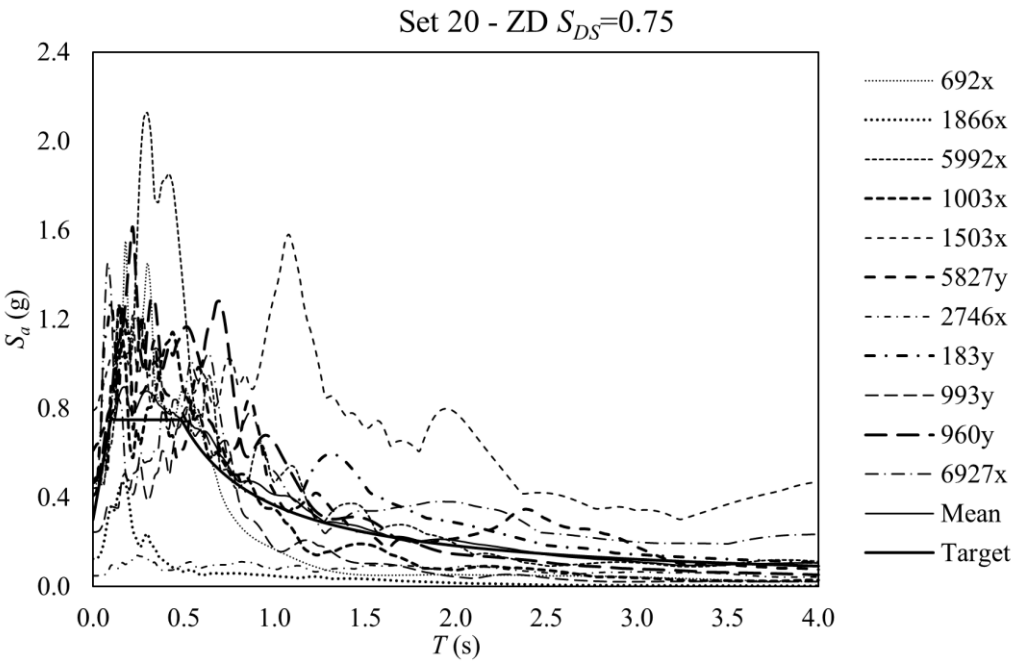

Figure B.80: Spectral acceleration of the ground motion records of Set 20 and their mean and target spectrum

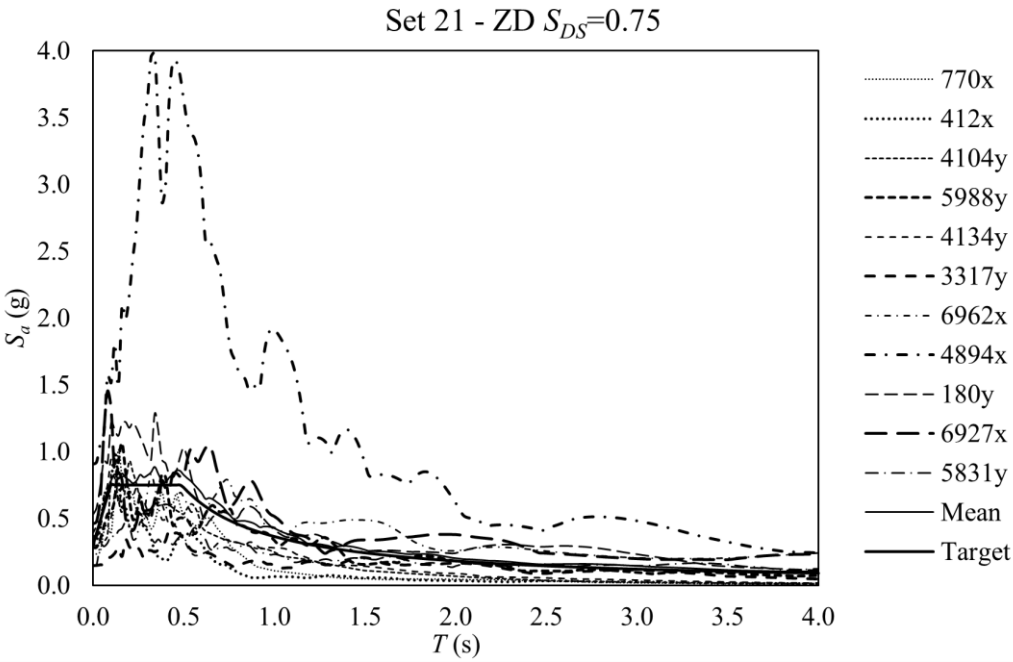

Figure B.81: Spectral acceleration of the ground motion records of Set 21 and their mean and target spectrum

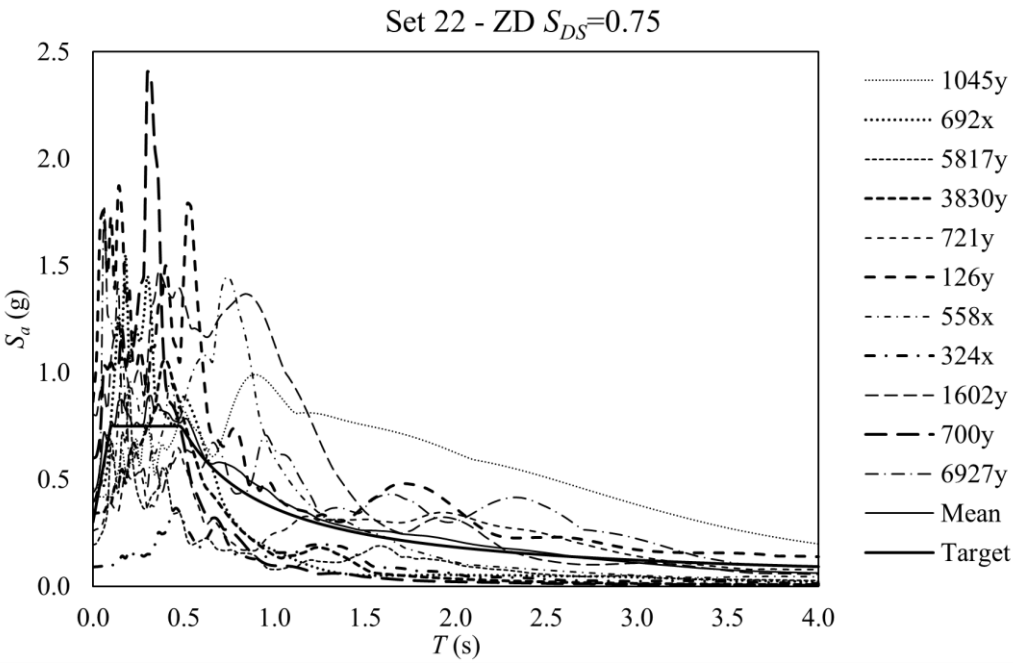

Figure B.82: Spectral acceleration of the ground motion records of Set 22 and their mean and target spectrum

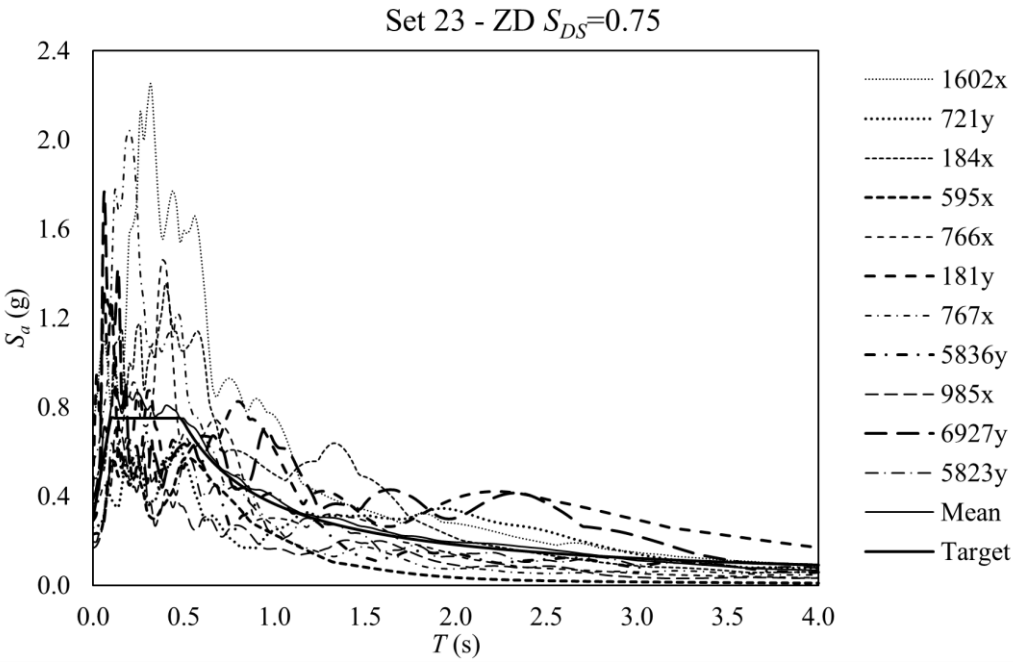

Figure B.83: Spectral acceleration of the ground motion records of Set 23 and their mean and target spectrum

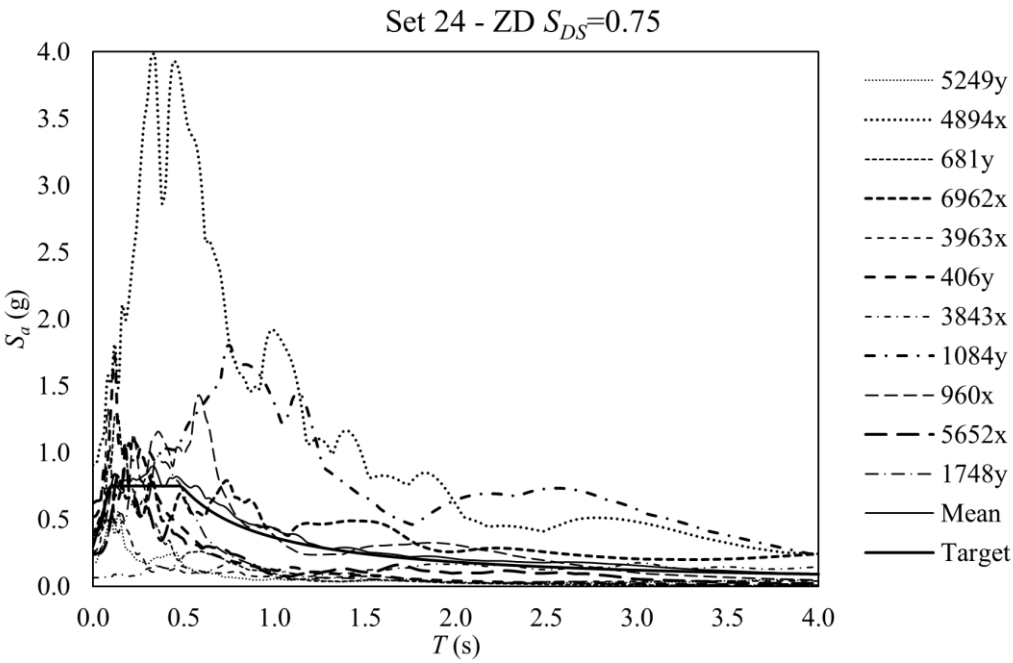

Figure B.84: Spectral acceleration of the ground motion records of Set 24 and their mean and target spectrum

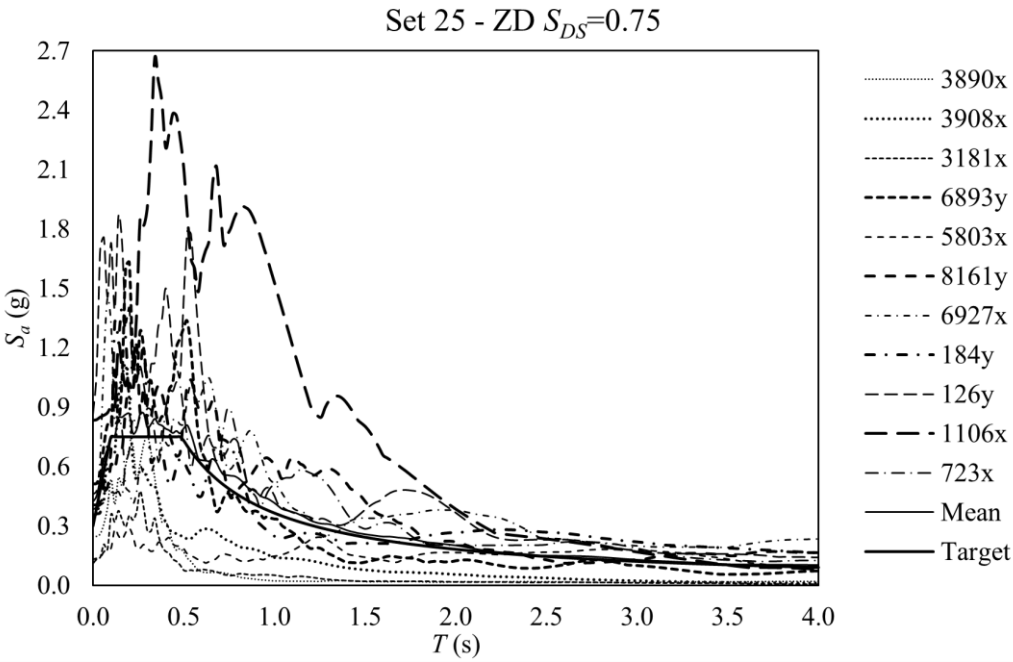

Figure B.85: Spectral acceleration of the ground motion records of Set 25 and their mean and target spectrum

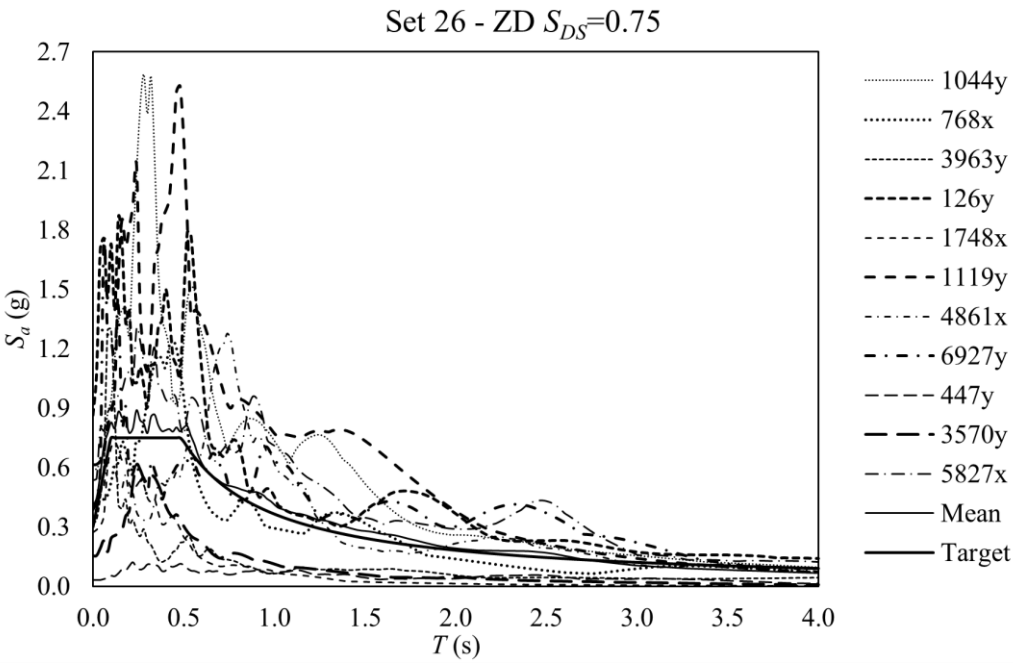

Figure B.86: Spectral acceleration of the ground motion records of Set 26 and their mean and target spectrum

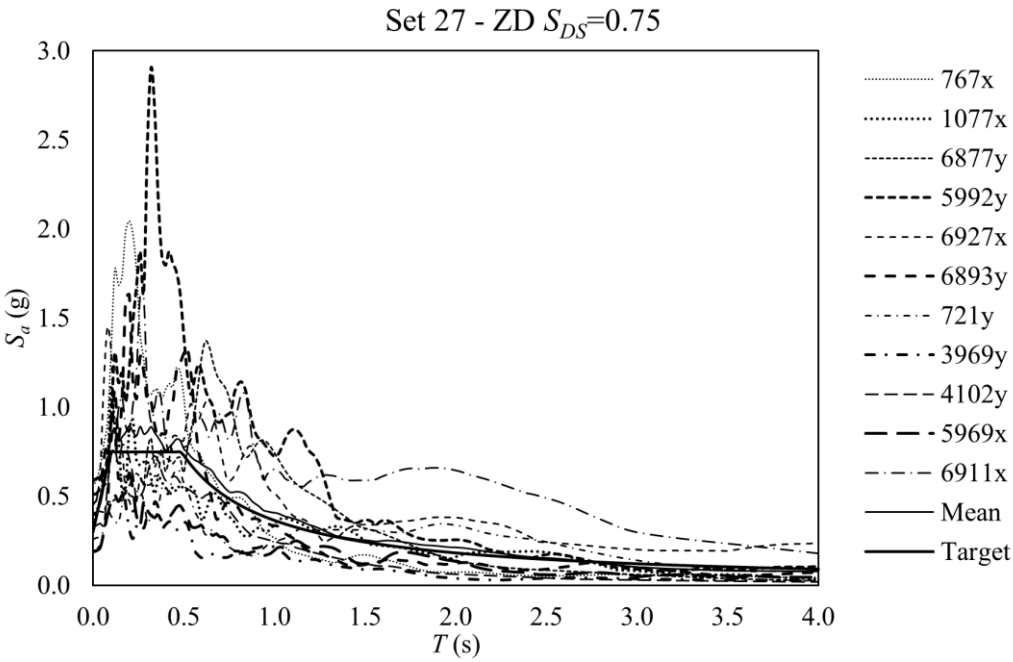

Figure B.87: Spectral acceleration of the ground motion records of Set 27 and their mean and target spectrum

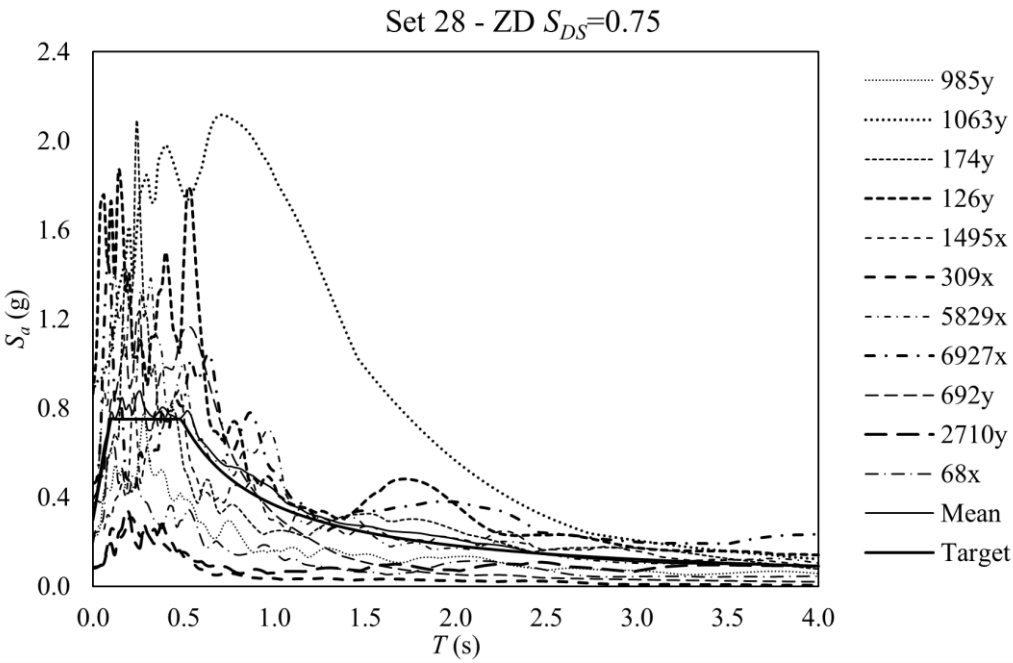

Figure B.88: Spectral acceleration of the ground motion records of Set 28 and their mean and target spectrum

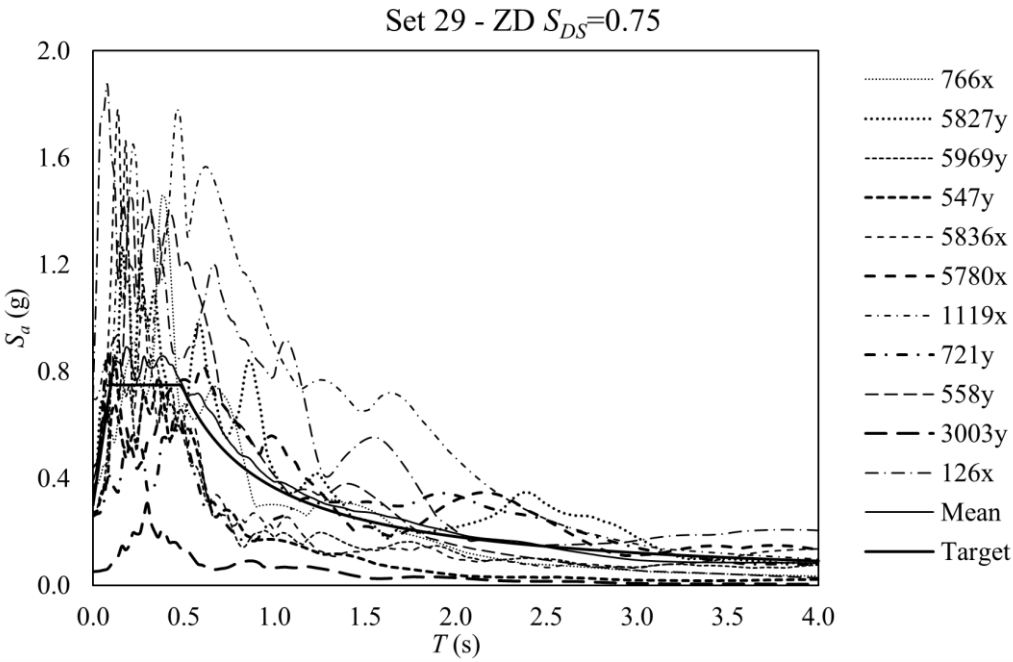

Figure B.89: Spectral acceleration of the ground motion records of Set 29 and their mean and target spectrum

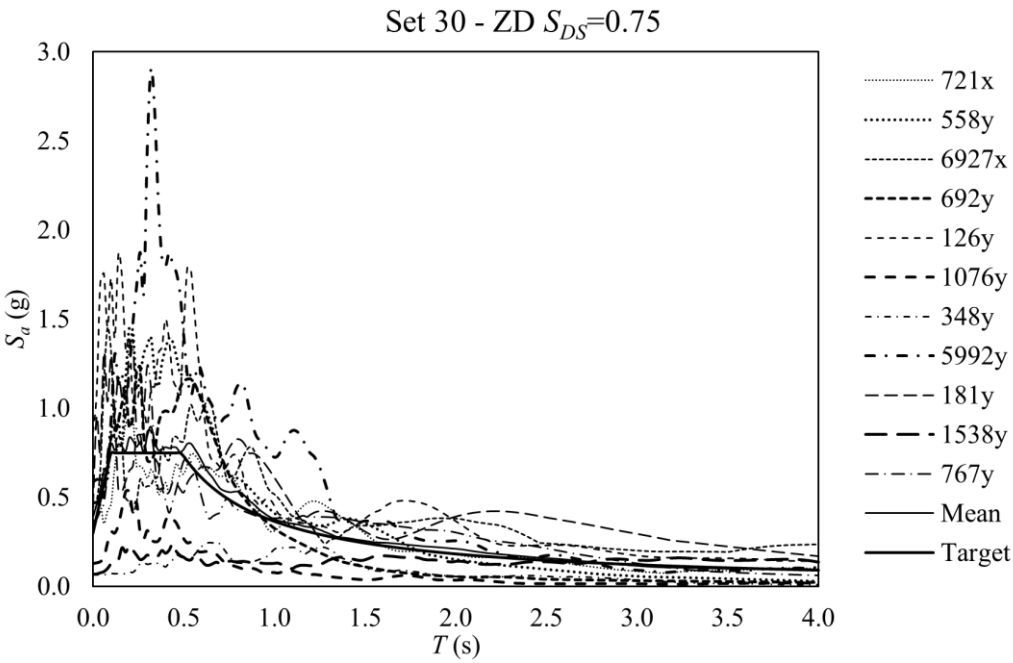

Figure B.90: Spectral acceleration of the ground motion records of Set 30 and their mean and target spectrum

Appendix C

m_{IDR} and CoV_{IDR} Graphs

In this appendix, the graphs of the CoV_{GDR}, m_{IDR} and CoV_{IDR} are displayed for all the frames.

C.1 Coefficient of Variance Graphs for GDR

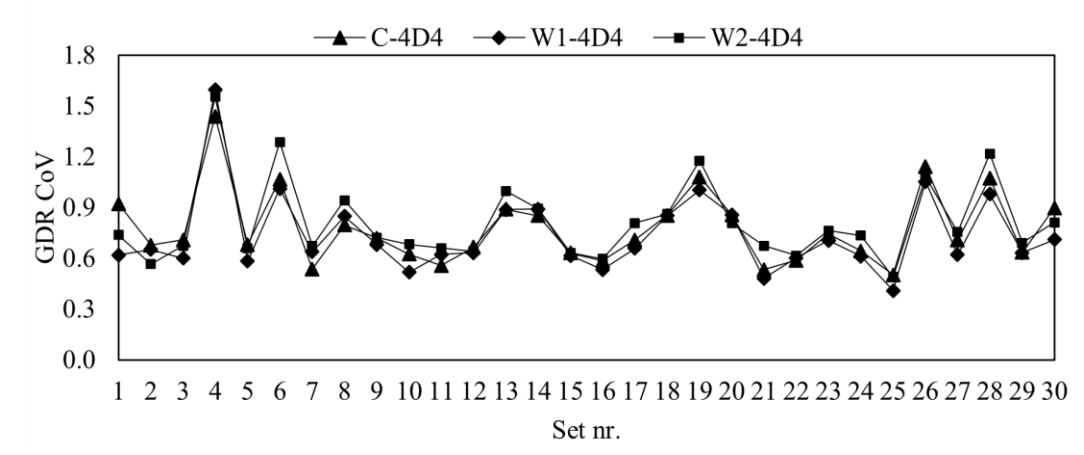

Figure C.1: CoV_{GDR} of frames 4D4

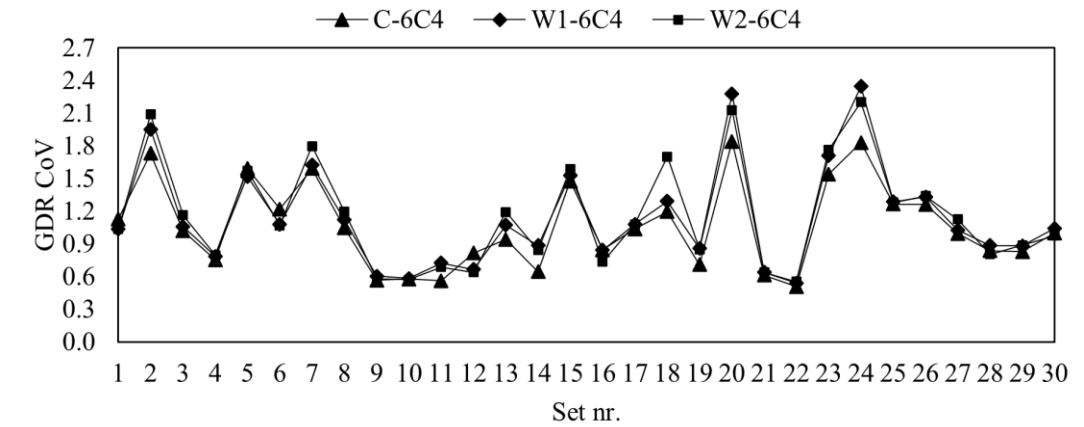

Figure C.2: CoV_{GDR} of frames 6C4

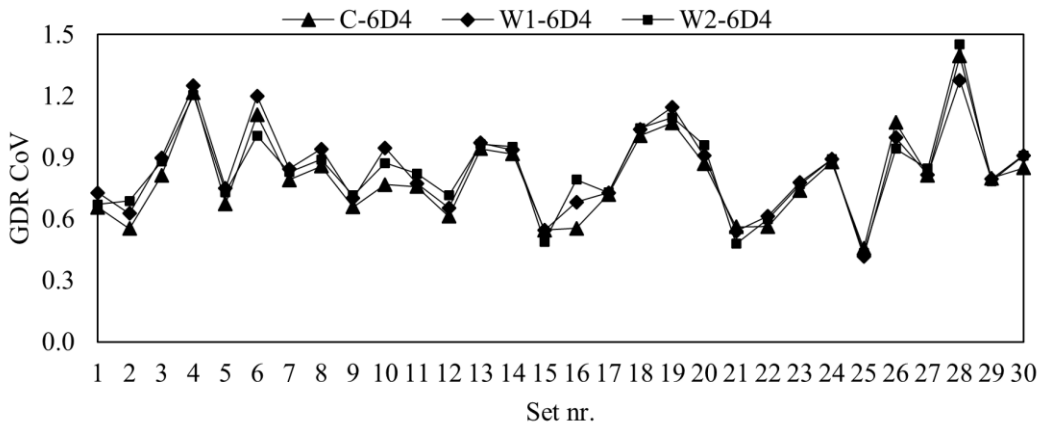

Figure C.3: CoV_{GDR} of frames 6D4

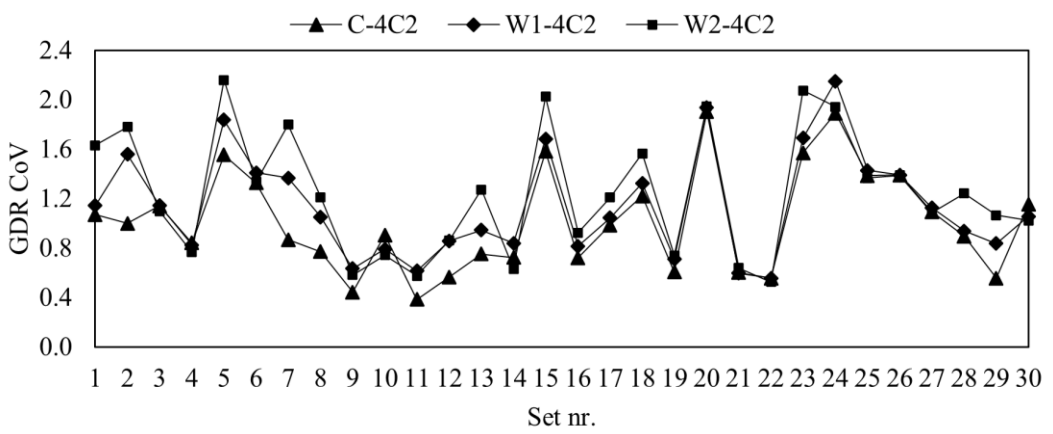

Figure C.4: CoV_{GDR} of frames 4C2

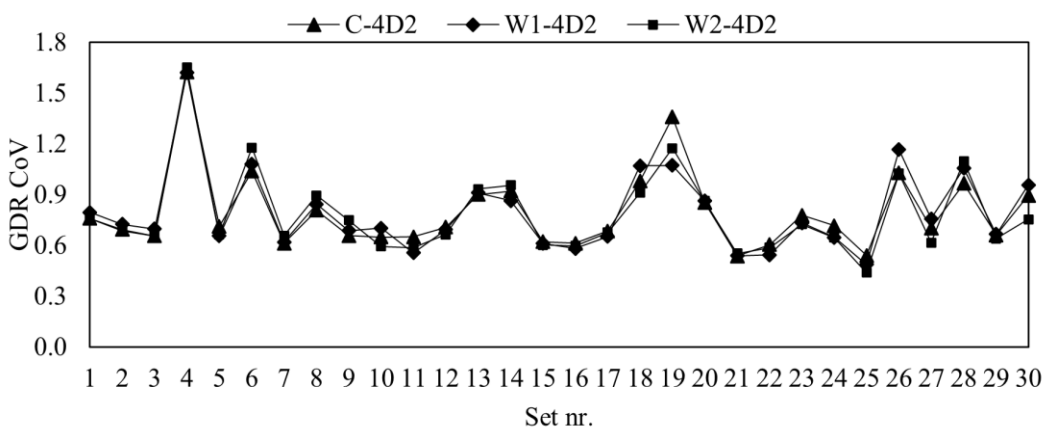

Figure C.5: CoV_{GDR} of frames 4D2

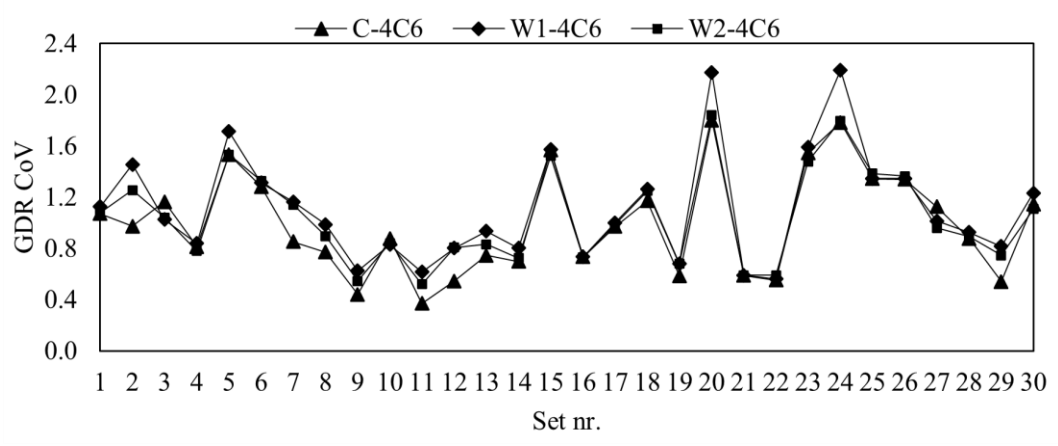

Figure C.6: CoV_{GDR} of frames 4C6

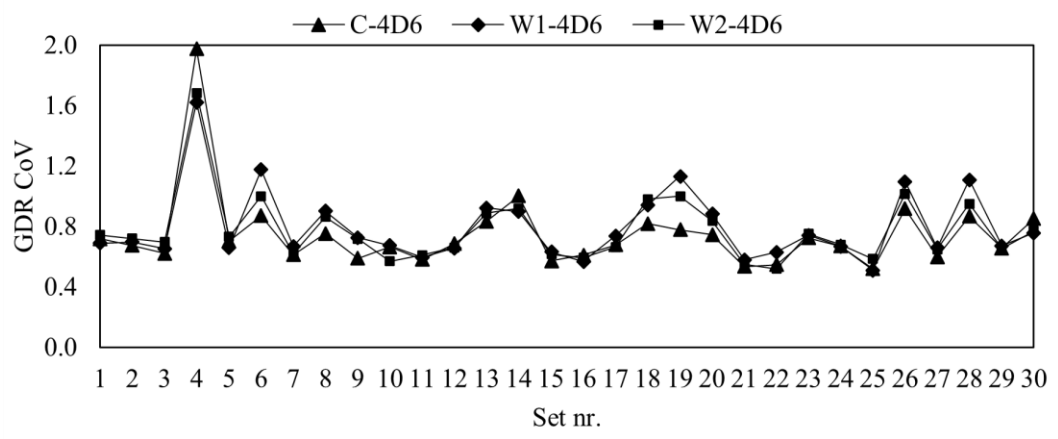

Figure C.7: CoV_{GDR} of frames 4D6

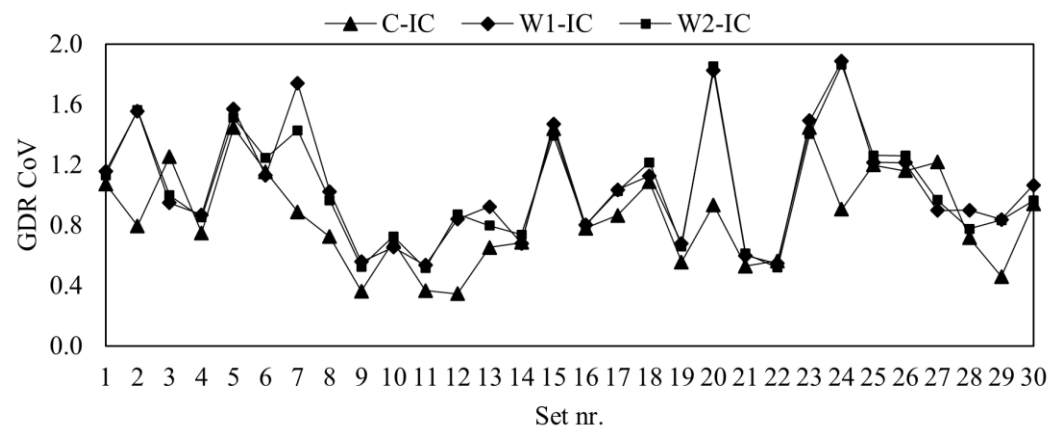

Figure C.8: CoV_{GDR} of frames IC

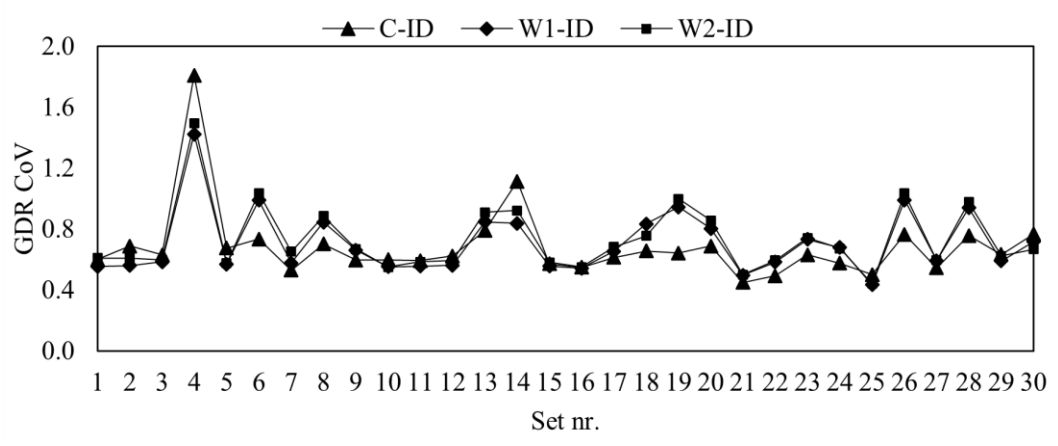

Figure C.9: CoV_{GDR} of frames ID

C.2 Four Story and Four Bay Frames

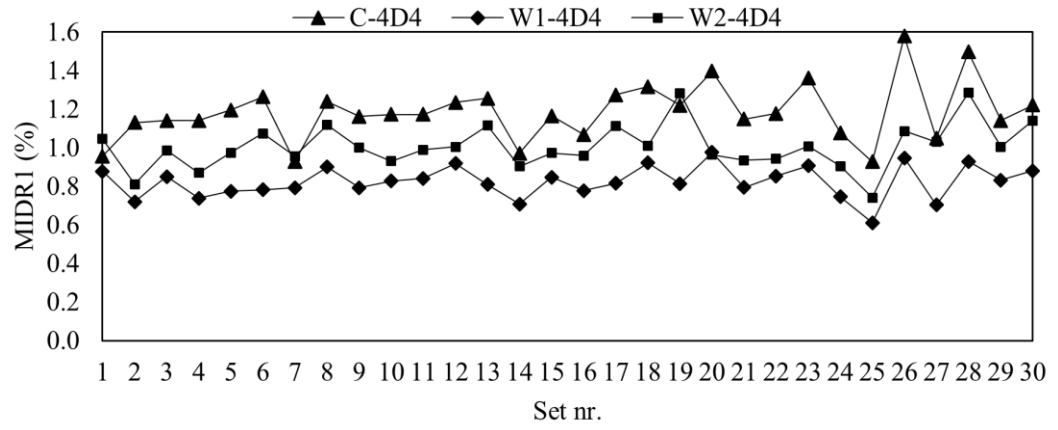

Figure C.10: m_{IDR1} of frames 4D4

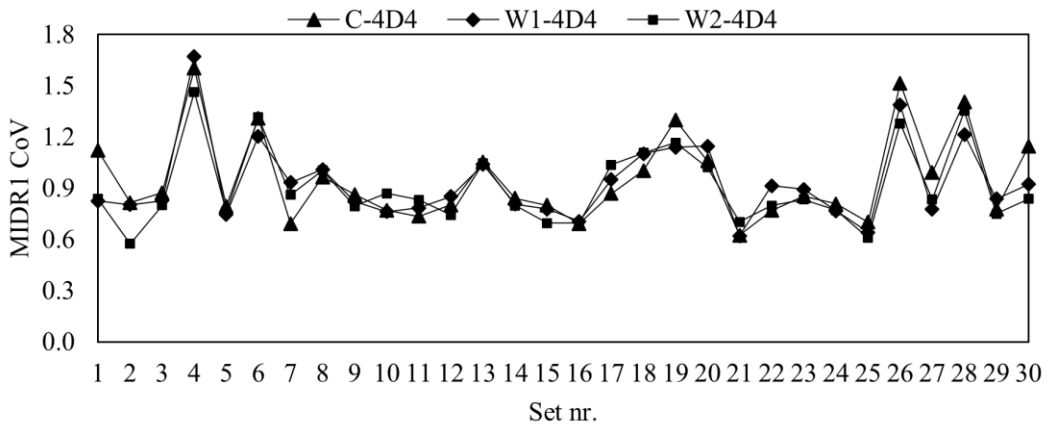

Figure C.11: CoV_{IDR1} of frames 4D4

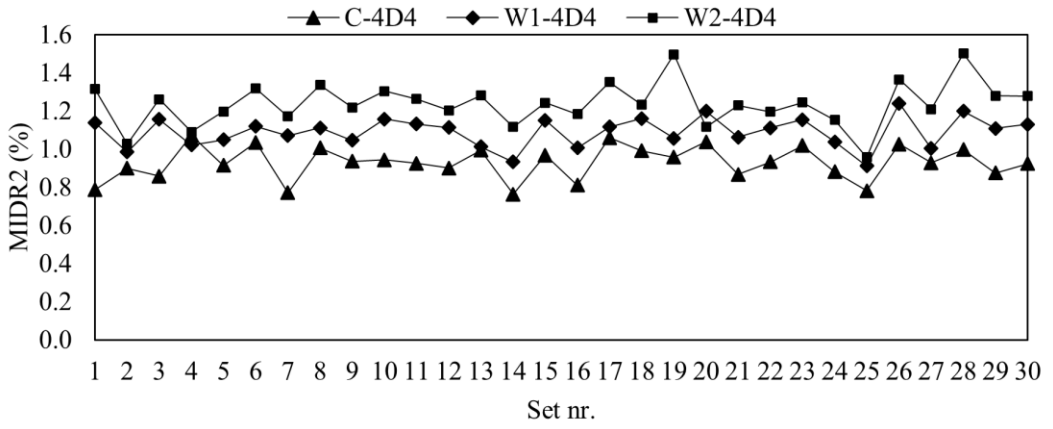

Figure C.12: m_{IDR2} of frames 4D4

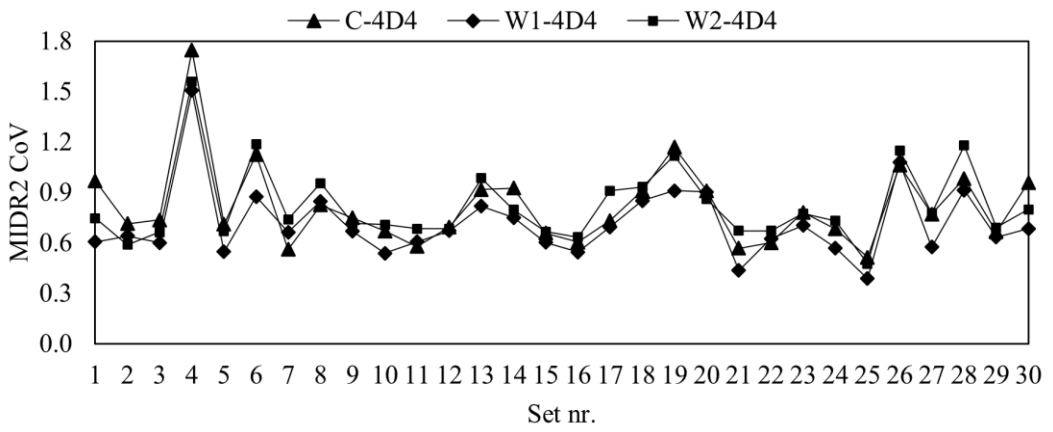

Figure C.13: CoV_{IDR2} of frames 4D4

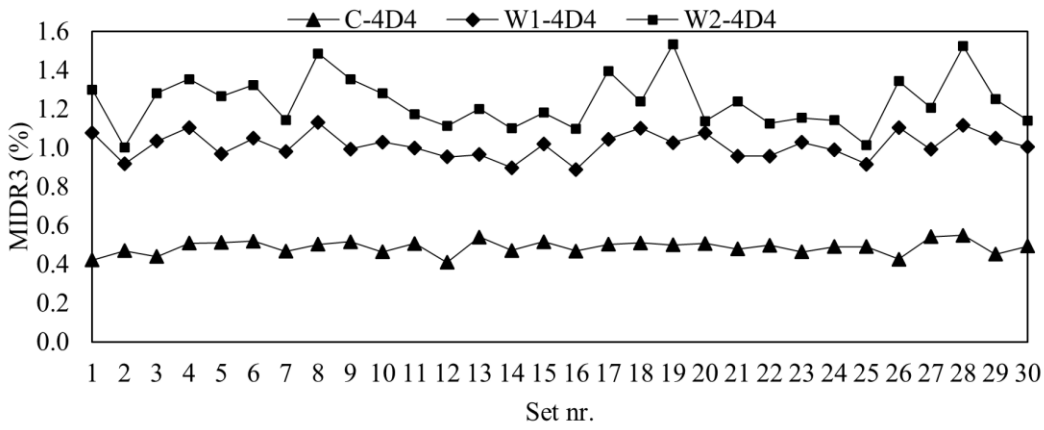

Figure C.14: m_{IDR3} of frames 4D4

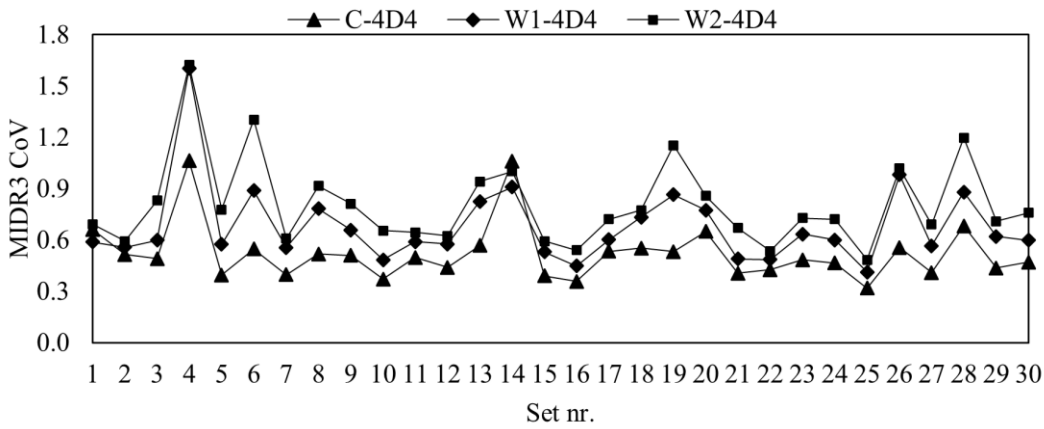

Figure C.15: CoV_{IDR3} of frames 4D4

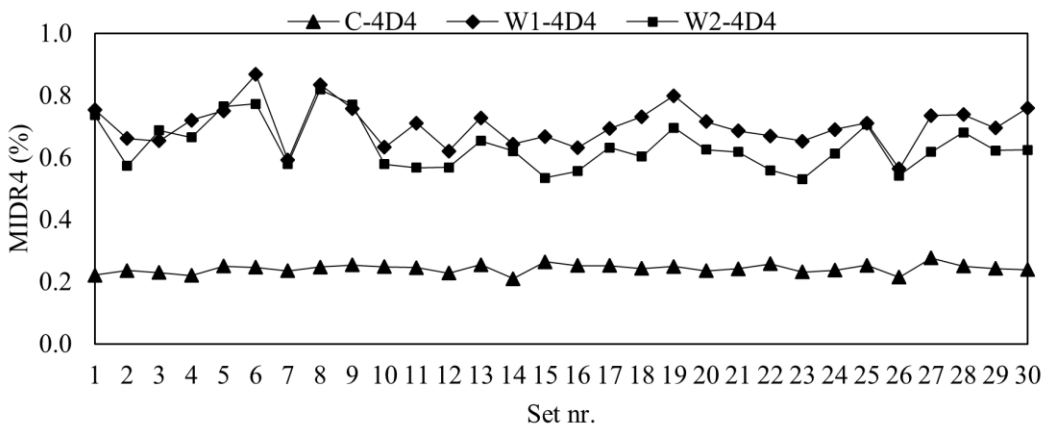

Figure C.16: m_{IDR4} of frames 4D4

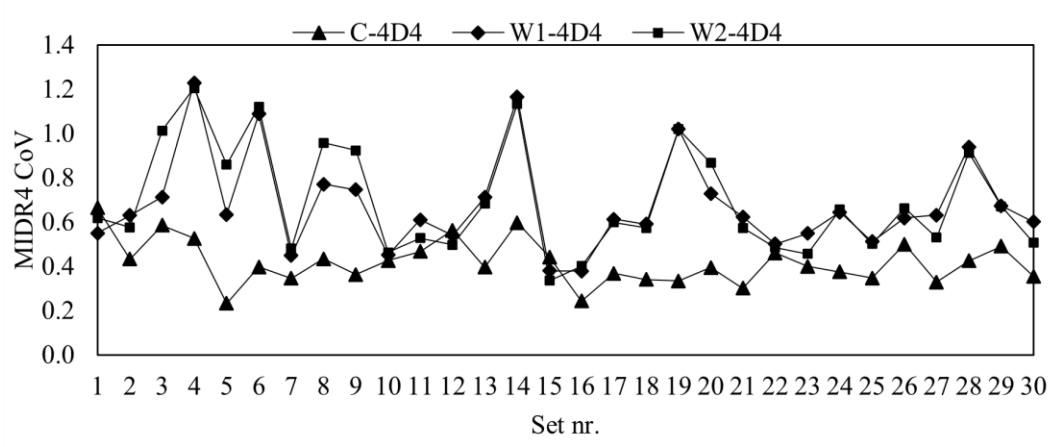

Figure C.17: CoV_{IDR4} of frames 4D4

C.3 Six Story and Four Bay Frames

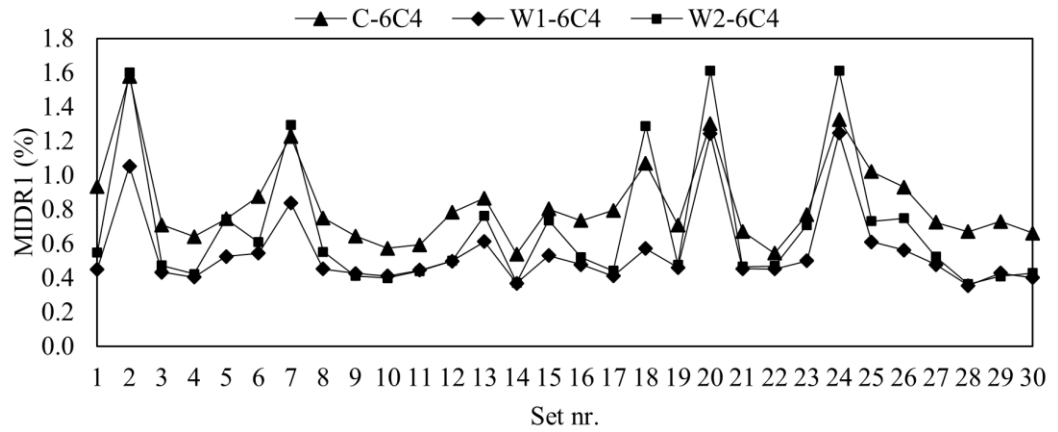

Figure C.18: m_{IDR1} of frames 6C4

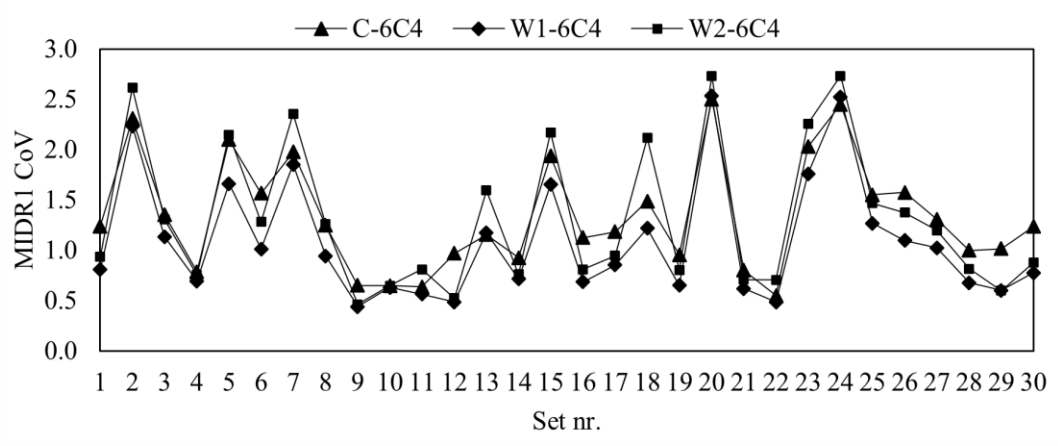

Figure C.19: CoV_{IDR1} of frames 6C4

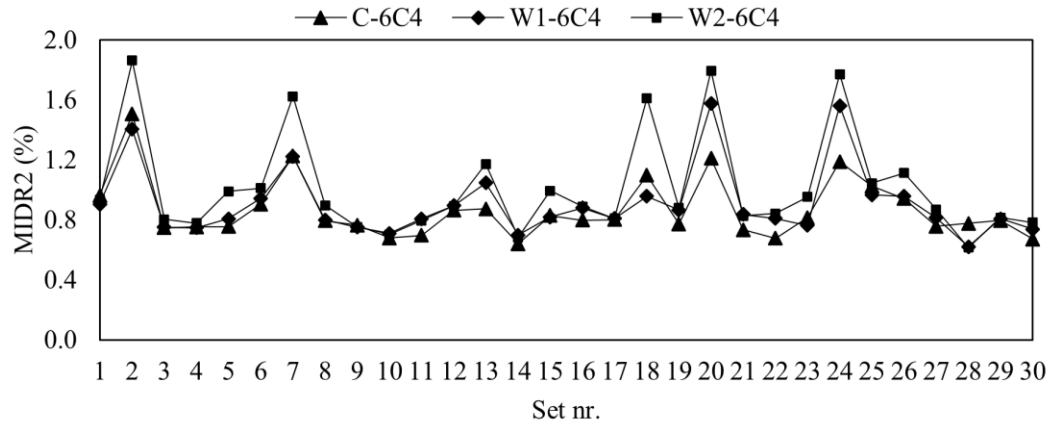

Figure C.20: m_{IDR2} of frames 6C4

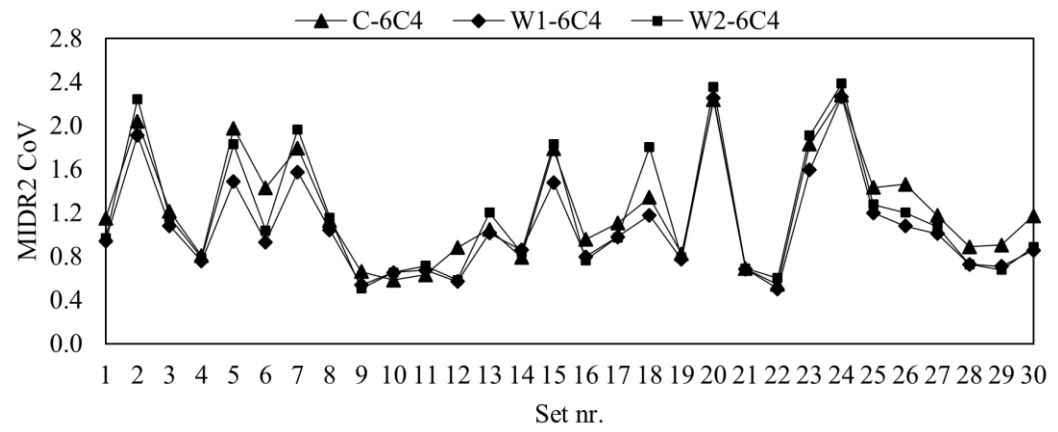

Figure C.21: CoV_{IDR2} of frames 6C4

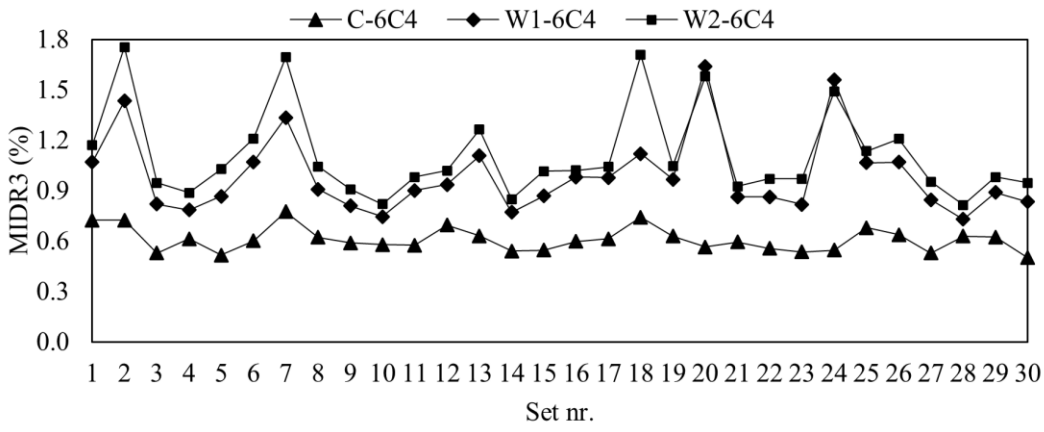

Figure C.22: m_{IDR3} of frames 6C4

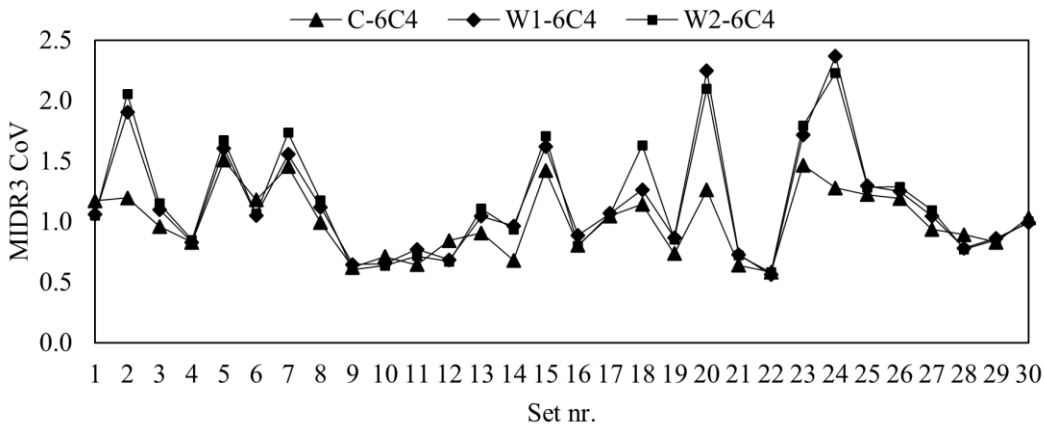

Figure C.23: CoV_{IDR3} of frames 6C4

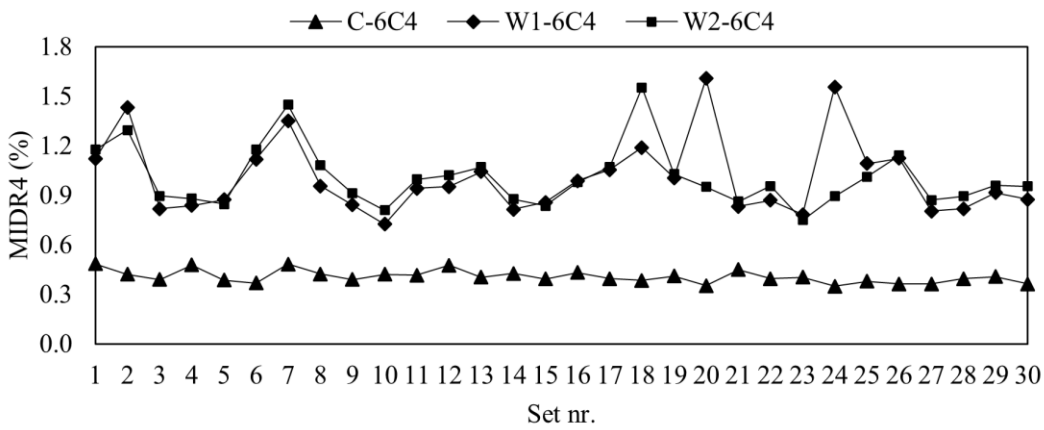

Figure C.24: m_{IDR4} of frames 6C4

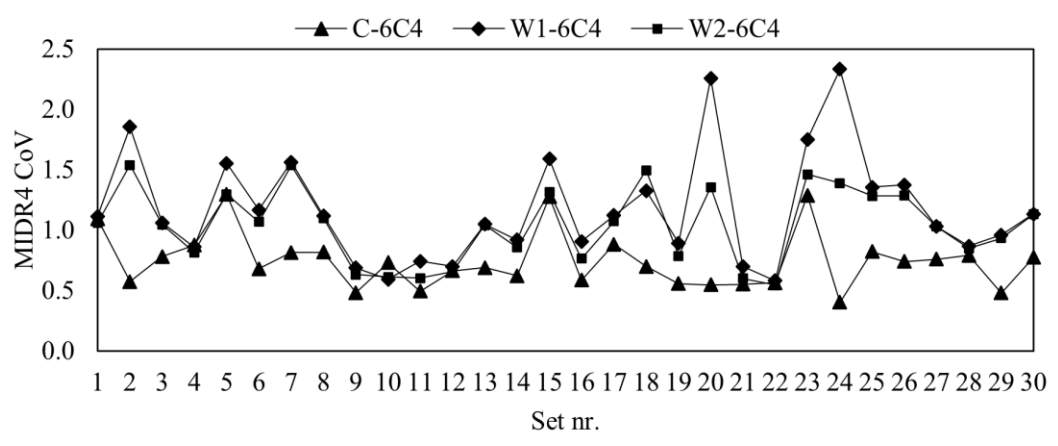

Figure C.25: CoV_{IDR4} of frames 6C4

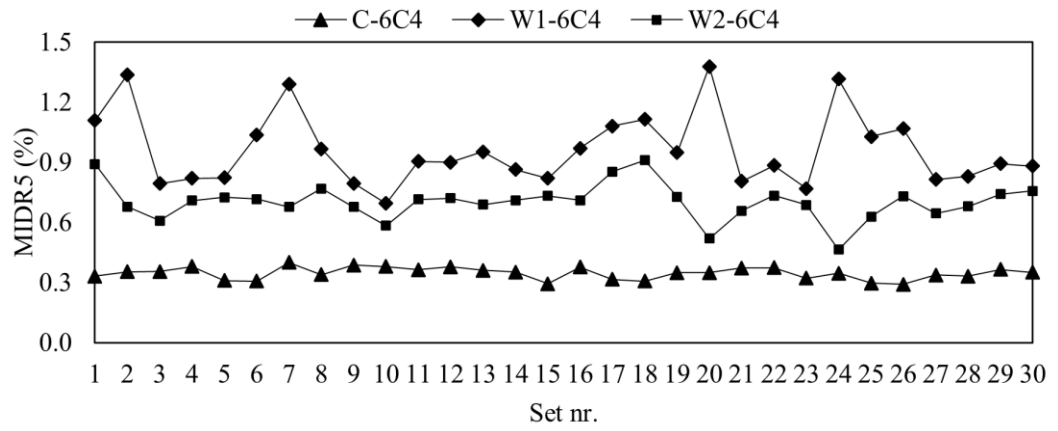

Figure C.26: m_{IDR5} of frames 6C4

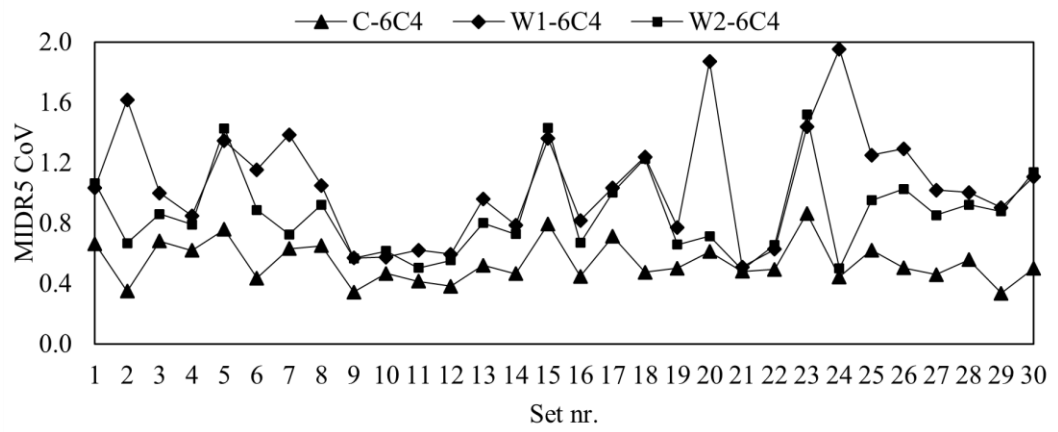

Figure C.27: CoV_{IDR5} of frames 6C4

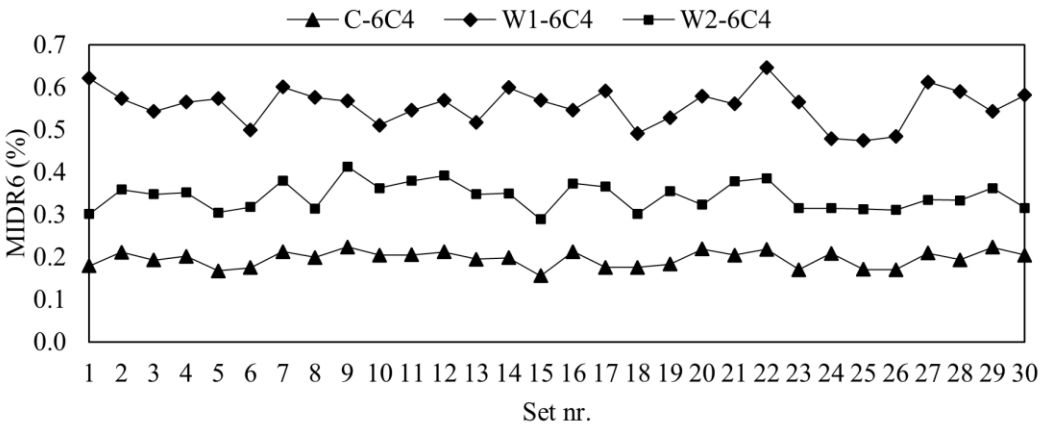

Figure C.28: m_{IDR6} of frames 6C4

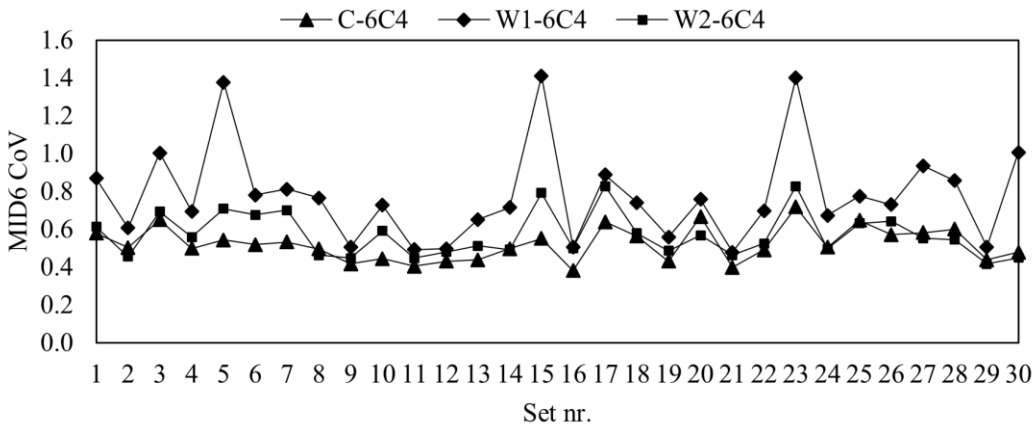

Figure C.29: CoV_{IDR6} of frames 6C4

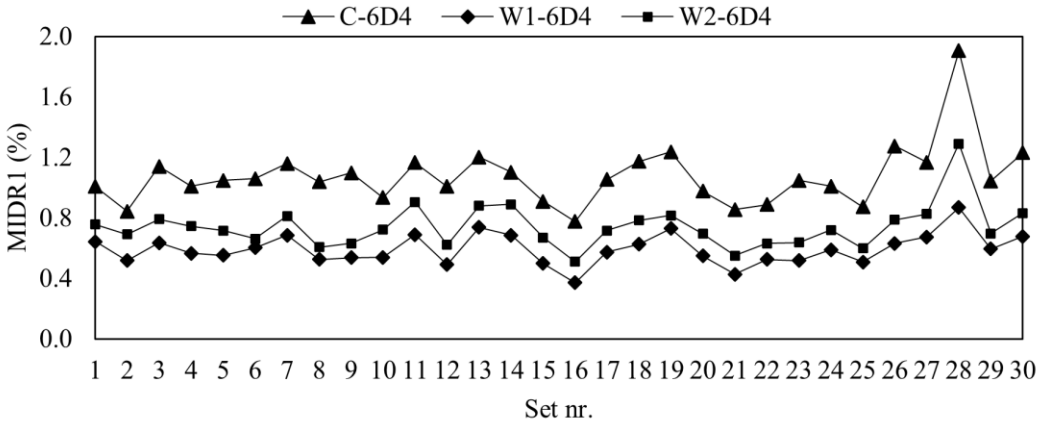

Figure C.30: m_{IDR1} of frames 6D4

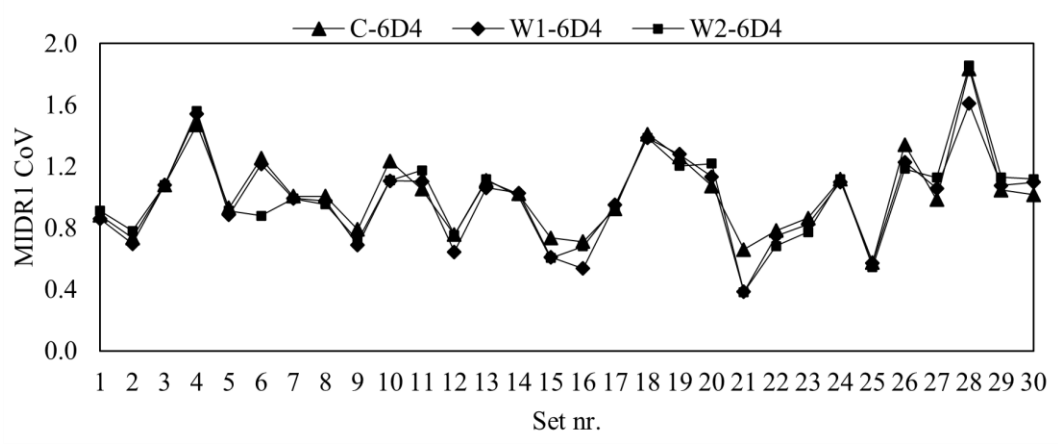

Figure C.31: CoV_{IDR1} of frames 6D4

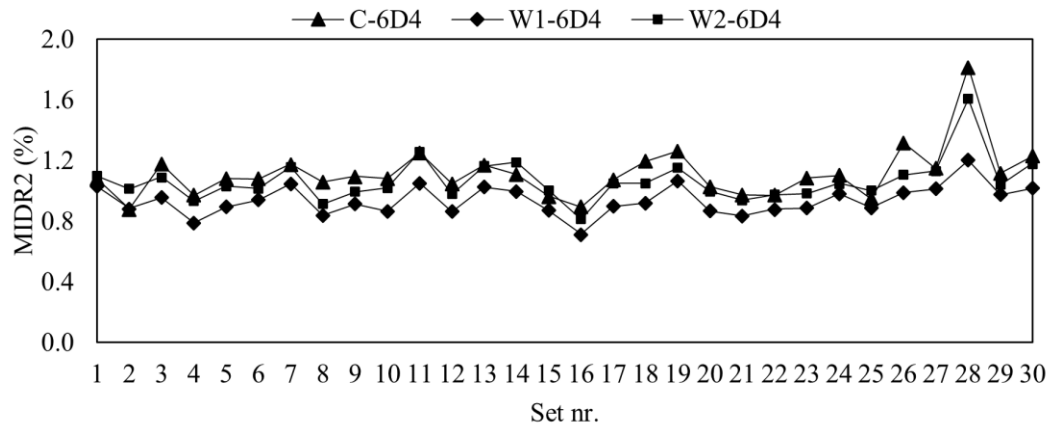

Figure C.32: m_{IDR2} of frames 6D4

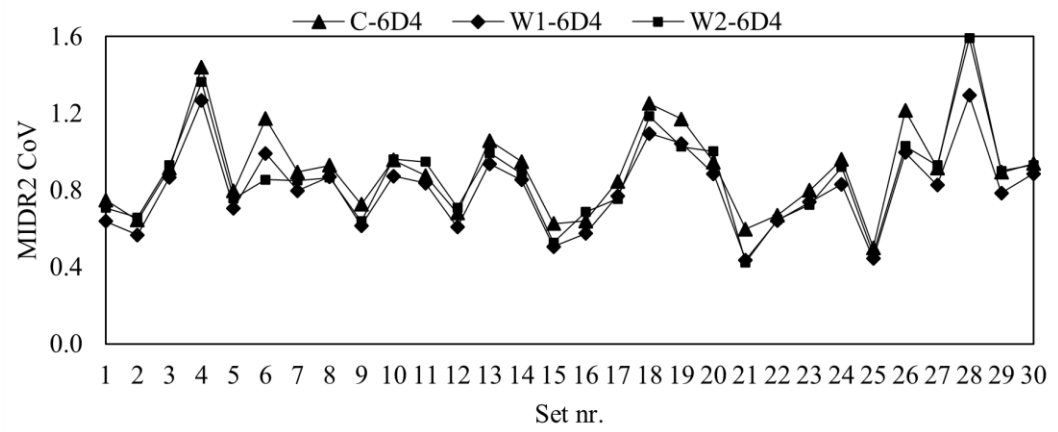

Figure C.33: CoV_{IDR2} of frames 6D4

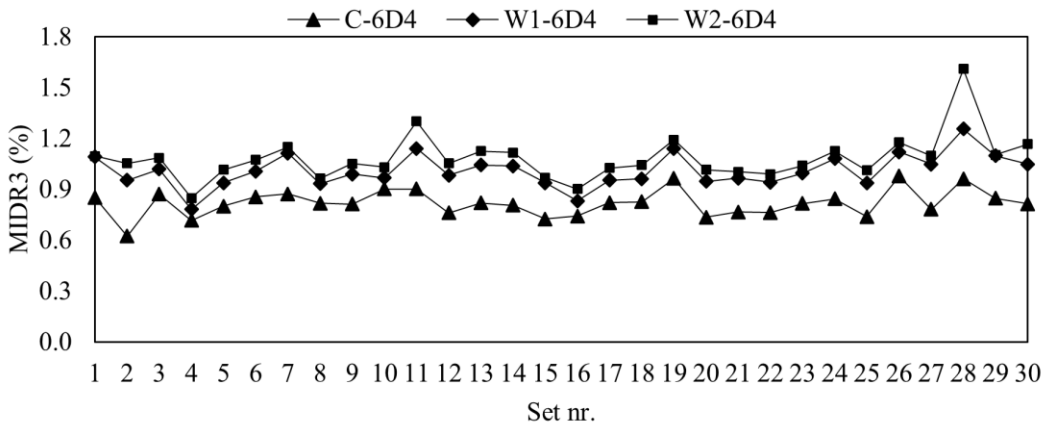

Figure C.34: m_{IDR3} of frames 6D4

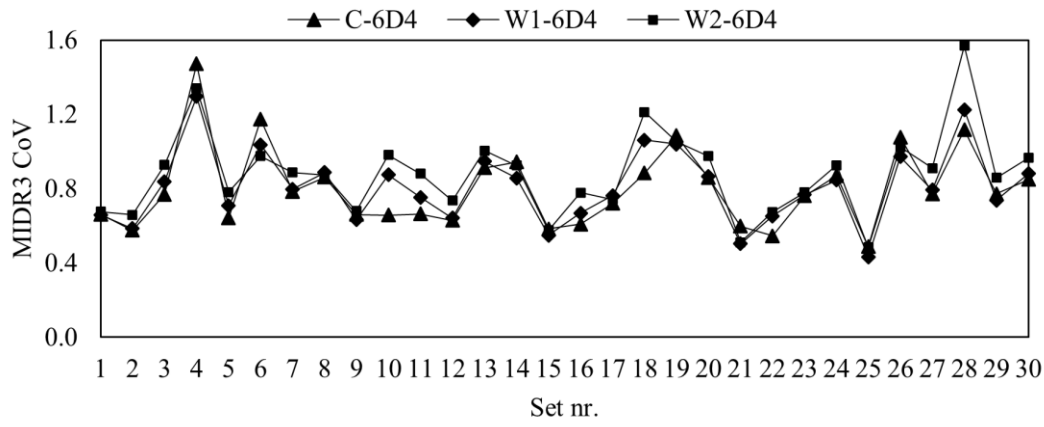

Figure C.35: CoV_{IDR3} of frames 6D4

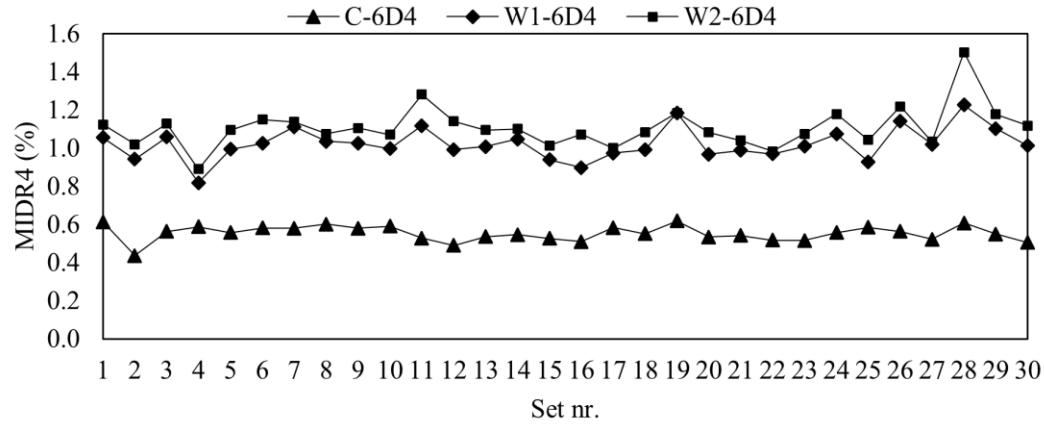

Figure C.36: m_{IDR4} of frames 6D4

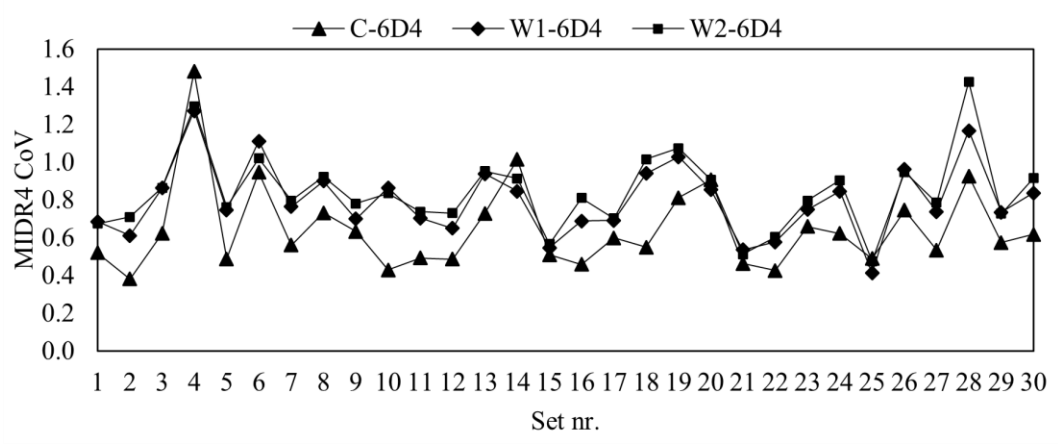

Figure C.37: CoV_{IDR4} of frames 6D4

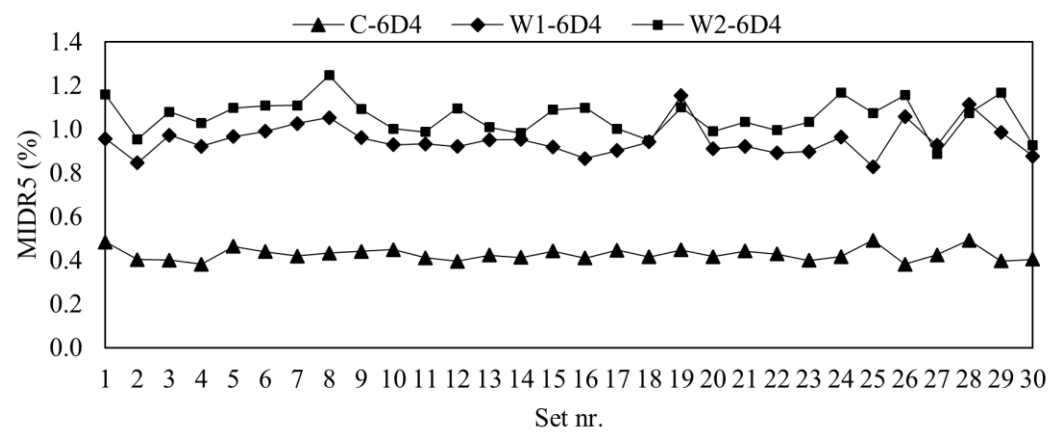

Figure C.38: m_{IDR5} of frames 6D4

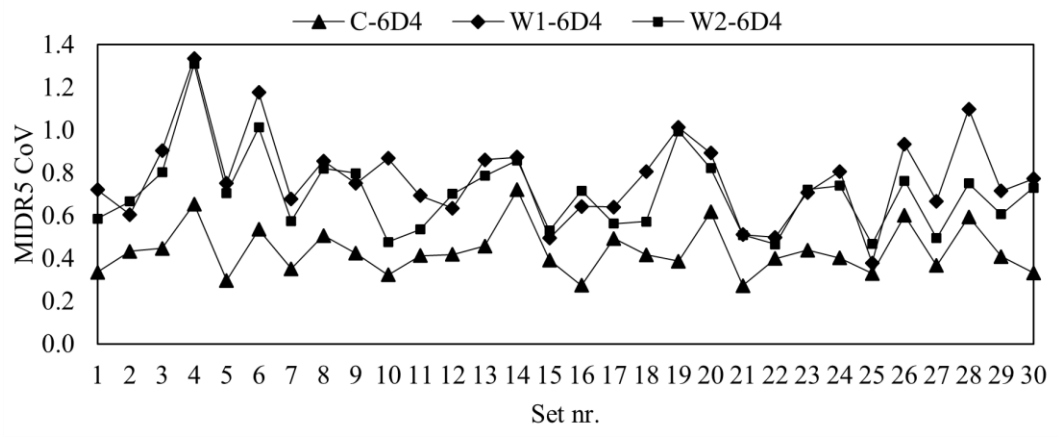

Figure C.39: CoV_{IDR5} of frames 6D4

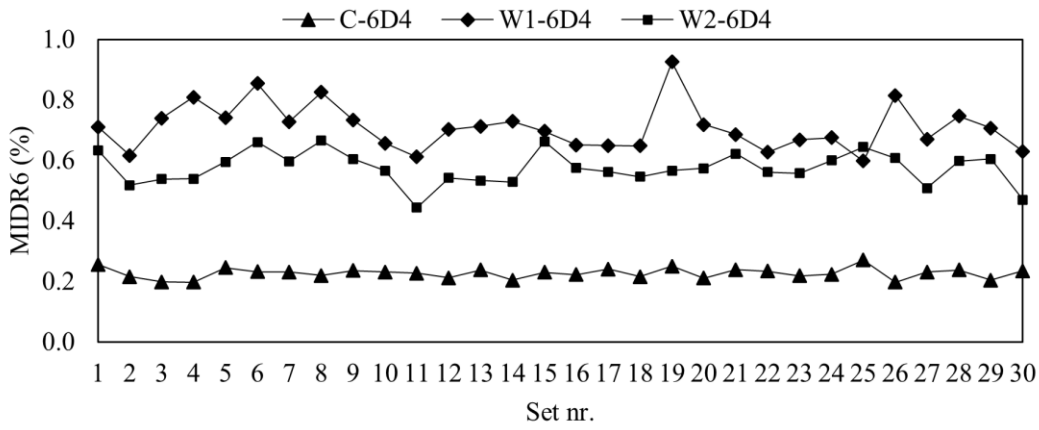

Figure C.40: m_{IDR6} of frames 6D4

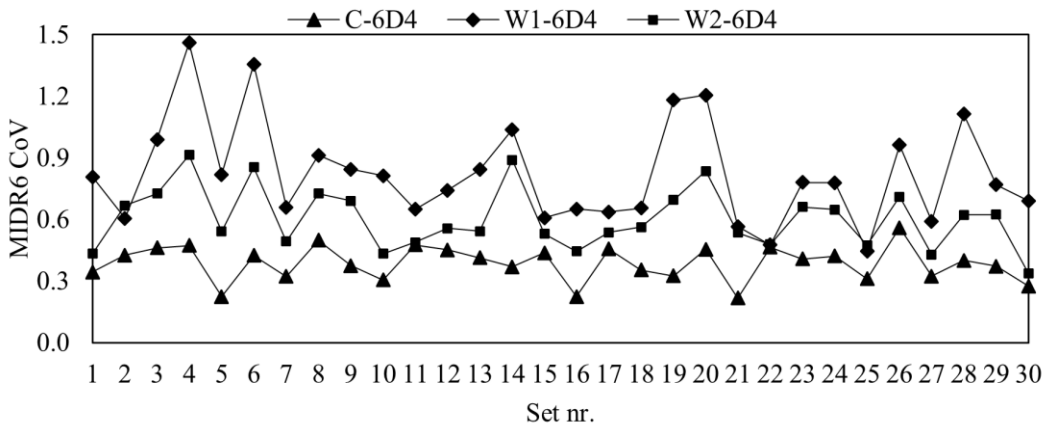

Figure C.41: CoV_{IDR6} of frames 6D4

C.4 Four Story and Two Bay Frames

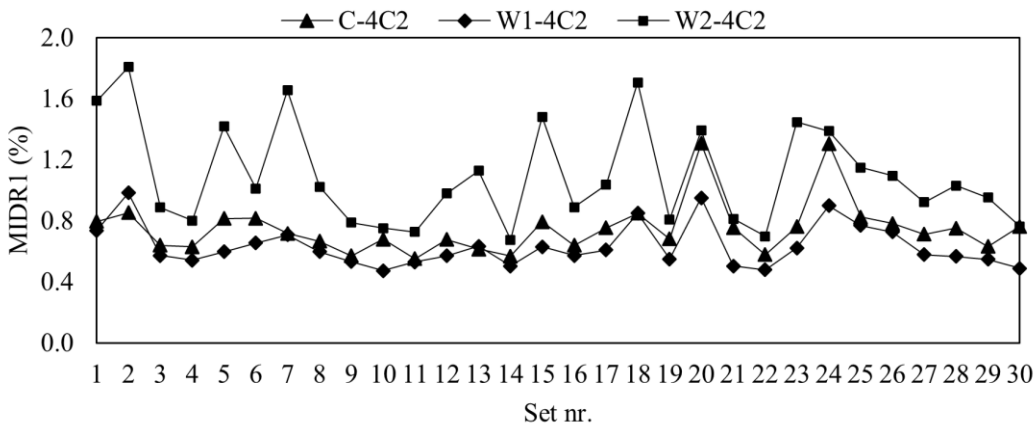

Figure C.42: m_{IDR1} of frames 4C2

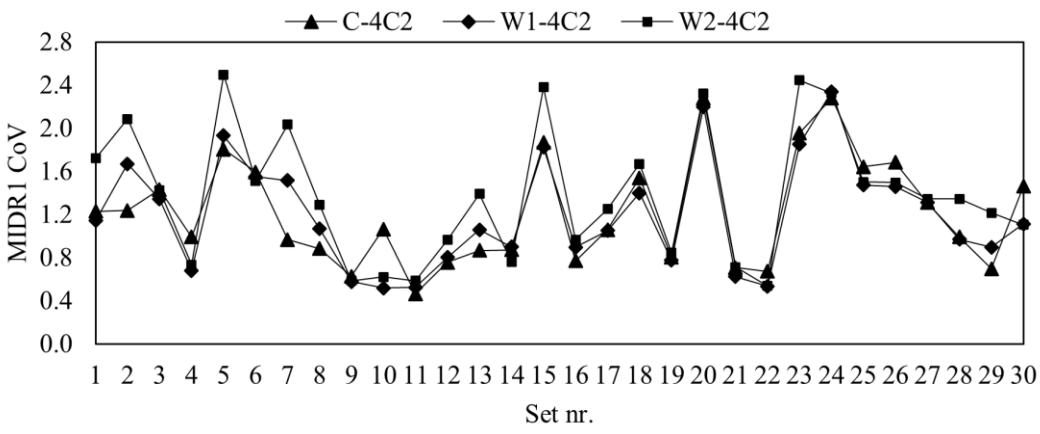

Figure C.43: CoV_{IDR1} of frames 4C2

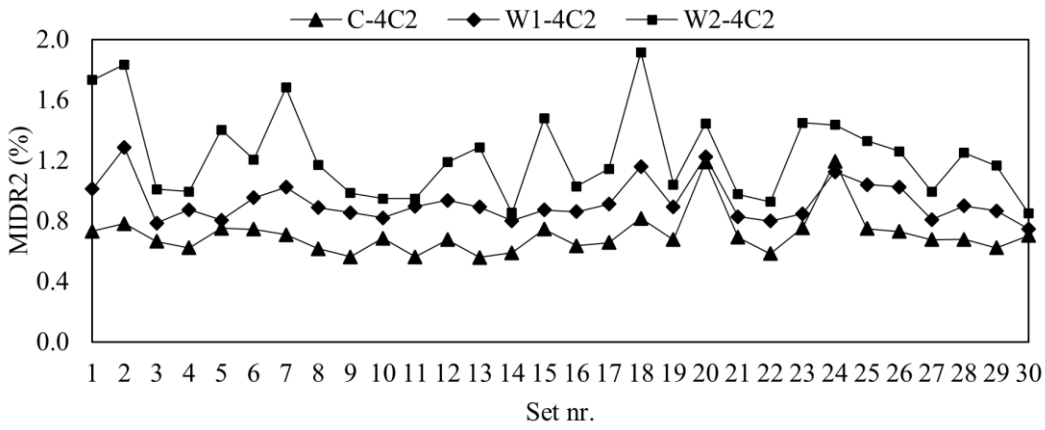

Figure C.44: m_{IDR2} of frames 4C2

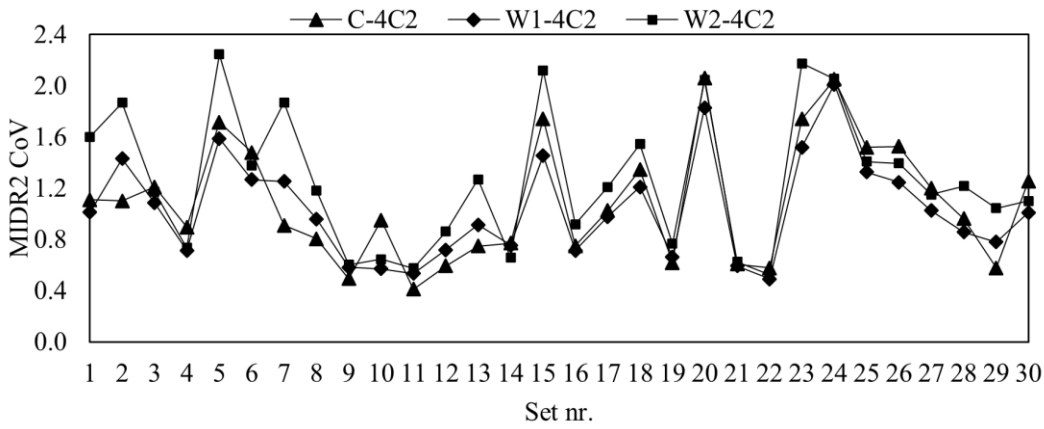

Figure C.45: CoV_{IDR2} of frames 4C2

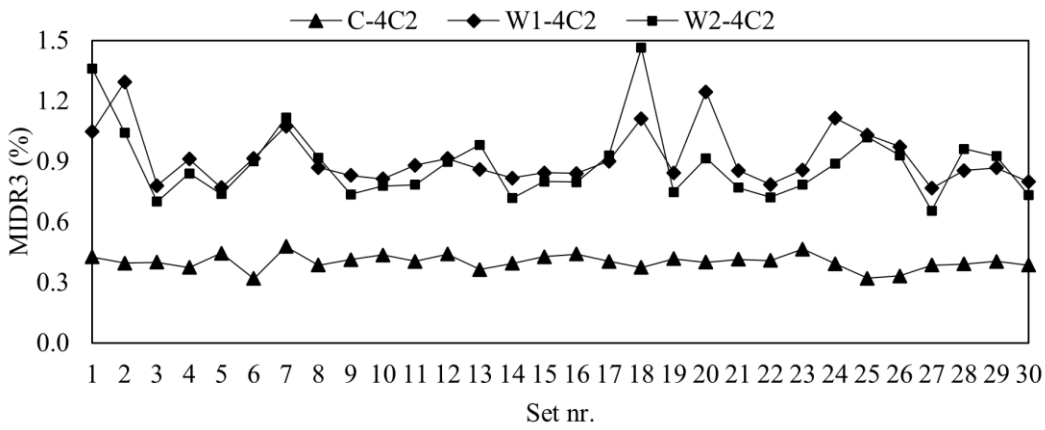

Figure C.46: m_{IDR3} of frames 4C2

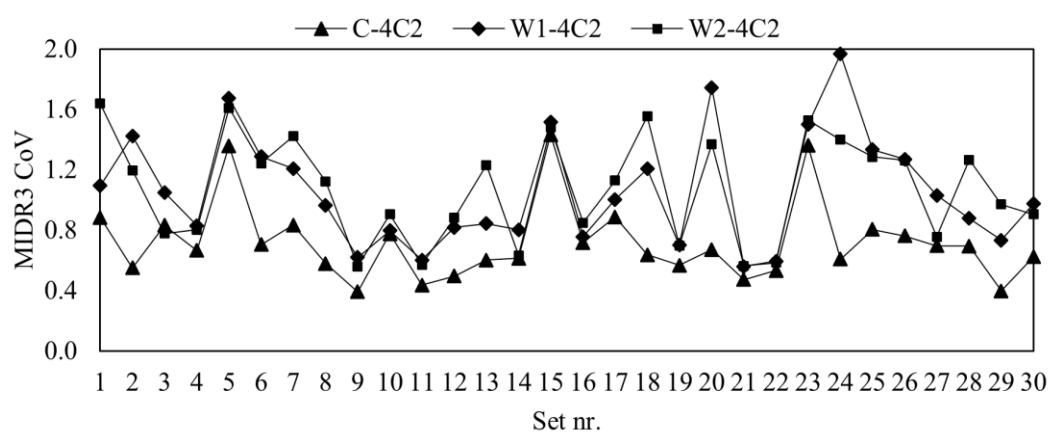

Figure C.47: CoV_{IDR3} of frames 4C2

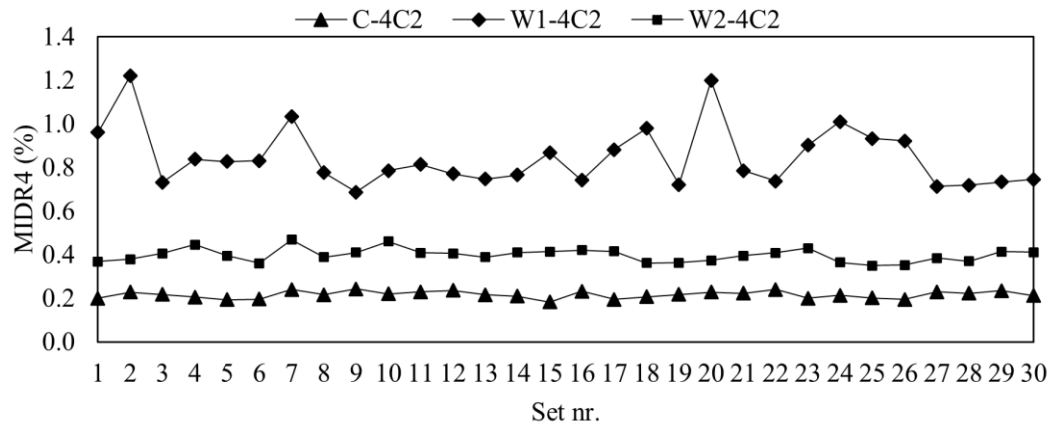

Figure C.48: m_{IDR4} of frames 4C2

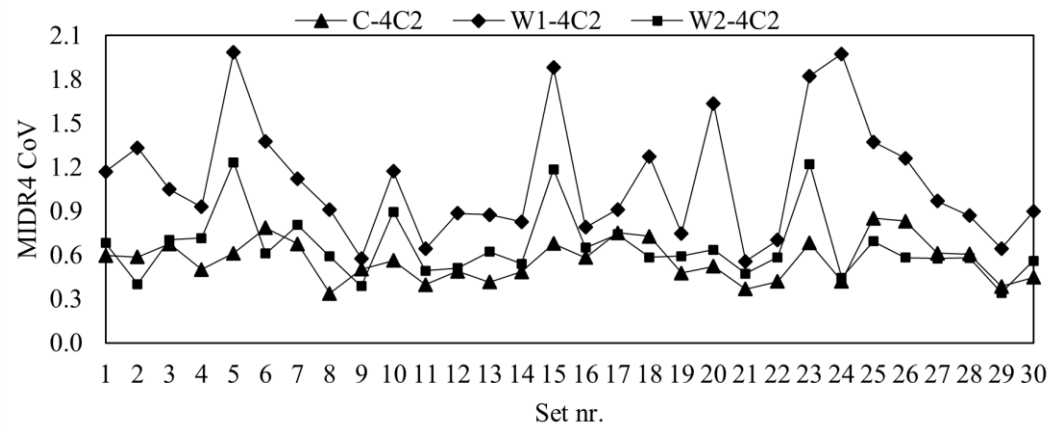

Figure C.49: CoV_{IDR4} of frames 4C2

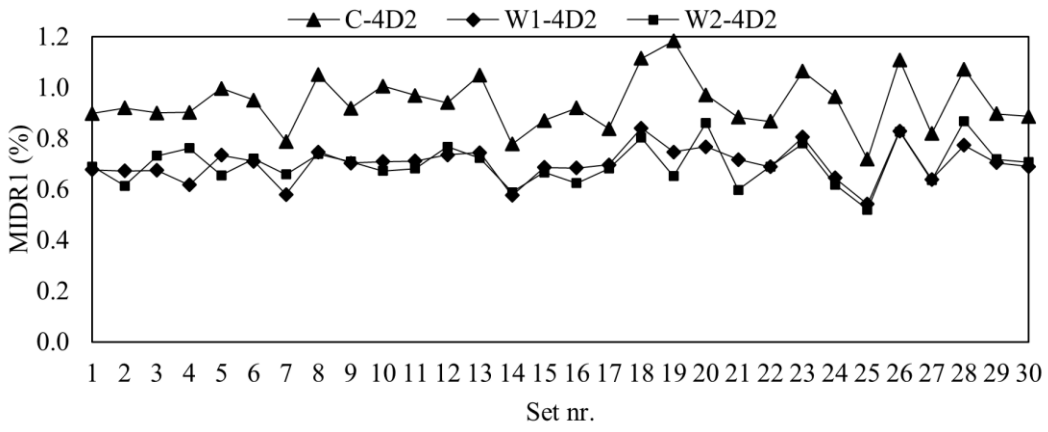

Figure C.50: m_{IDR1} of frames 4D2

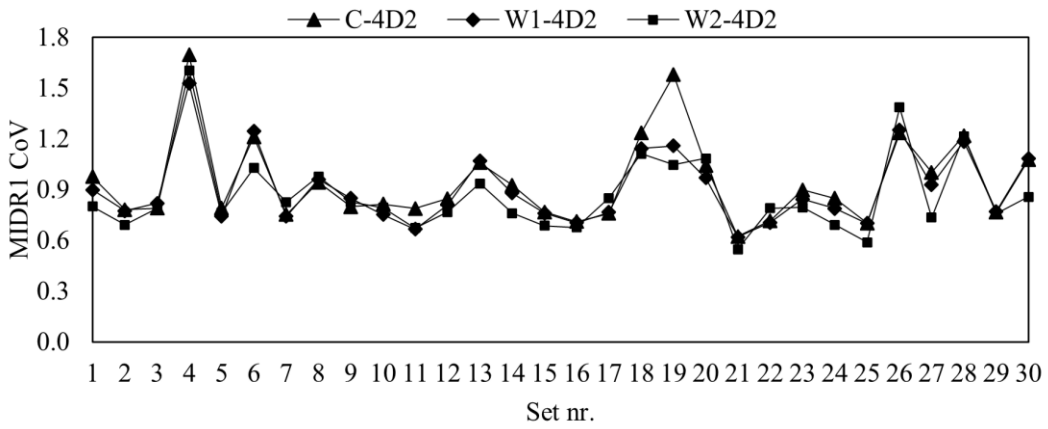

Figure C.51: CoV_{IDR1} of frames 4D2

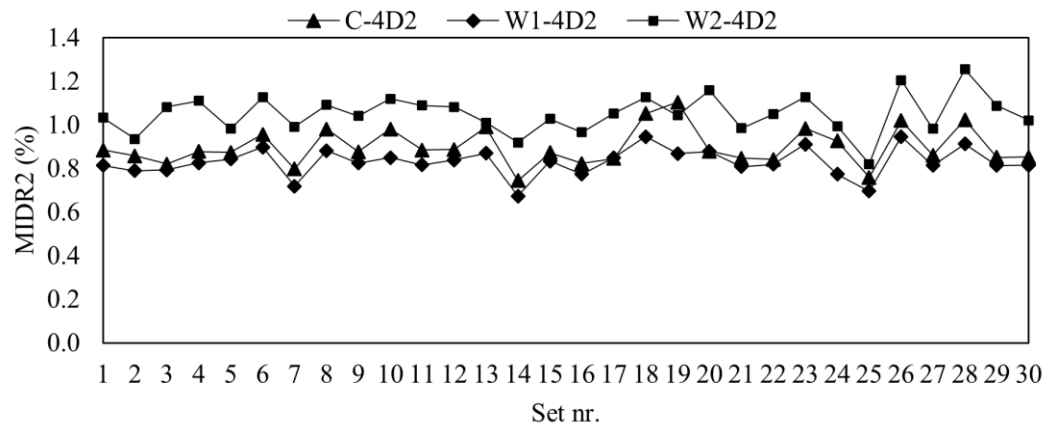

Figure C.52: m_{IDR2} of frames 4D2

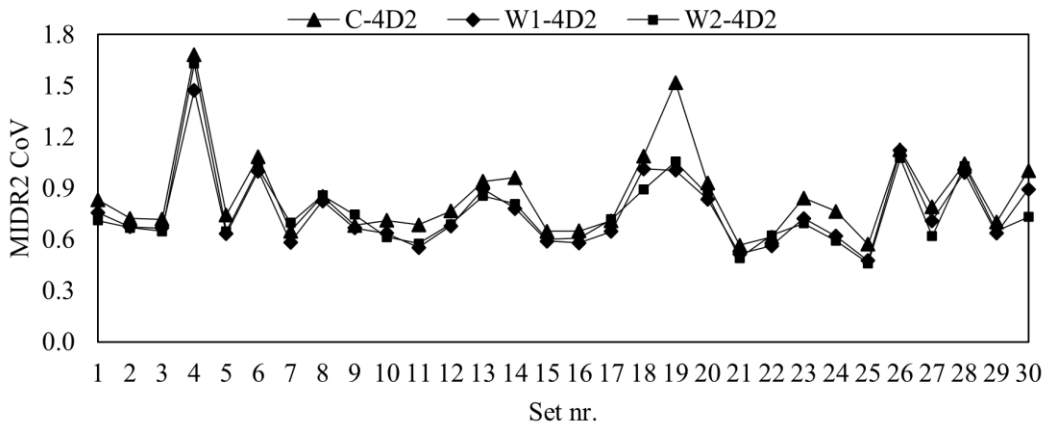

Figure C.53: CoV_{IDR2} of frames 4D2

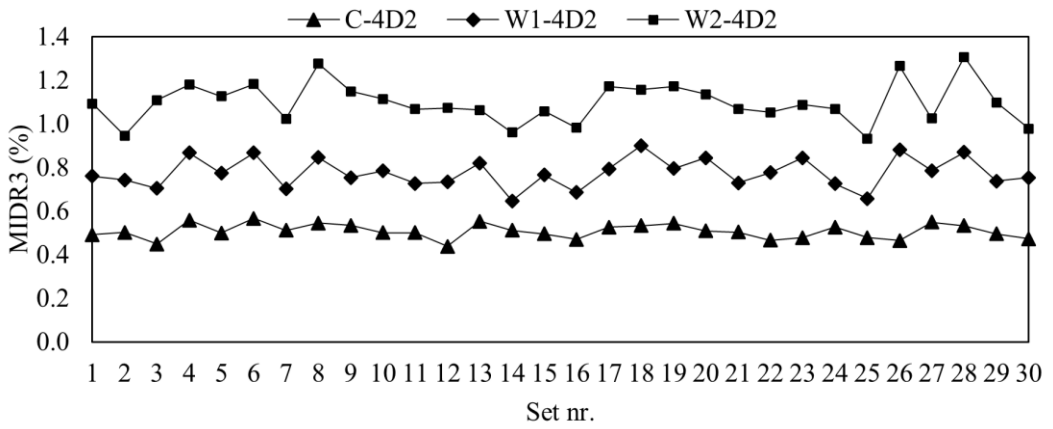

Figure C.54: m_{IDR3} of frames 4D2

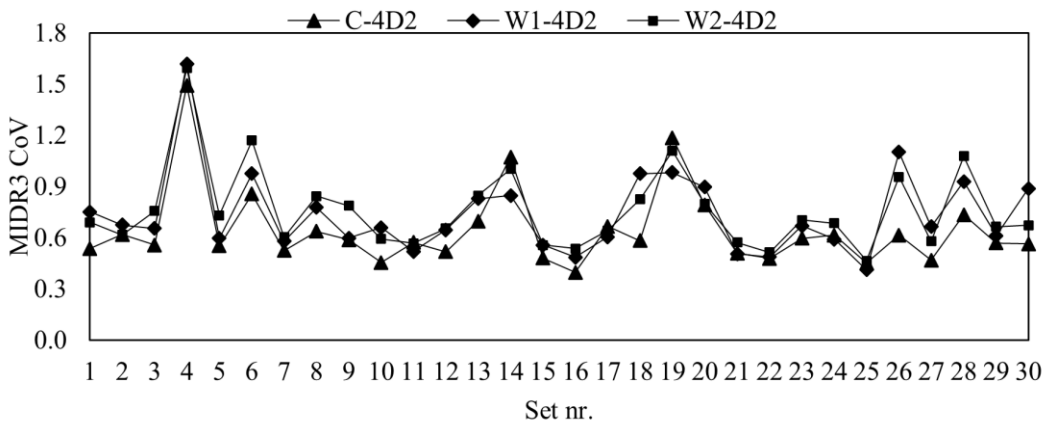

Figure C.55: CoV_{IDR3} of frames 4D2

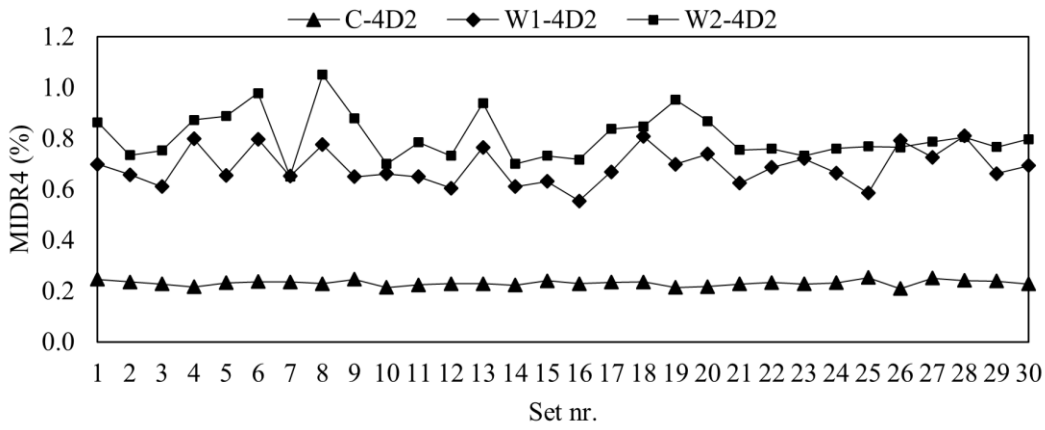

Figure C.56: m_{IDR4} of frames 4D2

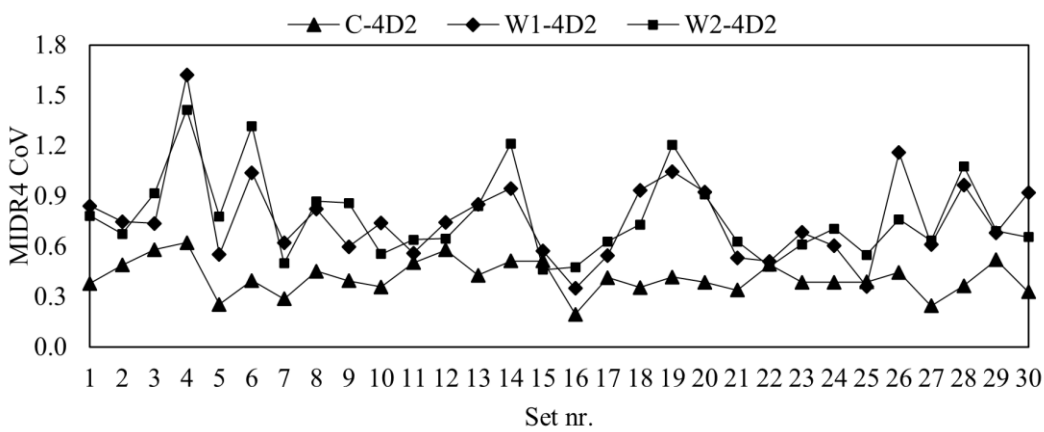

Figure C.57: CoV_{IDR4} of frames 4D2

C.5 Four Story and Six Bay Frames

A4. Section and reinforcement details for W2BF

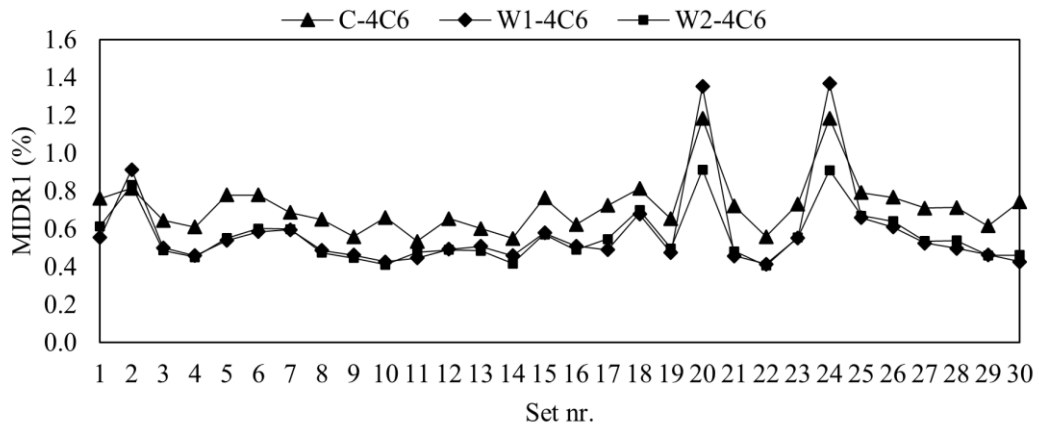

Figure C.58: m_{IDR1} of frames 4C6

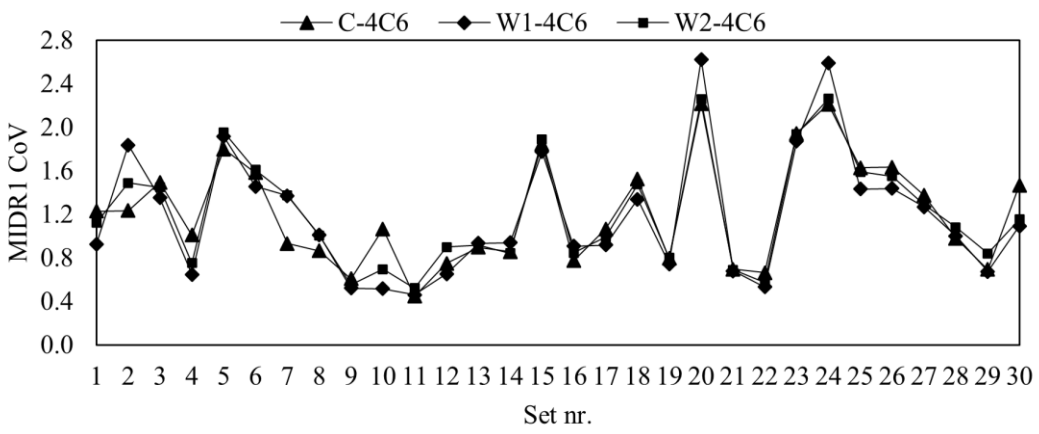

Figure C.59: CoV_{IDR1} of frames 4C6

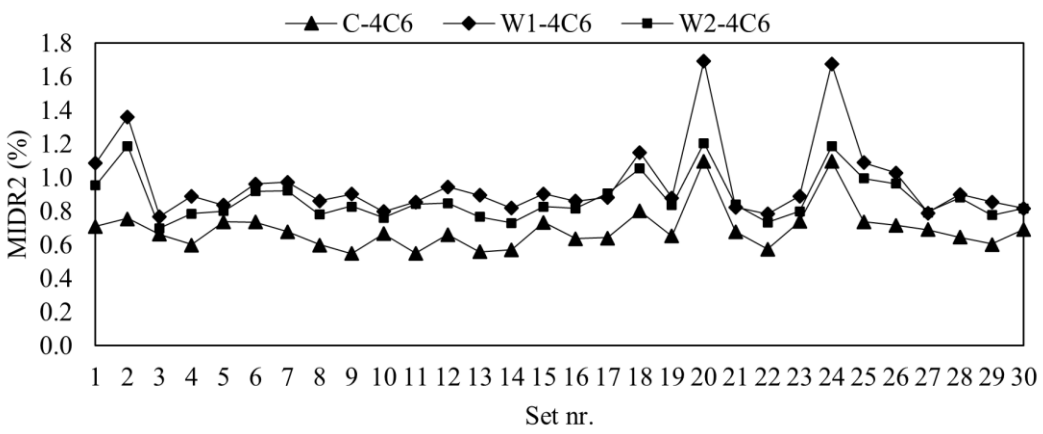

Figure C.60: m_{IDR2} of frames 4C6

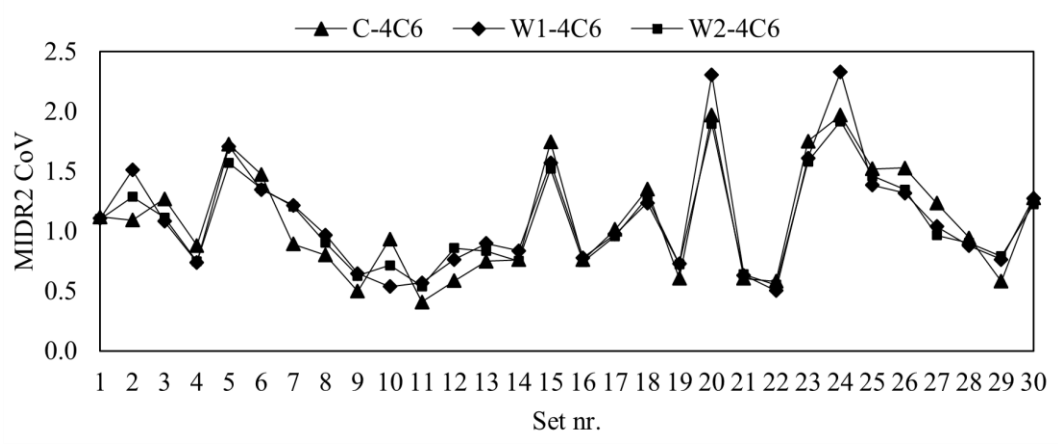

Figure C.61: CoV_{IDR2} of frames 4C6

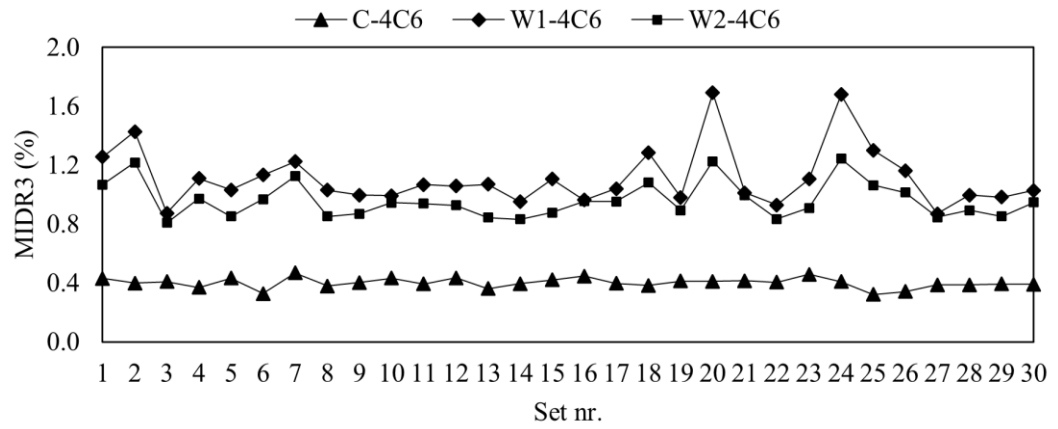

Figure C.62: m_{IDR3} of frames 4C6

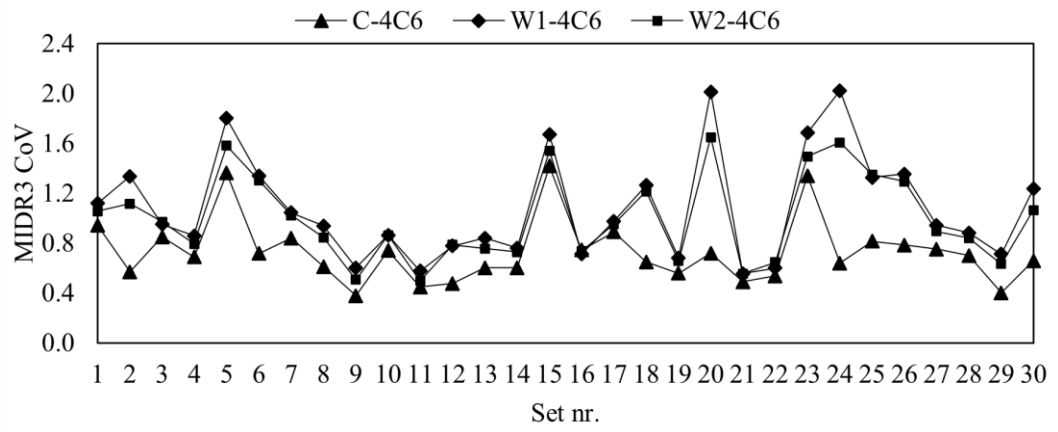

Figure C.63: CoV_{IDR3} of frames 4C6

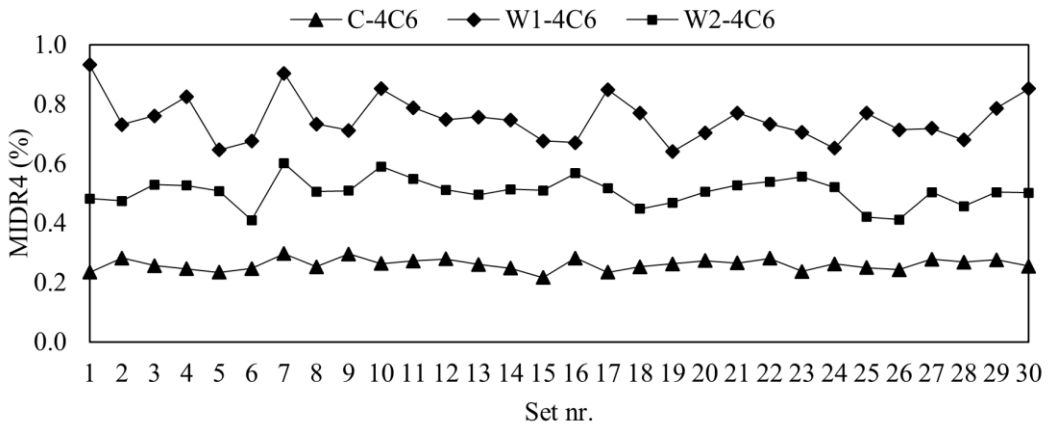

Figure C.64: m_{IDR4} of frames 4C6

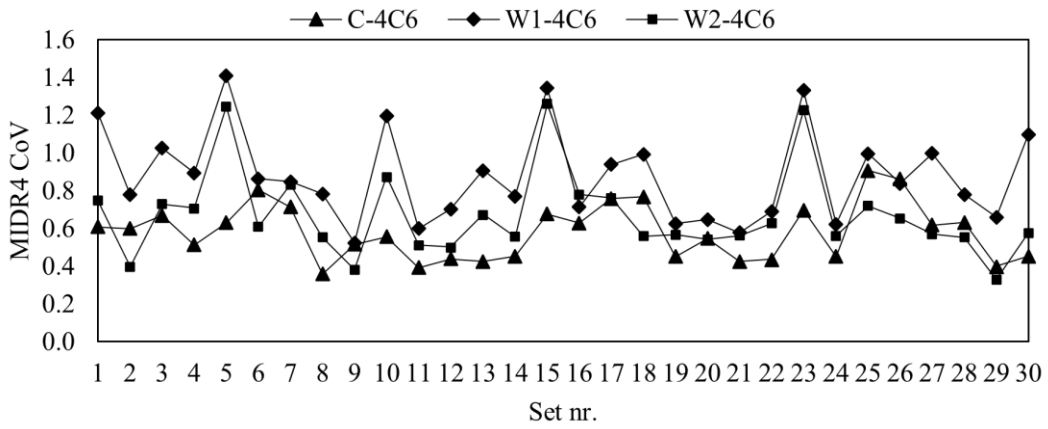

Figure C.65: CoV_{IDR4} of frames 4C6

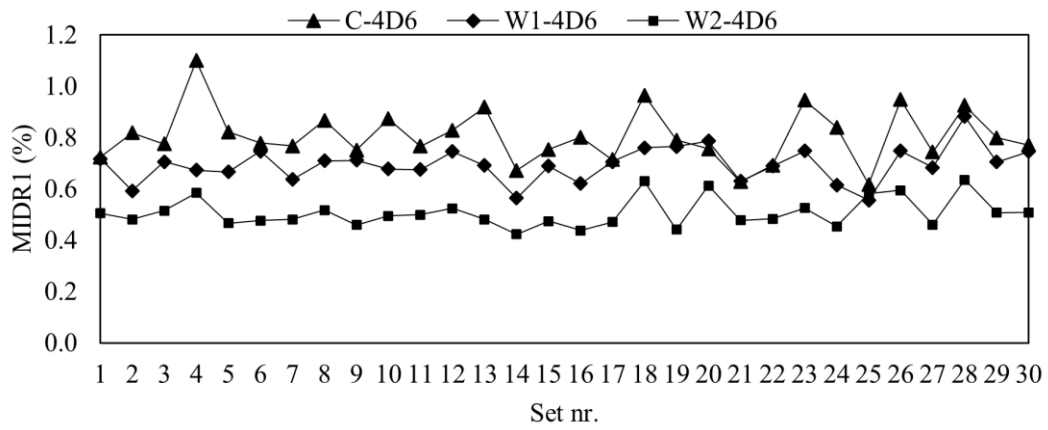

Figure C.66: m_{IDR1} of frames 4D6

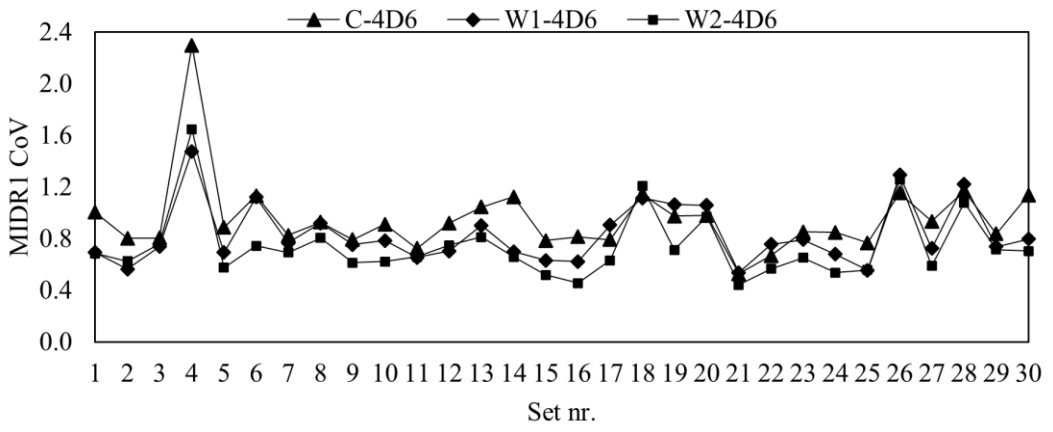

Figure C.67: CoV_{IDR1} of frames 4D6

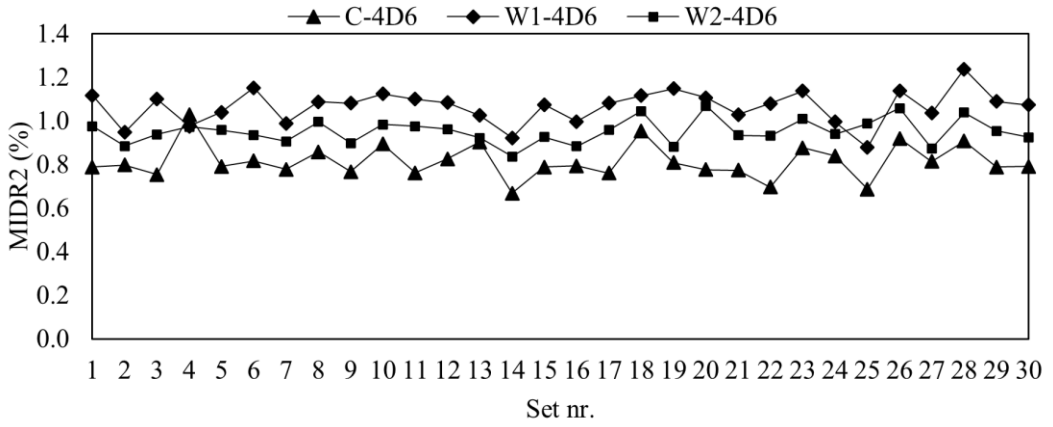

Figure C.68: m_{IDR2} of frames 4D6

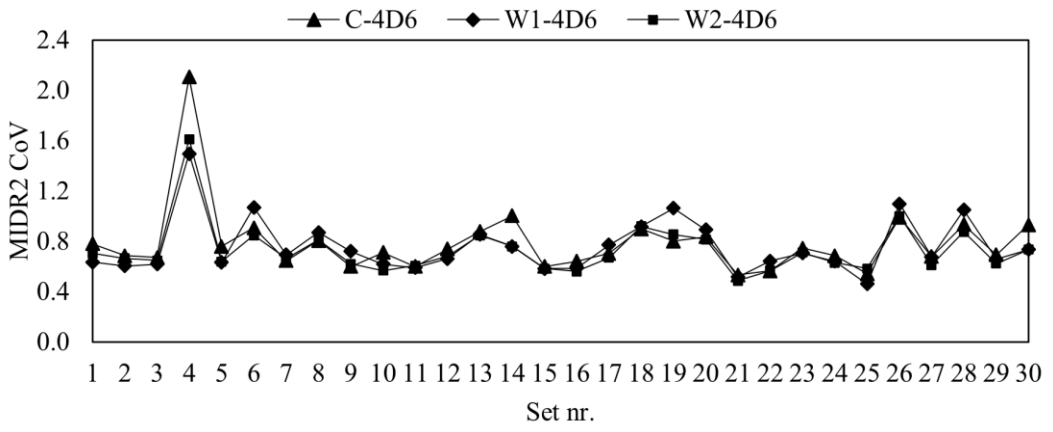

Figure C.69: CoV_{IDR2} of frames 4D6

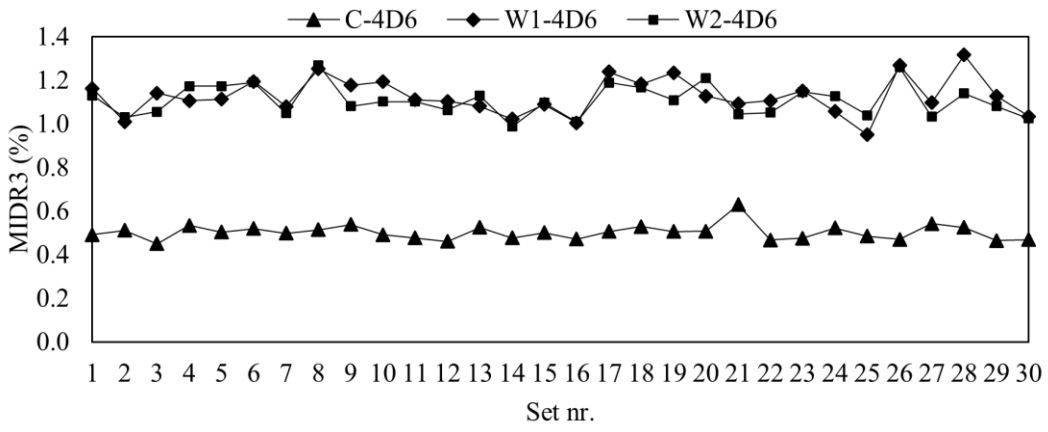

Figure C.70: m_{IDR3} of frames 4D6

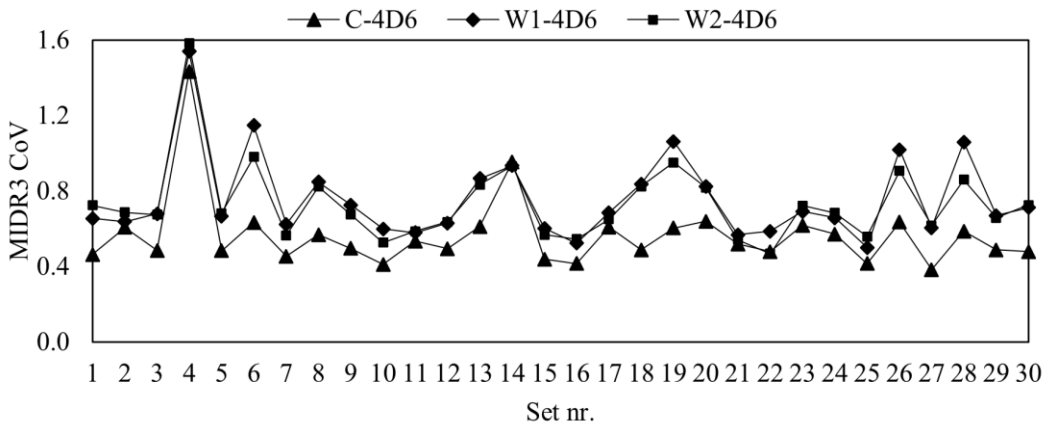

Figure C.71: CoV_{IDR3} of frames 4D6

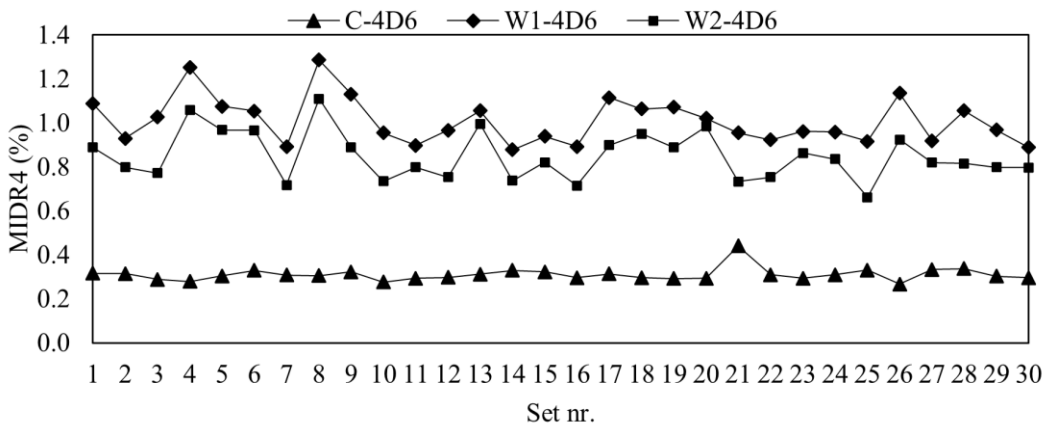

Figure C.72: m_{IDR4} of frames 4D6

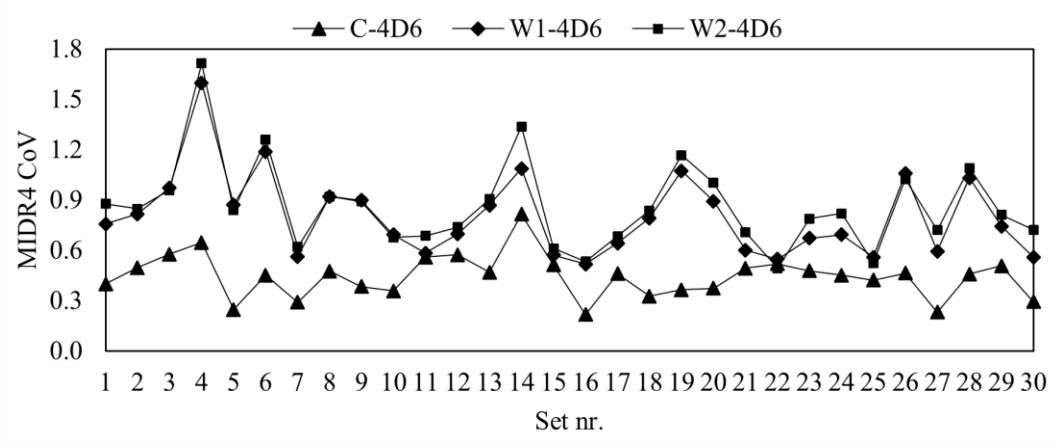

Figure C.73: CoV_{IDR4} of frames 4D6

C.6 Irregular Frames

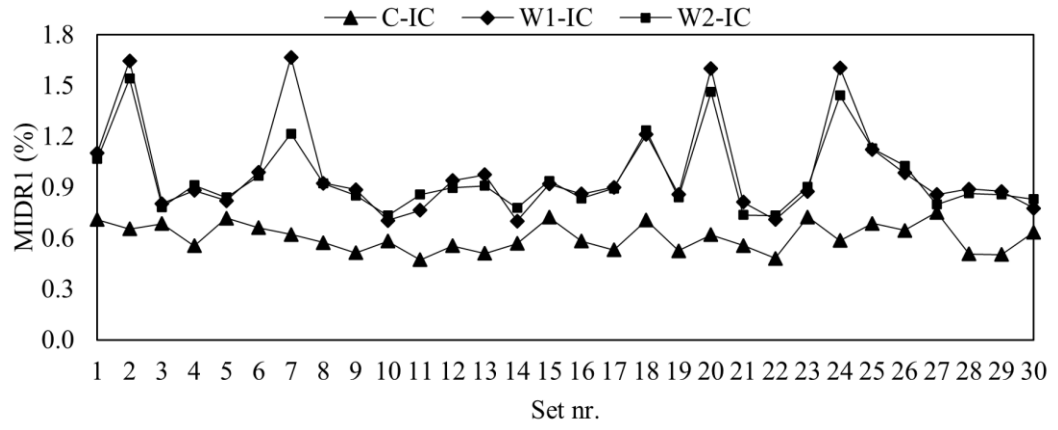

Figure C.74: m_{IDR1} of frames IC

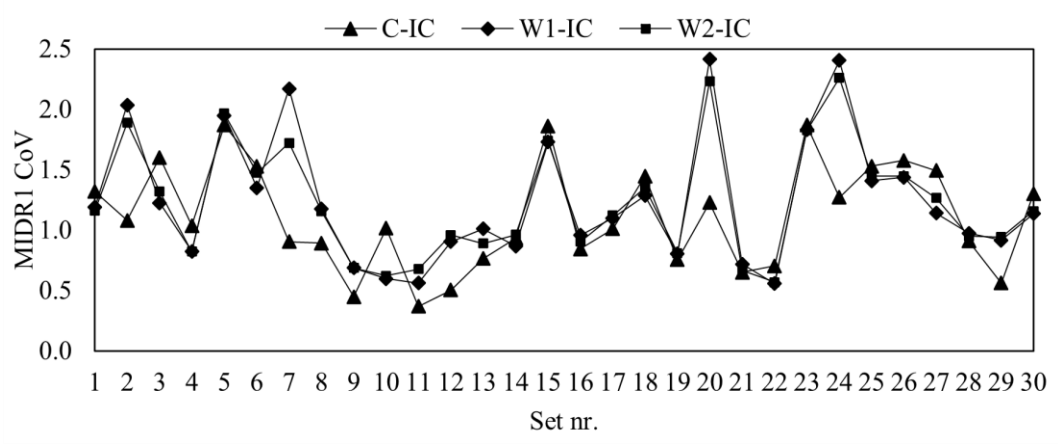

Figure C.75: CoV_{IDR1} of frames IC

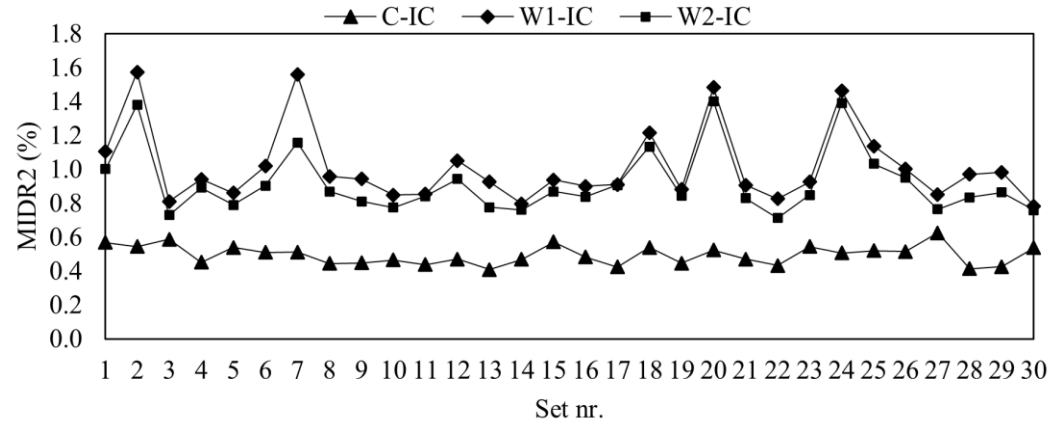

Figure C.76: m_{IDR2} of frames IC

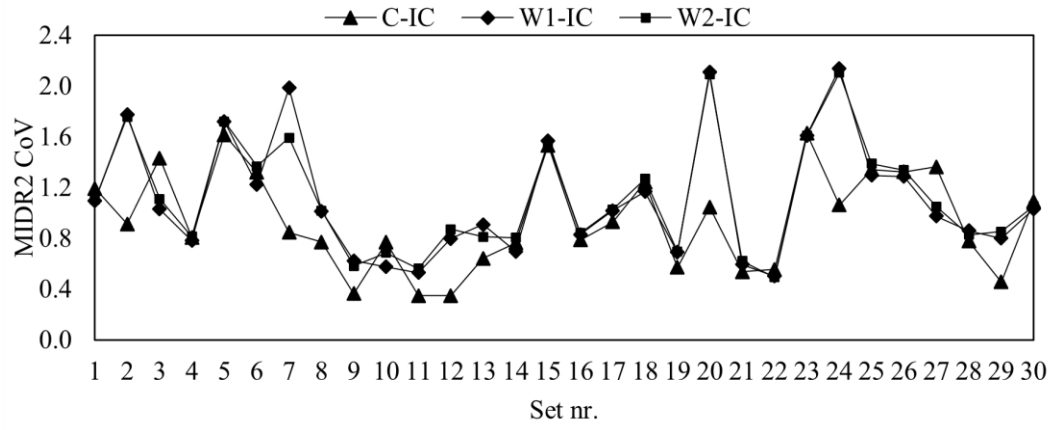

Figure C.77: CoV_{IDR2} of frames IC

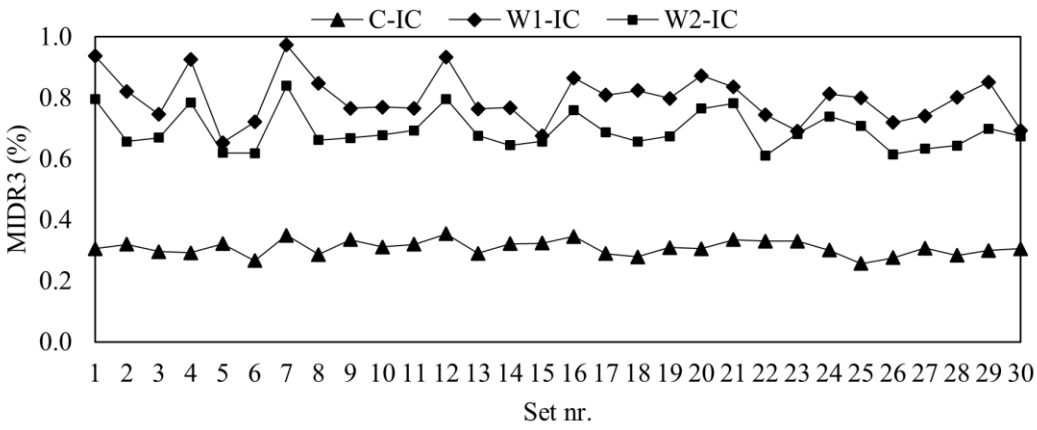

Figure C.78: m_{IDR3} of frames IC

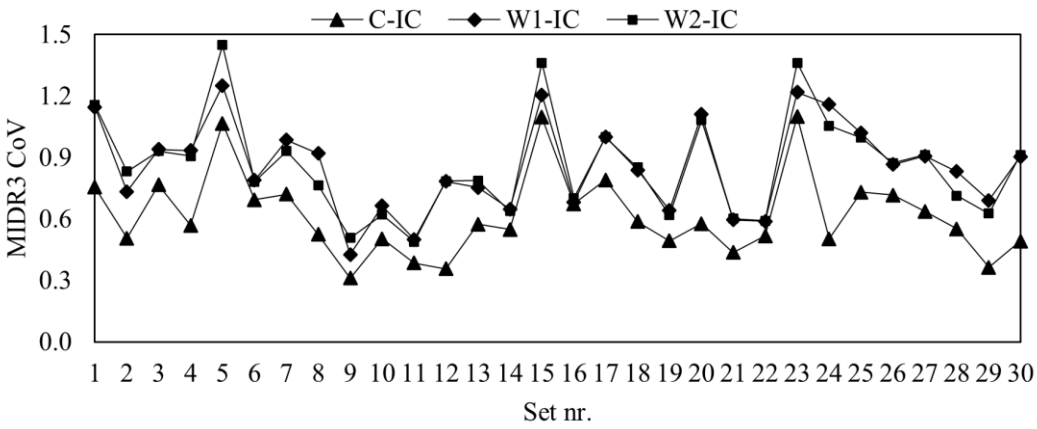

Figure C.79: CoV_{IDR3} of frames IC

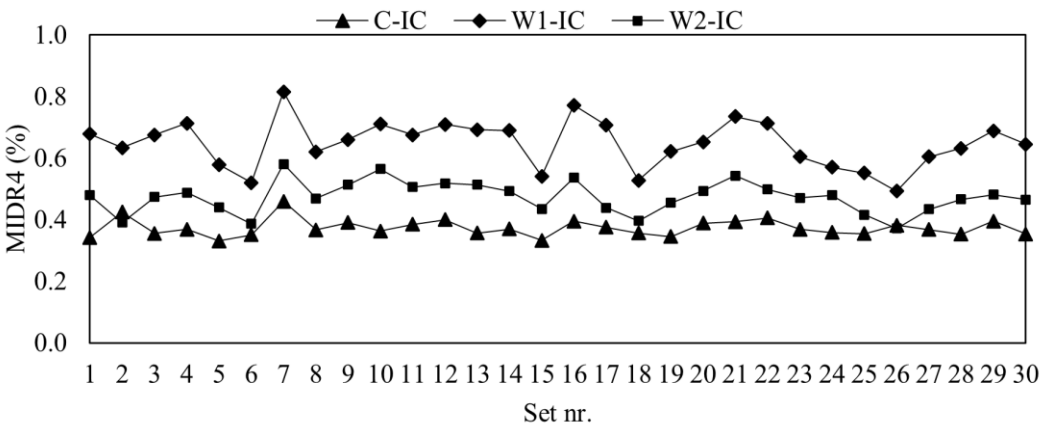

Figure C.80: m_{IDR4} of frames IC

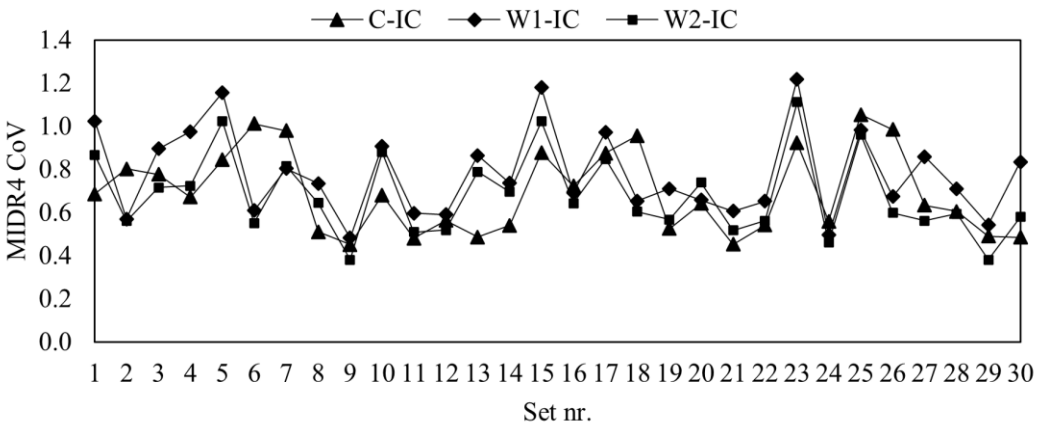

Figure C.81: CoV_{IDR4} of frames IC

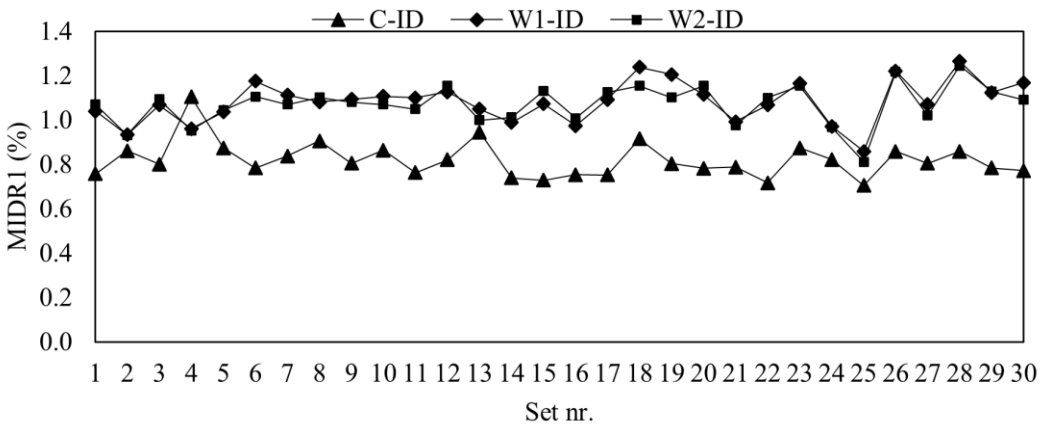

Figure C.82: m_{IDR1} of frames ID

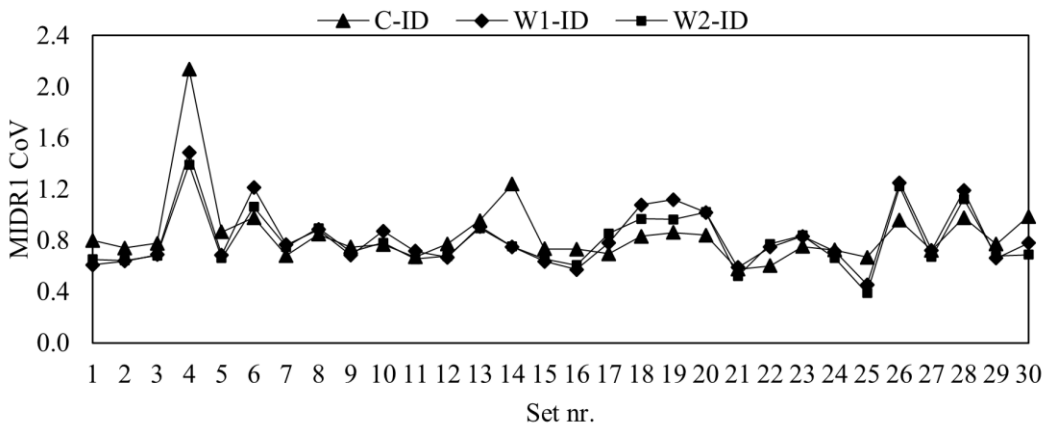

Figure C.83: CoV_{IDR1} of frames ID

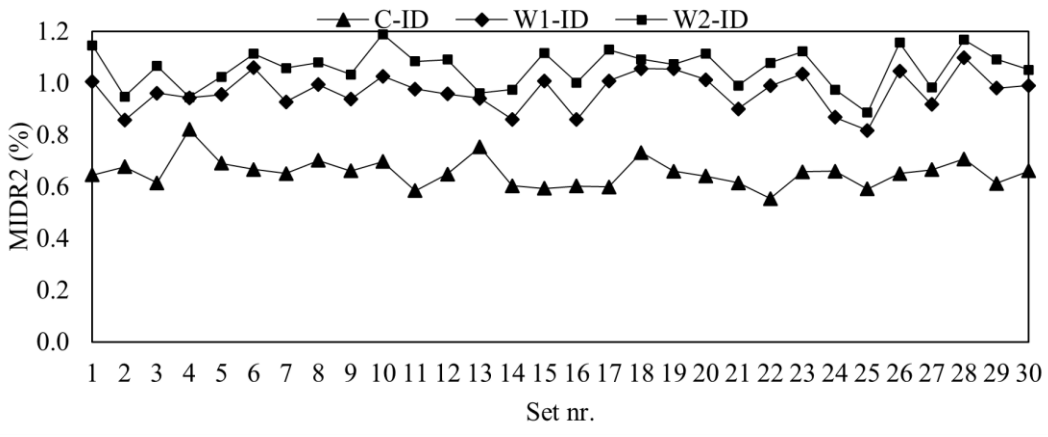

Figure C.84: m_{IDR2} of frames ID

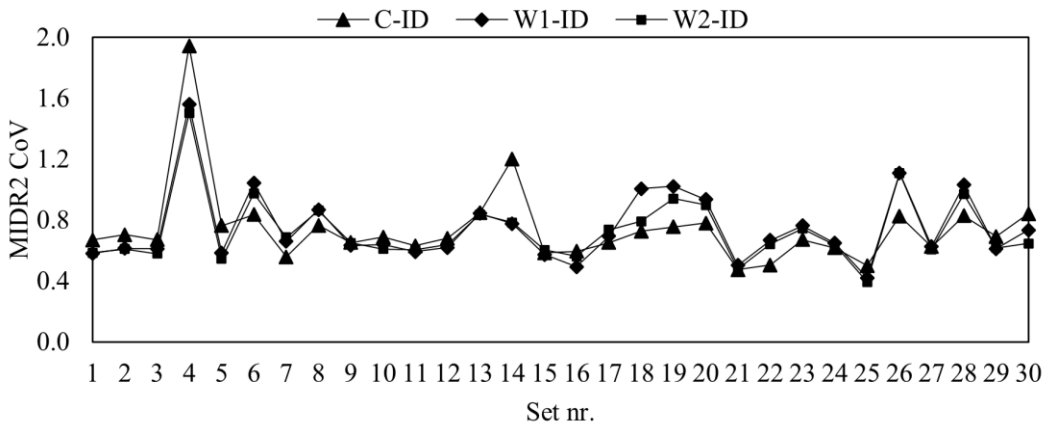

Figure C.85: CoV_{IDR2} of frames ID

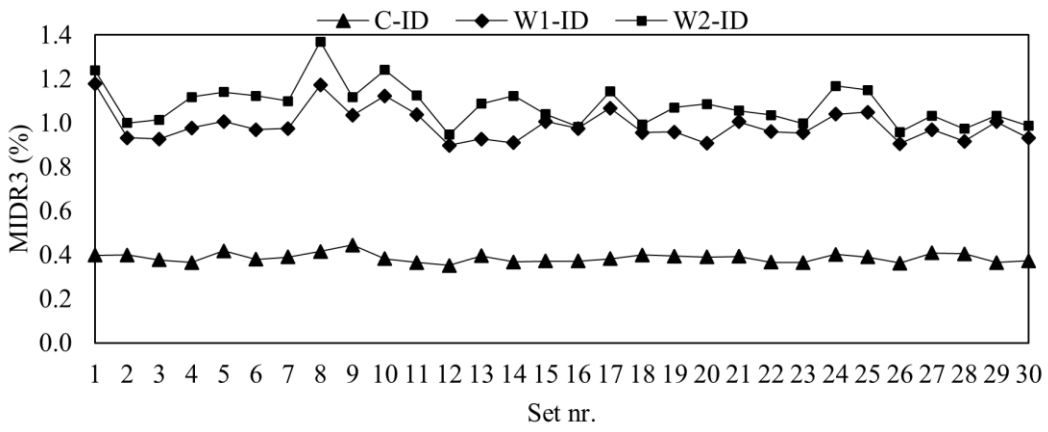

Figure C.86: m_{IDR3} of frames ID

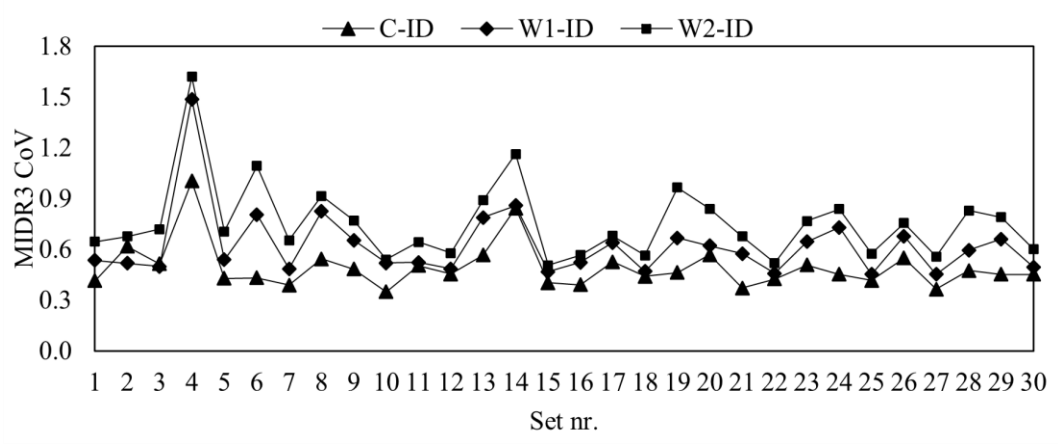

Figure C.87: CoV_{IDR3} of frames ID

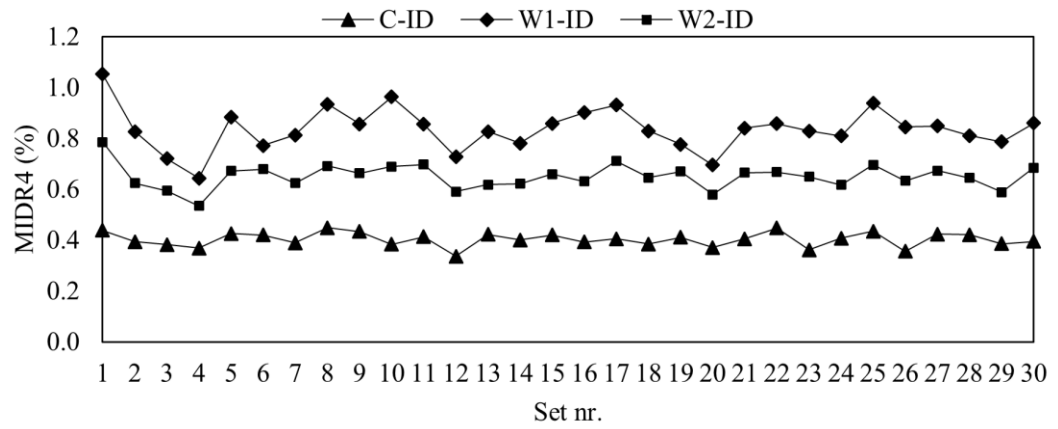

Figure C.88: m_{IDR4} of frames ID

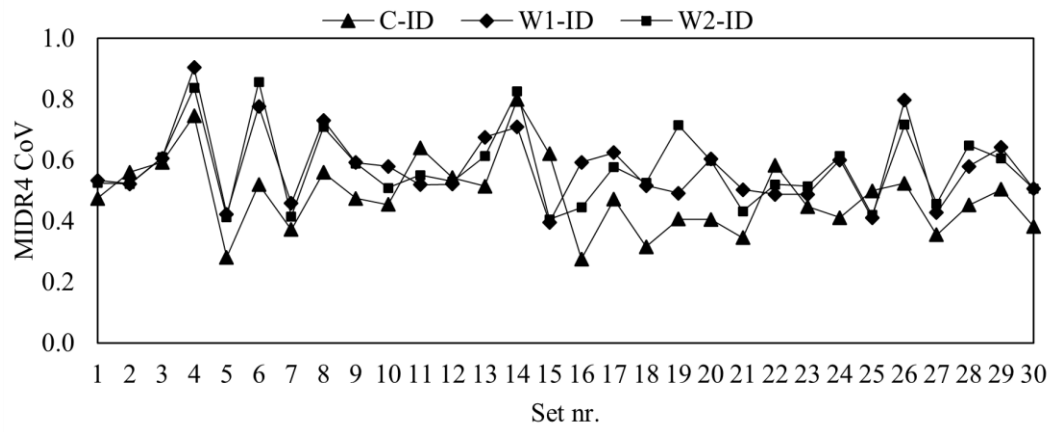

Figure C.89: CoV_{IDR4} of frames ID